

## Dynamics of a supersonic flow over a backward/forward-facing step

Hu, W.

**DOI**

[10.4233/uuid:bac11b77-b808-4700-8f8e-8179458e19bc](https://doi.org/10.4233/uuid:bac11b77-b808-4700-8f8e-8179458e19bc)

**Publication date**

2020

**Document Version**

Final published version

**Citation (APA)**

Hu, W. (2020). *Dynamics of a supersonic flow over a backward/forward-facing step*. [Dissertation (TU Delft), Delft University of Technology]. <https://doi.org/10.4233/uuid:bac11b77-b808-4700-8f8e-8179458e19bc>

**Important note**

To cite this publication, please use the final published version (if applicable).  
Please check the document version above.

**Copyright**

Other than for strictly personal use, it is not permitted to download, forward or distribute the text or part of it, without the consent of the author(s) and/or copyright holder(s), unless the work is under an open content license such as Creative Commons.

**Takedown policy**

Please contact us and provide details if you believe this document breaches copyrights.  
We will remove access to the work immediately and investigate your claim.

**DYNAMICS OF A SUPERSONIC FLOW OVER A  
BACKWARD/FORWARD-FACING STEP**



# **DYNAMICS OF A SUPERSONIC FLOW OVER A BACKWARD/FORWARD-FACING STEP**

## **Dissertation**

for the purpose of obtaining the degree of doctor  
at Delft University of Technology  
by the authority of the Rector Magnificus, Prof. dr. ir. T.H.J.J. van der Hagen  
chair of the Board for Doctorates  
to be defended publicly on  
Monday 14, December 2020 at 10:00 o'clock

by

**Weibo HU**

Bachelor of Engineering in Aerospace Engineering  
Air Force Engineering University, Xi'an, China  
born in Gongyi, China

This dissertation has been approved by the

Promotor: Prof. dr. S. Hickel

Copromotor: Dr. ir. B. W. van Oudheusden

Composition of the doctoral committee:

Rector Magnificus

Prof. dr. S. Hickel

Dr. ir. B. W. van Oudheusden

Chairperson

Delft University of Technology, promotor

Delft University of Technology, copromotor

Independent members:

Prof. dr. ir. B. J. Boersma

Prof. dr. J.-C. Robinet

Prof. dr. N. D. Sandham

Prof. dr. S. Pirozzoli

Dr. Z. Sun

Delft University of Technology

Arts et Metiers ParisTech

University of Southampton

Sapienza University of Rome

City University of London

Reserved:

Prof. dr. F. Scarano

Delft University of Technology



*Keywords:* compressible flow, boundary layer, transition, shock waves

*Cover designed by:* Weibo HU

Copyright © 2020 by W. Hu

ISBN 978-94-6366-346-5

An electronic version of this dissertation is available at

<http://repository.tudelft.nl/>.

# SUMMARY

The backward/forward-facing step (BFS/FFS) is one of the canonical geometries in aerospace engineering applications, the flow field over which has attracted extensive attention in the past decades. In a supersonic flow, laminar-to-turbulent transition and shock wave/boundary layer interaction (SWBLI) can occur over these configurations, which considerably affect the performance of aircraft, through, for example, an increase of flight drag and intense localized mechanical loads. In this thesis, a numerical study is carried out to scrutinize the dynamics of a supersonic flow over a backward/forward-facing step at  $Ma = 1.7$  and  $Re_{\delta_0} = 13718$  using well-resolved large eddy simulations (LES). For the transition aspect, our objective is to determine the transition path and the roles of the instabilities involved in this process. Considering the topic of SWBLI, the main objective is to scrutinize the various unsteady phenomena observed in SWBLI and, in particular, identify the origin of the low-frequency unsteadiness.

The first part of the thesis concerns the dynamics of BFS flows by analyzing four cases, differing in the character of the upstream flow conditions imposed at the inlet of the computational domain: including a fully laminar case, two perturbed laminar cases with low- and high-amplitude oblique Tollmien-Schlichting (T-S) waves, and a turbulent case. The results from the fully laminar case indicate that the boundary layer transition is initiated by a Kelvin-Helmholtz (K-H) instability of the separated shear layer, followed by secondary modal instabilities of the K-H vortices, leading to  $\Lambda$ -shaped vortices, hair-pin vortices and finally to a fully turbulent state. Imposed with low-amplitude T-S waves at the inlet, the transition follows a similar path as the fully laminar case although the linear growth of the oblique T-S waves is the prevailing instability upstream of the step and they also act as the primary mode via a quasi-linear growth within a short distance behind the step. In contrast, the case with high-amplitude T-S waves shows a rapid transition due to the high initial disturbance level such that the nonlinear interactions already occur upstream of the step, before the K-H instability could get involved. Overall, these three cases all follow a modal transition road, excited by a T-S or K-H instability. Together with the turbulent case, they all feature a broadband range of low-frequency unsteady phenomena in the SWBLI system, including vortex shedding in the shear layer, the flapping motion of the shock and the breathing of the separation bubble. The spectral analysis reveals that the low-frequency behavior of the system is related to the interaction between shock wave and separated shear layer, while the medium-frequency motions are associated with the shedding of shear-layer vortices. The dynamic mode decomposition (DMD) suggests that Görtler-like vortices,

which are induced by the centrifugal forces originating from the strong curvature of the streamlines in the reattachment region, are strongly correlated with the low-frequency unsteadiness. The comparison with the fully laminar case provides evidence that these unsteady counter-rotating vortices are also affected by fluctuations in the incoming boundary layer.

The second part of the thesis presents the similar investigation in FFS flows considering again four cases, covering a fully laminar case, two perturbed cases with low- and high-amplitude oblique T-S waves, and a turbulent case. All laminar cases follow a classic modal transition path, in which the transition is initiated by the growth of the oblique T-S waves, followed by the generation of spanwise vorticity, induced near-wall  $\Lambda$ -shaped vortices and finally turbulent spots with small hairpin vortices of different spatial scales. Similar with the BFS flows, all the FFS cases feature unsteady SWBLI with various spatial and temporal scales. Among the broadband frequencies, the low-frequency contents are relevant to the oscillation of the shock wave and the expansion/shrinking of the separation bubble, while the medium-frequency motions involve the vortex shedding in the shear layer. Similarly, the centrifugal forces and induced Görtler vortices are the main driving mechanism for the global low-frequency unsteadiness in the turbulent FFS case.

# SAMENVATTING

De achterwaarts/voorwaarts gerichte trede (BFS/FFS) is een van de canonieke geometrieën in de lucht-en ruimtevaarttechniek en het stroming veld waaraan veel aandacht is geschonken in de afgelopen decennia. In een supersonische stroming kan bij deze configuraties een laminair naar turbulente overgang en een schokgolf/grenslaag interactie (SWBLI) optreden. Deze kunnen leiden tot aanzienlijk gevaarlijke effecten op de prestaties van vliegtuigen, zoals een toename in luchtweerstand en zeer hoge lokale mechanische belastingen. In dit proefschrift wordt, met behulp van een goed opgeloste grote wervel simulatie (LES), een numerieke studie uitgevoerd om de dynamiek van de supersonische stroming over een achterwaarts/voorwaarts gerichte trede bij  $Ma = 1.7$  and  $Re_{\delta_0} = 13718$  te onderzoeken. Voor het transitie-aspect is ons doel het bepalen van het transitie pad en het identificeren van de verschillende rollen van de betrokken instabiliteiten in dit proces. Het belangrijkste doel is om de verschillende instabiele verschijnselen die in de SWBLI zijn waargenomen nauwkeurig te onderzoeken en, in het bijzonder, om de oorsprong van de lage-frequentie instabiliteit te identificeren.

Het eerste deel van het proefschrift onderzoekt de dynamiek van de BFS-stroming door vier gevallen te analyseren die verschillen in de opwaartse stromings omstandigheden. De verschillende gevallen die worden opgelegd aan de inlaat van het computerdomein zijn: een volledig laminair geval, twee verstoorde laminaire gevallen met lage en hoge-amplitude schuine Tollmien-Schlichting (T-S) golven, en een turbulent geval. De resultaten van het volledig laminaire geval geven aan dat de transitie van de grenslaag wordt geïnitieerd door een Kelvin-Helmholtz (K-H) instabiliteit van de gescheiden schuiflaag, gevolgd door secundaire modale instabiliteit van de K-H wervelingen, wat leidt tot  $\Lambda$ -vormige wervelingen, haarspeld wervelingen en uiteindelijk tot een volledig turbulente toestand. Wanneer bij de inlaat T-S golven met lage amplitude worden opgelegd, volgt de transitie hetzelfde pad dan het deed in het volledig laminaire geval, hoewel de lineaire groei van de schuine T-S golven de heersende instabiliteit stroomopwaarts van de trede is. Daarnaast fungeren ze ook als de primaire modus via een quasi-lineaire groei op korte afstand achter de trede. Daarentegen vertoont het geval met T-S golven met hoge amplitude een snelle transitie vanwege het hoge initiële verstoringsniveau, zodat de niet-lineaire interacties al stroomopwaarts van de trede plaatsvinden, voordat de K-H instabiliteit erbij betrokken zou kunnen raken. Over het algemeen volgen deze drie gevallen allemaal een modale transitie, geïnitieerd door een instabiliteit van de T-S of K-H. Samen met het turbulente geval vertonen ze allemaal een breedband bereik van lage frequentie, instabiele verschijnselen in het SWBLI-systeem, waaronder vortex

afscheiding in de afschuiflaag, de flapperende beweging van de schok en de ademhaling van de scheidingsbel. De spectrale analyse laat zien dat het laagfrequente gedrag van het systeem gerelateerd is aan de interactie tussen de schokgolf en de afzonderlijke afschuiflaag, terwijl de middenfrequente bewegingen geassocieerd zijn met het afstoten van de afschuiflaag wervelingen. De dynamische modus ontleding (DMD) suggereert dat Görtler-achtige wervelingen, die worden veroorzaakt door de middelpuntvliedende krachten die voortkomen uit de sterke kromming van de stroomlijnen in het herbevestigingsgebied, sterk verband houden met de lage frequentie instabiliteit. De vergelijking met het vergelijkbare, maar puur laminair geval, levert het bewijs dat deze onstabiele, tegengesteld draaiende wervelingen ook worden beïnvloed door schommelingen in de binnenkomende grenslaag.

Het tweede deel van het proefschrift presenteert een soortgelijk onderzoek in FFS-stromingen, waarbij opnieuw vier gevallen worden behandeld, een volledig laminair geval, twee verstoorde gevallen met respectievelijk lage en hoge amplitude schuine T-S golven en een turbulent geval. Alle laminaire gevallen volgen een klassiek modaal transitie pad, waarbij de transitie wordt geïnitieerd door de groei van de schuine T-S golven, gevolgd door de opwekking van spanwijdte-wervelingen, geïnduceerde  $\Lambda$ -vormige wervelingen in de buurt van de wand en tenslotte turbulente plekken met kleine haarspeld-wervelingen van verschillende ruimtelijke schalen. Net als bij de BFS-stromingen, bevatten alle FFS-gevallen instabiele SWBLI met verschillende ruimtelijke schalen en tijd schalen. Onder de breedbandfrequenties is de lage frequentie inhoud relevant voor de oscillatie van de schokgolf en het uitzetten/krimpen van de scheidingsbel, terwijl de midden frequentie bewegingen de werveling in de afschuiflaag met zich meebrengen. Evenzo zijn de middelpuntvliedende krachten en geïnduceerde Görtler-wervelingen het belangrijkste aandrijfmechanisme voor de globale lage frequentie instabiliteit in het turbulente FFS-geval.

# NOMENCLATURE

## LATIN SYMBOLS

$A$	area of the separation bubble or amplitude
$c$	chord length of an airfoil
$c_{ph}$	phase velocity
$C_f$	skin friction
$E$	total energy
$f$	frequency
$G$	filter kernel
$G_t$	Görtler number
$H$	shape factor
$h$	step height
$I$	integral length scale or fluctuation intensity
$l$	Blasius length
$L_r$	reattachment/separation length
$Ma$	Mach number
$p$	pressure
$Pr$	Prandtl number
$q$	heat flux or a general scalar
$R$	specific gas constant or curvature radius
$R_{ij}$	correlation coefficient between two signals
$Re$	Reynolds number
$S$	vortex stretching term
$St$	Strouhal number
$T$	temperature or vortex tilting term

$t$	time
$u$	streamwise velocity
$u_\infty$	free stream velocity
$v$	wall-normal velocity
$w$	spanwise velocity
$x$	streamwise coordinate
$x_l$	shock location
$x_r$	reattachment location
$x_s$	separation location
$y$	wall-normal coordinate
$z$	spanwise coordinate

## GREEK SYMBOLS

$\alpha_i$	streamwise growth rate
$\alpha_r$	streamwise wavenumber
$\beta_i$	spanwise growth rate
$\beta_r$	spanwise wavenumber
$\delta$	boundary layer thickness
$\delta^*$	displacement thickness
$\delta_{ij}$	Kronecker delta function
$\epsilon_{ijk}$	Levi-Civita symbol
$\eta$	shock angle
$\gamma$	specific heat ratio
$\kappa$	thermal conductivity
$\lambda$	wavelength or spatial spacing
$\mu$	dynamic viscosity or eigenvalue
$\nu$	kinematic viscosity
$\omega$	vorticity or angular frequency
$\omega_i$	temporal growth rate
$\omega_r$	angular frequency
$\phi$	mode from dynamic mode decomposition
$\rho$	density
$\sigma$	population standard deviation
$\tau_{ij}$	viscous stress tensor

$\theta$  momentum thickness or wave/phase angle

## SUBSCRIPTS/SUPERSCRIPTS

0 inlet or stagnation parameters  
 $\infty$  free stream parameters  
 $\tau$  based on wall friction velocity  
 $l$  based on Blasius length  
 $h$  based on step height  
 $\delta$  based on inlet boundary layer thickness  
 $r$  based on the separation length  $L_r$  or real part  
 $i$  imaginary part  
ref reference value  
 $w$  property at the wall

## ACRONYMS

ALDM adaptive local deconvolution method  
BFS backward-facing step  
CFD computational fluid dynamics  
CFL Courant-Friedrichs-Lewy (number)  
DF digital filter  
DMD dynamic mode decomposition  
DNS direct numerical simulation  
FFS forward-facing step  
FST free stream turbulence  
FWPSD frequency weighted power spectral density  
ILES implicit large eddy simulation  
K-H Kelvin-Helmholtz  
LES large eddy simulation  
LST linear stability theory  
N-S Navier-Stokes  
NPLS nano-tracer-based planar laser scattering  
O-S Orr-Sommerfeld  
PIV particle image velocimetry  
PLS planar laser scattering

PME	Prandtl-Meyer expansion
PSE	parabolized stability equations
RANS	Reynolds-averaged Navier-Stokes
RMS	root mean square
SGS	subgrid scale
SPDMD	sparsity-promoting dynamic mode decomposition
SVD	singular-value decomposition
SWBLI	shock wave/boundary layer interaction
T-S	Tollmien-Schlichting
TVD	total variation diminishing
WENO	weighted essentially non-oscillatory

## OTHER SYMBOLS

*	convolution
$\bar{\cdot}$	spatially filtered quantity
$\cdot'$	fluctuation
$\langle \cdot \rangle$	mean value or steady value
$\lceil \cdot \rceil$	ceiling function
$\nabla$	Nabla symbol
$\Sigma$	summation
$\times$	curl operator
$\tilde{\cdot}$	numerical (discrete) approximation
$\hat{\cdot}$	analytical (continuous) approximation
$\mathcal{E}$	enstrophy
$\mathcal{G}$	general error or residual
$\mathcal{P}$	power spectral density
$\Re$	real part
$\Im$	imaginary part

# CONTENTS

<b>Summary</b>	<b>v</b>
<b>Samenvatting</b>	<b>vii</b>
<b>Nomenclature</b>	<b>ix</b>
<b>1 Introduction</b>	<b>1</b>
1.1 Background . . . . .	2
1.2 Basics of laminar-to-turbulent transition . . . . .	4
1.2.1 Canonical transition paths . . . . .	4
1.2.2 Modal transition . . . . .	6
1.2.3 Transition over a backward-facing step . . . . .	8
1.2.4 Transition over a forward-facing step . . . . .	12
1.3 Shock wave and boundary layer interaction. . . . .	15
1.3.1 Unsteady SWBLI with separation . . . . .	16
1.3.2 SWBLI over a BFS . . . . .	19
1.3.3 SWBLI over a FFS . . . . .	20
1.4 Motivation and objectives of the dissertation . . . . .	22
1.5 Layout of the dissertation . . . . .	23
<b>2 Methodology</b>	<b>25</b>
2.1 Numerical method . . . . .	26
2.1.1 Governing equations. . . . .	26
2.1.2 Formulation of the filtered governing equations . . . . .	27
2.1.3 Discretization . . . . .	28
2.1.4 Boundary conditions. . . . .	29
Boundary conditions based on Riemann invariants . . . . .	29
Turbulent inflow conditions based on a digital filter . . . . .	30
2.2 Flow analysis techniques . . . . .	32
2.2.1 Linear stability theory . . . . .	33
2.2.2 Vortex dynamics . . . . .	34
2.2.3 Dynamic mode decomposition . . . . .	35
2.2.4 Sparsity-promoting dynamic mode decomposition . . . . .	39

<b>3</b>	<b>Backward-facing step</b>	<b>41</b>
3.1	Flow configuration and numerical setup . . . . .	42
3.1.1	Flow configuration. . . . .	42
3.1.2	Numerical setup . . . . .	43
3.1.3	Inflow conditions . . . . .	44
3.1.4	Grid validation. . . . .	46
3.2	Preliminary comparisons of different cases . . . . .	46
3.3	Laminar regime . . . . .	51
3.3.1	Mean flow visualization . . . . .	52
3.3.2	Instantaneous flow visualization. . . . .	55
3.3.3	Unsteady behavior. . . . .	58
3.3.4	Statistical analysis . . . . .	61
3.3.5	Two-dimensional dynamic mode decomposition . . . . .	62
3.3.6	Summary . . . . .	66
3.4	Transitional regime . . . . .	67
3.4.1	Tollmien-Schlichting instability . . . . .	67
3.4.2	Primary Kelvin-Helmholtz instability . . . . .	70
3.4.3	Secondary instability. . . . .	75
3.4.4	Breakdown and reattachment . . . . .	78
3.4.5	Summary . . . . .	79
3.5	Turbulent regime . . . . .	79
3.5.1	Mean flow features. . . . .	79
3.5.2	Unsteady characteristics. . . . .	81
3.5.3	Spectral analysis . . . . .	85
3.5.4	DMD analysis of the three-dimensional flow field . . . . .	89
3.5.5	Physical mechanism of low-frequency unsteadiness. . . . .	96
3.5.6	Summary . . . . .	100
<b>4</b>	<b>Forward-facing step</b>	<b>103</b>
4.1	Flow configuration and numerical setup . . . . .	104
4.1.1	Flow configuration. . . . .	104
4.1.2	Numerical setup . . . . .	105
4.1.3	Grid validation. . . . .	105
4.2	Preliminary comparisons of different cases . . . . .	106
4.3	Turbulent regime . . . . .	111
4.3.1	Mean flow features. . . . .	111
4.3.2	Unsteady characteristics. . . . .	114
4.3.3	Spectral analysis . . . . .	116
4.3.4	DMD analysis of the three-dimensional flow field . . . . .	120
4.3.5	Physical mechanism of low-frequency unsteadiness. . . . .	126
4.3.6	Summary . . . . .	128

---

<b>5</b>	<b>Conclusions and outlook</b>	<b>131</b>
5.1	Transition mechanisms . . . . .	132
5.2	Low-frequency unsteadiness of SWBLI . . . . .	133
5.3	Outlook in laminar-to-turbulent transition . . . . .	133
5.3.1	Effects of the step height . . . . .	134
5.3.2	Effects of Reynolds number . . . . .	134
5.3.3	Critical step height . . . . .	135
5.4	Outlook in SWBLI . . . . .	135
	<b>References</b>	<b>139</b>
	<b>Acknowledgements</b>	<b>153</b>
	<b>Supplementary Information</b>	<b>155</b>
	<b>Scientific Contributions</b>	<b>157</b>
	<b>Biography</b>	<b>159</b>



# 1

## INTRODUCTION

*Having a broad reading but only to absorb concisely.  
Reserving a large accumulation but only to exploit prudently.*

博观而约取，厚积而薄发

Su-Shi  
苏轼

## 1.1. BACKGROUND

Nowadays, green aviation has become an active topic and a general consensus of the entire aerospace community [1]. In order to achieve the goals of green aviation, i.e., pursuing reductions in noise, greenhouse gas emissions and specific fuel consumption, alongside the safety requirements, the configuration of aircraft must undergo effective aerodynamic optimization. Real aircraft, however, inevitably have geometry imperfections, such as the window frame of cockpits, skin joints of fuselage and inlets of the propulsion system, that significantly degrade the aerodynamic vehicle performance. The backward/forward-facing step (BFS/FFS) geometry can be seen as a canonical configuration that represents an abstraction of these aerospace applications. This geometry may accelerate the transition from laminar to turbulent flow (figure 1.1), which results in an increase of flight drag, aerodynamic noise, and unsteady pressure loads [2]. In addition, for high-speed flight applications, designing for space launchers and supersonic transport in the near future, shock wave/boundary layer interaction (SWBLI) can occur over these configurations due to the flow deflection. Figure 1.2 provides an instantaneous visualization of SWBLI on a generic space launcher. The unsteady effects caused by SWBLI can induce intense localized mechanical and thermal loads, possibly leading to the failure of material and structural integrity [3].

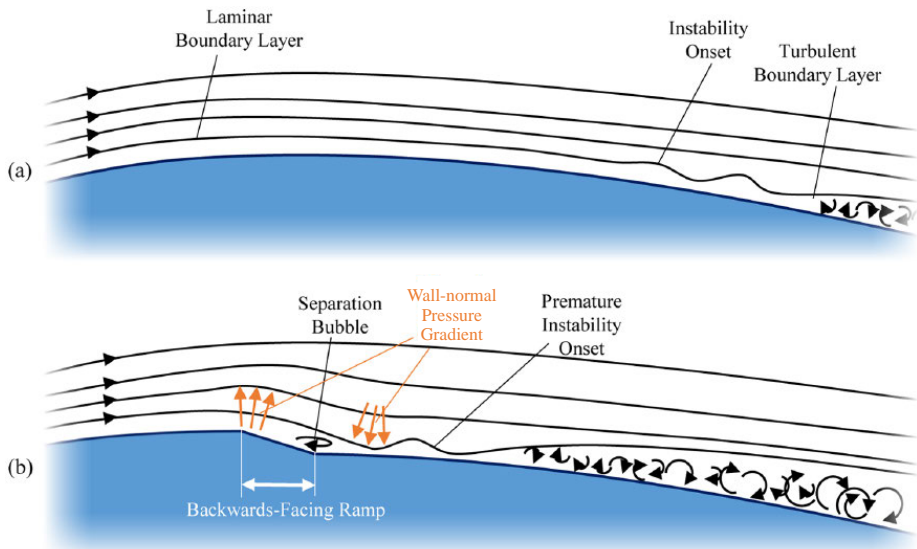


Figure 1.1: Schematic of the laminar-to-turbulent transition over an airfoil with (a) a smooth suction surface and (b) a backward-facing step [4].

The first concern of the flow dynamics over a BFS/FFS is the transition from laminar to turbulent flow. The first illustration of laminar-to-turbulent transition is traditionally attributed to an early well-known experiment of Reynolds [6] in 1883. He demonstrated a switch of the flow state from a smooth layered condition (laminar flow) to a chaotic mixing state (turbulent flow) using a pipe flow with a dyed water jet injected into

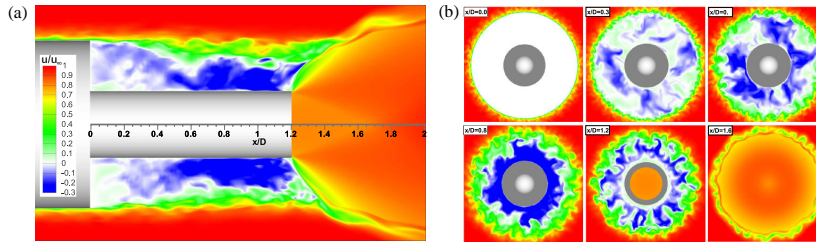


Figure 1.2: Instantaneous streamwise velocity contours (a) on the symmetry plane and (b) cross sections at several streamwise locations [5].

its center. A dimensionless governing parameter, named the Reynolds number and representing the ratio of inertial forces to viscous forces, was proposed to estimate the state of the flow. If the Reynolds number is above a (flow-configuration dependent) critical value, the flow is assumed to become turbulent. Since then the laminar-to-turbulent transition has been one of the most important and challenging topics in the research area of fluid mechanics. Particularly, the boundary layer transition over a wall-bounded surface is of utmost relevance. It is known that transition is governed by various instabilities of the laminar boundary layer excited by external disturbances, such as free stream disturbances, pressure gradient, surface roughness and curvature [7]. An early review of the fundamental transition mechanism was given by Tani [8], mainly based on experimental evidence from the low-speed regime. Later, Reshotko [7] gave a comprehensive review of the stability and laminar-to-turbulent boundary layer transition in high speed flows. Due to the different instabilities that may be involved, the boundary layer transition can display various paths to turbulence, for instance a natural transition caused by Tollmien-Schlichting (T-S) instability. A recent review by Fedorov [9] indicated that low- and high-speed boundary layers share similar transition paths although essential characteristics may be different in this process. The paths to turbulence and corresponding instabilities will be discussed in the following section.

Shock wave/boundary layer interaction is our second and related research subject. Generally, when a shock wave and a boundary layer interact, the boundary layer may undergo deformation, separation and reattachment due to the adverse pressure gradient imposed by the shock, while the shock wave foot bifurcates close to the boundary layer, such that its interaction with the solid surface is different from the inviscid case. The experiments of an airfoil in a high-speed wind tunnel by Ferri [10] probably constitute the first report about SWBLI. Later, extensive experimental studies were carried out, mainly on airfoils or other curved surfaces in the transonic regime [11]. They emphasized the effects of SWBLI on shock wave pattern and pressure distribution, which are particularly relevant to the state of the incoming boundary layer. Due to the existing streamwise pressure gradient over the curved geometry and partial supersonic region in these cases, however, the characteristics of SWBLI are difficult to be investigated independently and systematically [12]. Thereafter, numerous experimental works put efforts on several canonical two-dimensional configurations, including an impinging shock over a flat plate, a compression ramp, BFS and FFS configurations, in a fully supersonic flow. There are several crucial parameters reported to have significant impacts

on SWBLI, among which the effects of Mach number, Reynolds number, shock intensity and incoming boundary layer state have been studied in a series of early experiments by Gadd *et al.* [13]. Later, the typical structures of SWBLI in various configurations were reviewed by Green [14], mainly based on experimental results. In addition, they also concluded several basic analytical methods, which can provide an approximate prediction of the interaction properties in various forms, like free interaction theory, boundary layer integral and inviscid shear layer analysis. More recently, remarkable improvements of modern numerical tools and advanced flow measurement techniques have been achieved which allowed a more complete understanding of SWBLI to be obtained. Considering simplified two-dimensional interaction geometries in moderate supersonic flow conditions, the particular topics of interest involve the mechanisms of low-frequency unsteadiness and the application of flow control techniques [15]. A sound knowledge of physical mechanisms in SWBLI, especially supported by a well-resolved computational fluid dynamics (CFD) analysis, is the cornerstone for developing effective control methods. Extensive contributions have been made to enhance the understanding of this phenomenology and main conclusions obtained are detailed in the following section.

For a better aerodynamic performance of aircraft, the effects of the laminar-to-turbulent transition and SWBLI caused by surface imperfections must be assessed. From the perspective of geometrical simplicity, BFS/FFS are appealing prototypes for investigating the transition from laminar to turbulent flow without artificial disturbances in the non-parallel open flow [16, 17], and also for studying shock wave/boundary layer interaction (SWBLI) in the supersonic regime [18]. This forms the motivation to study these configurations in this thesis.

## 1.2. BASICS OF LAMINAR-TO-TURBULENT TRANSITION

This section provides a brief review of the current state of knowledge about the boundary layer transition in general, including the paths to turbulence and commonly used analytical tools. Special attention is then given to the state of the art work in laminar-turbulent transition over a BFS/FFS, especially in the supersonic regime.

### 1.2.1. CANONICAL TRANSITION PATHS

The boundary layer transition is a multifold process, which can take various paths depending on the type of external disturbances and flow configuration involved. Generally, the overall process of boundary layer transition can be divided into three main stages: the receptivity to the external disturbances, the gradual increase of the initial disturbances by linear/transient growth of the perturbations or a bypass process, and finally the breakdown to turbulence caused by nonlinear effects [19]. According to the specific road, five main paths of transition were identified by Morkovin [20], as shown in figure 1.3.

For the low levels of external disturbances ( $u'/u_\infty < 0.1\%$ ), the transition path usually consists of excitation, exponential growth of the primary instability, evolution of the second modes, mode breakdown to turbulence (path A). The first mode can be Tollmien-Schlichting (T-S) waves [21], cross-flow instability [22], Kelvin-Helmholtz (K-H) instabil-

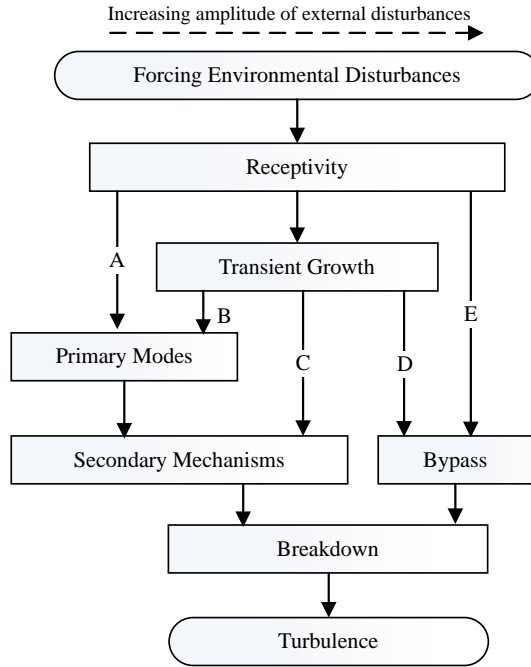


Figure 1.3: Roadmap of the boundary layer transition to turbulence [20].

ity [23], centrifugal instability [24], etc., depending mostly on the configuration of the underlying “base flow”. The growth of weak disturbances is initially governed by linear equations, which predict an exponential growth or decay of the perturbation amplitude, and followed by a nonlinear rapid growth to a certain level until three-dimensional interactions become significant. The resulting secondary perturbations quickly develop and break down to turbulence. This scenario is generally the appropriate road if the laminar-to-turbulent transition occurs over relatively smooth surfaces in a quiescent environment, like airfoils in a flight free-stream environment [25].

For higher initial amplitudes of disturbances, the transition scenario follows path B, the transient growth will be dominant at the initial stage. Several eigenmodes are then excited by disturbances with a higher amplitude, which may result in algebraic growth and the rapid onset of nonlinear interactions. In the spatial growth theory, transient growth is the optimal path for amplifying stationary streamwise disturbances, which is a consequence of the non-orthogonality of the eigenvectors and usually features an algebraic growth rate [26]. In contrast, linear growth, which usually refers to the exponential growth of the primary mode, is largest for travelling transverse disturbances at low speed and travelling oblique waves in a supersonic flow. There is no clear explanation of the coupling between streamwise and transverse disturbances in different stages. In addition, transient growth may induce spanwise differential amplification of two-dimensional waves in the mean flow [27]. In this process, alternating high and low levels of fluctuations are likely to be observed along the spanwise direction [28].

When the linear growth of eigenmodes is absent, the transient growth prevails the transition until secondary mechanisms are excited (path C). This transient growth is the most salient mechanism of various examples for non-modal transition [27]. For instance, the boundary layer transition over blunt geometry does not involve the growth of modal instability because the first mode is stable, decayed or less important. This case is known as blunt-body paradox and has been investigated widely in the previous numerical works [27]. The subcritical transition over a flat plate also follows this path. Andersson *et al.* [29] proposed a semi-empirical model that predicts the transition location based on the intensity of free stream turbulence (FST) in a framework of transient growth. Reshotko and Tumin [30] indicated that surface roughness plays an important role in this transition path and modified this model by considering the effects of surface roughness using a spatial transient growth theory. Paredes *et al.* [31] further improved this model by including curvature effects such that it can remain valid for other geometries, like hemispherical nose tips.

If the resulting amplitude of environmental disturbances by transient growth is larger, the boundary layer may enter a state where the spectra of fluctuations are similar to a turbulent one although the mean flow is still more or less laminar. In the late stage of path D, the turbulence intensity becomes stronger with the streamwise distance [32]. The transition path D is widely found in internal flows with an elevated turbulence level [33].

If the amplitude of forcing disturbances is sufficiently large, the growth of eigenmodes may be bypassed altogether. In this case, the boundary layer turbulence rapidly develops with the emergence of the turbulent spots or subcritical instabilities. This transition path E usually occurs when large roughness and high free stream turbulence ( $u'/u_\infty > 10\%$ ) are present [34].

### 1.2.2. MODAL TRANSITION

Modal transition is a classic transition path initiated by the growth of eigenmodes at low levels of environmental disturbances (path A, B, C in figure 1.3), which occurs on various flow configurations, like Blasius boundary layer, BFS and FFS, etc. For different flow conditions and geometry, however, the dominant unstable mode and the specific transition road could be very different. Correspondingly, different numerical tools are required for the analysis of flow instabilities.

If the prevailing primary mechanism is the T-S instability, the corresponding transition process is referred to as the natural transition, which usually occurs on smooth surfaces at low-turbulence free stream conditions. In this regime, the transition process is initiated by the linear growth of unstable T-S waves, followed by the occurrence of weakly and strongly nonlinear effects, and finally breakdown into turbulence, as illustrated in figure 1.4. In the early linear growth stage, small random disturbances are damped with the evolution of the transitional boundary layer along the streamwise direction and their interactions with T-S waves usually can be neglected. The T-S instability is one of the streamwise instabilities and also called viscous instability since the boundary layer is stable in the restriction of inviscid flows [25].

For subsonic flow, up to  $Ma \approx 0.7$ , the least-stable T-S waves remain as two-dimensional (spanwise wavenumber equals to zero) [36]. In the transonic and low

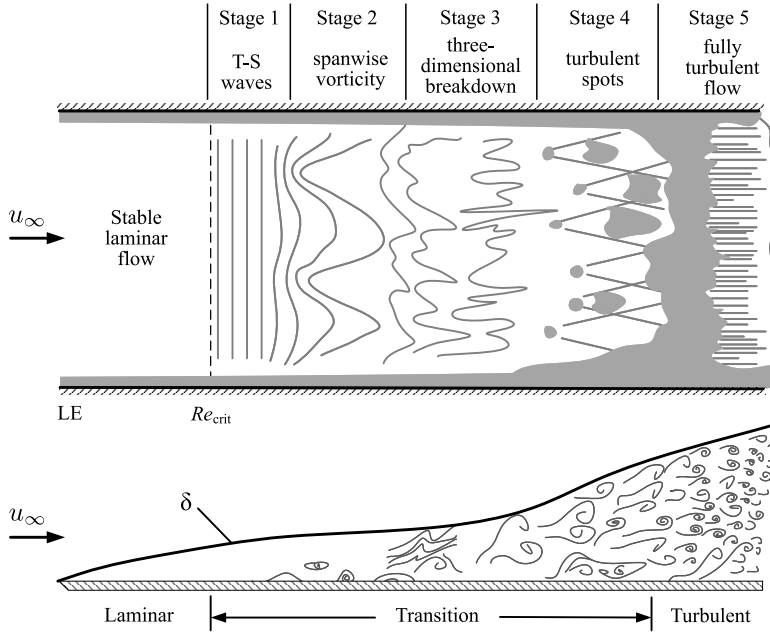


Figure 1.4: Schematic of natural boundary layer transition over a flat plate at zero incidence [35].

supersonic regime, the three-dimensional oblique T-S waves are more unstable than the two-dimensional waves. Mayer *et al.* [37] numerically confirmed that oblique waves can individually induce a fully turbulent boundary layer in a supersonic flow. The nonlinear process begins with a rapid (transient) growth of the primary modes caused by the interaction of a pair of oblique waves, leading to the generation of streamwise vorticity [38]. At much higher Mach numbers,  $Ma_\infty \geq 4.0$ , there are second and higher modes coexisting within the boundary layer [21]. These modes represent the inviscid instabilities related to trapped acoustic waves and may be the most unstable modes during the transition. Linear stability theory (LST) is widely used to identify these unstable modes and predicts their growth in the early linear stage of the transition process, the details of which are provided in section 2.2.1 of chapter 2. Reed *et al.* [25] provided a comprehensive review of the application of LST for the boundary layer stability analysis. In the present study, LST is used to calculate the least-stable modes at the domain inlet and analyze the development of the oblique T-S waves upstream of the step (see chapter 3).

In addition to T-S waves, other instabilities can also act as the primary mode in the transition path A. For concave walls, like the aft section on the pressure side of supercritical airfoils, the transition may be initialized by the Görtler instability caused by centrifugal forces [39]. In the first stage, the primary instability modulated by Görtler vortices undergoes linear growth. As the boundary layer develops, large counter-rotating vortices are produced and secondary instability becomes dominant. In the meantime, these streamwise-oriented Görtler vortices create alternating streamwise-

aligned streaks near the wall where the flow is washed down towards the wall or washed up away from the wall, as shown in figure 1.5. This behavior may result in a considerable nonlinear distortion of the flow field and the evolution of highly inflectional velocity profiles that give rise to strong K-H secondary instability. When the secondary waves reach a certain level with the emergence of mushroom-like structures, they finally will cause breakdown to turbulence. LST is not really applicable for modeling the development of this instability because the aforementioned nonlinear effects occur earlier and a nonparallel assumption is not always justified. In contrast to concave surfaces, convex curvature stabilizes Görtler vortices; therefore the deployment of wavy-wall can relieve the destabilizing effects of the Görtler instability on the boundary layer [40].

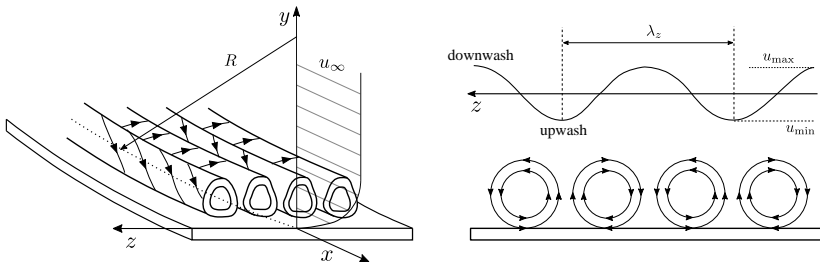


Figure 1.5: Description of counter-rotating Görtler vortices caused by the curvature of the surface [41].

The inviscid Kelvin-Helmholtz (K-H) mode is often the primary instability in the laminar-to-turbulent transition with a separation. The large eddy simulation (LES) of Yang and Voke [42] shows that with separation the transition begins via the K-H instability and the initial linear growth rate of the K-H waves is usually larger than that of T-S waves. As the K-H rolls increase in size, the shear layer undergoes a sinusoidal modulation via the secondary instability along the spanwise direction; the induced highly three-dimensional vortices break down into turbulence with the rolling-up of hairpin vortices [23]. The transition of the laminar separated shear layer with low-level environmental disturbances usually follows this path via the primary K-H instability [43]. Since the separation flow is in conflict with the assumption of the parallel flow, LST is not very appropriate for predicting the evolution of the K-H instability.

The laminar-to-turbulent transition induced by other instabilities can also follow the path A, like the viscous attachment-line instability originating from a stagnation point of a swept flow [44], or the inviscid crossflow instability over a swept geometry [45]. However, these instabilities are not directly related to the configuration of the two-dimensional unswept BFS/FFS and therefore are not of current interest.

### 1.2.3. TRANSITION OVER A BACKWARD-FACING STEP

The backward-facing step is one of the cases where other instabilities than T-S modes are likely to prevail in the transition process [2]. For a subsonic BFS flow, the main flow features include the separation bubble, shedding vortices in the shear layer and reattachment, as in figure 1.6. The laminar-to-turbulent transition usually occurs in the free shear layer and the boundary layer becomes turbulent behind the reattachment.

There is considerable experimental and numerical evidence of the flow instabilities behind a BFS. Overall, there are three main large-scale unsteady flow structures observed behind the BFS, including a large primary recirculation eddy, as well as Görtler-like and K-H vortices [17, 46, 47]. The leading transition mechanism depends on the geometry configuration, and is mainly governed by the step height relative to the incoming boundary layer thickness. For a BFS with a sufficiently large step height, the dominant transition mechanism is reported to be the large curvature induced by the centrifugal forces, as displayed in figure 1.7. The crucial feature of the flow field is a large primary eddy behind the step with almost circular streamlines at the center of the separation bubble. The highest perturbation levels are observed at the downward side of the shear flow, where the streamline curvature and the corresponding centrifugal forces are significant [17]. As the flow reattaches on the downstream wall, longitudinal high- and low-speed streaks [figure 1.8(a)] may be generated by the Görtler instability if the streamline curvature is large enough near the reattachment. The counter-rotating longitudinal Görtler vortices [figure 1.8(b)] produced by the lift-up effect are the main features of the near wall flow and they are self-sustained due to the feedback provided by the recirculating flow in the separation bubble.

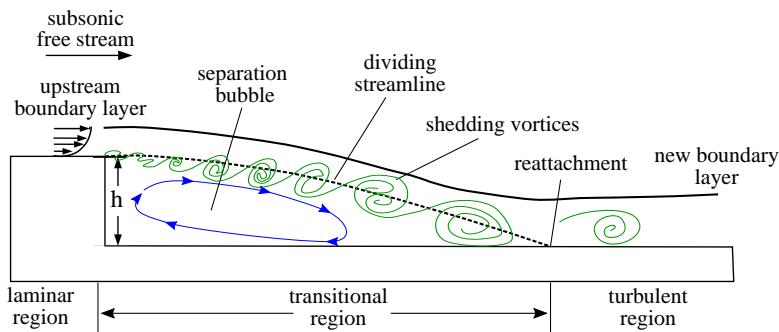


Figure 1.6: Schematic of a subsonic flow over a BFS.

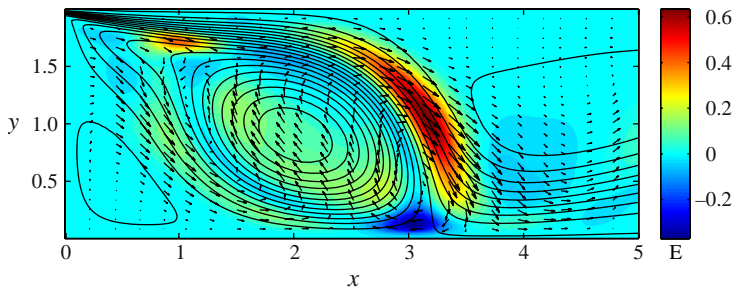


Figure 1.7: Contours of the total energy  $E$  behind a BFS on the  $x-y$  plane, showing the large centrifugal forces [17]. Black solid lines are the streamlines and the arrow lines represent the velocity field.

When the step height is smaller but exceeds a critical value, which is a function

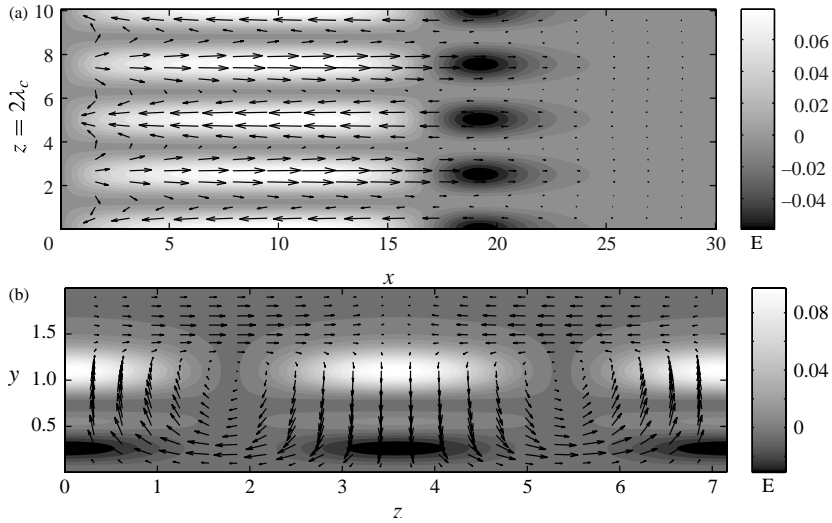


Figure 1.8: Contours of the total energy  $E$  behind a BFS on (a) the  $y-z$  plane, showing the counter-rotating vortices and (b) the  $x-z$  plane, illustrating the high- and low-speed streaks [17]. The arrow lines represent the velocity field.

of unit Reynolds number, the travelling and shedding of K-H vortices in the separated shear layer (figure 1.9) usually is the main driver of the transition process [46]. The classical transition path consists of the roll-up of the shear layer, the convection of quasi-periodic K-H vortices, flapping motions of the shear layer and corresponding periodic shrinking/expanding of the separation bubble, as well as the vortex breakdown to turbulence [48]. Furthermore, Eppink *et al.* [49] indicated that the transition can be accelerated by the interaction of various instability mechanisms behind the step, which can be considered as a modulation of three different types of disturbances with sufficient large amplitudes, but differing in a frequency band. The low-frequency disturbances are related to travelling crossflow-like waves, while the medium and high frequency contents are associated with T-S waves and shear layer instability, respectively. It seems that the various instabilities and their interactions, instead of the individual effects by the growth of T-S waves, have a great impact on the transition for such a configuration where a separation bubble is present. Simulations by Brinkerhoff and Yaras [50] observed that the streamwise vortices induced by the T-S waves are amplified inside the separated shear layer due to the local adverse pressure gradient and develop into coherent hairpin vortices eventually. In conclusion, the excitation of other instabilities, rather than the linear growth of T-S waves, plays a more important role in the transition process behind a BFS [22].

In the supersonic regime, the separated shear layer instability has also been widely reported for the BFS case [51–53]. However, there are additional mechanisms involved, that are related to compressibility and the occurrence of compression waves at flow reattachment [54, 55]. Therefore, it is reasonable to conjecture that a different mechanism may contribute to the transition process in the supersonic case. Additionally,

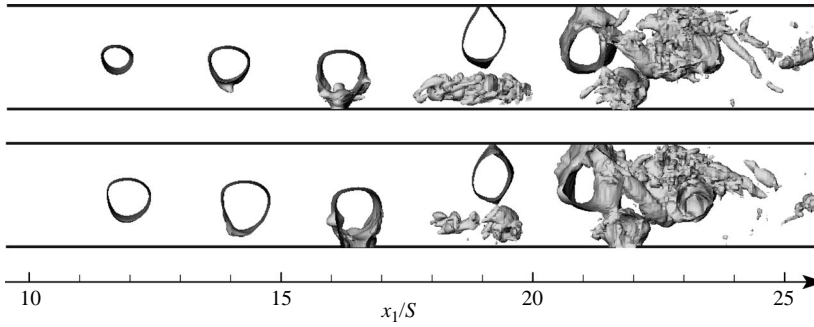


Figure 1.9: Temporal evolution of the K-H vortices at two instants, visualized by isosurfaces of the pressure values.

with the existing focus on the instability in the shear flow, the role of primary T-S modes in the incoming boundary layer in front of the step, and their interactions with the excited other primary instabilities, as well as the secondary waves, in the transition process of the free shear layer are not completely documented and understood. The evolution of the T-S instabilities and their interaction with the secondary waves have been well studied in the existing work, mainly for a Blasius boundary layer. Chang and Malik [38] numerically investigated the interactions of oblique T-S waves and secondary instabilities in the transition path. They addressed that the mutual and self-interaction between linear growth of T-S waves and rapid growth of vortex waves is a nonlinear wave-vortex triad process, which leads to the transient growth of secondary subharmonic waves and transition acceleration. This subharmonic resonance usually only occurs when the enforced waves have large spanwise wave numbers [56]. Mayer *et al.* [57] indicated that the breakdown to turbulence can be triggered solely by the development of a fundamental primary oblique wave. The interaction between one oblique fundamental wave and two oblique subharmonic waves is also reported. This subharmonic resonance triad can also accelerate the laminar-to-turbulent transition. Marxen *et al.* [58] proposed that the transition is a slow resonant process between primary and secondary waves in the presence of roughness, in which the amplitudes of excited fundamental and subharmonic secondary waves are augmented significantly. In addition, the primary waves tend to damp downstream when the excited secondary waves and other large vortices become significant [59]. Paredes *et al.* [60] found that the primary oblique wave can be stabilized by stationary streamwise streaks if the streak spacing is less than half the spanwise wavelength of the primary oblique wave. In contrast, when the streak spacing exceeds this critical value, the primary oblique wave is destabilized by the streaks, which accelerates the oblique breakdown. This nonlinear process usually features staggered  $\Lambda$ -shaped vortices along the boundary layer, the following hairpin vortices caused by lift-up effects, and a breakdown of these coherent vortices via nonlinear interactions between them [61].

In the above-mentioned investigations, the primary instability is mainly associated with either T-S or K-H waves solely. It is not well understood how incoming T-S waves behave in the background of the strong K-H instability for a separated shear layer. The

interaction between these primary instabilities and the induced secondary instability is also worthwhile to investigate. Similar work has been done in subsonic flow [49]. We will scrutinize the transition process for a supersonic flow over a BFS, and furthermore identify the dominant primary instability and the role of each instability in the transition.

#### 1.2.4. TRANSITION OVER A FORWARD-FACING STEP

In comparison to the BFS, a forward-facing step has a greater upstream effect on the laminar-to-turbulent transition and the flow topology over it is more complicated. In addition to the separation bubble in front of the step, there may exist a second separation region downstream of the step, as shown in figure 1.10. The exact flow topology depends on the free stream velocity and the relative step height [62].

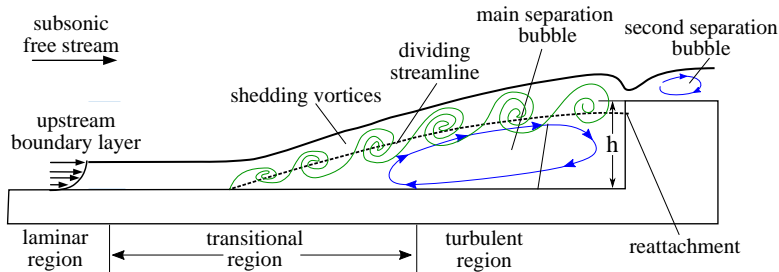


Figure 1.10: Schematic of a subsonic flow over a FFS.

In the subsonic regime, if the step height is large enough to accelerate the laminar-to-turbulent transition, two separation regions are usually observed, located upstream and downstream of the step, respectively [63]. Previous experimental works indicated that the separation length of the upstream and downstream recirculation region increases with the free stream velocity and the step height (equivalent to Reynolds number) [63, 64]. In an early direct numerical simulation (DNS), Worner *et al.* [65] made the interesting observation that a FFS can have a stabilizing effect on the developing boundary layer by damping the oncoming T-S waves. This conclusion was considered to be incorrect by later studies [66, 67] due to the misinterpretation of the numerical results. The early hot-wire anemometry measurements by Wang and Gaster [66] showed that the boundary layer transition occurs at an earlier location downstream of the step, compared to a smooth plate. The acceleration of the transition is caused by the stronger amplification of unstable waves downstream of the step. Rizzetta and Visbal [67] investigated the transition process over the FFS by forcing small amplitude waves at the inlet using implicit LES, and observed the amplification dynamics of the step. By analyzing the instantaneous flow field, they found that the transition starts with small two-dimensional structures and then these vortical structures are convected downstream of the step. Finally, these coherent vortices lose their coherence and breakdown into a turbulent boundary layer. The experimental work of Costantini *et al.* [68] showed that the transition is already initiated upstream of the step by the growth and amplification of the incoming disturbances inside the boundary layer, which can be inferred from the visualization of the laminar-to-turbulent transition over an airfoil with

different step heights, shown in figure 1.11. Edelmann and Rist [69] used DNS to further scrutinize the evolution of the instabilities across the transition process and observed a strong amplification of the upstream linear disturbances in front of and behind the step, as shown in figure 1.12. The experiments of Costantini *et al.* [68] showed that these amplified disturbances are in the form of spanwise alternative strips in front of the transition location. By means of parabolized stability equations (PSE), LST and linearized Navier-Stokes (N-S) equations, Thomas *et al.* [70] found the amplification of T-S waves inside the upstream boundary layer. Additionally, the growth rate of these T-S waves becomes larger with a higher step height. The analytical work of Dong and Zhang [71] also reported the amplification and deformation of T-S waves across the step. Compared with the BFS, they found that the amplification effects of the FFS are not as strong as those of a BFS.

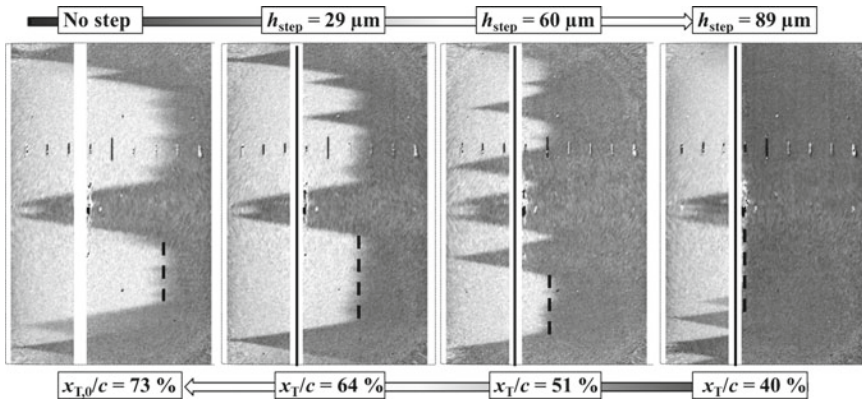


Figure 1.11: Effects of forward-facing steps on the boundary layer transition over an airfoil, visualized by the results of temperature-sensitive paint [68]. The black dashed lines indicate the location of the turbulent boundary layer and  $c$  represents the chord length.

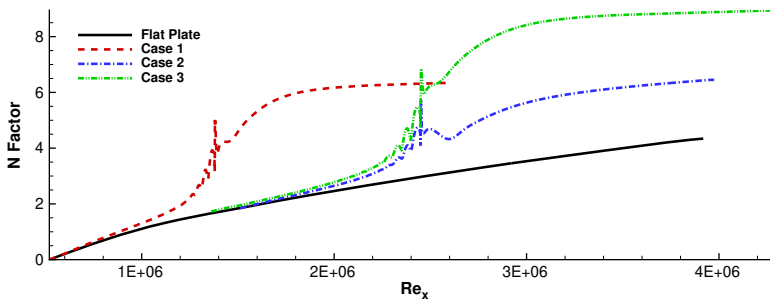


Figure 1.12: N-factor (additional amplification factor caused by the step, compared with a smooth surface) curves with Reynolds number at  $Ma = 0.8$  for a flat plate and different FFS cases [69]. The peak of the curves indicates the step location.

Similar to the BFS configuration, there are other instabilities involved in the laminar-to-turbulent transition over a FFS if the step height is larger. Wilhelm *et al.* [72]

investigated the response of the flow field over a FFS to random three-dimensional disturbances using DNS and LST. They found that the reaction of the boundary layer is sensitive and becomes stronger with a larger amplitude of the inflow disturbances. Forcing perturbations with an amplitude below  $1\%u_\infty$ , the separation flow ahead of the step already has significantly three-dimensional features. Spiral vortical structures in front of the step and counter-rotating vortices downstream of the step are observed in the development of the turbulent boundary layer, as shown in figure 1.13. These spanwise alternating streaks are also reported in the experimental work of Stürer *et al.* [73]. Lanzerstorfer and Kuhlmann [16] performed a global temporal stability analysis of the two-dimensional flow field and identified a critical mode corresponding to the high- and low-speed streaks alternating in the spanwise direction on the top of the step. The spanwise wavelength of these counter-rotating vortices is about three times the step height. They believe that this dynamics is caused by the lift-up effects and flow deceleration behind the step. In the LES of Abdalla *et al.* [74], the K-H instability is found in the transition process. The instantaneous flow visualization showed that the transition consists of the rolling and shedding of K-H vortices from the separated shear layer ahead of the step, vortices stretching and pairing, the breakdown of large coherent vortices into the turbulent flow upstream of the second mean reattachment location. The well-known  $\Lambda$ -shaped vortices were not observed in this process. Zhu and Fu [75] compared the evolution of disturbances in the boundary layer between the flat plate and FFS configuration using a well-resolved implicit LES. They reported that the forcing inlet disturbance does not grow with streamwise distance in the entire flow domain for the flat plate case, while they already begin to grow upstream of the first separation region ahead of the step for the FFS case. Mushroom-shaped vortices are induced in front of the step by the growth of the oncoming disturbances via the Görtler instability and they continue developing across the step. Secondary vortices then are generated near the step and evolve into hairpin vortices further downstream of the step. The transition process they observed resembles the Klebanoff-type transition in the boundary layer. If there are crossflow waves in the coming boundary layer, the FFS can affect the development of crossflow modes. Both the experimental work of Duncan Jr [46] and numerical efforts of Tufts *et al.* [76] stated that there exists a critical step height as a function of unit Reynolds number, below which the amplification of the crossflow instability caused by the FFS dominates the laminar-to-turbulent transition. When the step height is above the critical value, the shear layer instability is the prevailing mechanism of the transition.

In supersonic flows, there is a long separation region in front of the step, while the separation after the step is absent or very weak. Balakumar *et al.* [52] reported that the separation length in front of the step is around  $5 \sim 10$  times the step height. Their linear stability analysis showed that the general amplitudes of the disturbances are not noticeably modified across the step compared with the flat plate case, because the growth rate of the unstable waves becomes larger upstream of the step but decreases downstream of the step. In contrast, the DNS results of Edelmann and Rist [69] indicated that the transition process is overall accelerated by the step since the oncoming T-S waves are highly amplified in front of the step and only slightly decayed behind the step, as shown in figure 1.14. Additionally, a small secondary recirculation is observed within the separated zone ahead of the step.

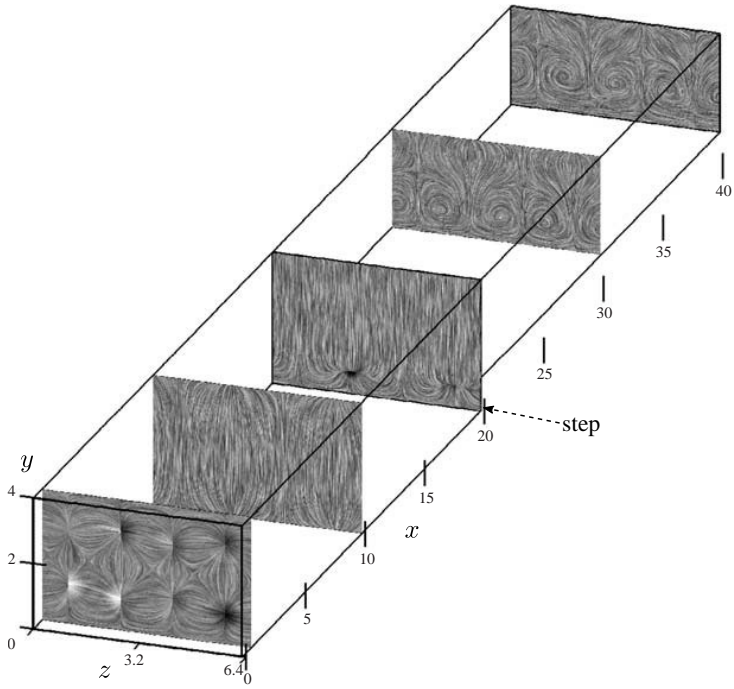


Figure 1.13: Streamlines on the  $y-z$  sections at different streamwise locations, illustrating the pairs of counter-rotating vortices [72].

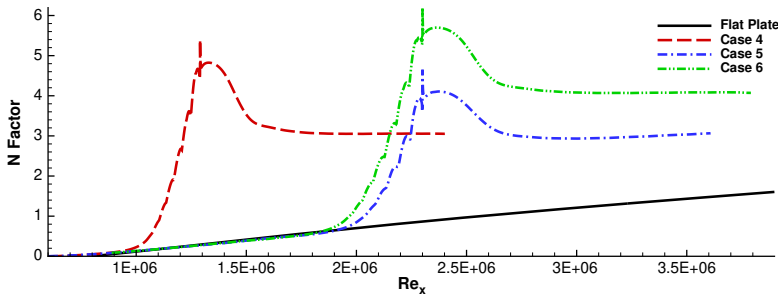


Figure 1.14: N-factor (additional amplification factor caused by the step, compared with a smooth surface) curves with Reynolds number at  $Ma = 1.06$  for a flat plate and different FFS cases [69]. The peak of the curves indicates the step location.

### 1.3. SHOCK WAVE AND BOUNDARY LAYER INTERACTION

Shock wave/boundary layer interaction (SWBLI) is ubiquitous in high-speed aerodynamics, such as supersonic inlets, over-expanded nozzles, high-speed aerofoils [12, 14]. Shock-induced boundary-layer separation is a main contributor to flight drag of transonic aerofoils and pressure loss in engine inlets, which illustrates its relevance. Moreover, significant fluctuations of pressure and temperature are widely observed

around the interaction regions. SWBLI can cause intense localized mechanical and thermal loads, which may eventually result in the collapse of material and structural integrity [3, 15]. It is therefore crucial to take the effects of SWBLI into account in the process of aircraft design and maintenance, including material selection, assessment of fatigue life and thermal protection systems.

### 1.3.1. UNSTEADY SWBLI WITH SEPARATION

Although SWBLI occurs on various types and parts of aircraft, canonical two-dimensional configurations can be abstracted into three simplified cases: (1) incident shock (impinging-reflecting), (2) compression ramp and (3) backward/forward-facing step [77, 78]. In terms of viscous effects, SWBLI can be furthermore classified into weak and strong interaction cases [18]. For the weakly interacting flows, thickening of the boundary layer is observed, but there is no separation in the interaction region. Weak SWBLI usually occurs in the weak incident shock induced interaction, compression ramp with small deflection angle and BFS/FFS with small step height. For the strong SWBLI, on the other hand, boundary layer separation occurs in the interaction region. Since strong SWBLI is more common in the real physical flows of aircraft and has more severe aerodynamic and thermodynamic impacts on aircraft, our focus is put on the strong SWBLI with separation.

Considerable progress has been achieved in understanding the unsteady phenomena and underlying mechanisms of SWBLI by means of advanced flow measurement techniques and well-resolved computations [15], particularly for the configurations of impinging-reflecting shocks and the compression ramp [18, 77]. These two cases share a similar mean flow topology although the shocks are produced by different mechanisms, as shown in figure 1.15(a) and (b). In the impinging/reflecting shock case, the incident shock induces a strong adverse pressure gradient on the boundary layer, which leads to the separation of the boundary layer. A separation shock is produced ahead of the separation point and a reattachment shock is generated around the reattachment location due to the compression of the boundary layer. For the ramp case, the strong flow compression caused by the ramp geometry induces a strong (separation) shock, which results in the separation of the incoming boundary layer. Subsequently, a reattachment shock is generated as the separated shear layer reattaches on the ramp downstream. In both cases, the SWBLI is accompanied by energetic unsteady motions at frequencies that are one or two orders lower than the boundary layer characteristic frequency  $u_\infty/\delta$  [18]. The unsteady characteristics can be quantified by the dimensionless Strouhal number  $St_r = fL_r/u_\infty$  based on the reattachment length and free stream velocity or  $St_\delta = f\delta_0/u_\infty$  based on the inlet boundary layer thickness and free stream velocity. Considerable research effort has been put into tracing the source of this low-frequency unsteadiness.

In general, theories regarding the origin of this low-frequency motion of the separation shock are categorized as resulting from either upstream or downstream dynamics. The first group of theories associates the unsteady motions with upstream fluctuations within the incoming turbulent boundary layer. In an early work, Plotkin [79] proposed a simple linear restoring model to explain the source of the shock wave oscillations, in which the shock is displaced by velocity fluctuations inside the upstream turbulent

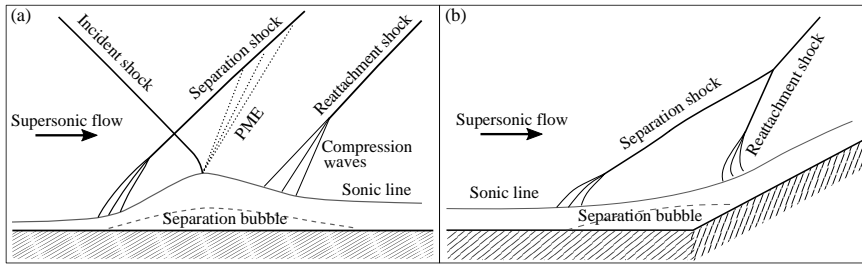


Figure 1.15: Mean flow structures of SWBLI in canonical two-dimensional configurations (a) impinging shock and (b) compression ramp.

boundary and tends to return to its mean location through a restoring mechanism determined by the stability of the mean flow. The pressure measurement by Andreopoulos and Muck [80] provided the first experimental evidence for a correlation of the shock wave unsteadiness with bursting events upstream the boundary layer in a compression ramp case at  $Ma = 1.7$ . Unalmis and Dolling [81] found low-frequency pressure fluctuations along the spanwise direction in the incoming boundary layer by measuring the pressure signal in the ramp case at  $Ma = 5$ . Poggie and Smits [82] performed measurements of wall pressure fluctuations and schlieren visualization in a backward-facing step/ramp configuration at  $Ma = 2.9$ . They reported that also in this case the shock motion was correlated with upstream large-scale wave structures. Based on the cross-correlation analysis, they concluded that their experimental results are in good agreement with the linear restoring mechanisms proposed by Plotkin [79]. Beresh *et al.* [83] used particle image velocimetry (PIV) and high-frequency response wall pressure transducers for a compression ramp interaction, and they found a clear correlation between streamwise velocity fluctuations in the lower part of the upstream boundary layer and low-frequency shock motions. In addition, they found no correlation between shock oscillations and the velocity fluctuations in the upper part of the upstream boundary layer, as well as the variation of the upstream boundary layer thickness, as reported by McClure [84] in earlier work. Ganapathisubramani *et al.* [85] also observed elongated superstructures with low- and high-speed streaks upstream of the separation region [figure 1.16(a)] in their stereoscopic PIV and planar laser scattering (PLS) measurements of a Mach 2 compression ramp interaction and they proposed these upstream large-scale structures are responsible for the low-frequency unsteadiness of the interaction region. Humble *et al.* [86] further confirmed the presence of streamwise-elongated low- and high-speed streaks inside the upstream boundary layer using tomographic PIV for an incident shock interaction at  $Ma = 2.1$  [figure 1.16(b)]. Their results show that this reorganization of the upstream boundary layer in both streamwise and spanwise directions conforms to the overall streamwise translation and spanwise rippling of the interaction region. However, Touber and Sandham [87] argued that the low-frequency interaction motions ( $0.01 < St_r < 0.1$ ) do not necessarily require a forcing source from upstream or downstream and are more like an intrinsic response to the broadband frequency spectrum of the upstream turbulent fluctuations. Porter and Poggie [88] consider that this response is a selective response of the separation region to certain

large-scale perturbations in the lower half part of the upstream boundary layer based on their high-fidelity simulation.

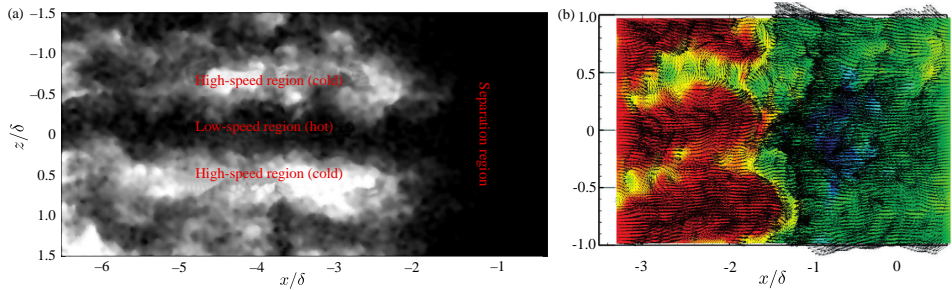


Figure 1.16: Streamwise high- and low-speed streaks upstream of the separation region on a  $x-z$  plane. (a) planar laser scattering image for a compression ramp case (the ramp corner is at  $x/\delta = 0$ ) [85] and (b) tomographic PIV measurements of the instantaneous streamwise velocity for an impinging shock case (the extrapolated wall-impingement point of the incident shock is at  $x/\delta = 0$ ) [86].

The second group of theories attributes the low-frequency dynamics to mechanisms intrinsic to the interaction system itself, that is, with an origin downstream of the separation line. Already early experimental studies suggested that the low-frequency motion of the separation shock is linked to the expansion and contraction of the separation bubble [89, 90]. For the impinging shock induced interaction, Dupont *et al.* [91] found a clear statistical link between low-frequency oscillation of the separation shock and the downstream interaction region by analysing experimental pressure signals. Furthermore, they also reported a quasi-linear relation between the separation shock and the reattachment shock motions. By DNS of a Mach 2.25 impinging shock case, Pirozzoli and Grasso [92] established a resonance theory, in which acoustic waves are produced by the interaction between coherent structures in the bubble and the incident shock. The upstream propagation of these acoustic waves is responsible for the low-frequency oscillations of the SWBLI system. Toubert and Sandham [93] performed a global linear stability analysis of the mean flow field from their LES and detected an unstable global mode inside the separation bubble, which provides a possible driving mechanism for the low-frequency unsteadiness by displacing the separation and reattachment points. Piponniau *et al.* [94] proposed a simple physical model that relates the low-frequency oscillations to the breathing motions of the separation bubble, in which the collapse of the separation bubble is caused by a continuous entrainment of mass flux, while the dilation corresponds to a radical expulsion of the mass injection in the bubble. A similar model was suggested by Wu and Martin [95] based on DNS of a compression ramp configuration. They consider that a feedback loop, involving the separation bubble, the detached shear layer and the shock system, is the underlying mechanism for low-frequency shock motions. The DMD analysis of Grilli *et al.* [96] provided further evidence that mixing across the separated shear layer leading to a contraction and expansion of the separation bubble is the dominant mechanism for the low-frequency unsteadiness. Numerical work of Grilli *et al.* [97] and Priebe *et al.* [98] identified streamwise-elongated Görtler vortices originating around the reattachment location for compression ramp configurations. For an impinging shock configuration, Pasquariello *et al.* [99] reported

very similar observations of low-frequency ( $0.01 < St_r < 0.2$ ) DMD modes characterised by streamwise-elongated regions of low and high momentum that are induced through Görtler-like vortices. As the separation-bubble dynamics is clearly coupled to these vortices, Görtler-like vortices might act as a source for continuous (coherent) forcing of the separation-shock-system dynamics.

In an attempt to resolve this discrepancy, Souverein *et al.* [100] proposed that actually both upstream and downstream mechanisms contribute to the SWBLI dynamics with case dependent intensity. Which type of mechanism is more dominant in producing the low-frequency dynamics depends on the shock strength and possibly the Reynolds number. In weak interactions, the low-frequency unsteady motions can be mainly associated with upstream effects, while the unsteadiness of the strong interactions is more likely driven by the dynamics of the downstream separation bubble and reattachment shock [77]. Also Priebe *et al.* [98] implied that upstream disturbances contribute to the low-frequency behavior although they consider that the downstream Görtler instability is the dominant one. Bonne *et al.* [101] indicated that the low-frequency oscillations involve both the amplification of upstream disturbances by the separated shear layer and a feedback excitation from the shock foot and backward travelling density waves.

### 1.3.2. SWBLI OVER A BFS

As discussed above, SWBLI in the impinging shock and compression ramp configuration share similar unsteady behavior and physical mechanisms [77, 78]. In contrast to these well-reported canonical cases, supersonic flow over a BFS shows a distinctly different flow topology, as shown in figure 1.17. The incoming turbulent flow undergoes a centred Prandtl-Meyer expansion (PME) with the separation location fixed at the step's convex corner due to the sudden geometry expansion. The free shear layer then develops towards the downstream wall on which the flow reattaches. Compression waves are generated around the reattachment location, which coalesce into a reattachment shock [55, 102]. In this configuration, the upstream limit of the separation bubble is fixed, hence, stationary and only the downstream reattachment shock is present.

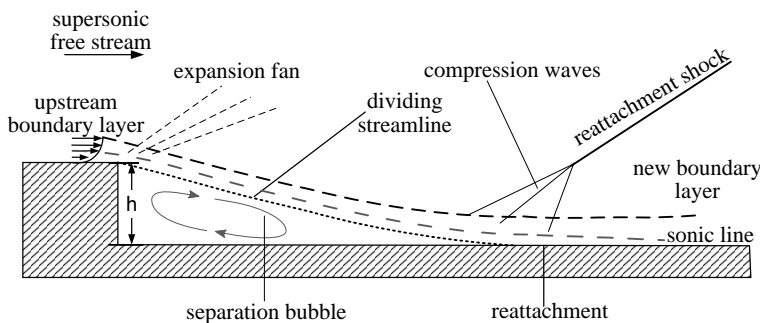


Figure 1.17: Schematic of a supersonic flow over a BFS

The dynamics of the recirculation and shock region is reported to be unsteady, similar as other more conventional SWBLI cases [103]. In an early experimental study, by examining the variation of skin friction, Ginoux [104] observed the systematic de-

velopment of counter-rotating streamwise vortices around the reattachment, occurring in laminar, transitional and turbulent flows alike. The wavelength of these vortices is equal to two or three times the boundary layer thickness for a wide range of Mach number. These spanwise well-aligned vortices were also reported in the experimental visualization of a BFS with and without roughness via nano-tracer-based planar laser scattering (NPLS) [53]. In addition, small unsteady shedding vortices along the shear layer are identified by Chen *et al.* [105] using the same flow visualization techniques. However, the common K-H vortices observed in the laminar and transitional cases are not present in the turbulent shear layer [106]. The observed coherent vortical structures cover in a wide range of length and frequency scales, involving the vortex shedding close to the step, longitudinal vortices and hairpin vortices downstream of the shear layer [47]. By means of particle image velocimetry and dynamic pressure measurements, Bolgar *et al.* [103] inferred that for a flow at  $Ma = 2.0$  the dominant low-frequency parts ( $St_r \approx 0.03$ ) are associated with the separation bubble.

In the aforementioned studies, the unsteady behavior of SWBLI over the BFS is not well investigated. More efforts are required to document in more detail the frequency characteristics of SWBLI over the BFS and scrutinize the possible source of the low-frequency unsteadiness. It is interesting to discover whether the BFS configuration has a similar origin of low-frequency unsteadiness with other well-studied impinging shock and ramp SWBLI cases. In addition, the unsteady SWBLI occurs both in the laminar and turbulent flows, it is interesting to investigate to what extent the laminar and turbulent cases share similar unsteady features and physical mechanisms. The acquired knowledge may also shed light upon potential control strategies to alleviate the negative effects caused by SWBLI.

### 1.3.3. SWBLI OVER A FFS

The flow topology over a supersonic FFS is more complicated than that over a BFS, but has similar features with that over a compression ramp. As shown in figure 1.18, the boundary layer separates relatively far upstream of the step and reattaches on the step wall or downstream of the step. Compression waves are generated around the separation point due to the deflection of the boundary layer by the separation. These compression waves then coalesce into a separation shock away from the wall. A second compression wave system forms in the vicinity of the step as the flow reattaches on the step wall and is then compressed into a reattachment shock. An expansion fan is formed close to the step corner due to the flow deflection by the upper surface. There may also be a small secondary separation and reattachment on the upper wall [18, 107].

Similar with other canonical SWBLI configurations, the triangular structure, consisting of the separation shock, shear layer and reattachment shock, represents a low-frequency unsteady system [108]. In their early experimental works, Kistler [109] and Behrens [110] observed low-frequency pressure and energy fluctuations in the separation region. Due to the limitation of former experimental equipment, they were not able to acquire quantitative values of these low frequencies. Zukoski [111] provided a review of experiments about the flow field induced by the FFS in a supersonic turbulent flow. He found that the dimensionless pressure rise across the interaction system is independent on the free stream Mach number and Reynolds number. By examining the instantaneous

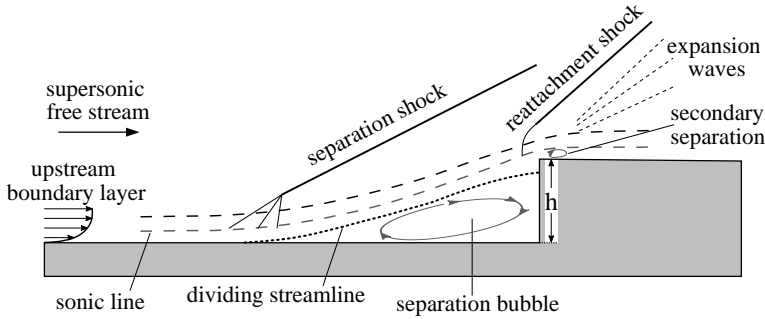


Figure 1.18: Schematic of a supersonic flow over a FFS.

flow field from LES and unsteady Reynolds-averaged Navier-Stokes (RANS) results, Morgan and Visbal [108] reported that the reattachment shock originating from the step edge has a larger unsteady spatial region compared with the separation shock emanating upstream of separation bubble. For a cylindrical FFS case, White and Visbal [112] calculated the pre-multiplied power spectral density of the wall pressure from a numerical simulation and found that the value of the dominant low frequency is approximately two orders lower than that of the wall turbulence. Recent PIV experiments also confirmed these unsteady motions of the interaction system [113].

The origin of the low-frequency unsteadiness was investigated in several recent studies. By means of a correlation analysis based on PIV measurements, Murugan and Govardhan [114] found that the shock location outside the boundary layer is well correlated to the separation bubble area but weakly connected to the disturbances within the upstream boundary layer. On the other hand, the compression waves around the shock foot are well correlated to the spanwise-aligned high- and low-speed streaks in the upstream near-wall boundary layer. Therefore, they believed that the upstream three-dimensional disturbances contribute most to the low-frequency unsteadiness of the interaction system in the FFS configuration. Simonenko *et al.* [115] also observed the longitudinal streaks, displayed as a counter-rotating vortex pair, upstream of the step in their numerical results. Estruch-Samper and Chandola [116] proposed a physical mechanism involving both upstream and downstream effects. Different from the physical model proposed by Piponnier *et al.* [94], they also consider the response of the upstream boundary layer to the shear layer and they believe that the induced shear layer instabilities are independent of the downstream dynamics according to the free-interaction theory [117]. The downstream effects are caused by the entrainment of the mass flow as the shear layer is shedding downstream and the recharging of the separation bubble when the shear layer reattaches on the downstream wall. The frequency of the breathing bubble scales effectively as the ratio of mass ejection rate to the reversed flow rate. Based on these observations, they believe that the separated shear layer is the main driver of the low-frequency unsteadiness.

## 1.4. MOTIVATION AND OBJECTIVES OF THE DISSERTATION

The objective of this research is the investigation of the dynamics of a supersonic flow over a backward/forward-facing step by numerical methods. Depending on the specific flow regime, our focus is mainly laid on two research topics, i.e., laminar-to-turbulent transition and shock wave/boundary layer interaction. High-fidelity large eddy simulation (LES) is the main method used for the current investigation. Since the boundary layer transition is very sensitive to the environmental disturbances, imposing appropriate flow conditions needs careful treatment. The uncertain and hard to control perturbation environment in supersonic wind tunnels renders experiments very difficult for the desired flow conditions, especially for the different levels of T-S waves. By contrast, LES is able to provide a well controlled environment with high accuracy and reasonable expense. Furthermore, all flow variables are simultaneously available in the whole flow field and can be accessed directly without measurement errors, which makes high-fidelity simulation very suitable for the investigation of fundamental mechanisms in various flow phenomena. The research goals for each topic are as follows.

The first area of the current research is the evolution of different instabilities and the path of the boundary layer transition as it occurs over a BFS/FFS in a supersonic flow. For a step height larger than the incoming boundary layer thickness, the transition across the step is usually not governed by the growth of T-S waves. Several other instabilities have been reported in the transition process from previous experimental and numerical works. A specific transition roadmap requires to be drawn for the BFS/FFS configuration in a supersonic flow and the development of the involved instabilities needs to be scrutinized to identify the prevailing instability among the various modes. In addition, the role of the incoming T-S waves is not clear in the transition process when other instabilities are excited in the separation region, notably K-H instability. Since previous efforts have only focused on one of the primary instabilities (either T-S mode or K-H mode), it is interesting to investigate how the incoming T-S waves behave in the background of the strong K-H instability. In the development of the turbulence, secondary instability may be excited by the growth and deformation of the primary mode. The interaction between different primary instabilities and the secondary instabilities is also one of our objectives for the first research topic.

Due to the instability of the separated shear flow, the boundary layer behind the separation region has usually become turbulent, while a shock wave is formed as the flow reattaches downstream in the supersonic step flow. Therefore the interaction of shock waves with the laminar, transitional or turbulent boundary layer reasonably turns into our second research subject. It is well reported that the SWBLI system is unsteady whatever the geometrical configuration is. Compared to the impinging shock and compression ramp cases, one side of the separation bubble is stationary and the height of the separation region is imposed (equal to the step height, only for the BFS) in the step flow. Thus, more efforts are required to establish the frequency characteristics of SWBLI over the step. Furthermore, the underlying mechanism related to the low-frequency unsteadiness may also have differences. To reveal the potentially different flow dynamics and clarify the discrepancy of the physical mechanisms in the existing literature, a further aim of this research is to trace the possible source of the low-frequency unsteadiness in the step flow.

## 1.5. LAYOUT OF THE DISSERTATION

The dissertation is divided into five chapters in total, including this introduction chapter. A brief description of the other chapters is as follows:

Chapter 2 provides a detailed introduction of the numerical method and flow analysis techniques used. In the first section, the formulation of the physical problems in a framework of implicit large eddy simulation (ILES) is presented, including the governing equations, boundary conditions, numerical discretization and subgrid-scale model. In the second section, techniques used for analyzing the results from LES are described. Specifically, linear stability theory is applied for generating the least stable mode imposed on the domain inlet and analyzing the growth of perturbations in the linear regime. From a perspective of vorticity dynamics, the generation, development and transformation of the vorticity are scrutinized and thus an understanding of the instability evolution are obtained. For decoupling the complex flow field with various dynamics, dynamic mode decomposition is implemented to identify the dominant flow dynamics in the overall system of the interaction.

Chapter 3 discusses the flow dynamics over the BFS in different flow regimes. First, the flow configuration and numerical setup for different BFS cases, especially the perturbations imposed at the inlet boundary conditions, are described. A brief comparison among these cases is made to identify the appropriate cases for the following two research topics. One focus of this chapter is the laminar-to-turbulent transition. The transition path is scrutinized in a clean laminar case (without imposed disturbance at the inlet) and the dominant flow phenomena in this process are analyzed. Then the evolution of various instabilities and their interactions in the transition are examined further in the perturbed cases, for which different levels of initial disturbances are considered. For the turbulent case, our attention is paid on the unsteady SWBLI, consisting of the unsteady motions, corresponding frequency characteristics and the origin of the low-frequency unsteadiness.

Chapter 4 investigates the laminar-to-turbulent transition and SWBLI over the FFS. The organization of this chapter is similar to that of chapter 3. Four cases are considered in the FFS part, including a fully laminar case, two perturbed cases with low- and high-amplitude oblique T-S waves, respectively, and a turbulent case. A detailed description of the flow configuration and numerical setup for them are presented first. After selecting the appropriate cases for the different research topics in the comparison section, the transition process is studied then based on the fully laminar case in the next section. In the transitional regime, the development of various instabilities and their interactions are discussed. Using the turbulent case, the unsteady SWBLI, especially the physical mechanism of the low-frequency unsteadiness, is studied.

Chapter 5 presents the research conclusions with a summary of the main findings for both the BFS and FFS cases. The outlook and recommendations for the future work are addressed at the end.



# 2

## METHODOLOGY

*Sharp tools are essential prerequisite to  
the accomplishment of the remarkable work.*

工欲善其事，必先利其器

Analects of Confucius  
论语

## 2.1. NUMERICAL METHOD

An implicit LES method of Hickel *et al.* [118] is employed to solve the compressible Navier-Stokes (N-S) equations for the current investigation. The physical and numerical models are briefly described in this section, including the governing equations, discretization scheme and boundary conditions.

### 2.1.1. GOVERNING EQUATIONS

The physical problem is governed by the three-dimensional compressible N-S equations with appropriate boundary and initial conditions, which represent the conservation of mass, momentum and total energy

$$\frac{\partial \rho}{\partial t} + \frac{\partial}{\partial x_i} (\rho u_i) = 0, \quad (2.1)$$

$$\frac{\partial \rho u_j}{\partial t} + \frac{\partial}{\partial x_i} (\rho u_i u_j + \delta_{ij} p - \sigma_{ij}) = 0, \quad (2.2)$$

$$\frac{\partial E}{\partial t} + \frac{\partial}{\partial x_i} (u_i E + u_i p - u_j \sigma_{ij} + q_i) = 0, \quad (2.3)$$

where  $\rho$  is the density,  $p$  the pressure and  $u_i$  are the components of the velocity vector in three directions. The total energy  $E$  is defined as

$$E = \frac{p}{\gamma - 1} + \frac{1}{2} \rho u_i u_i. \quad (2.4)$$

The viscous stress tensor  $\tau_{ij}$  follows the Stokes hypothesis for a Newtonian fluid

$$\sigma_{ij} = \mu \left( \frac{\partial u_i}{\partial x_j} + \frac{\partial u_j}{\partial x_i} - \frac{2}{3} \delta_{ij} \frac{\partial u_k}{\partial x_k} \right), \quad (2.5)$$

and the heat flux  $q_i$  is computed by the Fourier's law

$$q_j = -\kappa \frac{\partial T}{\partial x_j}. \quad (2.6)$$

The fluid is air and assumed to behave as a perfect gas with a specific heat ratio  $\gamma = 1.4$  and a specific gas constant  $R = 287.05 \text{ J}(\text{kg} \cdot \text{K})^{-1}$ . Accordingly, the thermodynamic properties follow the ideal-gas equation of state

$$p = \rho R T. \quad (2.7)$$

The dynamic viscosity  $\mu$  and thermal conductivity  $\kappa$  are a function of the static temperature  $T$  and are modelled according to Sutherland's law and the assumption of a constant Prandtl number  $Pr$

$$\mu = \mu_{\text{ref}} \frac{T_{\text{ref}} + S}{T + S} \left( \frac{T}{T_{\text{ref}}} \right)^{1.5}, \quad (2.8)$$

$$\kappa = \frac{\gamma R}{(\gamma - 1) Pr} \mu. \quad (2.9)$$

The reference values adopted for the computation are:  $\mu_{\text{ref}} = 18.21 \times 10^{-6} \text{ Pa} \cdot \text{s}$ ,  $T_{\text{ref}} = 293.15 \text{ K}$ ,  $S = 110.4 \text{ K}$  and  $Pr = 0.72$ .

### 2.1.2. FORMULATION OF THE FILTERED GOVERNING EQUATIONS

The principal idea of LES is imposing a scale separation or filtering on the governing equations, in which the effects of small scales are modeled, while the large scales are numerically resolved [119]. If we consider a simple scalar  $\phi$  with the generic nonlinear transport equation

$$\partial_t \phi + \partial_x F(\phi) = 0, \quad (2.10)$$

after applying a linear low-pass filter based on the convolution, the filtered scalar becomes

$$\bar{\phi}(x) = G * \phi. \quad (2.11)$$

The large and small spatial scales are then separated. The filter kernel  $G$ , such as the Box, top hat and Gaussian filter, is homogeneous and integrates to unity [120]. The filtered transport equation is obtained by convolution of equation (2.10) with the filter kernel  $G$ , which leads to

$$\partial_t \bar{\phi} + G * \partial_x F(\phi) = 0. \quad (2.12)$$

For three-dimensional compressible N-S equations, most researchers used a density-weighted variant of variables in LES, i.e., Favre filtering. The modification of variables is determined mathematically by

$$\overline{\rho \phi} = \bar{\rho} \tilde{\phi}. \quad (2.13)$$

Using the aforementioned filter and Favre filtering, the equation (2.1) - (2.3) become

$$\left\{ \begin{array}{l} \frac{\partial \bar{\rho}}{\partial t} + \frac{\partial \bar{\rho} \tilde{u}_j}{\partial x_j} = 0 \\ \frac{\partial \bar{\rho} \tilde{u}_i}{\partial t} + \frac{\partial \bar{\rho} \tilde{u}_i \tilde{u}_j}{\partial x_j} + \frac{\partial \bar{p}}{\partial x_i} - \frac{\partial \check{\sigma}_{ij}}{\partial x_j} = -\frac{\partial \tau_{ij}}{\partial x_j} + \frac{\partial}{\partial x_j} (\overline{\sigma_{ij}} - \check{\sigma}_{ij}) \\ \frac{\partial \bar{\rho} \tilde{E}}{\partial t} + \frac{\partial (\bar{\rho} \tilde{E} + \bar{p}) \tilde{u}_j}{\partial x_j} - \frac{\partial \check{\sigma}_{ij} \tilde{u}_i}{\partial x_j} + \frac{\partial \check{q}_j}{\partial x_j} \\ = -\frac{\partial}{\partial x_j} \left[ \left( \overline{\rho u_j E} - \bar{\rho} \tilde{u}_j \tilde{E} \right) + (\overline{u_j p} - \tilde{u}_j \bar{p}) - (\overline{\sigma_{ij} u_j} - \check{\sigma}_{ij} \tilde{u}_j) - (\overline{q_j} - \check{q}_j) \right] \end{array} \right. , \quad (2.14)$$

where

$$\tau_{ij} = \bar{\rho} (\overline{u_i u_j} - \tilde{u}_i \tilde{u}_j) \quad , \quad (2.15)$$

$$\check{\sigma}_{ij} = \mu(\tilde{T}) \left( 2\tilde{S}_{ij} - \frac{2}{3} \delta_{ij} \tilde{S}_{kk} \right) \quad , \quad (2.16)$$

$$\tilde{S}_{ij} = \frac{1}{2} \left( \frac{\partial \tilde{u}_i}{\partial x_j} + \frac{\partial \tilde{u}_j}{\partial x_i} \right) \quad , \quad (2.17)$$

$$\check{q}_j = -\kappa(\tilde{T}) \frac{\partial \tilde{T}}{\partial x_j} \quad . \quad (2.18)$$

However, we use the cell-averaged density, velocity, pressure and internal energy directly, instead of Favre variables, in the current implicit LES method [118].

### 2.1.3. DISCRETIZATION

The full right hand side of equation (2.14) must be modeled to consider the effects of unresolved subgrid scales (SGS) in LES. In the current in-house ILES solver INCA, the models for the different SGS terms are directly included in the numerical discretization scheme [118, 121]. To simplify the description, continue considering the filtered generic nonlinear transport equation (2.12) and it can be discretized onto a numerical grid  $x_N = \{x_j\}$  as

$$\partial_t \bar{\phi}_N + G * \partial_x F_N(\phi_N) = -G * \partial_x \mathcal{G}_{SGS}, \quad (2.19)$$

where the overbar denotes the filtering and the subscript  $N$  indicates grid functions. Since the non-represented scales cannot be recovered (i.e.,  $\phi_N \neq \phi$ ), the subgrid-stress residual is

$$\mathcal{G}_{SGS} = F(\phi) - F_N(\phi_N) \quad (2.20)$$

In equation (2.19), however, the model error and truncation error due to the numerical scheme are not included. Thus an exact solution considering these errors actually satisfies a modified differential equation (MDE) for a general LES discretization scheme

$$\partial_t \bar{\phi}_N + G * \partial_x F_N(\phi_N) = \mathcal{G}_N + \mathcal{G}_M - G * \partial_x \mathcal{G}_{SGS}, \quad (2.21)$$

where the modeling error  $\mathcal{G}_M$  is defined as

$$\mathcal{G}_M = G * \partial_x \mathcal{G}_{SGS} - G * \partial_x M_{SGS}. \quad (2.22)$$

If the numerical truncation error  $\mathcal{G}_N$  approximates to the filtered subgrid-stress residual, i.e.,

$$\mathcal{G}_N \approx -G * \partial_x \mathcal{G}_{SGS}, \quad (2.23)$$

the subgrid stress residual is no longer needed explicitly in equation (2.21). In other words, the truncation error from a suitable discretization scheme can act as an implicit SGS model that replaces  $M_{SGS}$  in this case.

A nonlinear finite-volume scheme, adaptive local deconvolution method (ALDM), was proposed by Hickel *et al.* [118] to exploit equation (2.23) for more accurate time advancement. ALDM is based on a solution-adaptive reconstruction operator and a numerical flux function that incorporates the essential elements of LES, filtering and deconvolution. The exact stable numerical scheme was calibrated through an optimization process. The main process consists of designing consistent but very general discretization methods with many free parameters, then analyzing the spectral energy transfer, and finally determining values of discretization parameters by preparing the objective implicit SGS model to approximate canonical turbulence problems as closely as possible. Both the final model form and the parameter values of ALDM are essentially designed to closely approximate the spectral energy transfer in turbulence. Since this procedure starts from a nonlinearly stable numerical scheme (usually not a suitable model of SGS turbulence in the first place) and towards a final ALDM scheme with the capability of acting as an accurate SGS model, it is much closer to explicit SGS modeling than a standard ILES. More details can be found in the dissertation of Hickel [122]. For the temporal discretization, an explicit third-order total variation diminishing (TVD) Runge-Kutta scheme is used [123].

### 2.1.4. BOUNDARY CONDITIONS

The solution for a specific flow is determined by the general governing equations given above and case-specific boundary conditions that result in a well posed problem. Most of the boundary conditions used in the current study are typical ones for a compressible viscous flow and the relevant details will be given in the case setup sections of the following chapters. Particularly, the inlet boundary conditions used are presented here briefly because they are different for the considered BFS/FFS cases.

#### BOUNDARY CONDITIONS BASED ON RIEMANN INVARIANTS

In the current study, the inlet boundary conditions for all laminar cases, as well as the non-reflecting far field conditions for all cases, are based on Riemann invariants. The characteristic analysis of Riemann invariants is on the basis of wave propagation across the boundary. Therefore, the imposed Riemann invariants depend on eigenvalues associated with their propagation speed and direction. Taking a supersonic far field boundary condition as an example, the inflow and outflow Riemann invariants  $R^-$  and  $R^+$  are determined by

$$R^- = u_\infty^n - \frac{2c_\infty}{\gamma - 1} \quad , \quad (2.24)$$

$$R^+ = u_e^n + \frac{2c_e}{\gamma - 1} \quad , \quad (2.25)$$

where  $c$  is the local speed of sound. Symbols with subscripts  $\infty$  and  $e$  represent the variables at the free stream (or at the ghost cells) and the inner points closest to the boundary, respectively. The velocity with the superscript  $n$  signifies the component of the velocity vector normal to the boundary, i.e.,  $u^n = \mathbf{u} \cdot \mathbf{n}$ , where  $\mathbf{n}$  is a space vector normal to the boundary.

The normal component of the velocity  $u_b^n$  and speed of sound  $c^n$  at the boundary are then calculated by

$$u_b^n = \frac{1}{2} (R^+ + R^-) \quad , \quad (2.26)$$

$$c_b = \frac{1}{4} (\gamma - 1) (R^+ - R^-) \quad . \quad (2.27)$$

If the normal velocity on the boundary  $u_b^n$  is positive, the flow is coming out of the computational domain and the entropy  $s$  is extrapolated from the interior. On the contrary, if  $u_b^n < 0$ , the flow is entering the flow domain and the free stream entropy is used, that is,

$$s_b = \begin{cases} \frac{p_e}{\rho_e^\gamma R}, & u_b^n \geq 0 \\ \frac{p_\infty}{\rho_\infty^\gamma R}, & u_b^n < 0 \end{cases} \quad . \quad (2.28)$$

The density and pressure on the boundary are then computed by

$$\rho_b = \left( \frac{c_b^2}{s_b \gamma R} \right)^{1/\gamma - 1} \quad , \quad (2.29)$$

$$p_b = \frac{\rho_b c_b^2}{\gamma} \quad . \quad (2.30)$$

For the inlet boundary conditions based on Riemann invariants, the computational process is similar to the far field boundary, but the inflow variables are used for the incoming Riemann invariants, instead of the free stream parameters.

2

#### TURBULENT INFLOW CONDITIONS BASED ON A DIGITAL FILTER

Imposing an accurate three-dimensional and time-evolving inlet boundary condition is always necessary and challenging for the numerical simulation with turbulent boundary layer as inflow. Therefore, special treatment is required to produce an appropriate turbulent inlet boundary condition.

The most easily conceivable and implemented method would be prescribing a laminar inflow and let it develop naturally in a sufficiently large domain to cover the whole laminar-to-turbulent transition region. However, this approach is impracticable in most cases due to its high computational cost, especially for DNS and LES. Probably, the rescaling/recycling technique is the most popular practical approach. The main idea of this method is extracting the turbulent data from a downstream location, which is then rescaled and imposed on the inlet of the main computational domain. Unfortunately, this technique can produce spurious low-frequency modes within the boundary layer and contaminate our flow field. Especially, when our attention is laid on the low-frequency unsteadiness related to the downstream boundary layer, for instance, the low-frequency unsteady SWBLL, the interesting phenomenon may be modulated by this artificial low-frequency content of the upstream boundary layer. Thus, an alternative synthetic turbulence generation method based on digital filter (DF) is used in the current study. This technique can model both given first- and second-order statistical moments and spectra without introducing undesired low-frequency contents [124]. In the following, more details about the DF technique are provided.

The overall procedure of DF technique is divided into three main steps. First, we generate a three-dimensional random fluctuation fields and then transform them into the real instantaneous velocity fluctuations that match the target auto-correlations, cross-correlations and length scales using the method developed by Klein *et al.* [124]. Finally, these instant fluctuations are added to the prescribed mean flow field to obtain the artificial turbulent inflow. Through this process, certain statistical characteristics are reproduced, including the mean flow, fluctuations, length and time scales, and second-order moments.

The first step is to have the desired intermediate velocity fluctuations with prescribed length scales. If we define a discrete filter operator  $F_N$  ( $N$  is a positive integer), the field of fluctuations  $q_k$  can be formulated and linearized as

$$q_k = F_N(r_k) = \sum_{l=-N}^N b_l r_{k+l}, \quad (2.31)$$

where  $\{r_k\}_{1 \leq k \leq m}$  is a set of  $m$  random numbers with zero-mean and unit-variance

$$\begin{aligned} \overline{r_k} &= \sum_{k=1}^m r_k / m = 0, \\ \overline{r_i r_j} &= \sum_{i,j=1}^m r_i r_j / m = \delta_{ij}, \end{aligned} \quad (2.32)$$

and  $\{b_l\}_{-N \leq l \leq N}$  is the coefficients of the “digital filter”. Here,  $\delta_{ij}$  is Kronecker delta function. Furthermore we can easily derive

$$\begin{aligned} \overline{q_k} &= 0, \\ \overline{q_k q_{k+n}} &= \sum_{l=-N+n}^N b_l b_{l-n}. \end{aligned} \quad (2.33)$$

The two-point auto-correlation function is modeled by an exponential function

$$R_{qq}(\Delta L) = \exp\left(-\frac{\pi \Delta L}{2I_y}\right), \quad (2.34)$$

which is reported to be closer to the real form of auto-correlation function than Gaussian [125]. In equation (2.34),  $\Delta L$  is the distance between two different points and  $I_y$  is a given integral scale [126].

If we implement equation (2.34) on a uniform grid, letting  $\Delta y$  is the grid space and  $I_y = n_y \Delta y$ , then equation (2.34) is written in a discretized form

$$R_{qq}(y_k + m\Delta y) \equiv \frac{\overline{q_k q_{k+m}}}{\overline{q_k q_k}} = \exp\left(-\frac{\pi m}{2n_y}\right). \quad (2.35)$$

Combined with equation (2.33), the filter coefficients  $b_m$  can be computed by solving the following equation

$$\frac{\sum_{l=-N+m}^N b_l b_{l-m}}{\sum_{l=-N}^N b_l^2} = \exp\left(-\frac{\pi m}{2n_y}\right). \quad (2.36)$$

The result is given approximately by [125]

$$b_m \approx \frac{\tilde{b}_m}{(\sum_{l=-N}^N \tilde{b}_l^2)^{1/2}}, \quad (2.37)$$

where

$$\tilde{b}_m = \exp\left(-\frac{\pi m}{n_y}\right). \quad (2.38)$$

A good filter size is set by  $N \geq 2n_y$ , which is large enough to capture twice the integral length scale and not computationally expensive [124].

We use a Mersenne Twister generator [127] to produce the required random numbers. After applying the  $F_N$ -operator with the above setup of the convolution coefficients  $b_m$ , the initial random field has featured with a coherence integral length scale  $I_y$ .

The aforementioned procedure can be extended to two dimensions by defining a two-dimensional filter coefficients

$$b(j', k') = b_{j'} \cdot b_{k'}, \quad (2.39)$$

and the corresponding filter operation

$$q(j, k) = \sum_{j'=-N_{Fy}}^{N_{Fy}} \sum_{k'=-N_{Fz}}^{N_{Fz}} b(j', k') r(j + j', k + k') \quad , \quad (2.40)$$

where  $1 \leq j \leq n_j$  and  $1 \leq k \leq n_k$  are the indices of the computational grid. The upper limit of the summation is determined by

$$N_{F_\alpha} = 2 \lceil I_\alpha / \Delta \alpha \rceil \text{ with } \alpha = y, z \text{ (}\lceil \cdot \rceil \text{ is the ceiling function)}. \quad (2.41)$$

Therefore we need a set of three two-dimensional random fields  $r$  with dimensions of  $(-N_{F_y} + 1 : N_{F_y} + n_j, -N_{F_z} + 1 : N_{F_z} + n_k, 3)$  for the three components of velocity.

Next the new field  $q_k^{t_n}$  and the previous one  $q_k^{t_{n-1}}$  are correlated with each other as follows,

$$\rho_k = q_k^{t_{n-1}} \exp\left(-\frac{\pi \Delta t}{2\tau}\right) + q_k^{t_n} \sqrt{1 - \exp\left(-\frac{\pi \Delta t}{\tau}\right)}, \quad (2.42)$$

where  $\Delta t$  is the time step. The Lagrangian time scale  $\tau$  is computed by  $\tau = I_x / \bar{u}$ , where  $I_x$  is the prescribed integral length scale in the streamwise direction. Using this transformation, the fluctuations field has the desired two-point correlations.

The single-point correlations are imposed by the Lund transform [128]

$$\begin{bmatrix} u(0, y, z, t) \\ v(0, y, z, t) \\ w(0, y, z, t) \end{bmatrix} = \underbrace{\begin{bmatrix} \langle u(0, y, z) \rangle \\ \langle v(0, y, z) \rangle \\ \langle w(0, y, z) \rangle \end{bmatrix}}_{U_i(0, y, z)} + \underbrace{\begin{bmatrix} a_{11} & 0 & 0 \\ a_{21} & a_{22} & 0 \\ a_{31} & a_{32} & a_{33} \end{bmatrix}}_{u'_i(0, y, z, t)} \begin{bmatrix} \rho^u(y, z) \\ \rho^v(y, z) \\ \rho^w(y, z) \end{bmatrix} \quad (2.43)$$

with  $a_{11} = (R_{11})^{1/2}$ ,  $a_{21} = R_{21}/a_{11}$ ,  $a_{22} = (R_{22} - a_{21}^2)^{1/2}$ ,  $a_{31} = R_{31}/a_{11}$ ,  $a_{32} = (R_{32} - a_{21}a_{31})/a_{22}$ ,  $a_{33} = (R_{33} - a_{31}^2 - a_{32}^2)^{1/2}$ , where  $\{R_{ij}\}_{i,j=1,2,3}$  is the prescribed Reynolds-stress tensor. Eventually, we have the expected velocity field for the turbulent inflow. The instantaneous temperature  $T'$  and density  $\rho'$  field can be computed from the Strong Reynolds Analogy [129]

$$\begin{aligned} T' &= -\frac{\gamma-1}{\gamma R} \bar{u} u' \quad , \\ \frac{\rho'}{\bar{\rho}} &= -\frac{T'}{\bar{T}} \quad . \end{aligned} \quad (2.44)$$

Prescribing accurate length scales are not crucial to the generation of precise enough turbulence in the LES, however, length scales closer to real values always give faster transition from synthetic to real physical turbulence. The imposed length scales should be as least as large as the values of the real turbulent flow. Moreover, the inflow plane for digital filter can be divided into several zones to accommodate that the flow field has different integral length scales in different sublayers of the boundary layer and the outer flow.

## 2.2. FLOW ANALYSIS TECHNIQUES

To analyse the results from LES, several well-established theoretical approaches and data analysis techniques are applied, including linear stability theory (LST), vortex dynamics, dynamic mode decomposition (DMD) and sparsity-promoting dynamic mode decomposition (SPDMD). The details of these methods are addressed in the following section.

### 2.2.1. LINEAR STABILITY THEORY

Linear stability theory is widely used to investigate the growth of perturbations in a parallel flow within the linear regime with relatively low computational cost compared with LES and DNS [130, 131]. There are two variants of LST depending on the considered physical problems, i.e., temporal and spatial model. The temporal stability analysis assumes that the growth of disturbances is constant in the streamwise direction and only varies with time. The spatial theory supposes that the evolution of unstable mode is only growing with the streamwise distance, which is relatively more realistic and closer to the real physics of the flow field [25]. In the current study, the spatial variant of LST was employed to scrutinize the streamwise evolution of the laminar-to-turbulent transition.

Considering the unsteady N-S equations, the instantaneous flow variables are decomposed into a base flow  $\bar{q}$  and unsteady perturbations  $q'$ ,

$$q(x, y, z, t) = \bar{q}(x, y, z) + q'(x, y, z, t). \quad (2.45)$$

Assuming the  $x$  (streamwise) and  $z$  (spanwise) directions are homogeneous, based on the linear assumption, the fluctuations can be represented by harmonic modes

$$q'(x, y, z, t) = \bar{q}(y) \cdot e^{i(\alpha x + \beta z - \omega t)} + c.c., \quad (2.46)$$

where the real part of  $\alpha$  and  $\beta$  determines the streamwise and spanwise wavenumber, and the imaginary part of  $\alpha$  shows the growth rate in the  $x$  direction. The wave angle  $\theta$  of the traveling modes with respect to the  $x$  axis is given by  $\arctan(\beta_r/\alpha_r)$ . The real and imaginary part of  $\omega$  represent the frequency and temporal growth rate respectively. The term  $c.c$  denotes the complex conjugate of the perturbation, in order to obtain a real-valued quantity. In the LST, the reference length for these parameters is the local Blasius length  $l = \sqrt{v_\infty x/u_\infty}$ , for instance the dimensionless streamwise wavenumber  $\alpha^l = \alpha l$ . In this dissertation, the parameters of wave properties with superscript  $l$  are normalized by the Blasius length  $l$ , and those with superscript  $\delta$  are normalized by the inlet boundary layer thickness  $\delta_0$ .

For the spatial stability analysis,  $\beta$  and  $\omega$  are prescribed real numbers, while  $\alpha$  is to-be-solved complex number. In this case, the formulation of the perturbations can be rewritten as

$$q'(x, y, z, t) = \underbrace{e^{-\alpha_i x}(\bar{q}_r \cos \theta - \bar{q}_i \sin \theta)}_{\text{real part}} + \underbrace{i e^{-\alpha_i x}(\bar{q}_r \sin \theta + \bar{q}_i \cos \theta)}_{\text{imaginary part}}, \quad (2.47)$$

where  $\theta = \alpha_r x + \beta z - \omega t$ . The base flow  $\bar{q}$  and perturbations  $\bar{q}$  are substituted into the compressible N-S equations [equation (2.1)-(2.3)], the resulting linearized N-S equations are then further simplified by the parallel-flow assumption to the Orr-Sommerfeld (O-S) equations. With appropriate boundary conditions, these equations represent an eigenvalue problem. In the spatial analysis, the resulting eigenvalues of the O-S equations are the complex wavenumber  $\alpha$  and the corresponding complex eigenfunctions are the disturbances of three velocity components, pressure and temperature. The LST solver used in the present study is a validated in-house code whose numerical details and validation have been reported previously [132–134].

### 2.2.2. VORTEX DYNAMICS

The dynamics of vorticity is one of the theoretical approaches to understand the evolution of disturbances. By analyzing the generation, development, and structural characteristics of the vorticity, like stretching, tilting and lift up, in the transition process, we can obtain a deeper understanding of the involving instabilities [135].

For a compressible flow without external and potential forces, the momentum equation (2.2) can be rewritten into a nonconservation form as

$$\frac{du_i}{dt} = \frac{\partial u_i}{\partial t} + u_i \cdot \nabla u_j = -\frac{\nabla p}{\rho} + \frac{\nabla \cdot \tau_{ij}}{\rho}. \quad (2.48)$$

Taking curl on both sides of this equation, and noticing  $\omega_i = \nabla \times u_i$ , it is finally reorganized as

$$\frac{d\omega_i}{dt} = \omega_j \frac{\partial u_i}{\partial x_j} - \omega_i \frac{\partial u_j}{\partial x_j} + \epsilon_{ijk} \frac{1}{\rho^2} \frac{\partial \rho}{\partial x_j} \frac{\partial p}{\partial x_k} + \epsilon_{ijk} \frac{\partial}{\partial x_j} \left( \frac{1}{\rho} \frac{\partial \tau_{kl}}{\partial x_l} \right), \quad (2.49)$$

if expressed in tensor notation using Einstein's summation convention and Levi-Civita symbol  $\epsilon_{ijk}$ ,

$$\epsilon_{ijk} = \begin{cases} +1 & \text{if } (i, j, k) \text{ is } (1, 2, 3), (2, 3, 1), \text{ or } (3, 1, 2) \\ -1 & \text{if } (i, j, k) \text{ is } (3, 2, 1), (1, 3, 2), \text{ or } (2, 1, 3) \\ 0 & \text{if } i = j, \text{ or } j = k, \text{ or } k = i \end{cases}. \quad (2.50)$$

In the above derivation, the following notations and relations,

$$(\mathbf{a} \times \mathbf{b})_i = \epsilon_{ijk} a_j b_k, \quad (2.51)$$

$$\nabla \times (\mathbf{u} \cdot \nabla) \mathbf{u} = \nabla \times \nabla \left( \frac{u^2}{2} \right) - \nabla \times (\mathbf{u} \times \boldsymbol{\omega}) = \nabla \times (\boldsymbol{\omega} \times \mathbf{u}), \quad (2.52)$$

$$\nabla \times (\boldsymbol{\omega} \times \mathbf{u}) = (\mathbf{u} \cdot \nabla) \boldsymbol{\omega} - (\boldsymbol{\omega} \cdot \nabla) \mathbf{u} + \boldsymbol{\omega} (\nabla \cdot \mathbf{u}) + \mathbf{u} (\nabla \cdot \boldsymbol{\omega}), \quad (2.53)$$

$$\frac{d\boldsymbol{\omega}}{dt} + (\mathbf{u} \cdot \nabla) \boldsymbol{\omega} = \frac{d\boldsymbol{\omega}}{dt}, \quad (2.54)$$

and

$$\nabla \cdot \boldsymbol{\omega} = \nabla \cdot (\nabla \times \mathbf{u}) = 0 \quad (2.55)$$

are useful.

The equivalent energy of vorticity can be quantified by enstrophy, which is defined as the integral of the square of the vorticity

$$\mathcal{E} = \frac{1}{2} \int_A \boldsymbol{\omega} \cdot \boldsymbol{\omega} dA, \quad (2.56)$$

where  $A$  is the area of the cross-section perpendicular to the  $i$ -direction (streamwise direction). The vorticity transport equation (2.49) for the local enstrophy is then formulated as

$$\frac{d}{dt} \left( \frac{1}{2} \omega_i^2 \right) = \underbrace{\omega_i \omega_j \frac{\partial u_i}{\partial x_j}}_{T+S} - \underbrace{\omega_i^2 \frac{\partial u_j}{\partial x_j}}_D + \underbrace{\epsilon_{ijk} \frac{\omega_i}{\rho^2} \frac{\partial \rho}{\partial x_j} \frac{\partial p}{\partial x_k}}_B + \underbrace{\omega_i \epsilon_{ijk} \frac{\partial}{\partial x_j} \left( \frac{1}{\rho} \frac{\partial \tau_{kl}}{\partial x_l} \right)}_V. \quad (2.57)$$

In the right side of the equation, the first term can be decomposed into three parts, for instance for the  $x$  direction,

$$\begin{aligned} T &= T_{xy} + T_{xz} = \frac{\partial u}{\partial y} \omega_y \omega_x + \frac{\partial u}{\partial z} \omega_z \omega_x, \\ S_{xx} &= \frac{\partial u}{\partial x} \omega_x \omega_x, \end{aligned} \quad (2.58)$$

where the first two terms  $T_{xy}$  and  $T_{xz}$  represent the vortex tilting caused by the wall-normal and spanwise vorticity, while  $S$  specifies the vortex stretching. The second term  $D$  represents the dilation effects in compressible flows. The function of this term is to redistribute the existing vorticity, instead of creating or destroying. In response to this term, the local enstrophy decreases if the flow field is undergoing expansion and it increases in compression regions. The terms  $B$  and  $V$  signify baroclinic torque and viscous dissipation, respectively. If the density gradient and pressure gradient are nearly parallel in the flow field, the baroclinic torque is negligible. In a high speed flow, especially when a large-scale vortex structure occurs, viscous dissipation can be neglected due to the high  $Re$ . For this reason,  $V$  will not be considered in the current investigation. The evolution of the instabilities and underlying vortical mechanism can be scrutinized by assessing the contribution of each term in the enstrophy transport equation. Suryanarayanan *et al.* [135] enhanced the mechanistic understanding of the transition process induced by discrete roughness elements based on this vorticity-based analysis.

### 2.2.3. DYNAMIC MODE DECOMPOSITION

Dynamic mode decomposition (DMD) is a reduced-order method to decouple the complex spatial and temporal dynamical system in order to extract the representative features. It was first proposed by Schmid [136] as a numerical tool to identify the most important dynamic information of time sequential data. Basically, given an equal-interval time series of data, DMD transforms this dynamical system into a set of modes, each of which is associated with a single orthogonal frequency behavior whose dynamics is governed by the corresponding eigenvalue. This algorithm has been widely applied for diverse flow problems, including the transition mechanism from laminar to turbulent flow [137], unsteadiness of the SWBLI [96], and the identification of coherent vortex structures [138].

The process of DMD can be divided into the following steps. First, we collect a set of time sequential snapshots from the numerical simulation or experimental data, given by a matrix  $\mathbf{P}_1^N$ ,

$$\mathbf{P}_1^N = \{\mathbf{p}_1, \mathbf{p}_2, \mathbf{p}_3, \dots, \mathbf{p}_N\}, \quad (2.59)$$

where  $\mathbf{p}_i$  represents the flow field at the  $i$ th moment and it belongs to  $\mathbb{R}^{M \times 1}$  where  $M$  is the spatial dimensions of the flow field. All these snapshots are in an ordered sequence, separated by a constant sampling time  $\Delta t$ . We assume that there exists a linear mapping  $\mathbf{A}$  which links the current snapshot  $\mathbf{p}_i$  to the subsequent flow field  $\mathbf{p}_{i+1}$ , that is,

$$\mathbf{p}_{i+1} = \mathbf{A} \mathbf{p}_i. \quad (2.60)$$

Matrix  $\mathbf{P}_1^N$  is thus rewritten by

$$\mathbf{P}_1^N = \{\mathbf{p}_1, \mathbf{A}\mathbf{p}_1, \mathbf{A}^2\mathbf{p}_1, \dots, \mathbf{A}^{N-1}\mathbf{p}_1\}. \quad (2.61)$$

Then define another set of sequential snapshots  $\mathbf{P}_2^N = \{\mathbf{p}_2, \mathbf{p}_3, \mathbf{p}_4, \dots, \mathbf{p}_N\}$ , and it can be formulated as

$$\mathbf{P}_2^N = \{\mathbf{A}\mathbf{p}_1, \mathbf{A}\mathbf{p}_2, \mathbf{A}\mathbf{p}_3, \dots, \mathbf{A}\mathbf{p}_{N-1}\} = \mathbf{A}\mathbf{P}_1^{N-1}. \quad (2.62)$$

The linear mapping  $\mathbf{A}$  is the system matrix of the dynamical flow system whose eigenvector can represent the intrinsic characteristics of the unsteady flow system. When continuously increasing the number of the snapshots, the vector space  $\mathbf{P}_1^N$  will become linearly dependent at a critical number, which means the rank of the vector space will remain constant if further adding the flow data sequence  $\mathbf{p}_i$ . After reaching this threshold, the vector  $\mathbf{p}_N$  can be expressed as a linear combination of the previous linearly independent data sequence, that is,

$$\mathbf{p}_N = a_1\mathbf{p}_1 + a_2\mathbf{p}_2 + \dots + a_{N-1}\mathbf{p}_{N-1} + \mathbf{r} = \mathbf{P}_1^{N-1}\mathbf{a} + \mathbf{r}, \quad (2.63)$$

where  $\mathbf{a} = \{a_1, a_2, \dots, a_{N-1}\}^T$  and  $\mathbf{r}$  is the residual vector. The second sequential snapshots can be further formulated as

$$\mathbf{P}_2^N = \{\mathbf{p}_2, \mathbf{p}_3, \mathbf{p}_4, \dots, \mathbf{p}_{N-1}, \mathbf{P}_1^{N-1}\mathbf{a}\} + \mathbf{R}, \quad (2.64)$$

where  $\mathbf{R} = \{\mathbf{0}, \mathbf{0}, \dots, \mathbf{r}\} \in \mathbb{R}^{M \times (N-1)}$ . Combine equation (2.62) and (2.64), and rewrite them in a matrix form

$$\mathbf{P}_2^N = \mathbf{A}\mathbf{P}_1^{N-1} = \mathbf{P}_1^{N-1}\mathbf{S} + \mathbf{R}. \quad (2.65)$$

The matrices  $\mathbf{A}$  and  $\mathbf{S}$  are similar and share approximate eigenvalues.

Comparing the equations (2.64) and (2.65), the following relation is obtained

$$\{\mathbf{p}_2, \mathbf{p}_3, \mathbf{p}_4, \dots, \mathbf{p}_{N-1}, \mathbf{P}_1^{N-1}\mathbf{a}\} = \{\mathbf{p}_1, \mathbf{p}_2, \mathbf{p}_3, \dots, \mathbf{p}_{N-1}\}\mathbf{S}. \quad (2.66)$$

Substituting equation (2.64) into equation (2.66), it is easy to find that the matrix  $\mathbf{S}$  is of a companion type with

$$\mathbf{S} = \begin{bmatrix} 0 & & & a_1 \\ 1 & 0 & & a_2 \\ & \ddots & \ddots & \vdots \\ & & 1 & 0 & a_{N-2} \\ & & & 1 & a_{N-1} \end{bmatrix}. \quad (2.67)$$

The eigenvalues of matrix  $\mathbf{S}$  are easier to solve and can approximate the eigenvalues of  $\mathbf{A}$ . Thus the matrix  $\mathbf{S}$  is computed by

$$\mathbf{S} = \underset{\tilde{\mathbf{S}}}{\operatorname{argmin}} \|\mathbf{P}_2^N - \mathbf{P}_1^{N-1}\tilde{\mathbf{S}}\|_F^2, \quad (2.68)$$

where the Frobenius norm of the matrix  $\mathbf{B}$  is defined by

$$\|\mathbf{B}\|_F^2 = \operatorname{trace}(\mathbf{B}\mathbf{B}^H) = \operatorname{trace}(\mathbf{B}^H\mathbf{B}). \quad (2.69)$$

The superscript  $H$  denotes the conjugate transpose of a matrix (or vector). This optimization problem can be solved by some standard algorithms, like the least square method. However, the standard method does not show a good convergence behavior. The robustness can be improved by a preprocessing procedure using a singular value decomposition (SVD) of the vector space

$$\mathbf{P}_1^{N-1} = \mathbf{U}\mathbf{\Sigma}\mathbf{V}^H. \quad (2.70)$$

In this SVD, the matrix  $\mathbf{U}$  contains the proper orthogonal modes of the snapshots  $\mathbf{P}_1$ ,  $\mathbf{\Sigma}$  is a diagonal matrix containing the singular values, and  $\mathbf{V}$  is the right singular matrix. Because the matrix  $\mathbf{U}$  and  $\mathbf{V}$  both are orthogonal matrix, the following relations are met:  $\mathbf{U}\mathbf{U}^H = \mathbf{I}$ ,  $\mathbf{V}\mathbf{V}^H = \mathbf{I}$ . In equation (2.65), replacing  $\mathbf{P}_1^{N-1}$  by equation (2.70), left multiplying  $\mathbf{U}^H$  and right multiplying  $\mathbf{V}\mathbf{\Sigma}^{-1}$ , we can get

$$\mathbf{U}^H\mathbf{P}_2^N\mathbf{V}\mathbf{\Sigma}^{-1} = \mathbf{U}^H\mathbf{A}\mathbf{U} = \mathbf{\Sigma}\mathbf{V}^H\mathbf{S}\mathbf{V}\mathbf{\Sigma}^{-1} + \tilde{\mathbf{R}}. \quad (2.71)$$

Let  $\tilde{\mathbf{S}} \equiv \mathbf{\Sigma}\mathbf{V}^H\mathbf{S}\mathbf{V}\mathbf{\Sigma}^{-1} + \tilde{\mathbf{R}}$ . As a result,  $\tilde{\mathbf{S}}$ ,  $\mathbf{S}$  and  $\mathbf{A}$  are similar and share the same dynamical properties. The rank deficiency of the snapshots matrix can also be accounted by discarding the singular values from SVD below a critical value. The eigenvectors of  $\mathbf{A}$ , namely dynamic modes  $\phi_i$ , is determined by

$$\phi_i = \mathbf{U}\mathbf{y}_i, \quad (2.72)$$

where  $\mathbf{y}_i$  is the  $i$ th eigenvector of  $\tilde{\mathbf{S}}$ . The similar matrix  $\tilde{\mathbf{S}}$  can be obtained by the eigen decomposition of  $\tilde{\mathbf{S}}$

$$\tilde{\mathbf{S}}\mathbf{y}_i = \mu_i\mathbf{y}_i, \quad (2.73)$$

where  $\mu_i$  denotes the  $i$ th eigenvalue of  $\tilde{\mathbf{S}}$  corresponding to  $\mathbf{y}_i$ . Based on the above decomposition, the experimental or numerical snapshots can be approximately represented by a linear combination of the DMD modes

$$\mathbf{p}_m = \sum_{i=1}^{N-1} \phi_i \mu_i^m \alpha_i, \quad m \in \{1, 2, \dots, N-1\}, \quad (2.74)$$

where  $\alpha_i \in \mathbb{C}$  can be considered as the amplitude of  $i$ th DMD mode  $\phi_i$ . Rewrite this reconstruction in a matrix form as

$$\mathbf{P}_1^{N-1} = \underbrace{[\phi_1, \phi_2, \dots, \phi_{N-1}]}_{\phi} \underbrace{\begin{bmatrix} \alpha_1 & & & \\ & \alpha_2 & & \\ & & \ddots & \\ & & & \alpha_{N-1} \end{bmatrix}}_{D_\alpha = \text{diag}\{\alpha\}} \underbrace{\begin{bmatrix} 1 & \mu_1 & \dots & \mu_1^{N-1} \\ 1 & \mu_2 & \dots & \mu_2^{N-1} \\ \vdots & \vdots & \ddots & \vdots \\ 1 & \mu_{N-1} & \dots & \mu_{N-1}^{N-1} \end{bmatrix}}_{V_{\text{and}}}. \quad (2.75)$$

The Vandermonde matrix  $V_{\text{and}} \in \mathbb{C}^{(N-1) \times (N-1)}$  signifies the temporal evolution of the dynamic modes. The eigenvalues  $\mu_i$  are usually further converted onto a more familiar complex stability plane through the logarithmic mapping  $\lambda_i = \ln(\mu_i)/\Delta t$  [139]. The dynamic

information about the growth rate  $\beta_i$  and angular frequency  $\omega_i$  of a specific DMD mode are then computed by

$$\begin{aligned}\beta_i &= \Re(\lambda_i) = \ln|\mu_i|/\Delta t \\ \omega_i &= \Im(\lambda_i) = \arctan(\mu_i)/\Delta t.\end{aligned}\quad (2.76)$$

The computation of the unknown amplitude vector  $\alpha$  is an optimization problem, formulated by

$$\alpha = \underset{\alpha}{\operatorname{argmin}} \|\mathbf{P}_1^{N-1} - \phi \mathbf{D}_\alpha \mathbf{V}_{\text{and}}\|_F^2. \quad (2.77)$$

There are several methods to solve this optimization problem, like the least-mean-square and Lagrange multipliers. Here we follow the method proposed by Jovanović *et al.* [140]. Left multiply equation (2.77) with  $U^H$ , and transform this problem into the following form,

$$\underset{\alpha}{\operatorname{argmin}} J(\alpha) = \|\Sigma \mathbf{V}^H - \mathbf{Y} \mathbf{D}_\alpha \mathbf{V}_{\text{and}}\|_F^2. \quad (2.78)$$

According to the deduction of Jovanović *et al.* [140], the objective function  $J(\alpha)$  can be equivalently expressed as

$$J(\alpha) = \alpha^H \mathbf{C} \alpha - \mathbf{D}^H \alpha - \alpha^H \mathbf{D} + s, \quad (2.79)$$

where

$$\mathbf{C} = (\mathbf{Y}^H \mathbf{Y}) \circ (\overline{\mathbf{V}_{\text{and}}} \mathbf{V}_{\text{and}}^H), \quad \mathbf{D} = \overline{\operatorname{diag}(\mathbf{V}_{\text{and}} \mathbf{V}_{\text{and}}^H \mathbf{Y})}, \quad s = \operatorname{trace}(\Sigma^H \Sigma). \quad (2.80)$$

Here,  $\circ$  represents the elementwise multiplication of two matrices, an overbar denotes the complex conjugate of a matrix, and  $\operatorname{diag}$  of a matrix is a vector consisting of its main diagonal values.

Letting  $\partial J(\alpha)/\partial \alpha = 0$  in the objective function, equation (2.79), the optimal solution of minimum-value problem equation (2.78) can be computed by

$$\alpha_{\text{opt}} = \mathbf{P}^{-1} \mathbf{q}. \quad (2.81)$$

By this method, we can obtain all the DMD modes  $\phi$  for the dynamical system, weighted by their amplitudes  $\alpha$ . These modes may grow, decay or oscillate, revealed by their temporal growth rate  $\beta$ , with a single angular frequency  $\omega$ . The original flow field can be reconstructed by superimposing the fluctuations from each mode  $\phi_i$  onto the mean flow  $q_m$ , formulated as

$$q(x, t) = q_m + a_f \cdot \Re \left\{ \alpha_i \phi_i e^{i\theta_i} \right\}, \quad \theta_i = \omega_i t, \quad (2.82)$$

where  $a_f$  is the optional amplification factor of the corresponding mode  $\phi_i$ . The reconstructed flow field at different phase angles  $\theta_i$  represents the temporal evolution of the dynamic system, In this way, the imaginary part of the reconstruction at a phase angle  $\theta_i = 0$  is equivalent to the real part at  $\theta_i = \pi$ , and vice versa.

#### 2.2.4. SPARSITY-PROMOTING DYNAMIC MODE DECOMPOSITION

There is still an unsolved challenge after obtaining the DMD modes, identifying the most important dynamical modes among them. Jovanović *et al.* [140] introduced a sparsity-promoting dynamic mode decomposition (SPDMD) method to select a subset of calculated DMD modes that have the most significant effects on the approximation quality of the original snapshots.

The SPDMD mainly involves two steps. In the first step, the main objective is to find a sparse structure which is a balance between the accuracy of approximation of snapshots and the number of DMD modes. Thus an extra term is introduced into equation (2.78),

$$\underset{\alpha}{\operatorname{argmin}} J(\alpha) + \gamma \sum_{i=1}^{N-1} |\alpha_i|, \quad (2.83)$$

where  $\gamma$  is a positive regularization factor that is associated with the emphasis on sparsity of the eigenvalue vector  $\alpha$ . This additional term penalizes the number of the non-zero values in the amplitude vector  $\alpha$  and larger values of  $\gamma$  put more stress on the total number of non-zero elements in  $\alpha$  (a sparser structure). Jovanović *et al.* [140] also provides the alternating direction method of multipliers (ADMM) to solve this convex optimization problem.

In the next step, the non-zero amplitudes are obtained by fixing the sparsity structure at a specific  $\gamma$  based on the previous tradeoff between decomposition accuracy and the number of DMD modes. Therefore, a constrained convex optimization problem is formed

$$\begin{aligned} & \underset{\alpha}{\operatorname{argmin}} && J(\alpha) \\ & \text{subject to} && E\alpha = 0 \end{aligned}, \quad (2.84)$$

where  $E \in \mathbb{R}^{M \times (N-1)}$  contains the information of sparsity structure of the vector  $\alpha$ . The rows of  $E$  are unit vectors in  $\mathbb{R}^{N-1}$  with non-zero elements corresponding to zero values in  $\alpha$ . For example, if we get a vector  $\alpha^{5 \times 1} = [\alpha_1 \ 0 \ \alpha_3 \ 0 \ 0]^T$  at a specific  $\gamma$ , the matrix  $E^{3 \times 5}$  is given as

$$E = \begin{bmatrix} 0 & 1 & 0 & 0 & 0 \\ 0 & 0 & 0 & 1 & 0 \\ 0 & 0 & 0 & 0 & 1 \end{bmatrix}.$$

The method of Lagrange multiplier can be used to solve the optimization problem [equation (2.84)]. See Jovanović *et al.* [140] for more details.



# 3

## BACKWARD-FACING STEP

*Learning without thinking leads to confusion;  
thinking without learning falls into danger.*

学而不思则罔，思而不学则殆

Analects of Confucius  
论语

---

Parts of this chapter have been published, as follows.

**W. Hu**, S. Hickel, B. W. van Oudheusden, *Dynamics of a supersonic transitional flow over a backward-facing step*, *Physical Review Fluids* 4, 103904 (2019).

**W. Hu**, S. Hickel, B. W. van Oudheusden, *Influence of upstream disturbances on the primary and secondary instabilities in a supersonic separated flow over a backward-facing step*, *Physics of Fluids* 32, 56102 (2020).

### 3.1. FLOW CONFIGURATION AND NUMERICAL SETUP

This section describes the flow configuration and numerical method for the present BFS cases. Specifically, the generation of the unstable oblique waves and turbulence for the inflow are introduced.

#### 3.1.1. FLOW CONFIGURATION

The setup for the current study is an open BFS (no upper wall) with a supersonic inflow, a schematic of which is shown in figure 3.1. With this configuration, we can remove the effects of wave reflections from the upper wall. Four cases are considered on the same geometry with different inflow conditions, featuring a laminar zero-pressure gradient boundary layer superimposed with zero-amplitude (case BZA, i.e., clean laminar inflow), low-amplitude (case BLA) and high-amplitude (case BHA) oblique waves at the inlet, as well as a turbulent inflow (case BTB), respectively.

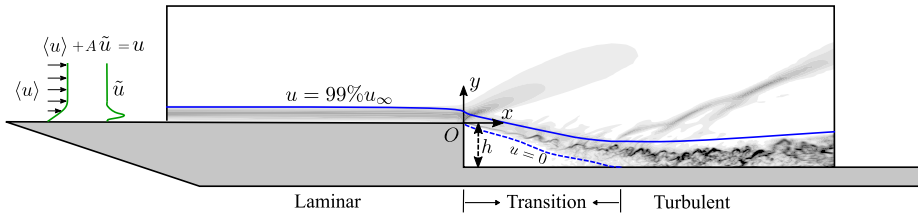


Figure 3.1: Schematic of the region of interest, which is in the center of the large computational domain with the size of  $([-40, 70] \times [-3, 30] \times [-8.0, 8.0])\delta_0$  in the  $x, y, z$  directions. The figure represents an instantaneous numerical schlieren graph in the  $x - y$  cross section for the low-amplitude perturbed laminar inflow case. Indicated are the wall-normal profiles of the mean velocity and perturbations.

The inflow is characterized by the free-stream Mach number  $Ma_\infty = 1.7$  and the Reynolds number  $Re_{\delta_0} = 13718$  based on the inlet boundary layer thickness  $\delta_0$  (at  $99\%u_\infty$ ) and free-stream velocity  $u_\infty$ . The main flow parameters are summarized in table 3.1. We indicate free stream flow parameters with subscript  $\infty$  and stagnation parameters with subscript 0. The size of the computational domain is  $[L_x, L_y, L_z] = [110\delta_0, 33\delta_0, 16\delta_0]$  including a length of  $40\delta_0$  upstream of the step in order to exclude potential uncertain effects from the numerical inlet boundary conditions on the flow in the region of interest. The height of the step is three times larger than the inlet boundary layer thickness, which is large enough to induce the transition from laminar to turbulent flow [46].

Table 3.1: Main flow parameters of the current case

$Ma_\infty$	$u_\infty$	$\delta_0$	$\theta_0$	$Re_\infty$	$T_0$	$p_0$	$h$	$p_\infty$
1.7	469.85 m/s	1 mm	0.107 mm	$1.3718 \times 10^7 \text{ m}^{-1}$	300K	$1 \times 10^5 \text{ Pa}$	3 mm	20259 Pa

### 3.1.2. NUMERICAL SETUP

The in-house ILES code INCA introduced in chapter 2 was employed to solve the compressible Navier-Stokes equations. This solver has been successfully applied to various supersonic flow cases, including shock wave/boundary layer interaction (SWBLI) on a flat plate [99] and compression ramp [96], and transition between regular and irregular shock patterns in SWBLI [141]. More details about the numerical method can be found in Hickel *et al.* [118].

For the spatial discretization, a Cartesian grid structure with block-based local refinement was applied for the entire domain, as displayed in figure 3.2. In addition, hyperbolic grid stretching was used in the wall-normal direction downstream of the step. Upstream of the step, the near wall grids are distributed uniformly. The mesh is sufficiently refined near all walls to ensure a well-resolved wall shear stress. The grid spacing becomes coarser with increasing wall distance but the expansion ratio is not larger than two. Using this discretization strategy, the computation domain has around  $3.6 \times 10^7$  cells; thus we obtain a spatial resolution of the flow field with  $\Delta x_{\max}^+ \times \Delta y_{\max}^+ \times \Delta z_{\max}^+ \approx 36 \times 0.9 \times 18$  in wall units for the first level grid near the wall in the entire domain ( $\Delta x_{\max}^+ = 0.9$  on the step wall). The temporal resolution, that is the time step, is approximately  $\Delta t u_{\infty} / \delta_0 = 7.6 \times 10^{-4}$ , corresponding to a Courant–Friedrichs–Lewy condition  $\text{CFL} < 0.5$ .

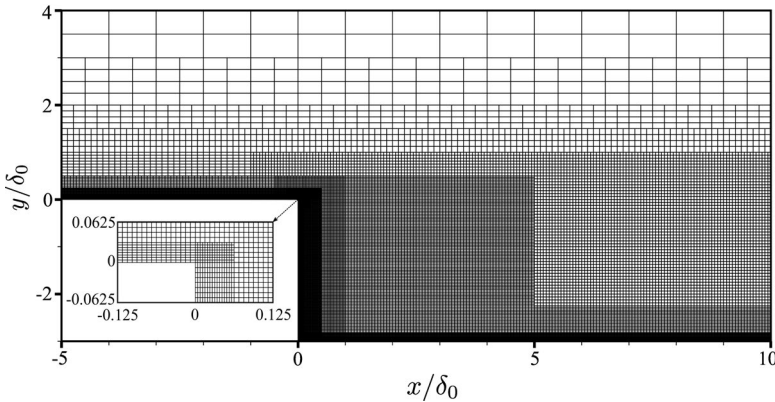


Figure 3.2: Grid distribution in the x-y plane in the computational domain near the step.

The step and wall are modeled as non-slip adiabatic surfaces. All the flow variables are extrapolated at the outlet of the domain. At the inflow and on top of the domain, non-reflecting boundary conditions based on Riemann invariants are used. Periodic boundary conditions are imposed in the spanwise direction. The grid and numerical approach used in the current study are the same for all four cases, except for the inlet boundary conditions. Case BZA has a clean compressible self-similar laminar inflow boundary layer profile, while cases BLA and BHA contain oblique T-S waves superimposed on the same mean laminar boundary layer profile at the inlet. The setup of the imposed T-S mode will be described in the next section. The case BTB features a turbulent inflow boundary layer generated by the digital filter technique.

### 3.1.3. INFLOW CONDITIONS

For the present transitional case BLA and BHA, the compressible base flow was computed by using a selective frequency damping technique [142]. Next, spatial LST is used to find the local most unstable mode, i.e., corresponding to the smallest negative value of  $\alpha_i^l$ , within a range of  $0.03 \leq \beta^l \leq 0.12$  and  $0.008 \leq \omega^l \leq 0.024$ . The parameters of wave properties with superscript  $l$  are normalized by the Blasius length  $l$ , and those with superscript  $\delta$  are normalized by the inlet boundary thickness  $\delta_0$ . Figure 3.3 shows the contours of  $\alpha_i^l$  at the local Reynolds number  $Re_l = 2167$  based on Blasius length. As we can see, the maximum  $|\alpha_i^l|$  is reached at  $\alpha_i^l = -0.00255$  for  $\beta^l = 0.06202$  and  $\omega^l = 0.01605$ . The corresponding streamwise wave number and wave angle are  $\alpha_r^l = 0.04001$  and  $\phi = 57.17^\circ$ . It has been reported that for corresponding flow conditions the wave angle of the primary mode is between  $\phi = 55^\circ \sim 60^\circ$  (at  $Ma > 1.6$ ), the streamwise wave number  $\alpha_r^l = 0.035 \sim 0.09$  (at  $Re_l = 2000, Ma = 1.6$ ) and angular frequency  $\omega^l = 0.006 \sim 0.03$  (at  $Re_l = 2000, Ma = 1.6$ ) [21, 38, 143]. Our results fall into this reported range.

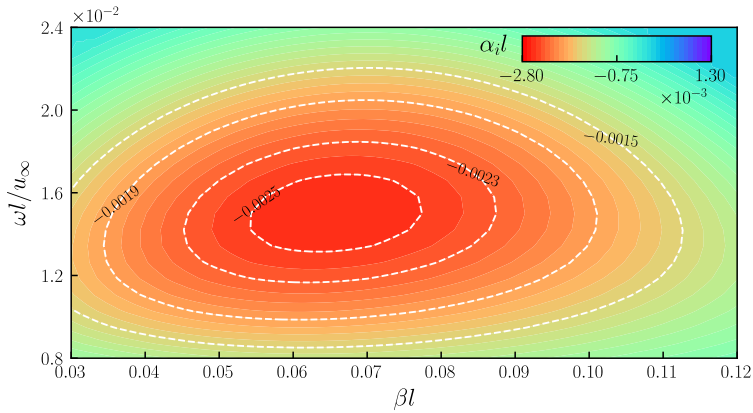


Figure 3.3: Contours of  $\alpha_i^l$  at the domain inlet obtained from LST

The eigenvalues spectra and corresponding disturbances profiles of the most unstable oblique wave are plotted in figure 3.4. The horizontal branch on the left represents the fast acoustic wave spectrum and the one on the right the slow acoustic wave spectrum, see figure 3.4(a) [144]. These two continuous horizontal spectra are generated from the streamwise wavenumber  $\alpha_r$  corresponding to the phase velocities  $c_{ph} = 1 \pm 1/Ma$ . The vertical branch denotes the continuous vorticity and entropy spectra  $c_{ph} = 1$ . At the current Reynolds number, these two branches overlap and become indistinguishable, which is a common behavior in high Reynolds number flow, as reported by Balakumar and Malik [145]. The mode with minimum negative value belongs to another continuous spectrum (most of them are not shown in the plot due to their large imaginary magnitudes), which will decay rapidly with the streamwise distance and therefore is not our current concern. These spurious modes can be identified by examining their eigenfunctions. The other discrete mode in the fourth quadrant is the T-S mode and has the largest growth rate among all the physical modes.

Figure 3.4(b) shows the perturbation profiles of the velocity components, pressure and temperature for this mode. We substitute the computed  $\alpha_r$ ,  $\beta$  and  $\omega$  into equation (2.47), retaining only the real part of  $q'$ , where  $e^{-\alpha_i x}$  is set as a constant initial amplitude. We superimpose this single least stable T-S mode  $q'$  onto the laminar flow profile and create two cases: one with low amplitude ( $e^{-\alpha_i x} = 0.026$ , case BLA) and the other one with high amplitude ( $e^{-\alpha_i x} = 0.13$ , case BHA). Correspondingly, the averaged amplitude of the streamwise velocity fluctuations is equivalent to  $A_{\text{in}} = 0.1\%u_\infty$  (case BLA) and  $A_{\text{in}} = 0.5\%u_\infty$  (case BHA) in the disturbed region ( $0 \leq y/\delta_0 \leq 5.0$ ).

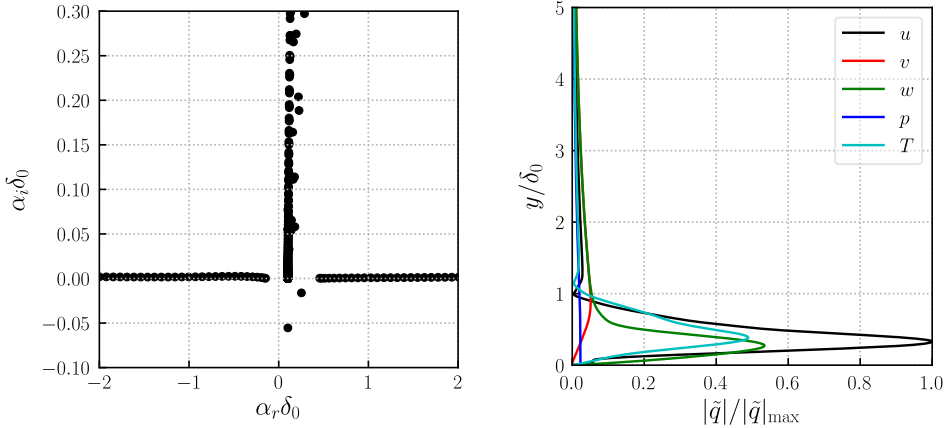


Figure 3.4: (a) Eigenvalue spectra and (b) the wall-normal disturbances of the local least stable T-S mode at  $\omega\delta_0/u_\infty = 0.10164$  and  $\beta\delta_0 = 0.39270$  obtained from LST.

For the turbulent case BTB, the synthetic turbulence generation method based on digital filter technique [124] was used to produce the appropriate turbulent inflow. This method can reproduce both given first- and second-order statistical moments and spectra without introducing the low-frequency contents which may modulate with the interested low-frequency phenomenon downstream. The reference data used are from Petrache *et al.* [146] to specify realistic integral length scales and mean boundary layer profiles. According to the existing work [97, 147], a transient length of around  $10\delta_0$  is sufficient for turbulence to develop in the supersonic boundary layer. Here, we summarize the flow conditions for the four cases investigated in table 3.2.

Table 3.2: Flow information for all the investigated BFS cases

Case	BZA	BLA	BHA	BTB
flow regime	laminar	laminar	laminar	turbulent
fluctuation intensity	$I = 0$	$I = 0.8\%$	$I = 4\%$	$I = 6\%$

### 3.1.4. GRID VALIDATION

We only study case BTB to scrutinize the grid sensitivity since all the cases use the same mesh. The computed flow field reached a fully developed statistically steady state after an initial transient period of  $tu_\infty/\delta_0 = 800$ . The samples then were collected every  $u_\infty/\delta_0 = 0.25$  over an interval of another  $tu_\infty/\delta_0 = 400$ , yielding an ensemble size of 1200. The van Driest transformed mean velocity profile and Reynolds stresses in Morkovin scaling are provided at  $x/\delta_0 = -5.0$  in figure 3.5. For comparison, the figure also includes the theoretical law of the wall and incompressible DNS data of Schlatter and Örlü [148] at  $Re_\tau = 360$  and  $Re_\theta = 1000$ . The present mean velocity profile is consistent with both the logarithmic law of the wall ( $u^+ = \frac{1}{\kappa} \log y^+ + C$  with the constants  $\kappa = 0.41$  and  $C = 5.2$ ) and the DNS data. The Reynolds stresses from the current LES are also in a good agreement with the reference data. Since the current LES data is for a compressible boundary layer that has a higher momentum thickness Reynolds number  $Re_\theta = 2000$  and friction Reynolds number  $Re_\tau = 400$ , the velocity profile has a slight larger plateau value and streamwise Reynolds stress profile features with a higher peak value in the buffer layer [149].

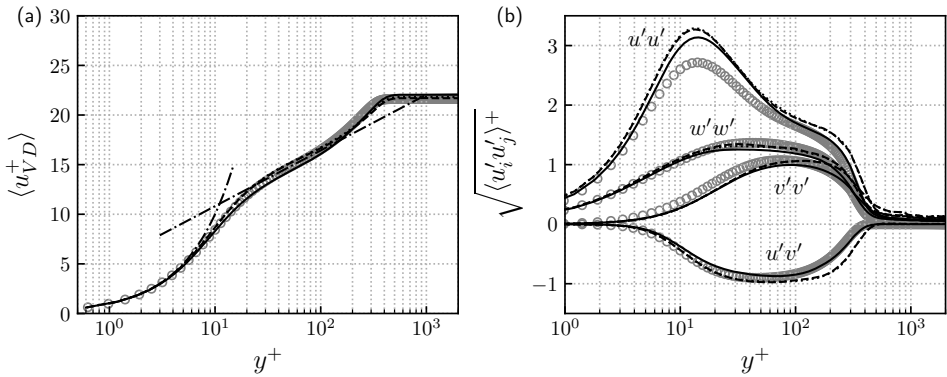


Figure 3.5: Mean profiles of the upstream turbulent boundary layer (case BTB) in inner scaling at  $x/\delta_0 = -5.0$  with  $Re_\tau = 400$  and  $Re_\theta = 2000$ . (a) Van Driest transformed mean velocity profile and (b) Reynolds stresses normalized by  $\sqrt{\rho/\rho_w}$ . ---, law of the wall; —, present LES with the chosen fine grid; ·····, coarser grid GX; -·-·-, coarser grid GZ; ○, incompressible DNS data of Schlatter and Örlü [148] at  $Re_\tau = 360$  and  $Re_\theta = 1000$ .

The grid sensitivity has been checked using two coarser grids with  $\Delta x_{\max}^+ \times \Delta y_{\max}^+ \times \Delta z_{\max}^+ = 72 \times 0.9 \times 18$  and  $\Delta x_{\max}^+ \times \Delta y_{\max}^+ \times \Delta z_{\max}^+ = 72 \times 0.9 \times 36$ . As we can see from figure 3.5, these two coarser grids give very similar results as the fine grid for the mean velocity and Reynolds stress profiles. For the peak value and log layer of the Reynolds stress profiles, a slight improvement is obtained using the fine grid.

## 3.2. PRELIMINARY COMPARISONS OF DIFFERENT CASES

The flow field is compared in this section to obtain a general view of the disturbance evolution with different inflow conditions, i.e., among the four cases BZA, BLA, BHA, BTB. First of all, an overview of the boundary layer development is provided by dis-

crossing the streamwise variation of the time- and spanwise-averaged skin friction, as shown in figure 3.6(a). The curves for the cases BZA and BLA coincide. The boundary layer remains laminar upstream of the step as can be inferred from the low level of  $\langle C_f \rangle$ . In the first half of the separation bubble ( $0.0 \leq x/\delta_0 \leq 5.1$ ), the recirculating flow is still laminar and  $\langle C_f \rangle$  is approximately zero. Then  $\langle C_f \rangle$  decreases towards a global minimum at  $x/\delta_0 \approx 8.0$ , followed by an increase of  $\langle C_f \rangle$ . In both cases, the shear layer reattaches around  $x/\delta_0 = 10.9$ . For the case BHA, the transition occurs much faster than for the other two cases. Skin friction begins to grow shortly downstream of the inlet at  $x/\delta_0 \approx -23.0$ , which indicates an early onset of transition. After a quick growth between  $-14.0 \leq x/\delta_0 \leq -4.0$ ,  $\langle C_f \rangle$  reaches a typical turbulent level [150], indicating that the boundary layer is already quite turbulent upstream of the step. For case BTB, the initial variations of the skin friction are caused by the DF technique because the boundary layer needs to develop physical coherent structures. Case BHA and BTB nearly follow the same path behind the step because they are both in a similar turbulent state around the step. As a result of the more energetic shear layer and thus the promotion of mixing, their reattachment length ( $L_r/\delta_0 = 8.8$ ) is 19% shorter than for the other two cases. The skin friction coefficient reaches a steady value at about  $\langle C_f \rangle = 2.9 \times 10^{-3}$  for all the cases at  $x/\delta_0 > 30$ .

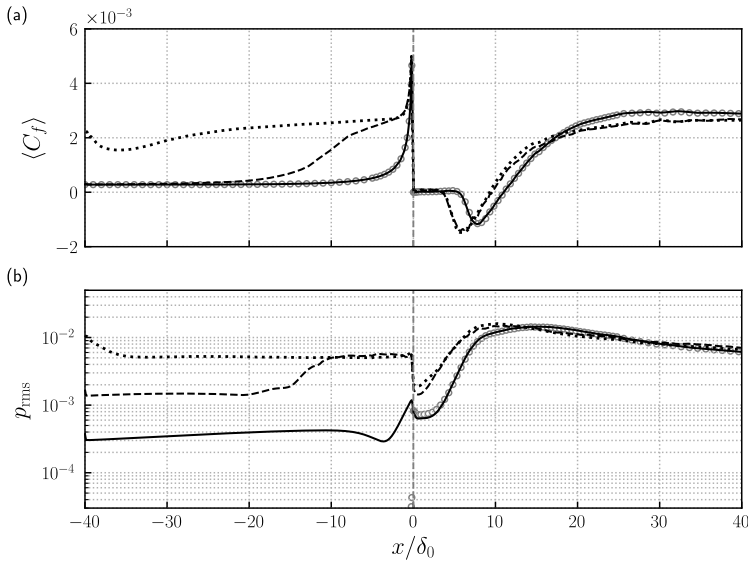


Figure 3.6: Streamwise development of time and spanwise-averaged (a) skin friction and (b) root mean square of wall pressure fluctuations (normalized by  $\rho_\infty u_\infty^2$ ) for case BZA ( $\circ$ ), case BLA (—), case BHA (---), case BTB (.....).

Table 3.3 compares the reattachment length  $L_r$  from the current LES with existing experimental and numerical results normalized with the step height  $h$ . In the laminar case, the obtained  $L_r/h = 3.63$  agrees well with the value reported by Karimi *et al.* [151] for their low-turbulence case (turbulence intensity  $I = 0.5\%$ ) and is smaller than the one

reported by Zhu *et al.* [53] due to the lower  $Ma$  in the current case. For the turbulent cases (case BHA and BTB), it can be seen that  $L_r/h = 2.93$  is very close to the reported values, for example  $L_r/h = 3.0$  reported by Chakravarthy *et al.* [152].

Table 3.3: Comparison of the reattachment length reported in various studies of BFS cases. Note that the reference length  $\delta_0$  is the boundary layer thickness in front of the step in some cases and  $I$  is the free stream or maximum inflow turbulence intensity.

Authors	$Ma$	$Re_\infty, \text{m}^{-1}$	h, mm	$\delta_0/h$	$L_r/h$	Comments
Chakravarthy <i>et al.</i> [152]	1.5	$4.41 \times 10^7$	6.35	0.32	3.0	LES, $I \approx 6\%$
Roshko and Thomke [153]	2.0	$3.74 \times 10^7$	6.35	0.54	3.36	experiment, turbulent
Liu <i>et al.</i> [154]	2.0	$3.35 \times 10^7$	3.18	0.25	3.0	LES, $I \approx 1\%$
Soni <i>et al.</i> [47]	2.0	$3.34 \times 10^7$	3.2	-	4.1	LES, $I \approx 2.9\%$
Karimi <i>et al.</i> [151]	2.0	$3.32 \times 10^7$	3.18	-	3.56	RANS, $I \approx 0.5\%$
Bolgar <i>et al.</i> [103]	2.0	$2.77 \times 10^7$	7.5	0.47	3.24	experiment, $I \approx 2\%$
Chen <i>et al.</i> [105]	3.0	$0.77 \times 10^7$	5	-	3-4	experiment, turbulent
Zhu <i>et al.</i> [53]	3.4	$0.61 \times 10^7$	3	0.33	5.9	experiment, laminar
Zhu <i>et al.</i> [53]	3.4	$0.61 \times 10^7$	3	0.33	3.6	experiment, turbulent
Present case BZA	1.7	$1.37 \times 10^7$	3	0.33	3.63	LES, laminar
Present case BLA	1.7	$1.37 \times 10^7$	3	0.33	3.63	LES, $I \approx 0.8\%$
Present case BHA	1.7	$1.37 \times 10^7$	3	0.33	2.93	LES, $I \approx 4\%$
Present case BTB	1.7	$1.37 \times 10^7$	3	0.33	3.0	LES, $I \approx 6\%$

The root mean square (RMS) of the wall pressure  $p_{\text{rms}} = \sqrt{\langle p'p' \rangle} / \rho_\infty u_\infty^2$  is plotted in figure 3.6(b), illustrating the level of fluctuations and the generation of turbulence. Due to the imposed oblique waves, the RMS of wall pressure for the cases BLA and BHA are around two and three orders higher than for the clean laminar inflow case at the inlet [not visible in figure 3.6(b) due to its level lower than  $10^{-5}$ ]. In the case BHA, the pressure fluctuations start to increase at  $x/\delta_0 = -20.0$  which confirms that transition is initiated at this point. After reaching a local maximum at  $x/\delta_0 = -10.0$ ,  $p_{\text{rms}}$ , they keep steady at a level of  $p_{\text{rms}} = 0.005$  upstream of the step. For the case BTB, the RMS of wall pressure remains a steady high level upstream of the step after an initial drop caused by the DF technique and overlaps with that of case BHA when  $x/\delta_0 > -10$ . For the cases BZA and BLA, the pressure fluctuations grow very slowly upstream of the step. Behind the step, all four cases display a similar variation tendency but with different rates. Case BHA and BTB have a higher initial level of the pressure fluctuations behind the step and a higher peak value than the other two cases. The case BLA follows nearly the same trajectory as the case BZA downstream of the step, notwithstanding it being imposed with low-amplitude oblique waves, which provides further support to the assumption that these two cases share the same transition path throughout the separated shear layer region. The wall pressure fluctuations finally reach identical levels for all three cases at  $x/\delta_0 > 30$ .

The visualization of instantaneous vortical structures for all four cases is presented by means of iso-surfaces of the  $\lambda_2$  vortex criterion [155] in figure 3.7, 3.8 and 3.9. For

both case BZA and BLA, there is a strong shear layer produced at separation which is subject to the inviscid instability, inducing large K-H vortices. Subsequently, these large vortices break down into small vortices as they move towards the bottom wall, which is likely caused by the secondary instability. Finally, a fully turbulent boundary layer flow develops downstream of the separation bubble, as illustrated by the small hairpin vortices resulting from the breakdown of the large  $\Lambda$ -shaped vortices and reattachment of all these unsteady waves. These similar features of the instantaneous flow field provide further confirmation that cases BZA and BLA follow the same transition path. For the low-amplitude case, however, the development of the upstream boundary layer also shows the imposed oblique T-S waves upstream of the step, as shown in figure 3.6 and will be discussed in more detail in section 3.4.

In contrast, case BHA undergoes a much earlier transition, which takes place already in the attached boundary layer upstream of the step [figure 3.8(a)]. The visualization shows oblique vortices that are excited by the large-amplitude T-S waves and their secondary instabilities which form the arc-shaped vortices. These disturbances of the boundary layer already become highly three dimensional upstream of the step. Since the incoming flow is effectively turbulent at the step [figure 3.8(b)], the free shear layer of case BHA is more energetic than for the case BZA/BLA. Note that the increased level of  $\lambda_2$  in figure 3.8(b) is aimed to remove the small homogenous vortices and better visualize the interesting vortical structures. The shear layer reattaches earlier because of the more energetic shear layer, while the generated reattachment shock has a smaller shock angle and stronger intensity (see the included numerical schlieren in figure 3.8). The latter observations are in qualitative agreement with the predictions from a theoretical inviscid model of the flow reattachment configuration.

For the turbulent case BTB, we see the expected small-scale coherent structures in the incoming turbulent boundary layer, as shown in figure 3.9. Since the separated shear layer is inviscidly unstable, it rolls up and larger and stronger vortical structures are generated over the bubble region. As the shear layer evolves downstream, the upstream small turbulent structures develop into larger coherent structures due to the shear layer instability, indicated by the arc-shaped vortices in the outer region of the boundary layer downstream of the bubble. These coherent vortical structures propagate above the reversed flow from the separation to the reattachment location, and they also exist within the turbulent boundary layer downstream of the bubble. These large coherent vortices are caused by the vortex pairing process behind the step, as reported by Soni *et al.* [47]. Similar with the case BHA, the typical K-H vortex structure present in the laminar case is not observed in the turbulent regime where the quasi two-dimensional vortices are probably distorted by the highly three-dimensional turbulence. In the middle of the shear layer, large coherent  $\Lambda$ -shaped vortices are formed and transformed into arc-shaped vortices downstream in the laminar case as a result of vortex stretching and tilting, whereas only arc-shaped vortices are present downstream in the turbulent case. From the numerical schlieren image shown on the  $x - y$  slice, the shock intensity in the laminar case is weaker than that of the turbulent one.

By comparison, the transition path of case BLA is very similar to what was observed in case BZA. However, we can not rule out the effects of the imposed oblique waves without the further quantitative comparison and analysis. In the following sections, we

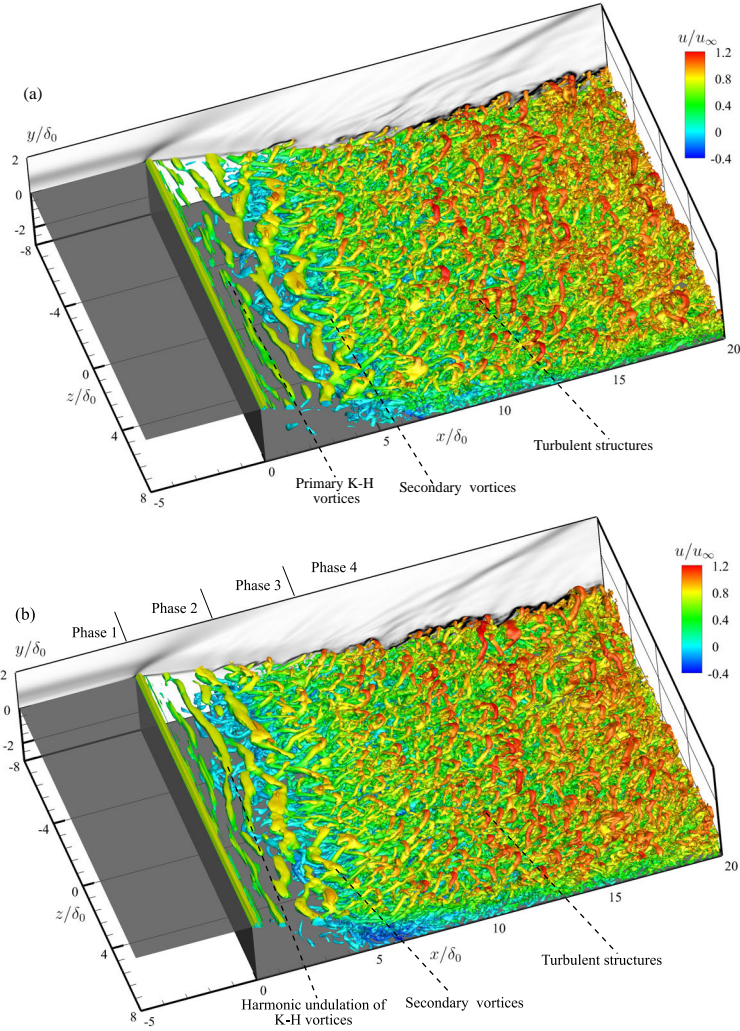


Figure 3.7: Instantaneous vortical structures at  $tu_\infty/\delta_0 = 912$ , visualized by isosurfaces of  $\lambda_2$ . A numerical schlieren based on  $z = 0$  slice is also included with  $|\nabla\rho|/\rho_\infty = 0 \sim 1.4$ . (a) case BZA and (b) case BLA at  $\lambda_2 = -0.02$ .

first scrutinize the transition process of the fully laminar case BZA and then examine the effects of possible T-S, K-H and secondary instability interactions in the transition focusing on the case BLA. For the case BHA, on the other hand, the gradual growth of the oblique T-S waves appears to saturate soon and other instabilities already take effect well upstream of the step. Consequently, the flow field is highly turbulent in the shear layer, which may be the cause that the rolling up of large K-H vortices is suppressed, as the same with case BTB. Last, our concern is laid on the unsteady behavior of the shock wave/turbulent boundary layer interaction system, especially the low-frequency

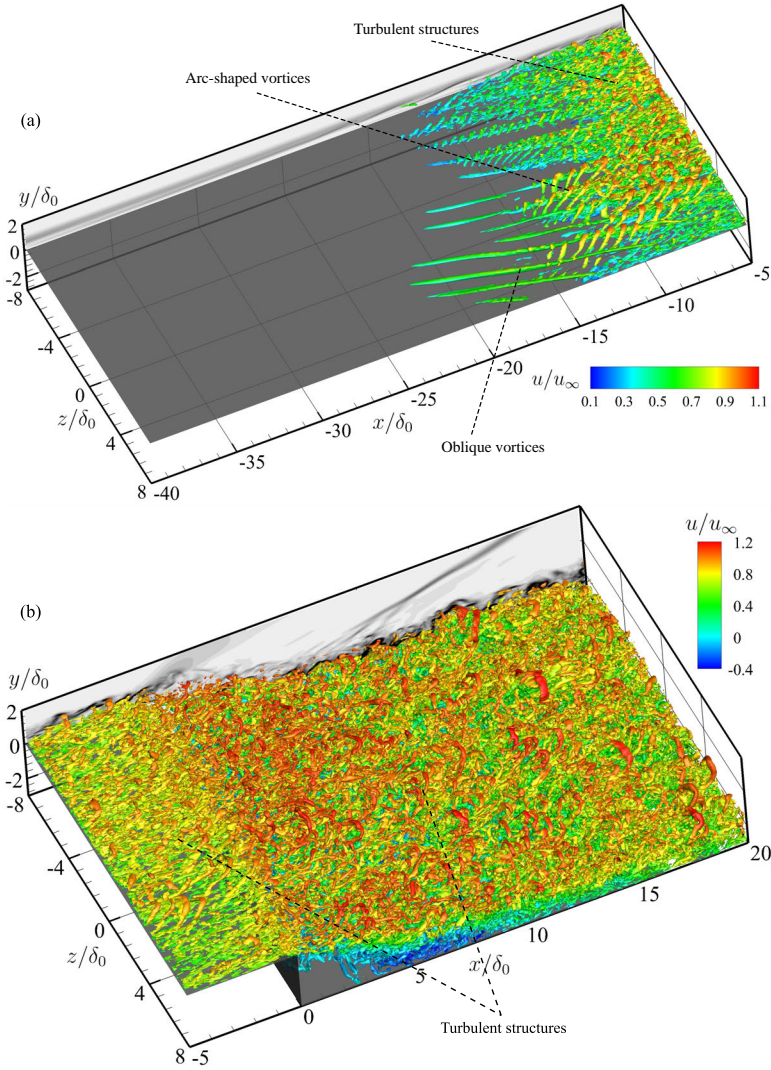


Figure 3.8: Instantaneous vortical structures at  $tu_\infty/\delta_0 = 912$  for case BHA, visualized by isosurfaces of  $\lambda_2$ . A numerical schlieren based on  $z = 0$  slice is also included with  $|\nabla\rho|/\rho_\infty = 0 \sim 1.4$ . (a) upstream of the step at  $\lambda_2 = -0.02$  and (b) downstream at  $\lambda_2 = -0.08$ .

unsteadiness, by analyzing the case BTB in detail.

### 3.3. LAMINAR REGIME

In this section, we investigate the self-excited transition process and unsteady features of the BFS case with a undisturbed laminar inflow by analyzing the case BZA. The transition process of the current case is presented by examining the mean and instantaneous

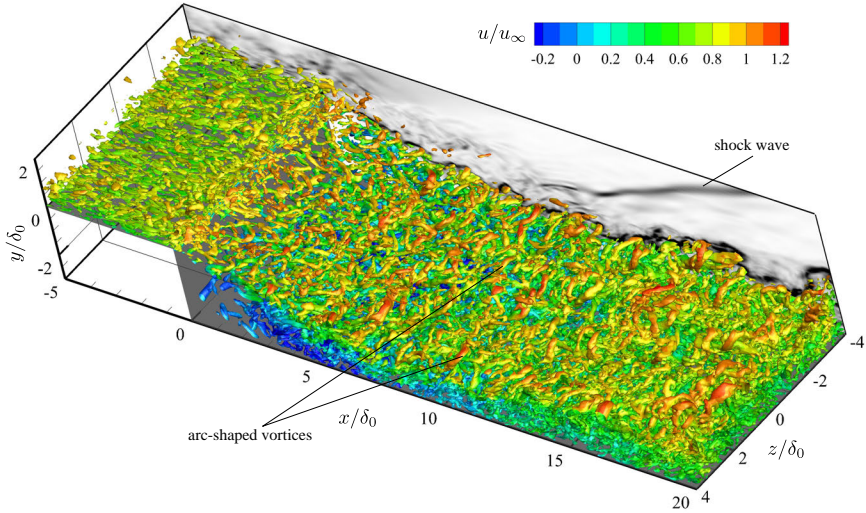


Figure 3.9: Instantaneous vortical structures at  $tu_\infty/\delta_0 = 912$  for case BTB, visualized by isosurfaces of  $\lambda_2 = -0.08$ . A numerical schlieren based on  $z = -4$  slice is also included with  $|\nabla\rho|/\rho_\infty = 0 \sim 1.4$ .

flow structures. The effects of shock and reattachment on the transition are inspected by spectral and statistical analysis. Finally, the dominant modes in the evolution of the transitional flow are discussed using dynamic mode decomposition. In addition, different with the incompressible BFS case which has been well studied in the existing works, there are probably additional mechanisms involved in the supersonic flow, that are related to compressibility and the occurrence of compression waves at flow reattachment. It is reasonable to conjecture that a different mechanism may contribute to the transition process in the supersonic flow. Therefore, the comparison between incompressible and compressible cases are also included in the following discussion.

### 3.3.1. MEAN FLOW VISUALIZATION

The main flow features are visualized by the time- and spanwise-averaged density contours shown in figure 3.10. The incoming laminar flow experiences a centered Prandtl-Meyer expansion when it separates at the step corner due to the sudden geometry expansion. Then the free shear layer develops towards the downstream wall and finally impinges on the wall surface. Compression waves are generated around the reattachment location, which coalesce into a reattachment shock (white solid line). The low-speed recirculating flow forms a separation bubble underneath the dividing line (here defined for convenience as the isoline of  $u = 0$  indicated by black dashed line), while the high-speed part proceeds downstream by overcoming the slight pressure rise [154]. The mean reattachment length is about  $L_r = 10.9\delta_0$  ( $3.6h$ ), which is consistent with the existing results, reporting that the reattachment length is usually within  $3.0 \sim 4.0h$  around the current Mach number [151, 154]. Behind the reattachment point, the distance between the sonic line (white dashed line) and wall decreases with the streamwise distance as a result of the increasing velocity gradient near the wall, which

indicates the evolution towards a fully turbulent boundary layer. The reattachment length  $L_r = 3.6h$  is much smaller than the typical values reported for incompressible cases (e.g.  $19.8h$  [48]) due to the more energetic mixing of the shear layer with the increasing Reynolds number. This interpretation is in accordance with the finding that the reattachment length is reduced with the Reynolds number in the transitional regime [156].

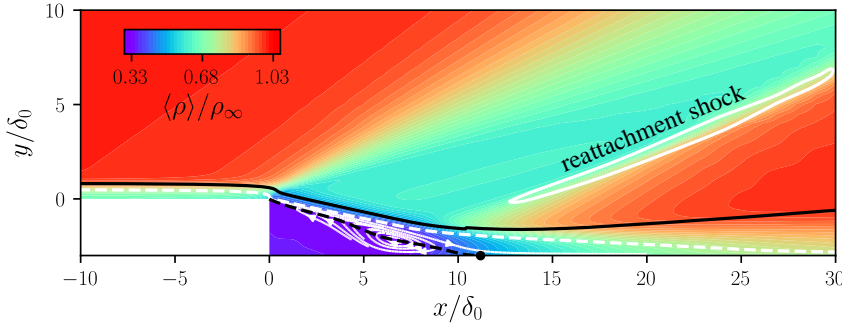


Figure 3.10: Time and spanwise-averaged contour of density with isolines of streamwise velocity and Mach number (case BZA). A solid circle (•) indicates the reattachment point. The white dashed and solid lines denote the isolines of  $Ma = 1.0$  and  $|\nabla p|\delta_0/p_\infty = 0.24$ . The black dashed and solid lines signify isolines of  $u = 0.0$  and  $u/u_e = 0.99$ .

The reattachment length is further confirmed by the mean skin friction distribution in figure 3.11(a), where  $\langle C_f \rangle$  represents the skin friction normalized by  $0.5\rho_\infty U_\infty^2$ . The intensity of separated flow is not uniform in terms of  $\langle C_f \rangle$ , varying with streamwise distance along the separation bubble. The level of  $\langle C_f \rangle$  remains almost zero in the upstream part of the separation bubble ( $0 < x/\delta_0 < 6.3$ ), which is followed by a decrease of  $\langle C_f \rangle$  towards a global minimum at  $x/\delta_0 = 8.4$ . Then  $\langle C_f \rangle$  slowly climbs up and eventually stays steady at about  $\langle C_f \rangle = 2.9 \cdot 10^{-3}$  for  $x/\delta_0 > 25$ , which is a typical level of the turbulent boundary layer at the current Reynolds number range. The trend and level of  $\langle C_f \rangle$  match well with the numerical results of Spazzini *et al.* [157] despite the different inlet boundary conditions and reattachment length. As will be shown later, this structure of  $\langle C_f \rangle$  inside the recirculating region seems to be related to the low-frequency unsteadiness.

The wall pressure in figure 3.11(b) displays a sharp drop by about 50% in front of the step. The wall pressure then gradually reduces further to reach its global minimum at  $x/\delta_0 = 7.3$  in the separation bubble. In terms of the trend and relative variation, our results are in good agreement with the numerical works of Karimi *et al.* [151]. The three inflection points of the wall-pressure distribution are considered to be associated with the separation, emergence of compression waves and reattachment, as reported by Déleroy *et al.* [158].

The boundary layer state can be characterized basically by the evolution of the wall-normal velocity profile along the streamwise direction, see figure 3.12, where  $\Delta y/\delta_0$  signifies the normalized wall distance. Sufficiently upstream of the step edge, the

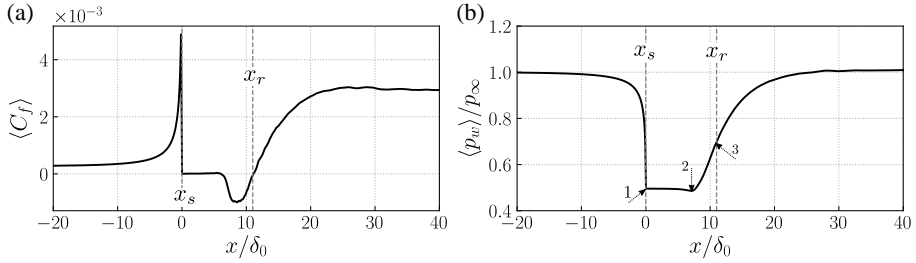


Figure 3.11: Time- and spanwise-averaged (a) skin friction and (b) wall pressure for case BZA. The dash line indicates the averaged separation and reattachment location.

velocity profile corresponds to a typical laminar boundary layer. At the step corner ( $x/\delta_0 = 0$ ), the streamwise velocity gradient increases significantly due to the upstream effect of the sharp expansion of the geometry. Accordingly, the boundary layer thickness gradually decreases along the streamwise distance upstream of the step (see figure 3.10). It is noticeable that there exists an inflection point of the velocity profile at this location, which means that the boundary layer has an inviscid instability at the step. The mean streamwise velocity increases across the expansion due to the favorable pressure gradient [see also figure 3.11(b)]. Compared to the upstream velocity profile, the boundary layer profile displays a large momentum deficit in the separated region, for example, at  $x/\delta_0 = 5$  there is only a small reverse flow region, however, the velocity deficit of  $1.0u_\infty$  extends up to around  $\Delta y/\delta_0 = 1.5$ . Also shortly downstream of reattachment (which takes place near  $x/\delta_0 = 11$ ), the shape of the velocity profile, at  $x/\delta_0 = 15$  and  $x/\delta_0 = 20$ , has not yet reached an equilibrium state. The outer flow velocity gradually returns to its initial level with the adverse pressure gradient behind the reattachment shock, see figure 3.11(b). The flattening of the velocity profile and steeper velocity gradient near the wall, compared to the upstream velocity profile, both indicate the development of the turbulent boundary layer.

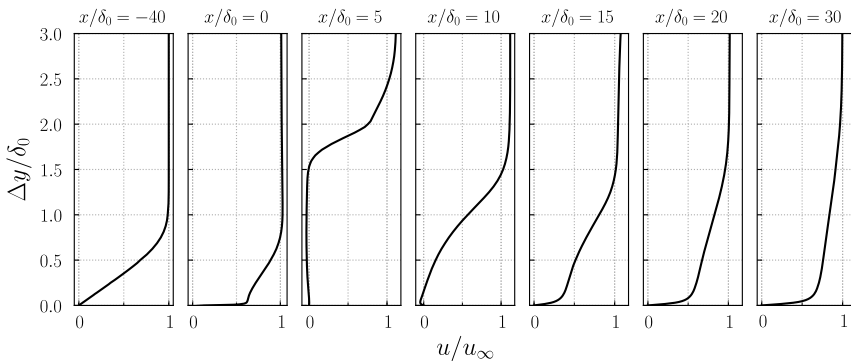


Figure 3.12: Streamwise evolution of spanwise and time-averaged streamwise velocity profile for case BZA. Note: the y-axis is the non-dimensional normal distance from the wall.

### 3.3.2. INSTANTANEOUS FLOW VISUALIZATION

The instantaneous vortical structures in a typical instantaneous flow realization are visualized by means of the  $\lambda_2$  vortex criterion, providing an overall view in figure 3.7(a) and a zoom-in view in figure 3.13. The laminar-to-turbulent transition process can be divided into five stages based on the appearance of the vortical structures. The first stage is the relatively short range where two-dimensional spanwise structures are initiated due to the inviscid K-H instability of the shear layer, as shown in figure 3.13(a).

In the second stage, the spanwise structures evolve further into large quasi two-dimensional vortices [figure 3.13(b)]. These spanwise-aligned K-H vortices are subsequently deforming into oblique waves as a result of their secondary instability, probably triggered by small horseshoe vortices beneath as the free shear layer flow develops downstream.

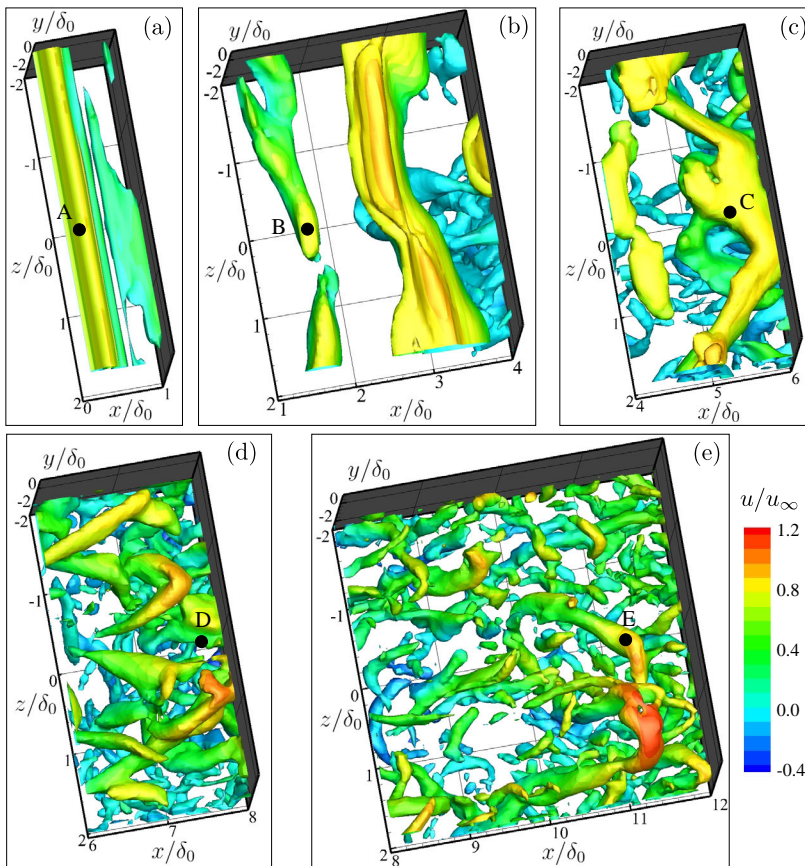


Figure 3.13: Instantaneous vortical structures of case BZA at  $t u_\infty / \delta_0 = 793$ , colored by contours of streamwise velocity, visualized by isosurfaces of (a)  $\lambda_2 = -0.005$ , (b)  $\lambda_2 = -0.005$ , (c)  $\lambda_2 = -0.02$ , (d)  $\lambda_2 = -0.1$  and (e)  $\lambda_2 = -0.5$ .

The streamwise velocity is not distributed uniformly along the oblique waves, which

induces the formation of low and high momentum zones along the spanwise direction. With the spanwise modulation of the vortices, the low-momentum parts form into the legs of a  $\Lambda$ -shaped vortex structure and the high-momentum parts develop into the head of a  $\Lambda$ -shaped vortex in the third stage, see figure 3.13(c). At the same time, the distorted vortices pair with each other since the high-speed part of upstream vortices catch up with the low-speed part of downstream vortices. The separated shear layer flow thus exhibits the formation of large-scale vortices via K-H and secondary instability, and then these vortices keep stretching, pairing as the shear layer evolves. In the incompressible case of Schäfer *et al.* [48], the vortex pairing is not observed and thus the K-H vortices keep aligned in the spanwise direction upstream of the reattachment point. However, compressible shear layers exhibit three-dimensional instabilities at a high Mach number, as reported by Sandham and Reynolds [159]. Therefore, the oblique waves emerge in the shear layer, which makes the K-H vortices tilting in the spanwise direction and pairing with each other due to the promotion of the shear layer mixing. Existing experimental results have confirmed the behavior of the vortex pairing in the supersonic laminar flow [53]. However, if the separation length is too short, like in supersonic turbulent flow, there is not enough resident time for K-H vortices to grow and pair within the shear layer.

In the next stage, the large coherent  $\Lambda$ -shaped vortices break down into several small  $\Lambda$ -shaped vortices staggered in the spanwise direction due to the streamwise stretching of vortices, in which the head part of the vortex (relatively far away from the wall) is convected faster than the leg parts until this behavior tears down the large vortex [figure 3.13(d)]. Emerging smaller  $\Lambda$ -shaped vortices indicate the onset of the nonlinear regime, which originates from the upstream self-excited quasi-periodical K-H vortices, instead of the natural spanwise differential amplification of the Tollmien-Schlichting waves [160]. There also exist low-momentum zones in leg parts and high-momentum zones in head parts of the small  $\Lambda$ -shaped vortices.

In the last stage, the vortex-stretching mechanism continues and the hairpin vortices appear to be lifted up due to the stretched legs [161, 162]. This rolling up contributes to the formation of large hairpin vortices, which is the signature of turbulent boundary layer flow, illustrated in figure 3.13(e).

We do not observe Görtler vortex pairs from the visualizations of the vortical structure. This suggests that the Görtler instability may not be a predominant mechanism in the transition. We evaluated the Görtler number  $G_t$  to quantify the development of the Görtler instability along the streamwise distance to provide more physical evidence. The characteristic Görtler number  $G_t$  is defined as

$$G_t = \frac{\theta}{0.018\delta^*} \sqrt{\frac{\theta}{R}} \quad (3.1)$$

where  $\delta^*$ ,  $\theta$  and  $R$  signify the local displacement thickness, the momentum thickness and the curvature radius along a specific streamline, respectively. When the local Görtler number exceeds the critical value  $G_t = 0.6$  for a wide range of compressible laminar flow conditions, Görtler vortices will emerge in the boundary layer [78, 99]. We computed the value of the local Görtler number along the boundary layer edge and found that it remains below this threshold at every  $x$  coordinate as far downstream as the mean

reattachment location, where significant turbulence is already observed. Based on the combined evidence of vortical visualizations and the analytical values, we conclude that the Görtler instability does not play an important role in this transitional case.

For each stage of the transition process, spanwise profiles of the fluctuations of the streamwise velocity are shown in figure 3.14 (note the smaller scale for the first two stations). We can clearly see the differences of dimensional features of the traveling waves in each stage. In the first stage, the spanwise waves are completely two-dimensional, and their wavelength is about half of the spanwise domain size, figure 3.14(a). Then these two-dimensional waves modulate into oblique waves and their amplitudes increase by approximately one order, figure 3.14(b). The three-dimensional features of unstable waves are obvious and their fluctuations becomes more energetic in the following three stages. As reviewed by Herbert [163], the vortex pairing process is usually observed in inflectional boundary layers at very large amplitudes of the periodic modulation. It seems that the three-dimensional characteristics of the unstable waves emerge in a very short distance behind the step and soon become highly energetic before reaching half of the reattachment length.

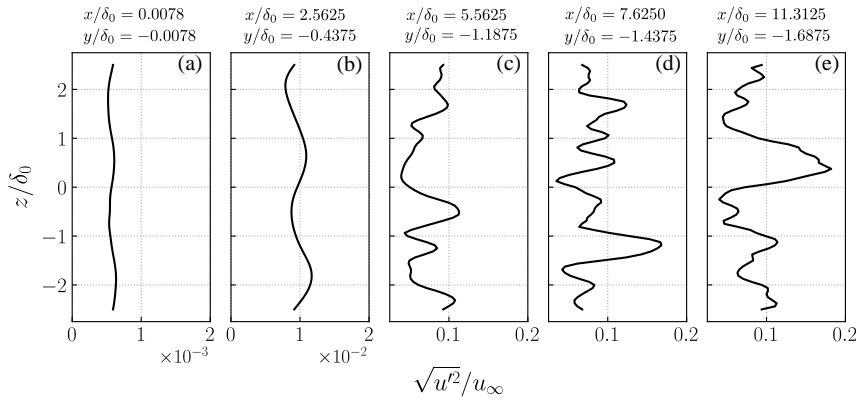


Figure 3.14: Fluctuations of streamwise velocity (case BZA) along the spanwise direction at five different locations shown in figure 3.13 (marked as A, B, C, D and E, each of which corresponds to one stage of the transition process).

The root-mean-square (RMS) and amplification factor of the streamwise velocity fluctuations are plotted as function of the streamwise direction through the five stages of the transition in figure 3.15. Based on the profile of streamwise velocity RMS at a specific  $x_i$  location, we find  $y_i$  where the local profile has the maximum. The position  $(x_i, y_i)$  is considered to be the local most unstable point and computed along the streamwise direction. The RMS of the streamwise velocity we display (solid line in figure 3.15) are the results at these locations  $(x_i, y_i)$ . Then we compute the perturbation amplitudes  $A_i$  from the time series data at  $(x_i, y_i)$ . The amplification factor is normalized based on the amplitude  $A_0$  at  $x = 0$ . The level of fluctuations grows smoothly in the first two stages and experiences an accelerated growth caused by the secondary instability and vortex breakdown in the third and fourth stage (solid line in figure 3.15). The streamwise modulation of low and high momentum parts of  $\Lambda$ -shaped vortices also

contributes to the accelerated growth. In the last stage, the fluctuations reach their maximum around the reattachment point and return to an almost constant level in the turbulent boundary layer (not shown in the figure). Concerning the amplification factor (dashed line in figure 3.15), at first, the amplitude of fluctuations displays a rapid modal growth of K-H vortices. In the next two stages, the growth rate (presented by the slope of the amplification factor) is much smaller than before although the amplification factor still slowly increases. Then the amplification factor continues increasing because of a rapid onset of non-linear distortion and breakdown to turbulence in the fourth stage. In the last stage, the amplification factor almost keeps steady at a high level.

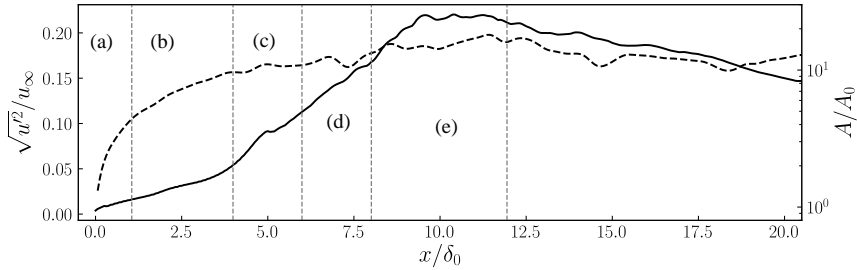


Figure 3.15: RMS (solid line) and amplification factor (dashed line) of streamwise velocity fluctuations (case BZA) along streamwise direction through the five stages of the transition in figure 3.13 based on the spanwise-averaged flow field.

In conclusion, the above visualization and analysis show rapid modal growth of K-H type transition right behind the step. The amplitude of fluctuations exceeds  $0.1\%u_\infty$  after a short distance from the step, which indicates that nonlinear interactions become important. Therefore, we believe the transition process consists of onset and modal growth of K-H vortices (stage 1, 2), secondary instability (stage 3), breakdown of the large coherent vortices (stage 4) and turbulent state (stage 5).

### 3.3.3. UNSTEADY BEHAVIOR

The unsteadiness of the flow field is examined to find the most energetic mechanism in the laminar-to-turbulent transition. First, the map of RMS values for the wall-normal velocity fluctuations is considered, as plotted in figure 3.16. We do not see any energetic activity upstream of the step. The velocity fluctuations are only noticeable starting from the separated shear layer and reach a global maximum around the reattachment region. In addition, relatively small fluctuations are observed in the reattachment shock area, which is likely indication of the unsteadiness of the shock position.

We analyze the dynamic behavior by means of the frequency weighted power spectral density (FWPSD) of the pressure along the dividing line in figure 3.17. Note that all values of FWPSD have been normalized by the local integral values  $\int P(f)df$  in order to better highlight the relative local contributions at different frequencies, independent of the overall fluctuations strength. The sampling interval is  $tu_\infty/\delta_0 = 800 \sim 1150$  with a sampling frequency of  $f_s\delta_0/u_\infty \approx 2$ . Welch's method with Hanning window was applied to compute the PSD using eight segments with 50% overlap (the same for the

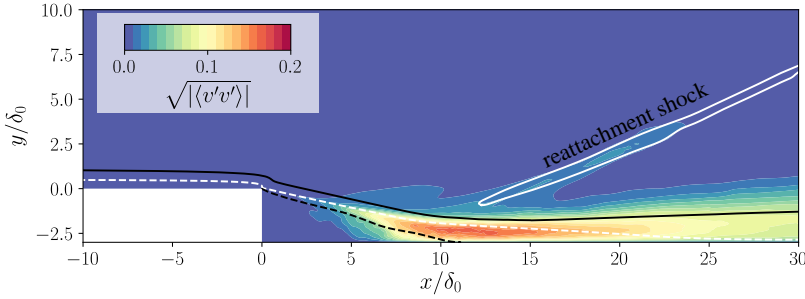


Figure 3.16: Contours of the variance of the wall-normal velocity for case BZA. A solid circle (•) indicates the mean reattachment point. The white dashed and solid line denote the isolines of  $Ma = 1.0$  and  $\nabla p = 0.24$ . The black dashed and solid lines signify isolines of  $u/u_\infty = 0.0$  and  $u/u_\infty = 0.99$ .

following PSD calculations of this section). As we can see in figure 3.17, in the first stage, the separated shear layer features a significant low-frequency oscillation with  $f\delta_0/u_\infty \approx 0.02$  immediately behind the step. This unsteady behavior is believed to be associated with the breathing motion of the separation bubble, as we will discuss in the following section. The dominant frequency then shifts towards higher values of  $f\delta_0/u_\infty \approx 0.2$  in the second stage where the oblique K-H vortices are observed. Although we can infer that there is still low-frequency breathing unsteadiness in this stage, the dominant frequency is around the characteristic frequency of the K-H vortices, which underlines the important role of the K-H instability in the transition scenario. As the shear layer develops, the energetic content of the shear layer gradually shifts to lower frequencies in the following stages ( $3.2 < x/\delta_0 < 12$ ) and evolves towards a broadband frequency spectrum from the low to high frequency. Downstream of the transition region ( $x/\delta_0 \geq 12$ ), the fluctuations in the turbulent boundary layer are distributed over the spectrum without a clear preferred frequency.

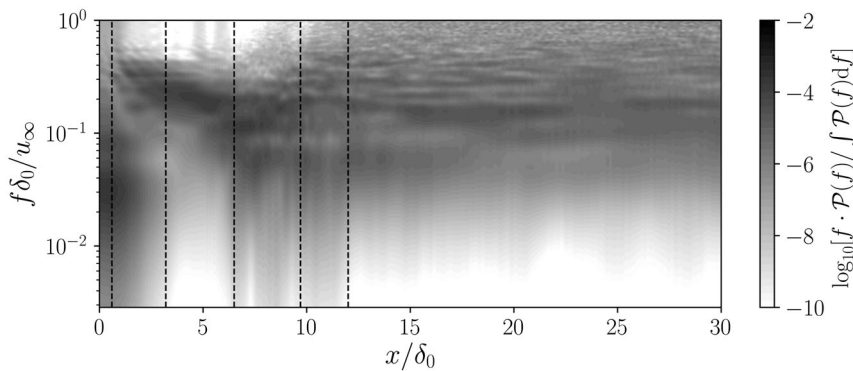


Figure 3.17: Frequency weighted power spectral density map of pressure signals along the dividing line based on  $z = 0$  slice (case BZA). At every streamwise location the weighted spectra are normalized by  $\int P(f) df$ . The five stages of the transition process are indicated by vertical dashed lines.

Time signals of three aerodynamic parameters are shown in figure 3.18 to further characterize the unsteady behavior of the interaction, including the spanwise-averaged reattachment point  $x_r$ , the reattachment shock location  $x_l$  and the cross-sectional area of the separation bubble  $A$ . The value of  $x_r$  is computed as the intersection of the dividing line (isoline of  $u = 0$ ) and the wall in the range from  $x/\delta_0 = 8.5$  to  $13.5$ . The separation bubble area  $A$  is the area of the zone below the dividing line. The shock location  $x_l$  is determined based on the pressure gradient outside the boundary layer by fitting the isolines of  $|\nabla p| \delta_0 / p_\infty = 0.24$ . We obtain two  $x$  values by intersecting the isolines of  $|\nabla p| \delta_0 / p_\infty = 0.24$  at  $y/\delta_0 = 0.0$  and then take the average of these two  $x$  values as the first streamwise coordinate of shock position. A second point of the shock position is obtained by repeating the same operation at  $y/\delta_0 = 5.0$ . A straight line is fitted based on these two points and the intersection between the fitting line and wall is considered as the shock location  $x_l$ . A similar method of obtaining these parameters has been applied to investigate SWBLI [114, 164].

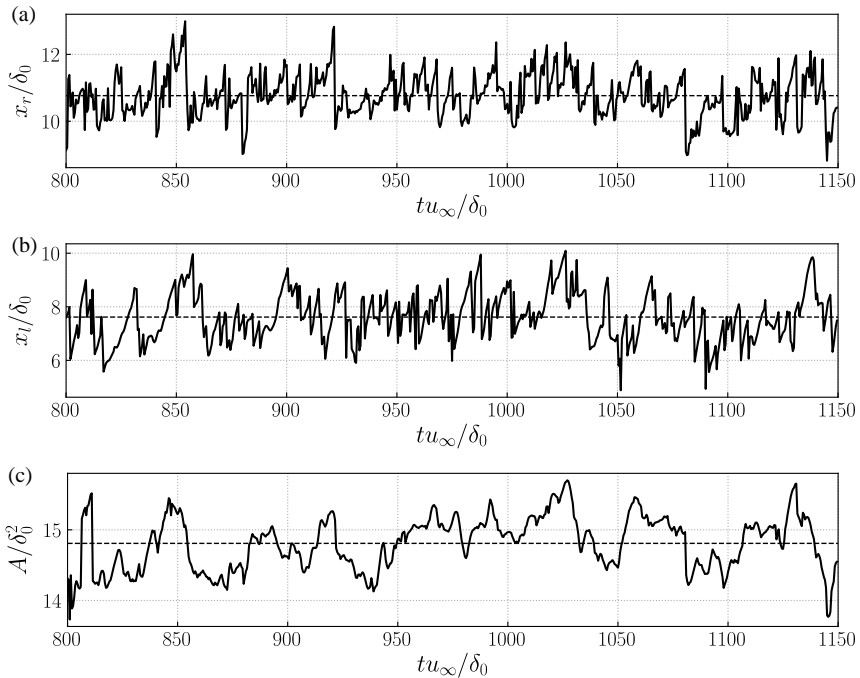


Figure 3.18: Temporal variation of the spanwise-averaged (a) reattachment point, (b) shock location and (c) separation bubble (case BZA). The dashed line denotes the mean value.

These temporal signals are extracted in time ranges  $t u_\infty / \delta_0 = 800 \sim 1150$  with a sampling frequency  $f_s \delta_0 / u_\infty = 2$  as the frequencies above the characteristic frequency of the turbulent integral scales  $u_\infty / \delta_0$  are not of the current interest. All these signals include broadband frequency scales because all the plots are irregular and aperiodic. The curve of the reattachment position in figure 3.18(a), displays an almost instantaneous drop when it moves upstream, for example at around  $t u_\infty / \delta_0 = 924$ . When the reattachment

location shifts downstream, it experiences a less rapid relaxation. This sawtooth-like trajectory of the reattachment point was also reported in direct numerical simulation (DNS) results of a compression ramp by Priebe and Martín [164]. The dynamics of the shock location, figure 3.18(b), is slightly smoother, without such strong sawtooth-like behavior. The passage of large-scale vortices in the shear layer and their shedding into the downstream flow contributes to sawtooth-like motions [165, 166]. In terms of the separation bubble size, shown in figure 3.18(c), its temporal behavior seems more periodical, with the absence of high-frequency fluctuations.

The FWPSD for the three signals is shown in figure 3.19. The spectra of reattachment and shock location both have two narrow-band peaks around  $f\delta_0/u_\infty = 0.06$  and 0.2. For the reattachment point, figure 3.19(a), most of the energy is contained at  $f\delta_0/u_\infty = 0.2$ , near the characteristic frequency of the K-H vortices. The K-H frequency  $f\delta_0/u_\infty = 0.2$  is in good agreement with the incompressible data of Schäfer *et al.* [48], which, however, does not show the second peak around  $f\delta_0/u_\infty = 0.06$ . We thus conclude that the lower-frequency content is a characteristic compressible feature due to the occurrence of the compression waves. As for the shock position in figure 3.19(b), the spectrum peaks are located at around  $f\delta_0/u_\infty = 0.06$ , while the oscillation of the separation bubble has a single dominant frequency peak at  $f\delta_0/u_\infty \approx 0.03$  displayed in figure 3.19(c), which is two orders of magnitude lower than the characteristic frequency of the energetic turbulent scales  $u_\infty/\delta_0$ , in agreement with the widely reported low-frequency unsteadiness in SWBLI [93, 96, 98]. The experimental work of supersonic BFS flows reported two types of low frequencies centered at  $f\delta_0/u_\infty \approx 0.02$  and  $f\delta_0/u_\infty \approx 0.05$  [103], which is very close to our current results.

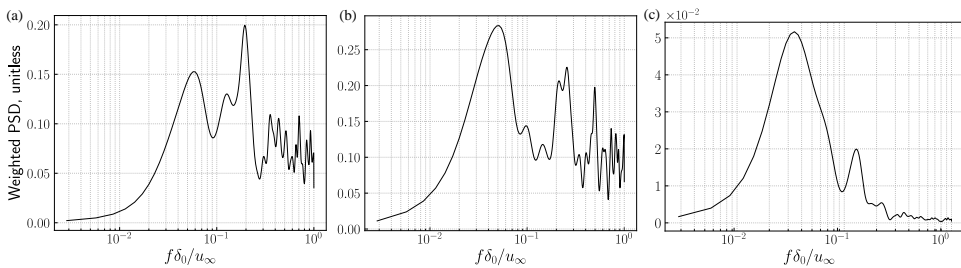


Figure 3.19: Frequency weighted power spectral density of the spanwise-averaged (a) reattachment point, (b) shock location and (c) separation bubble size (case BZA).

### 3.3.4. STATISTICAL ANALYSIS

Three distinct dominant frequencies of the unsteady motions in the interacting system are identified in the previous section. In order to explore their origin, the statistical connections between the reattachment point and several signals, including pressure fluctuations induced by K-H vortices, shock location and the area of separation bubble, are investigated using the temporal correlation coefficient  $R_{ij}$  between two signals  $q_i$

and  $q_j$  with time delay, defined as

$$R_{ij}(\Delta t) = \frac{\text{Cov}(q_i(t), q_j(t + \Delta t))}{\sigma_i \cdot \sigma_j} \quad (3.2)$$

where Cov is the covariance between these two signals and  $\sigma$  indicates the population standard deviation of the specific signal.

The correlation between the reattachment point and pressure fluctuations of the K-H vortices is shown in figure 3.20(a). The pressure signals used are obtained at the same location of B in figure 3.13, i.e.,  $x/\delta_0 = 2.5625, y/\delta_0 = -0.4375, z/\delta_0 = 0$ . High values of the correlation are observed around every multiple of  $\Delta t u_\infty / \delta_0 \approx 5.0$ , which suggests that these two signals are slightly correlated to each other at a frequency  $f \delta_0 / u_\infty \approx 0.2$ . In terms of correlation coefficients between reattachment location and bubble size, figure 3.20(b), there are strong positive and immediate connections between them with a quasi period  $\Delta t u_\infty / \delta_0 \approx 40.0$ . Therefore, the area of the separation bubble increases when the reattachment location moves downstream, and vice versa. This confirms that the low frequency ( $f \delta_0 / u_\infty \approx 0.025$ ) appears to originate from the breathing motion of the separation bubble. Concerning the connections between reattachment and shock location, they are obviously in the phase but with a slight time delay around  $\Delta t u_\infty / \delta_0 \approx 6.1$ . Physically, when the reattachment location moves upstream, the shock location also moves upstream after  $\Delta t u_\infty / \delta_0 \approx 6.1$ . It can be explained that the reattachment shock shifts upstream because the reattachment-induced compression waves, which coalesce into the reattachment shock, move upstream. The slight time delay is due to the wave propagation speed and probes causality. It should be noted that the sensitivity of above statistical correlations to the number of samples was verified by calculating the cross-correlation coefficients with half of the total time samples.

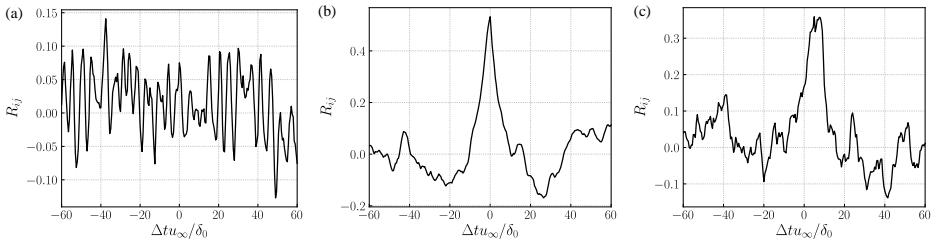


Figure 3.20: Temporal cross-correlations between the spanwise-averaged reattachment location and (a) pressures fluctuations inside the shear layer, (b) area of the separation bubble and (c) shock location (case BZA).

### 3.3.5. TWO-DIMENSIONAL DYNAMIC MODE DECOMPOSITION

The above analysis provides a first characterization of the unsteady features of the interactions and statistical links between them. In order to better decouple various frequency dynamics and further validate our obtained results, a modal decomposition of the two-dimensional flow field is carried out based on dynamic mode decomposition (DMD). The current DMD analysis is based on 700 snapshots of the spanwise-averaged flow field

(covering the time interval  $tu_\infty/\delta_0 = 800 \sim 1150$ ) at a sampling frequency  $f_s\delta_0/u_\infty = 2$ , which yields a frequency resolution of  $2.9 \cdot 10^{-3} < St_{\delta_0} < 1$ . In figure 3.21(a), we provide the eigenvalue spectrum resulting from the standard DMD. The input snapshots are real numbers while the computed modes appear as complex conjugate pairs, which results in a symmetric spectrum. The magnitudes of the corresponding DMD modes are shown in figure 3.21(b) for the positive frequencies. All the magnitudes are normalized by the maximum magnitude. This is a statistically stationary system since all of the eigenvalues are distributed near the unit circle  $|\mu_i| = 1$ , which means the snapshots sequence falls in an attracting set[167].

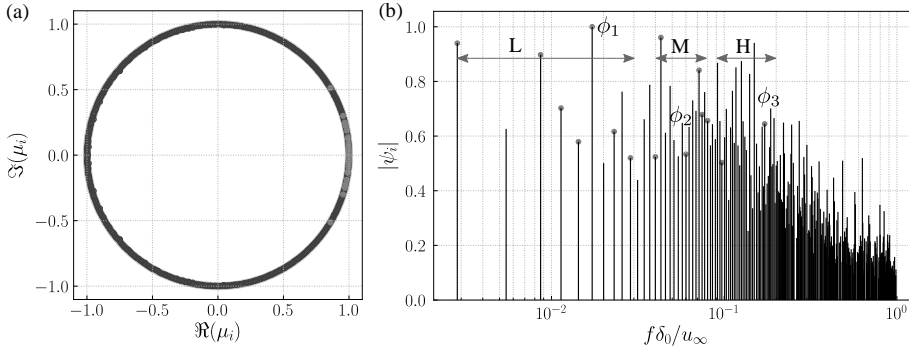


Figure 3.21: (a) Eigenvalues spectrum from the standard DMD algorithm (b) Normalized magnitudes of all the DMD modes with positive frequency (case BZA, • illustrates the most important 15 pairs of modes calculated by SPDMD).

The sparsity-promoting DMD (SPDMD) [140] is employed to select the dynamically important modes. This method picks modes based on their contribution to a reproduction of the original dynamic system over the given time interval. By taking the positive regularization parameter equal to 780, we obtained the 15 pairs of modes that are indicated by the gray solid circles in figure 3.21. They are considered to be the most dynamically important modes and have the most significant influence on data sequences. These modes can be categorized as three sets based on their main flow structures and frequency range, with  $0.003 \leq f\delta_0/u_\infty \leq 0.029$ ,  $0.04 \leq f\delta_0/u_\infty \leq 0.08$  and  $0.09 \leq f\delta_0/u_\infty \leq 0.20$ , respectively. These frequency ranges have been indicated in figure 3.21(b) and labeled as L, M, H, which stands for low, medium and high frequency. The frequencies of dominant modes are seen to be consistent with our previous spectral and statistical analysis in the preceding section.

For the branch with lower frequencies, we choose the mode with frequency  $St_\delta = 0.017$ , indicated as mode  $\phi_1$ , to scrutinize the flow dynamics. The selected modes in the other two branches are labeled as mode  $\phi_2$  ( $St_\delta = 0.06$ ) and  $\phi_3$  ( $St_\delta = 0.172$ ). In figure 3.22, 3.23 and 3.24, the real and imaginary part of these modes illustrating the contour of streamwise velocity and pressure fluctuations are shown. To assist interpretation, we also reconstructed the real-valued flow field of the individual modes by superimposing the fluctuations of each mode  $\phi_i$  onto the mean flow  $\phi_m$ , formulated as  $q(x, t) = \phi_m + a_f \cdot \Re\{\alpha_i \phi_i e^{i\omega_i t}\}$ , to examine the dynamical behavior represented by

every mode, where  $\alpha_i$  and  $a_f$  are the amplitude and optional amplification factor of the corresponding mode  $\phi_i$ . In the following analysis, these amplification factors are  $a_f = 10$  for the velocity fluctuations and  $a_f = 90$  for pressure disturbance for all the modes in order to have a distinguishing visualization.

The lower frequency mode  $\phi_1$  falls into the frequency of the breathing motion of the separation bubble, which is the reason that high fluctuations of the streamwise velocity are distributed along the dividing line as a consequence of the flapping of the shear layer, shown in figure 3.22(a). In addition, strong pressure fluctuations are observed along the reattachment shock in figure 3.22(b) due to flapping motion of the shock wave, which is caused by the contraction and dilatation of separation bubble. Hence, we conclude that this mode involves a breathing behavior of the separation bubble and concurrent streamwise motion of the shock wave system.

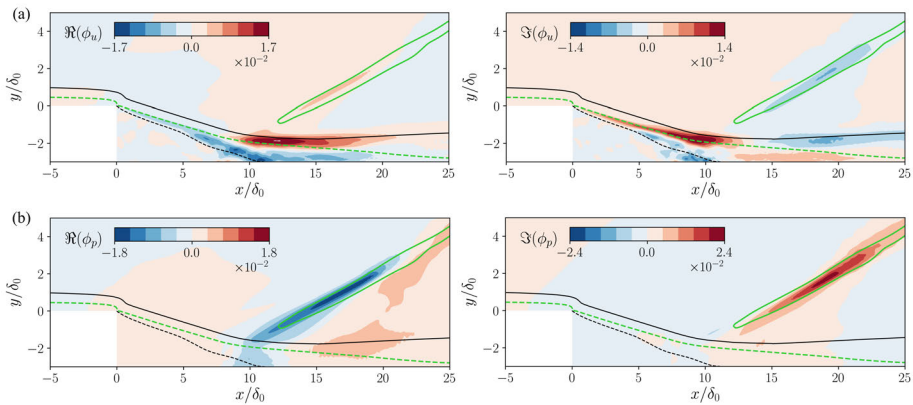


Figure 3.22: Real and Imaginary part of DMD mode  $\phi_1$  indicating contours of modal (a) streamwise velocity and (b) pressure fluctuations for case BZA. The green solid and dashed lines indicate the mean reattachment shock and sonic line. The black solid and dashed lines signify the boundary layer edge and dividing line.

The contours of mode  $\phi_2$  show strong streamwise velocity fluctuations around the reattachment location, see figure 3.23(a), which illustrates the large vortices originating in the shear layer. These vortices rapidly decay in downstream turbulent boundary layer, indicated by the low levels of the streamwise velocity fluctuations. Additionally, the reattachment compression and convection of large vortices produce high pressure fluctuations in the supersonic part along the reattachment shock, as shown in figure 3.23(b). A shock wrinkling dynamics is observed in the transient process of mode  $\phi_2$ . The corrugation of the shock is a result of the interaction between the large coherent vortices and the reattachment compression. Similar results have been reported in the LES of an incident shock wave and boundary layer interactions by Pasquariello *et al.* [99].

Considering mode  $\phi_3$  in figure 3.24, we find alternative high positive and negative fluctuations along the streamwise direction both in streamwise velocity and pressure contour. The frequency of mode  $\phi_3$  is  $St_\delta = 0.172$ , which is close to the characteristic frequency of the K-H vortex based on the spectral analysis. The traveling of K-H vortices induces eddy Mach waves in the supersonic portion of the flow field. From the temporal evolution of this mode, we can clearly observe the shedding of the K-H vortices with a

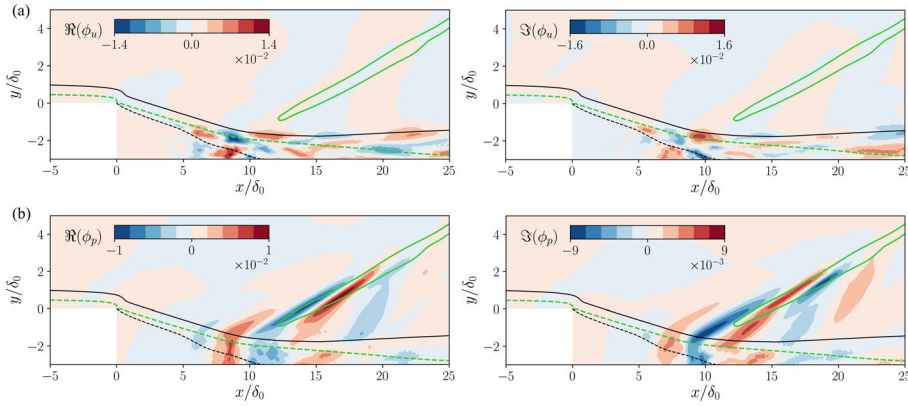


Figure 3.23: Real and Imaginary part of DMD mode  $\phi_2$  indicating contours of modal (a) streamwise velocity fluctuations and (b) pressure fluctuations for case BZA. The green solid and dashed lines indicate the mean reattachment shock and sonic line. The black solid and dashed lines signify the boundary layer edge and dividing line.

relatively steady intensity along the streamwise direction and the propagation of Mach waves along the reattachment shock. Therefore, we consider that this mode is associated with the convection of the K-H vortices.

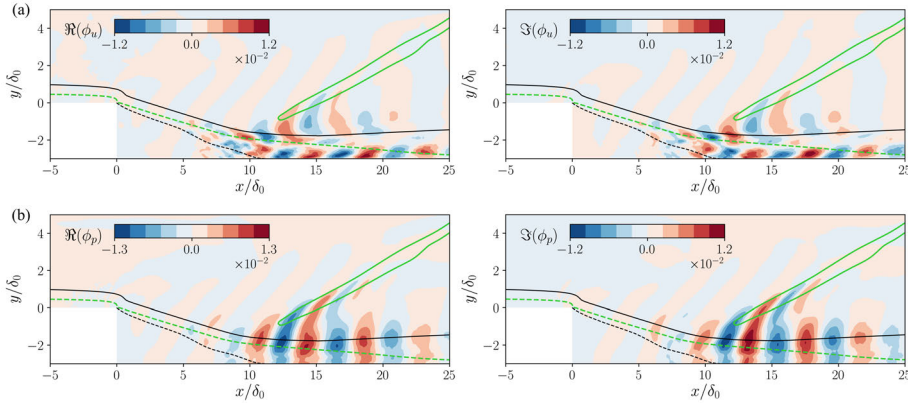


Figure 3.24: Real and Imaginary part of DMD mode  $\phi_3$  indicating contours of modal (a) streamwise velocity fluctuations and (b) pressure fluctuations for case BZA. The green solid and dashed lines indicate the mean reattachment shock and sonic line. The black solid and dashed lines signify the boundary layer edge and dividing line.

Based on the above analysis, the unsteady motions of the interacting flow field contain three types of dynamic behavior. The lower frequency branch ( $0.003 \leq St_\delta \leq 0.03$ ) describes a flow modulation that involves the breathing motion of shock and separation bubble system; the medium-frequency ( $0.04 \leq St_\delta \leq 0.08$ ) modes relate to the reattachment compression; while the higher-frequency part ( $0.09 \leq St_\delta \leq 0.20$ ) is

associated with the convection of K-H vortices and induced Mach waves.

### 3.3.6. SUMMARY

The dynamics of a BFS in a laminar backward-facing step flow was investigated at  $Ma = 1.7$  and  $Re_{\delta_0} = 13718$ , with special attention on the laminar-to-turbulent transition mechanism and the global unsteady behavior. The mean flow shows that the boundary layer is turbulent behind the reattachment location. The instantaneous flow visualizations provide a clear view of the transition process, which is summarized in the schematic drawing in figure 3.25. Five distinct stages are identified in the transition process. At the first stage, upon separation a quasi-steady two-dimensional shear layer is formed due to the velocity difference of the flow on both sides of the separation line. Then clockwise rotating spanwise vortices are induced by the K-H instability with a frequency of  $St_{\delta} \approx 0.2$ .

These K-H vortices grow rapidly and are subsequently deforming as a result of the ejection from the horseshoe vortices below as the free shear flow travels downstream in the second stage. The wavy K-H vortices have different traveling velocity in the spanwise direction and thus spanwise modulation occurs (third stage), which reduces the frequency of the breathing separation bubble to  $f\delta_0/u_{\infty} \approx 0.02$ . The high-speed parts develop into the head of  $\Lambda$ -shaped vortex and the low-speed parts develop into the legs parts due to the secondary instability. At the fourth stage, the large coherent vortices break down into several small  $\Lambda$ -shaped vortices caused by the streamwise stretching of vortices and the reattachment. The convection of the coherent structure and induced compression waves have an intermediate frequency with  $\delta_0/u_{\infty} \approx 0.06$ . Then the small vortices roll up and develop into larger hairpin vortices in the last phase, which is the indicator of the turbulent flow. The transition to turbulence is almost completed with the appearance of turbulent streaks.

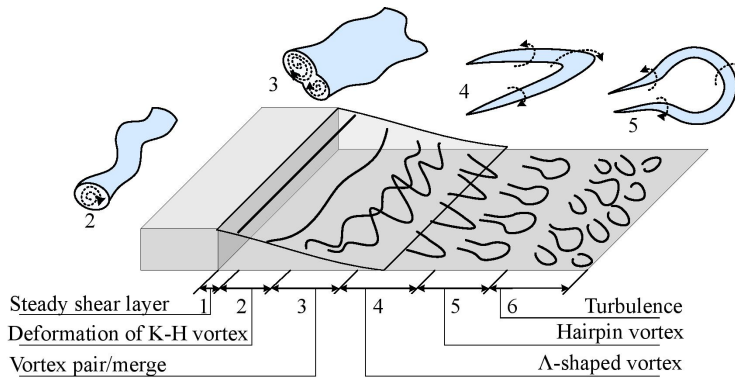


Figure 3.25: Conceptual model of the laminar-to-turbulent transition process in the supersonic BFS.

Given the rapid modal growth of the disturbances behind the step and high levels of amplitudes, we believe the nonlinear behavior is significant in the transition process, which involves the modal growth of K-H and secondary instability, vortices breakdown and eventually fully developed turbulence, in the current case. The power density

spectrum indicates that the unsteadiness of the interacting system is characterized by a modulation of a broadband frequency dynamics. Furthermore, the spectral and statistical analysis associates the flow phenomena with the unsteady behavior at different frequencies. The low-frequency breathing motions of the separation bubble exists in the whole transition process. However, the K-H instability seems to take the lead in the second stage and secondary instability in the third stage. We infer that the reattachment events and the oscillation of the shock appear to accelerate the transition process in the fourth stage.

The unsteadiness of the interacting system is characterized by a modulation of a broadband frequency dynamics. By means of SPDMD, we further extracted the most important modes representing the dynamics of the flow field that are characteristic for specific frequency ranges. The flapping motion of the shock and separation bubble is associated with a lower frequency centered at  $f\delta_0/u_\infty = 0.017$ . The medium frequency mode ( $f\delta_0/u_\infty = 0.06$ ) is related to the large coherent vortex shedding around the reattachment location and the wrinkling behavior of the shock, while the higher frequency mode ( $f\delta_0/u_\infty = 0.172$ ) is associated with the traveling of K-H vortices and induced Mach waves. Flow reconstruction based on the selected DMD modes further elucidates the dynamic behavior of the interaction system.

### 3.4. TRANSITIONAL REGIME

Laminar case BZA and transitional case BLA share the similar transition path behind the step, as we indicate in section 3.2. By comparison, for case BLA, the growth of the T-S modes is the main source of the disturbances upstream of the step (phase 1:  $x/\delta_0 < 0$ ). In the second phase (phase 2:  $0 \leq x/\delta_0 \leq 4$ ), the development of large K-H vortices is the most significant feature of the flow field. However, in the current BLA simulation case, we can also observe the effect of the oblique waves in this region, such as the harmonic undulation of the K-H vortices compared to the more straight K-H vortices in case BZA. The secondary instability dominates the growth of the turbulence in the third phase (phase 3:  $4 \leq x/\delta_0 \leq 7.5$ ). Near the reattachment location, the breakdown of vortices promotes the transition to fully developed turbulence (phase 4:  $x/\delta_0 \geq 7.5$ ). The role of oncoming primary T-S modes, their interactions with the excited K-H modes, and the secondary waves in the transition process of the free shear layer are not completely documented and understood. Therefore, our interest is laid on the evolution of possible primary and secondary instabilities, as well as their interactions, in this section.

#### 3.4.1. TOLLMIEN-SCHLICHTING INSTABILITY

The wavenumber and frequency of the least stable waves depend on the local Reynolds number  $Re_l$  based on Blasius length [36]. We traced the eigenvalues of the unstable modes, including the least unstable one, along the streamwise direction. The stability diagram is displayed in figure 3.26, where three levels of  $\alpha_i^l$  are computed at a constant spanwise wavenumber  $\beta^l = 0.06202$  and angular frequency  $\omega^l = 0.01605$  against  $Re_l$ . Since the Reynolds number of our case is very close to the critical one, the variation of  $\omega$  is relatively small for each level of  $\alpha_i^l$  when  $Re_l < 2225$  at  $\beta^l = 0.06202$  [figure 3.26(a)]. For increasing  $Re_l$  (moving downstream), the upper and lower branches of the stability

diagram move towards each other until they finally meet. The unstable region of the oblique waves is decreasing with increasing  $Re_l$  and  $|\alpha_i^l|$ . Figure 3.26(b) shows the same levels of  $\alpha_i^l$  with different  $Re_l$  and  $\beta^l$  at a specific angular frequency  $\omega^l = 0.01605$ . A similar trend of  $\beta^l$  with  $Re_l$  is observed as that of  $\omega^l$  in figure 3.26(a). The development of the most unstable mode (the one with maximum  $|\alpha_i^l|$ ) at the given  $\beta^l$  and  $\omega^l$  is also included in figure 3.26 (the dash-dot lines). We can see that the frequency and spanwise wavenumber of the least unstable modes are relatively constant along the streamwise distance. In conclusion, the wavenumber and frequency of the oblique wave imposed at the inlet remain in the unstable region and are very close to the values of the local most unstable oblique T-S wave upstream of the step. Therefore, in the following discussion, we only look into the spatial development of the unstable mode with the imposed wavenumber and frequency using both LST and LES.

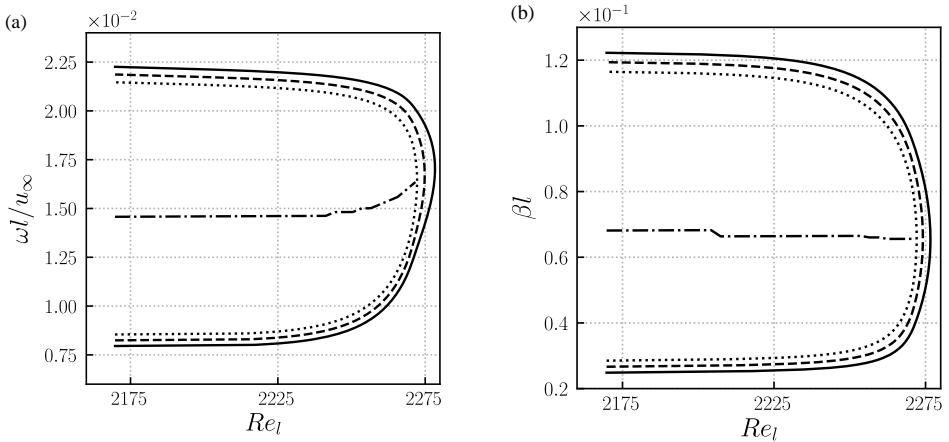


Figure 3.26: Contours of  $\alpha_i^l$  computed from LST at the imposed (a) spanwise wavenumber  $\beta^l = 0.06202$  and (b) angular frequency  $\omega^l = 0.01605$  for case BLA (—,  $\alpha_i^l = -0.0014$ ; ---,  $\alpha_i^l = -0.0015$ ; ····,  $\alpha_i^l = -0.0016$ ; -·-·-,  $|\alpha_i^l|_{\max}$ ).

The evolution of the oblique waves computed by LES can be measured by the maximum root mean square of the streamwise velocity fluctuations. The semi-log plot in figure 3.27 already indicates that the current LES can well predict the exponential growth rate of the oblique T-S waves. The averaged streamwise growth rate is given by the slope of the curve, whose value approximates to 0.0155 and is very close to LST result  $\alpha^\delta = 0.0161$  for the inflow perturbation. We also provide the shape factor of the boundary layer in figure 3.27 (dashed line). The shape factor is almost a constant upstream of the step and its mean value equals to 4.36. Chang *et al.* [168] proposed that the shape factor is a function of pressure gradient and free stream Mach number in compressible laminar flow with adiabatic wall and provided the following empirical fit

$$H(Ma_\infty, \lambda'_\theta) = \frac{3.182\lambda'_\theta + 0.57757}{\lambda'^2_\theta + 1.49\lambda'_\theta + 0.223} \cdot \left(1 + \frac{\gamma-1}{2} Ma_\infty^2\right) \quad (3.3)$$

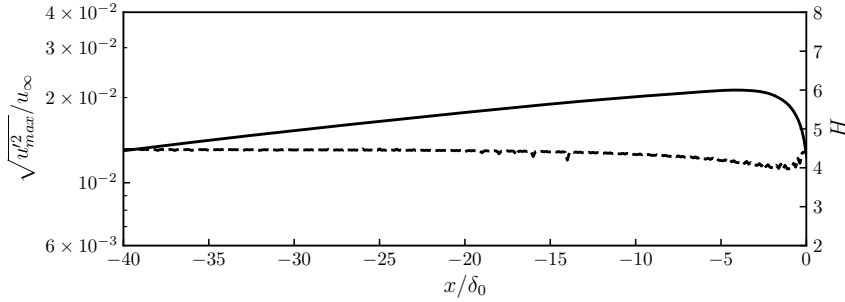


Figure 3.27: Maximum RMS of streamwise velocity fluctuations (solid line) and shape factor of the boundary layer (dashed line) along the streamwise direction (case BLA).

where  $\lambda_\theta$  is a corrected pressure gradient factor in compressible flow, which equals to zero in our case without pressure gradient. We obtain  $H = 4.09$  using this empirical formula, which is close to the current mean shape factor.

Next, we calculate the streamwise wavenumber and growth rate using LES results. The temporal Fourier transform of the LES data is computed at every streamwise location

$$Q'(x, f) = \sum_{k=1}^N q'(x, t_k) e^{if t_k}, \quad (3.4)$$

where  $t_k$  denotes the discrete time samples. In the present case, the extracted signals are from the wall pressure and include 1200 samples within five periods of the imposed oblique waves. Next, the corresponding phase angle  $\theta(x)$  and amplitude  $A(x)$  of the perturbation  $q'$  are obtained via

$$\begin{cases} \theta = \arctan \frac{\Im(Q')}{\Re(Q')} \\ A = \|Q'\| \end{cases} \quad (3.5)$$

After  $\theta(x)$  and  $A(x)$  are collected at every streamwise location, the streamwise wave number and growth rate finally are determined by [56, 169]

$$\begin{cases} \alpha_r(x) = \frac{\partial \theta(x)}{\partial x} \\ \alpha_i(x) = -\frac{1}{A(x)} \frac{\partial A(x)}{\partial x} \end{cases} \quad (3.6)$$

The obtained results are compared with the results from LST in figure 3.28. The LES results give slightly oscillating wave number and growth rates upstream of the step ( $x/\delta_0 < -10.0$ ). This modulation usually happens when the forcing amplitude is relatively large and is caused by weak acoustic disturbances traveling within the boundary layer [37, 56]. Near the step, the large variation of  $\alpha_r$  and  $\alpha_i$  is caused by the non-parallel effects and acceleration in front of the step. We are very satisfied with the agreement of LST and LES.

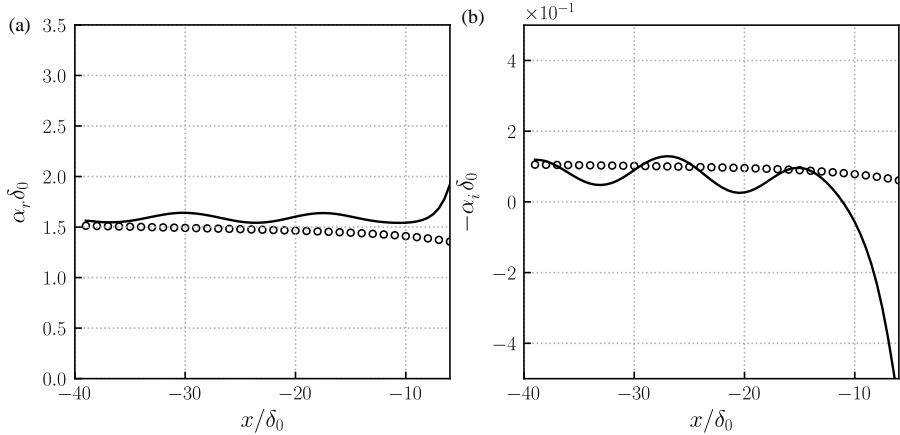


Figure 3.28: Streamwise development of (a) wavenumber  $\alpha_r$  and (b) growth rate  $\alpha_i$  for case BLA, resulting from LST (o) and LES (—).

For further comparisons, the wall-normal amplitude distributions for streamwise velocity and pressure fluctuations are plotted for both LST and LES in figure 3.29, at  $x/\delta_0 = -25.0$ ,  $\beta^l = 0.062$  and  $\omega^l = 0.016$ . The values of all variables are normalized by their respective maximum value of the profiles. Results from these two techniques are found to be in excellent agreement. It manifests that our current LES can reproduce the exponential growth of the oblique T-S waves predicted by LST in the present study. Therefore, we are confident that well-resolved LES is an appropriate method for computing the spatial evolution of these T-S waves downstream.

### 3.4.2. PRIMARY KELVIN-HELMHOLTZ INSTABILITY

The incoming laminar boundary layer separates at the step edge, upon which a strong initially two-dimensional shear layer is generated (see figure 3.7). The spanwise vorticity propagates and redistributes along the free shear layer via the K-H instability. Immediately downstream of the step, two-dimensional vortices are produced due to the K-H instability which is absolutely unstable to small disturbances, such as incoming T-S waves and the additional effect of the small numerical round-off errors. Then these two-dimensional waves undergo deformation and distortion caused by the growing disturbances. In the meantime, the region of strong spanwise vorticity gradually expands and simultaneously vorticity peaks develop at certain locations where the quasi two-dimensional K-H vortices are formed. These spanwise vortical structures behind the step are also visualized by the pressure contours of spanwise-normal slices in figure 3.30. The vortex lines (black) point to the negative spanwise direction, corresponding to clockwise rotation looking from the left side. In the case BZA, the vortex lines are straight in the spanwise direction, whereas these lines are sinusoidal due to the incoming oblique T-S waves in the case BLA, corresponding to the harmonic undulation of the K-H vortices in figure 3.7(b).

In the following sections, we provide a further analysis of the involved instabilities

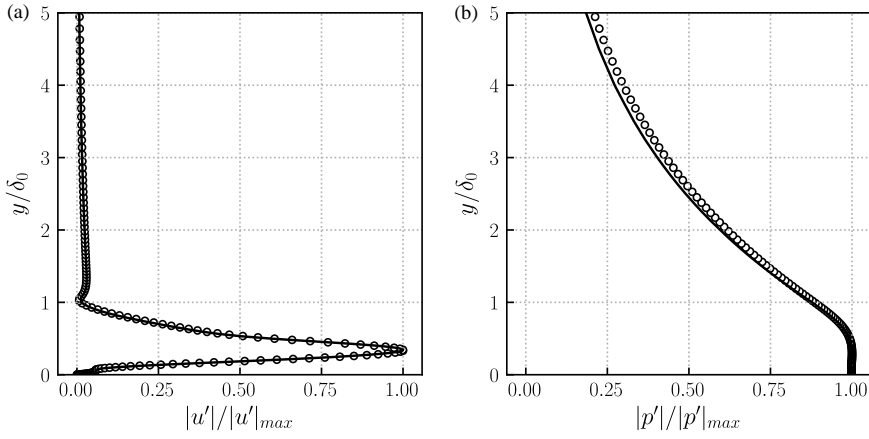


Figure 3.29: Comparison of wall-normal profiles of perturbation amplitudes between LST (◦) and LES (—) for (a) streamwise velocity and (b) pressure at  $x/\delta_0 = -25.0$ ,  $\beta^l = 0.062$  and  $\omega^l = 0.016$  (case BLA).

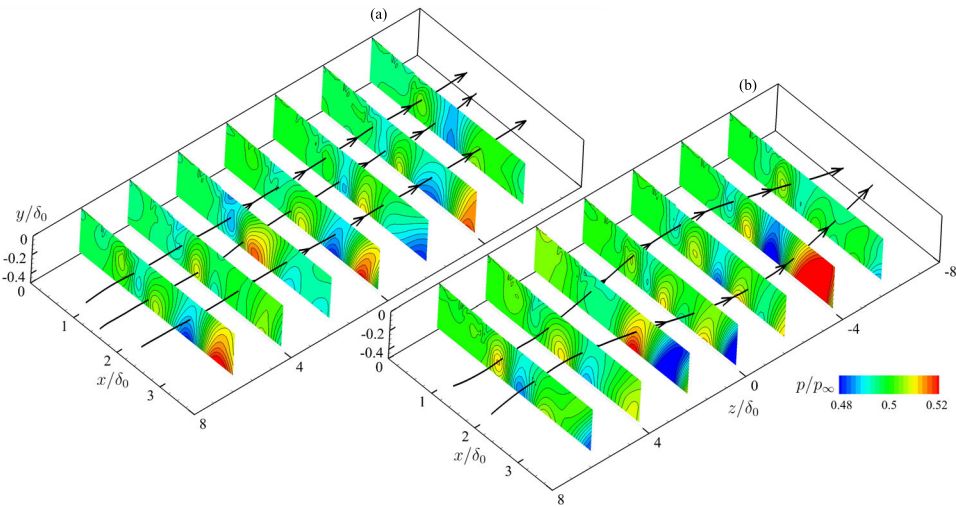


Figure 3.30: K-H vortices illustrated by contours of pressure at  $tu_\infty/\delta_0 = 912$ . Black arrow lines represent the vortex lines. (a) case BZA and (b) case BLA.

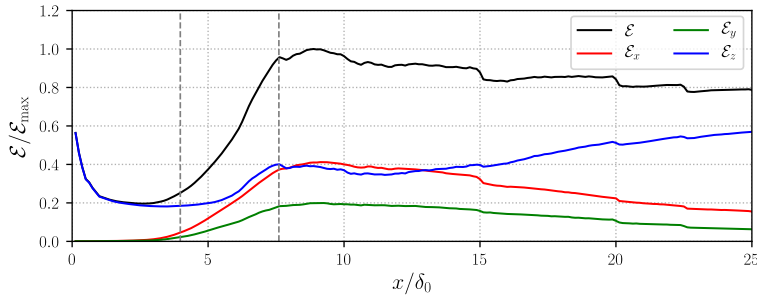


Figure 3.31: Streamwise development of the integrated enstrophy in  $y-z$  plane for case BLA. The grey dashed lines distinguish the different phases in the transition process.

from the perspective of vorticity dynamics. By analyzing the generation, development, and structural characteristics of the vorticity, like stretching, tilting and lift up, in the transition process, we obtain an understanding of how the primary instability evolves and the secondary instability is excited. The streamwise distribution of the integral enstrophy is computed using equation (2.56), for the three individual coordinate directions, as well as for the total enstrophy, with the results as shown in figure 3.31. The integration area is selected as  $-8.0 \leq z/\delta_0 \leq 8.0$  and  $-3.0 \leq y/\delta_0 \leq 0.0$ , where most of the vortical activity occurs. At the step ( $x/\delta_0 = 0$ ), the large spanwise enstrophy component is caused by the strong inviscid instability of the shear layer. The total enstrophy subsequently decays and reaches a minimum at  $x/\delta_0 \approx 2.5$  due to the spatial redistribution of the spanwise vorticity (as will be shown in figure 3.34). The total enstrophy increases gradually with the streamwise distance in the second phase between  $2.5 < x/\delta_0 < 7.5$ , mainly due to the evolution of spanwise and streamwise vorticity. Then the enstrophy remains at a high and relatively constant level in the vortex breakdown and reattachment region ( $7.5 < x/\delta_0 < 14.0$ ). This observation provides supporting evidence that the vortex breakdown usually occurs in the vicinity of the location where a local maximum of enstrophy is present [170]. The spanwise enstrophy  $\mathcal{E}_z$  is the most significant one in the region of  $0.0 < x/\delta_0 < 5.0$ , and then again in the downstream region  $x/\delta_0 > 15.0$ .

Using the decomposition according to the separate terms in equation (2.57) and (2.58), the balance of the most important enstrophy  $\mathcal{E}_z$  and its evolution along the streamwise direction is shown in figure 3.32. The integration area in the  $y-z$  plane is the same as for figure 3.31. The dilatation term is the most significant contribution near the step, which is expected because the vorticity field is subject to a strong expansion.

For  $2.5 < x/\delta_0 < 4.0$ , the development of the vorticity field is dominated by  $S_{zz}$ , i.e., the vortex stretching of the induced K-H vortices, caused by the gradient of the spanwise velocity  $\partial w/\partial z$ . Based on the above vortex visualization and vorticity dynamics analysis, the most significant disturbances are the K-H vortices in this stage and the development of the eddies is mainly due to the dilation and stretching of the spanwise vorticity itself. It can be inferred that the primary K-H instability plays the most important role in this process, instead of T-S and secondary instabilities.

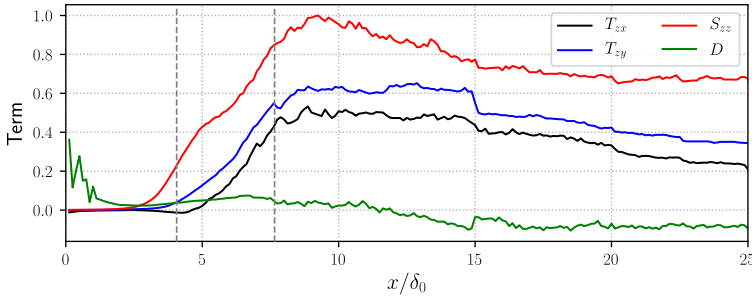


Figure 3.32: Streamwise variation of the integrated production terms for  $\mathcal{E}_z$  behind the step for case BLA. The grey dashed lines distinguish the different phases in the transition process.

Although the T-S waves are not clearly visible in figure 3.30, they still coexist with the K-H modes in the second phase. They do not show up prominently in the visualization because T-S waves only have a weak velocity gradient, which is overwhelmed by the strong contribution of the K-H vortices. To better assess the development of the T-S waves, three stations have been selected (one just upstream of the step and two in the separated shear layer downstream of it) to analyse the spatial evolution of the wave pattern across the step. Figure 3.33 provides the signals of the streamwise velocity at these stations, alongside with their frequency weighted power spectral density. Compared with the case BZA, the case BLA shows large amplitude fluctuations and a single dominant frequency peak at  $f\delta_0/u_\infty \approx 0.016$  for station A, corresponding to the amplitude and frequency of the imposed oblique waves. Shortly downstream (station B), the sinusoidal footprint of the oblique waves can still be recognized but it is mixed with higher frequency fluctuations. At the same time, it is observed that the oblique waves are strongly amplified and their energy is about 20 times larger than at the upstream station A. In this small region, the original information of the T-S waves can be extracted with amplified amplitude by a low-pass filter since the interacting signals are not strongly coupled yet. Further downstream (station C), the velocity fluctuations exhibit a wide-band frequency spectrum. The most significant peak is at  $f\delta_0/u_\infty \approx 0.2$ , which corresponds to the natural frequency of the K-H vortices for the current configuration according to the previous section. The fluctuation energy of the case BLA is still larger than for the case BZA, for example, around two times larger at  $f\delta_0/u_\infty = 0.2$ . Additionally, the incoming T-S waves and intrinsic K-H waves are fully coupled already without a significant low-frequency feature of the T-S waves. Therefore, we believe that the K-H instability acts as an amplifier of the incoming weak oblique waves and spanwise K-H waves themselves in the interaction between primary T-S and K-H modes [171, 172].

On the other hand, the spanwise wavenumber modulation also contributes to the interaction. As we can see in figure 3.7 (b), the large quasi two-dimensional K-H vortices are undulated in the shape of the incoming T-S waves along the spanwise direction between  $2.0 < x/\delta_0 < 3.0$ ). Compared to the straight vortex lines in the case BZA [figure 3.30(a)], the vortex lines of case BLA present harmonic (sinusoidal) wave forms with the spanwise wavelength of the incoming T-S waves [figure 3.30(b)]. The vortex pairing may occur

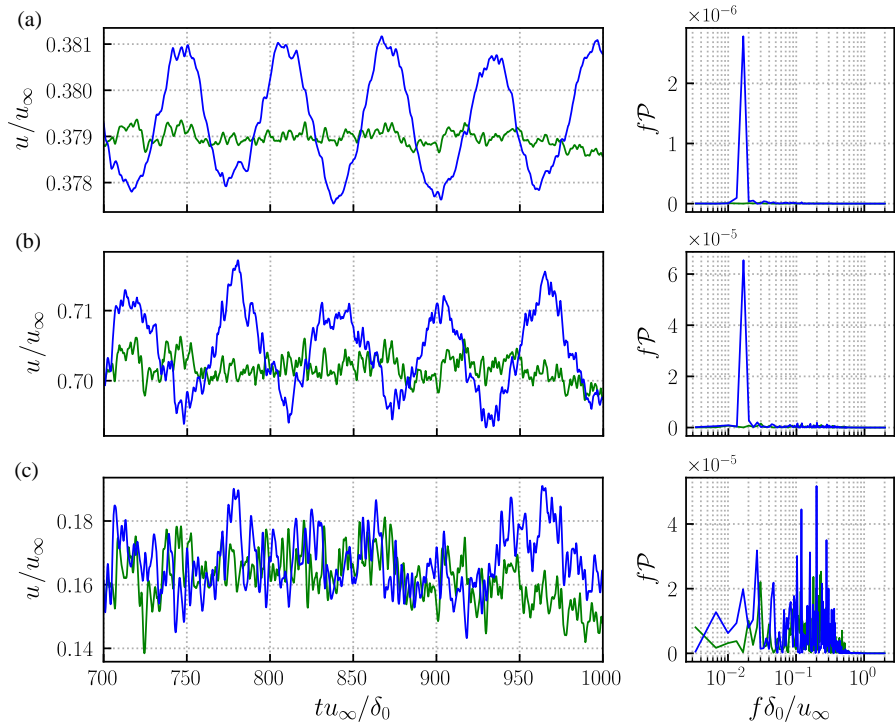


Figure 3.33: Temporal evolution of the streamwise velocity perturbations (left) and the corresponding frequency weighted power spectral density (right) at (a) station A ( $x/\delta_0 = -0.1875, y/\delta_0 = 0.03125$ ), (b) station B ( $x/\delta_0 = 0.203125, y/\delta_0 = 0.0390625$ ) and (c) station C ( $x/\delta_0 = 0.59375, y/\delta_0 = -0.171875$ ) based on the slice  $z = 0$  for case BZA (green line) and BLA (blue line).

with the mutual interaction of the neighboring wavy vortices, as well as the convected shear layer. The vortex merging process is visualized by the streamlines in figure 3.34. At the initialization phase of the vortices pairing, the upstream K-H vortices are slightly weaker and smaller [figure 3.34(a)]. As both of the vortices are convected downstream, the weaker vortices cannot resist the stronger strain field generated by the other one and are stretched by the velocity gradient [figure 3.34(b)]. Finally, the upstream vortices are striped off from the outer recirculation region downstream and merged into the stronger one during the convection process [figure 3.34(c)] [173, 174].

In the weak coupling region, both of the T-S and K-H modes are the primary mode. The growth rate of the fluctuations caused by them is examined in figure 3.35(a). In a very short distance ( $0 < x/\delta_0 < 0.8$ ), the growth rate of existing waves within the shear layer falls into a quasi linear regime, but with a much larger value compared to the growth rate of the upstream T-S waves. Wu *et al.* [175] also reported the linear growing behavior of the K-H waves in the early roll-up process of the large K-H vortex. In contrast, the small disturbances (around  $10^{-6}u_\infty$ ) upstream of the step in the case BZA are drastically amplified in the redistribution region of the spanwise vorticity. Once the spanwise K-H

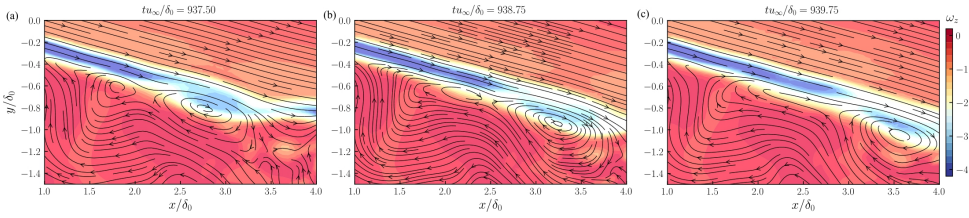


Figure 3.34: Contour of spanwise vorticity with the streamlines in the  $x-y$  plane at three instants, showing the K-H vortices pairing (case BLA).

vortices emerge, both cases BZA and BLA display a similar level of fluctuations in the shear layer. The dominant frequency of the unsteady waves shifts from the low value ( $f\delta_0/u_\infty \approx 0.016$ ) to a much higher one ( $f\delta_0/u_\infty \approx 0.2 \sim 0.4$ ), which suggest the leading instability switching from the T-S instability to K-H instability, shown in figure 3.35(b). When the maximum amplitude of the fluctuations exceed  $2\%u_\infty$ , the K-H mode plays a more important role and undergoes a rapid growth ( $0.8 < x/\delta_0 < 4.0$ ). We infer that the redistribution of the spanwise vorticity (the dilatation term in figure 3.32) has a greater effect on the high-frequency waves caused by the shear layer instability than on the low-frequency oblique waves. Subharmonic K-H waves are produced between  $2.5 < x/\delta_0 < 4.0$  due to the vortex pairing of the fundamental K-H vortices, which reduces the leading frequency to  $f\delta_0/u_\infty \approx 0.2$ .

### 3.4.3. SECONDARY INSTABILITY

The velocity is not uniform along the spanwise direction and the K-H vortices are not strictly two dimensional in the shear layer, which induces two types of secondary instability in the transition. As we can see in figure 3.31, there is significant creation of wall-normal and streamwise vorticity after the first phase ( $x/\delta_0 \geq 4.0$ ). First of all, the wall-normal velocity is non-uniform in the spanwise direction due to the existing disturbances within the shear layer. The originally spanwise-aligned vortices then may be lifted up at some locations where there is high wall-normal velocity. These high-velocity regions are obvious in the instantaneous vortical structures visualization of figure 3.36(a). This secondary lift-up effect produces wall-normal vorticity. As we can see in figure 3.36(d), the coherent vortices are gradually lifted up in the streamwise direction. If we consider the enstrophy balance for the wall-normal direction (figure 3.37), it is obvious that the upward tilting of spanwise vorticity is the dominant mechanism in producing the wall-normal vorticity.

Moreover, the bent-up parts of the vortices are convected faster than the other parts due to larger streamwise velocity in the upper region of the shear layer. This secondary behavior leads to the non-uniformity of the streamwise velocity in the spanwise direction, which generates streamwise vorticity. By the analysis of the enstrophy balance for the  $x$ -direction (figure 3.38), we can see that the tilting of wall-normal vortices is a significant contributor to increasing the streamwise vorticity. In turn, the streamwise velocity gradient along the induced vortex line  $\partial u/\partial x$  lead to the stretching of the streamwise vortices, which also is the main mechanism for the enstrophy evolution in

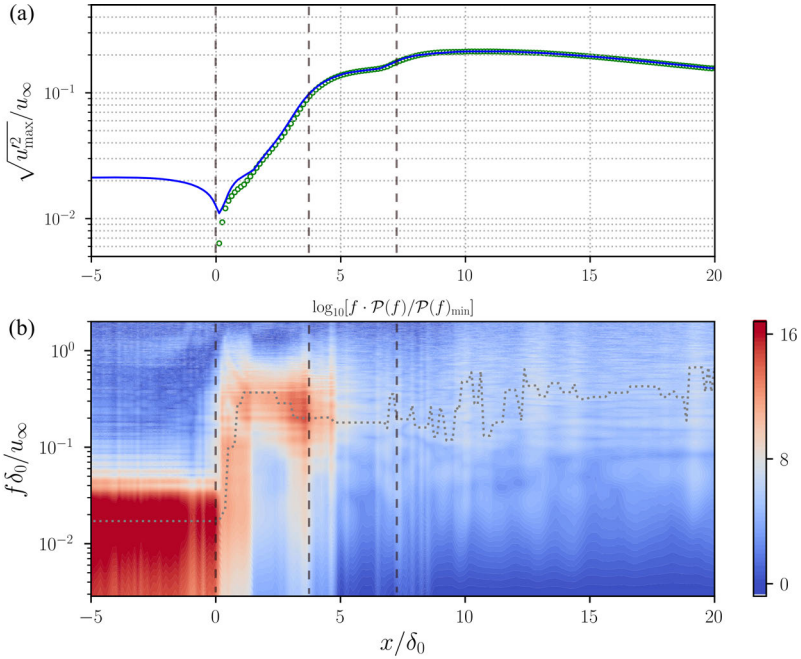


Figure 3.35: (a) Maximum RMS of streamwise velocity fluctuations along streamwise direction (case BZA, green circle; case BLA, blue solid line) and (b) Frequency weighted power spectral density map of maximum pressure signals along the streamwise direction based on  $z = 0$  slice between  $-5.0 \leq x/\delta_0 \leq 20.0$  for case BLA. At every streamwise position the weighted spectra are normalized by the minimum of  $\mathcal{P}(f)$ . The gray dashed line signifies the frequency at which  $f\mathcal{P}(f)$  is maximum. The grey dashed lines distinguish the different phases in the transition process.

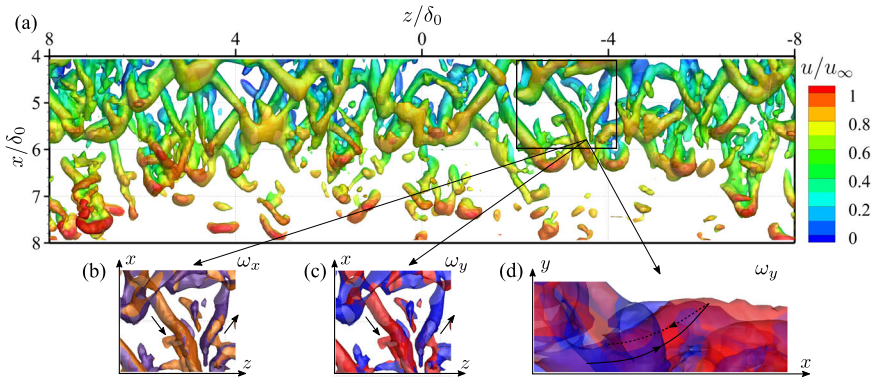


Figure 3.36: Iso-surfaces of vortical criterion  $Q = 0.08$  at  $t u_\infty / \delta_0 = 912$  (case BLA), contoured by (a) streamwise velocity, (b) streamwise vorticity (purple:  $\omega_x < 0$ , orange:  $\omega_x > 0$ ), (c) wall-normal vorticity in the  $x - z$  plane and (d) wall-normal vorticity in the  $x - y$  plane (blue:  $\omega_y < 0$ , red:  $\omega_y > 0$ ).

this stage.

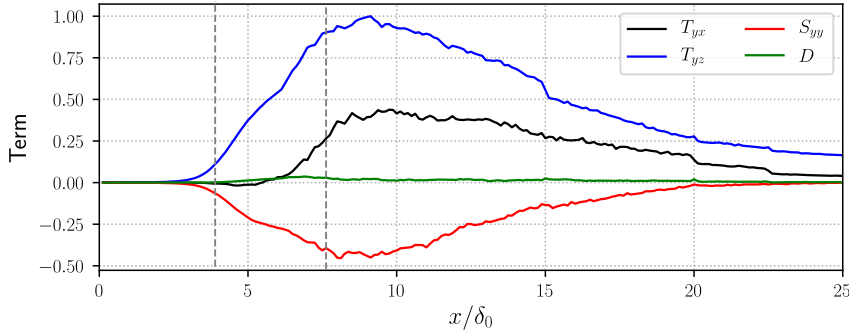


Figure 3.37: Streamwise variation of the integrated production terms for  $\mathcal{E}_y$  behind the step for case BLA. The grey dashed lines distinguish the different phases in the transition process.

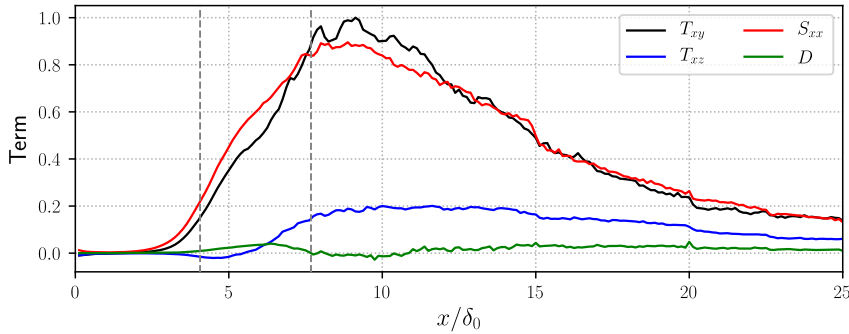


Figure 3.38: Streamwise variation of the integrated production terms for  $\mathcal{E}_x$  behind the step for case BLA. The grey dashed lines distinguish the different phases in the transition process.

The combination of these two secondary instabilities results in the initiation of the large  $\Lambda$ -shaped vortices (see figure 3.36), in which high-speed parts of the spanwise vortices are elevated by the secondary lift-up effects and subsequently the streamwise vorticity is produced due to the secondary streamwise tilting dynamics. The low-momentum parts form into the legs of the  $\Lambda$ -shaped vortices and the high-momentum parts develop into the head of  $\Lambda$ -shaped vortices in this region. Since the strong spanwise vorticity has a negative sign, the left leg of the  $\Lambda$ -shaped vortex has positive streamwise [figure 3.36(b)] and wall-normal [figure 3.36(c)] vorticity, while the right leg has negative vorticity. As long as the streamwise vortices are produced, they will keep stretching because of the higher speed in the bending parts until they break down. In general, the streamwise enstrophy is more significant than the wall-normal enstrophy in this stage (see figure 3.31).

As shown in figure 3.35, the secondary instability undergoes a rapid growth to  $20\%u_\infty$  in this stage and the frequency characteristic shifts from a dominant value  $f\delta_0/u_\infty \approx 0.2$ , the same value of subharmonic K-H waves, to a low-frequency broadband spectrum, which is also reported by Sansica *et al.* [176] in their shock-induced laminar separation

bubble case. The unsteadiness of the primary T-S modes is much less energetic than the subharmonic waves. We believe that the primary T-S waves appear to be contaminated or retarded. Our observations support the opinion that the primary T-S waves diminish in the region where the excited secondary disturbances have a large amplitude [56]. The dominant mechanism is the slow resonance between subharmonic K-H vortices and the secondary instability in this region, in which disturbances slowly grow due to the induced secondary instability and their frequency features still remain the same as those of subharmonic K-H vortices.

## 3

### 3.4.4. BREAKDOWN AND REATTACHMENT

In the following stage ( $x/\delta_0 \geq 7.5$ ), the streamwise vortices keep being elongated in the streamwise direction and lifted up due to stretching dynamics (see figure 3.37 and 3.38). This rolling up and prolongation lead to the formation of the small hairpin vortices, which is the signature of fully developed turbulent flow, illustrated in figure 3.39. The enstrophy reaches its global maximum before the shear flow impinges on the wall, which occurs around  $x/\delta_0 = 10.9$ . Then the strong vorticity tilting and stretching terms start to decrease until they vanish gradually far downstream. Across the reattachment, the hairpin vortices keep their typical structure, apparently without significant effects from the compression waves in their proximity. The streamwise and spanwise spacing of the hairpin vortices are  $\lambda_x \approx \lambda_z \approx 90\nu/u_\tau$  based on the local wall shear stress, which is the typical spacing of the coherent structures as reported in previous experimental studies [177]. The fluctuations of velocity reach their highest level at the mean reattachment point, shown in figure 3.35(a). The pressure power spectral density [figure 3.35(b)] shows a broadband distribution typical for developed turbulence. In addition, more energy is observed around the reattachment in the low-frequency parts ( $f\delta_0/u_\infty \approx 0.2$ ).

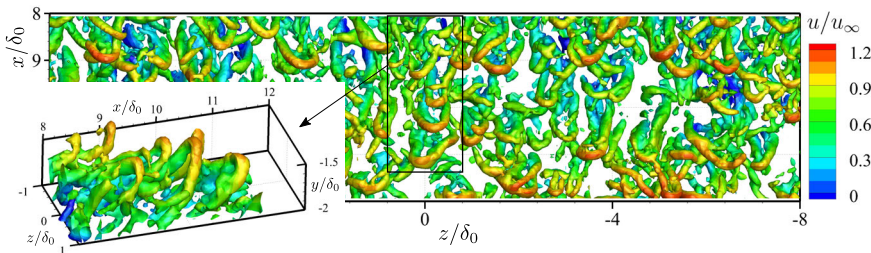


Figure 3.39: Iso-surfaces of vortical criterion  $\lambda_2 = -0.1$  at  $tu_\infty/\delta_0 = 908$  (case BLA), contoured by the streamwise velocity.

In summary, the imposed low-amplitude oblique waves undergo slow growth in agreement with the expected linear dynamics upstream of the step and damp close to the step due to the expansion fan. In a short distance behind the step, both oblique T-S waves and generated K-H waves act as the primary mode. The interaction of T-S and K-H waves leads to the rapid growth of the disturbances within  $0 \leq x/\delta_0 \leq 1$ . Pairing of the adjacent undulating K-H vortices generates subharmonic K-H waves. Then the large-amplitude secondary instability, including the lift-up effects and streamwise tilting, begins to take the lead. In the meantime, the weak T-S waves vanish in the

competition with the strong subharmonic waves and can no longer be discerned. As the flow reattaches downstream, the transition to fully developed three-dimensional turbulence with a broadband frequency spectrum (cf. figure 3.35) is almost completed.

### 3.4.5. SUMMARY

The transition path and unsteady behavior of the supersonic flow over a backward-facing step geometry show large differences between the two cases with low- and high-amplitude upstream disturbances. For the case BHA with high-amplitude initial perturbation, we obtain the excitation of oblique and secondary vortices, as well as non-linear breakdown already upstream of the step. This leads to a turbulent boundary layer upstream of the separation bubble. In contrast, the imposed low-amplitude oblique T-S wave (case BLA) remains within the linear growth regime, which is the initial stage of the natural transition. Therefore, the laminar-to-turbulent transition scenario does not differ much from the fully laminar case BZA, *i.e.*, initiation of the K-H instability, followed by the secondary instability, leading to  $\Lambda$ -shaped vortices, hairpin vortices and finally to a fully turbulent state. In a short distance behind the step, the interaction between T-S and K-H modes is a weak coupling process, in which the amplitude of T-S waves is amplified significantly by the strong shear layer but their frequency remains unchanged. In addition, the spanwise K-H vortices show a harmonic undulation with the wavelength of the T-S wave. Due to effects of the energetic three dimensional fluctuations downstream of the separation bubble, the interaction enters a non-linear stage and the unsteady behavior features a broad range of space and time scales. Behind the reattachment point, the boundary layer is highly turbulent.

## 3.5. TURBULENT REGIME

Shock wave/boundary layer interaction is also a major topic for a supersonic flow over a BFS. From the previous sections, the significant unsteady behavior of the interaction system has been observed in both the laminar and transitional cases. Since the shear layer is almost turbulent in the interaction region (proximity to the reattachment location), we use the turbulent case BTB to investigate the unsteady SWBLI, especially the low-frequency dynamics in this section. In this way, we can avoid the nonlinear effects of the transition on the unsteady SWBLI.

### 3.5.1. MEAN FLOW FEATURES

Figure 3.40 provides an overall view of the main flow topology. The upstream turbulent flow separates at the step edge and undergoes a centred Prandtl-Meyer expansion. The deflected shear layer travels downstream and finally reattaches on the downstream wall at  $x/\delta_0 = 8.9$ . Compression waves are produced around the reattachment point, which coalesce into a reattachment shock oriented at an angle of  $21^\circ$  to the positive streamwise direction. Compared to the ramp and incident shock cases [101, 164], the freestream variables behind the interaction recover almost to their initial levels in the BFS configuration because there is only the weak reattachment shock generated by the compression waves whereas there are at least two stronger shocks in the other cases. The mean flow features of the laminar case are very similar to the present turbulent one, but

the separated flow reattaches later at  $x/\delta = 10.9$  and the mean shock angle is smaller, around  $19^\circ$  [178]. These differences are caused by the stronger mixing in the turbulent case and are qualitatively consistent with existing experimental work [106].

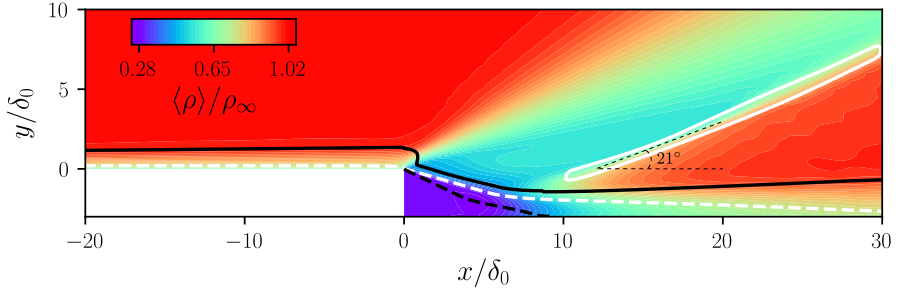


Figure 3.40: Density contours of the time- and spanwise-average flow field. The white dashed and solid lines denote the isolines of  $Ma = 1.0$  and  $|\nabla p|\delta_0/p_\infty = 0.24$  (case BTB). The black dashed and solid lines signify isolines of  $u = 0.0$  and  $u/u_e = 0.99$ .

The mean reattachment length (equal to  $L_r = x_r = 8.9\delta_0 \approx 3.0h$ ) is defined by the location of zero mean skin friction,  $\langle C_f \rangle = 0$ , in figure 3.41(a). The value of  $\langle C_f \rangle$  increases upstream of the step due to the flow acceleration induced by the expansion near the separation point ( $x = 0$ ). Behind the step, there is a ‘dead-air’ zone where the recirculating velocity is extremely low. Thus, uniform  $\langle C_f \rangle \approx 0$  is observed in the first 30% of the separation bubble ( $0.0 \leq x/\delta_0 \leq 2.8$ ). The separated flow then rapidly reaches its strong level at  $x \approx 2.1h \approx 6.2\delta_0$ , which is very close to the value ( $x \approx 2h \approx 6.4\delta_0$ ) reported by Chakravarthy *et al.* [152]. As the free shear layer reattaches on the downstream wall ( $x/\delta_0 = 8.9$ ), the turbulent boundary layer recovers and  $\langle C_f \rangle$  returns to a typical turbulent level ( $\langle C_f \rangle = 0.0027$ ). The reattachment length  $L_r \approx 3.0h$  based on the step height is in a good agreement with the previous experimental work by Bolgar *et al.* [103] and the numerical study by Chakravarthy *et al.* [152], who reported values of  $L_r = 3.2h$  and  $L_r = 3.0h$ , respectively. Compared with the laminar case (blue dotted lines), the mean skin friction further confirms the shorter separation length in the turbulent case. The turbulent case has a much higher  $\langle C_f \rangle$  upstream of the step. The laminar case reaches, however, a similar level downstream of the separation region, because laminar-to-turbulent transition is triggered within the separated shear layer.

Figure 3.41(b) shows the streamwise variation of the wall pressure. As we can see, upstream of the step, the wall pressure remains at almost the same level. The pressure ratio drops drastically by more than half of the initial values in the first half of the separation bubble due to the expansion and the less energetic recirculating flow. The wall pressure then continues decreasing slowly to its global minimum at  $x/\delta_0 = 4.6$ , corresponding to the relatively strong reversed flow in terms of  $\langle C_f \rangle$  in figure 3.41(a). As the boundary layer reattaches on the wall and undergoes compression, the wall pressure quickly returns to the initial level. In terms of the trend and relative variation, the current results are in a good agreement with the experimental work of Hartfield *et al.* [179]. In the laminar regime, the expansion fan is not as strong as for the turbulent case. Similarly,

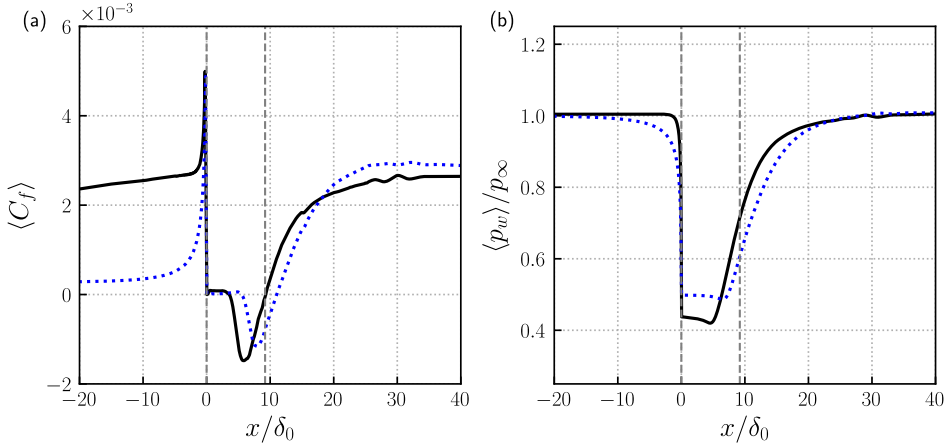


Figure 3.41: Streamwise variation of (a) skin friction and (b) wall pressure. The time- and spanwise-averaged values are indicated by the black solid lines (turbulent case BTB) and blue dotted lines (laminar case BZA). The vertical dashed line denotes the averaged separation and reattachment location for the turbulent case.

the intensity of the reattachment shock is weaker in the laminar case corresponding to a slower wall-pressure rise downstream.

### 3.5.2. UNSTEADY CHARACTERISTICS

The flow field over the BFS is highly unsteady, with vortices of various spatial scales observed in the visualization of figure 3.9. To characterize the regions of most prominent unsteadiness, the variance of the wall-normal velocity is provided in figure 3.42. As we can see, the most active region can be found along the separated shear layer (between the isoline of  $u = 0$  and boundary layer edge), especially in the proximity of the reattachment location with a maximum of approximately  $0.18u_\infty$  occurring at  $x/\delta_0 = 7.2$ ,  $y/\delta_0 = -2.2$ . These major fluctuations caused by the recompression have also been reported in previous experimental work [103]. Additionally, relatively weak fluctuations are found along the reattachment shock, reflecting its unsteady position. For the other normal Reynolds stress components  $\langle u'u' \rangle$  and  $\langle w'w' \rangle$ , high levels of fluctuations are similarly observed around the reattachment point. We see that the separated shear layer and shock wave system is highly unsteady over the BFS with similar fluctuation intensities as in other canonical SWBLI geometries [87, 99].

Our attention then is put on the zones of the shear layer, reattachment location and shock wave to scrutinize the dynamic motions by examining a number of snapshots of the instantaneous flow field. First of all, we take a closer look at the shear layer. Figure 3.43 displays the contours of the streamwise velocity and isolines of spanwise vorticity at two arbitrarily selected instants  $tu_\infty/\delta_0 = 1292, 1295$ . There are positive and negative streamwise velocity fluctuations alternating along the shear layer, which is the expected footprint of the K-H instability behind the step. The isolines of the spanwise vorticity show the roll-up of the vortex street. As the free shear flow evolves downstream, the instantaneous spanwise vorticity of the free shear layer becomes weaker due to the

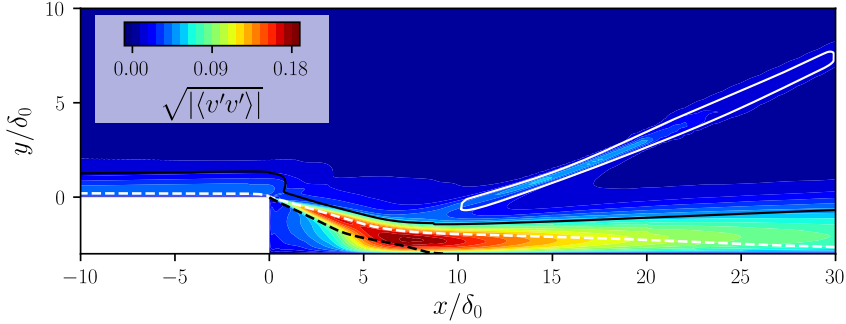


Figure 3.42: Contours of time- and spanwise-averaged variance of the wall-normal velocity for case BTB. The white dashed and solid lines denote the isolines of  $Ma = 1.0$  and  $|\nabla p| \delta_0 / p_\infty = 0.24$ . The black dashed and solid lines signify isolines of  $u = 0.0$  and  $u/u_e = 0.99$ .

attenuation of the K-H instability. However, these shedding vortices are not typical two-dimensional structures in the turbulent regime, as we observe in figure 3.9. For a BFS case, similar shedding vortices are observed both in subsonic and supersonic regimes [53, 180].

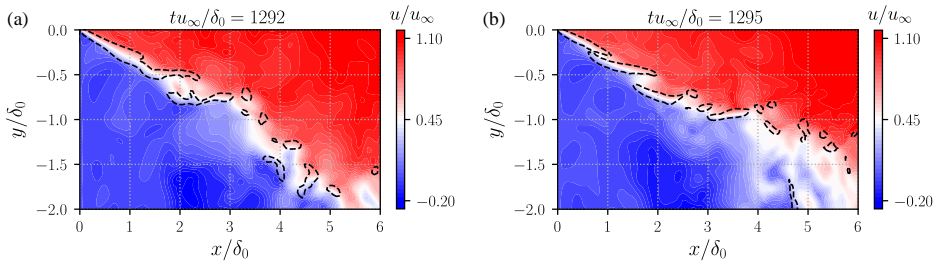


Figure 3.43: Contours of the instantaneous streamwise velocity for slice  $z = 0$  at (a)  $tu_\infty/\delta_0 = 1292$  and (b)  $tu_\infty/\delta_0 = 1295$  (case BTB). The black dashed lines signify the isolines of  $\omega_z \delta_0 / u_\infty = -3.6$ .

Figure 3.44(a) shows the contours of the instantaneous skin friction coefficient. Distinctly different features are observed in the different regions of the flow field. In the upstream turbulent boundary layer, the levels of  $C_f$  are homogeneously distributed and show clear evidence of the streamwise preferential orientation of the near-wall coherent structures. Figure 3.44(b) provides the weighted power spectral density of the streamwise wall shear stress for the spanwise wavenumber  $k_z$  at two stations. As we can see, the dominant wavenumber of the upstream structures ( $x/\delta_0 = -5.0$ ) is  $k_z \approx 2.0$ , corresponding to a spanwise wavelength  $\lambda_z \approx 0.5\delta_0$ . The shear stress is relatively uniform at a low level downstream of the step ( $0 < x/\delta_0 < 5.0$ ) due to the less energetic flow in this region. Shortly upstream of the mean reattachment location ( $5 < x/\delta_0 < 8.9$ ), there is significant reverse flow, cf. figure 3.41(a), and  $C_f$  indicates an increased spanwise length of the coherent structures. After reattachment, streamwise-

oriented features are observed in the skin friction maps that indicate large scale streaks with a spanwise alternation of high and low velocity. For example at  $x/\delta_0 = 10$ , the prevailing spanwise wavenumber of the streamwise skin friction is  $k_z \approx 0.35$  ( $\lambda_z = 2.9\delta_0$ ), as shown in figure 3.44(b). Further downstream, the distribution of  $C_f$  becomes more homogeneous again in the spanwise direction. Similar phenomena have been reported in previous experiments of BFS with a wide range of Mach number [104]. The up-wash and down-wash effects of the Görtler-like vortices are believed to induce the alternating low and high skin friction in the spanwise direction around the reattachment, as will be discussed in the following sections. The characteristic wavelength of these streaks is between  $\lambda_z = 2.0\delta_0$  and  $3.3\delta_0$ , which is consistent with previous experimental and numerical observations, reporting that the wavelength of these vortices is between two and three times the boundary layer thickness [97, 99, 104, 164].

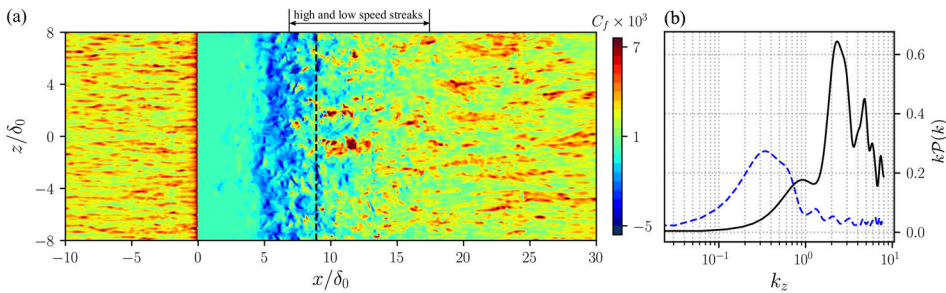


Figure 3.44: Contours of the instantaneous skin friction for the turbulent case BTB. The dashed line indicates the mean reattachment location. (b) weighted power spectral density of the skin friction over the spanwise wavenumber  $k_z$  (black line:  $x/\delta_0 = -5.0$ ; blue dashed line:  $x/\delta_0 = 10.0$ ).

In addition to these relatively local phenomena, a large-scale unsteady motion is identified in the interaction system, as shown by the instantaneous velocity fields at two instants in figure 3.45. These two instants represent different states of the separation bubble, i.e., expansion and shrinking. At  $tu_\infty/\delta_0 = 954.5$ , the length of separation bubble is around  $L_r/\delta_0 = 7.5$ , while the flow reattaches further downstream at about  $x/\delta_0 = 9.0$  when expanding at  $tu_\infty/\delta_0 = 1080$ . In addition, the position of the shock (marked as white isolines of  $|\nabla p|\delta_0/p_\infty = 0.4$ ) moves, most notably in the shock foot region. At  $tu_\infty/\delta_0 = 954.5$ , the shock foot locates somewhere between  $x/\delta_0 = 7.5 \sim 10.0$  and the shock angle is  $\eta = 22.2^\circ$ . At  $tu_\infty/\delta_0 = 1080$ , shock foot is between  $x/\delta_0 = 5.0 \sim 7.5$  and shock angle reduces to  $\eta = 16.8^\circ$ . It is clear from this comparison that the recirculation area and shock location vary in time.

For the laminar case, we also observe vortex shedding along the shear layer and the flapping motions of the shock [178]. However, there are notable differences in the near wall dynamics, as can be seen when comparing the instantaneous skin friction contours and the weighted power spectral density in figure 3.44 (turbulent case) with figure 3.46 (laminar case). The distribution of the skin friction is obviously spanwise uniform upstream of the step in the laminar case. As the separated shear layer undergoes laminar-to-turbulent transition, the skin friction contours develop weak two-dimensional features around the reattachment location and further downstream. The

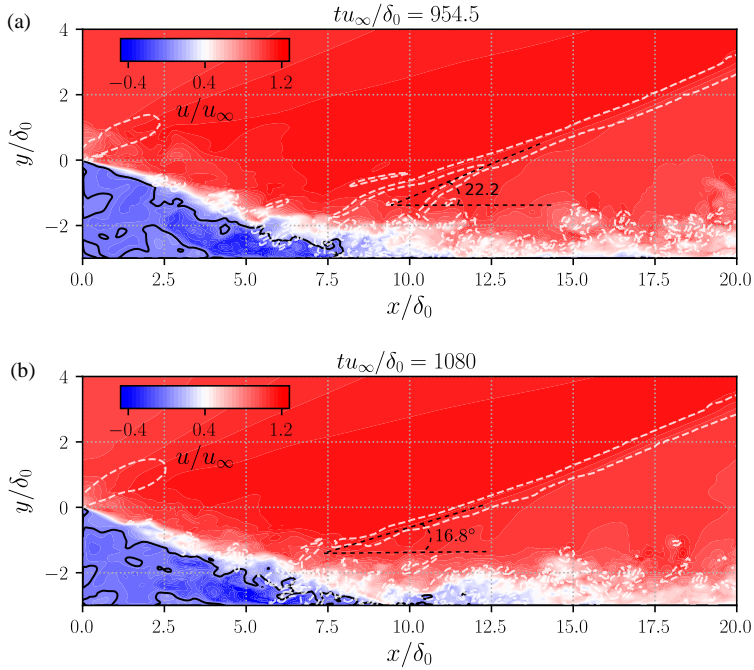


Figure 3.45: Contours of the instantaneous streamwise velocity for slice  $z = 0$  at (a)  $tu_\infty/\delta_0 = 954.5$  and (b)  $tu_\infty/\delta_0 = 1080$  (case BTB). Black solid line denotes the isoline of  $u = 0$  and white dashed line signifies the isoline of  $|\nabla p|\delta_0/p_\infty = 0.4$ .

dominant spanwise wavenumber near the reattachment location is  $k_z \approx 0.8$  ( $\lambda_z \approx 1.2\delta_0$ ). The large low- and high-speed streaks are not observed near the reattachment point in the laminar case ( $\lambda_z \approx 2.9\delta_0$  around the reattachment in the turbulent case). This difference suggests that there are probably no counter-rotating Görtler vortices in the laminar case.

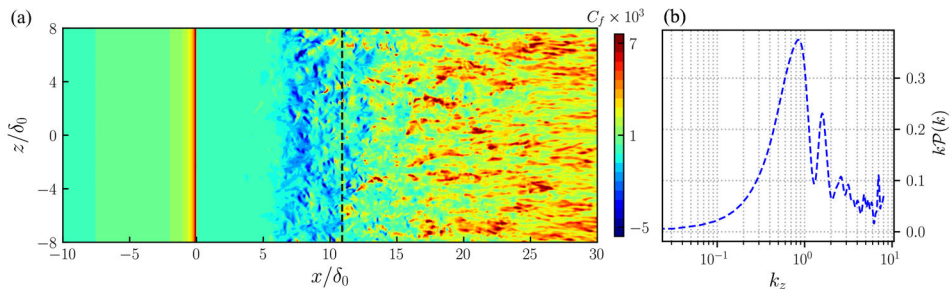


Figure 3.46: Contours of the instantaneous skin friction for the laminar case BZA. The dashed line indicates the mean reattachment location. (b) weighted power spectral density of the skin friction over the spanwise wavenumber  $k_z$  at  $x/\delta_0 = 10$ .

### 3.5.3. SPECTRAL ANALYSIS

An overview of frequency characteristics for the shock wave and separated boundary layer system is provided by the frequency weighted power spectral density of the wall pressure at selected streamwise locations in figure 3.47. The sampling interval is  $tu_\infty/\delta_0 = 950 \sim 1350$  with a sample frequency  $f_s\delta_0/u_\infty = 4$ . Welch's method with Hanning window was applied to compute the PSD using eight segments with 50% overlap (the same for the following PSD calculations). Upstream of the step ( $x/\delta_0 = -3.0$ ), the spectrum shows a broadband bump centred around  $St_\delta = f\delta_0/u_\infty = 0.8$ , which is close to the characteristic frequency ( $u_\infty/\delta$ ) of the upstream turbulent boundary layer [12]. Upstream of the step, the amplitude of the low-frequency content is very small, which demonstrates that the digital filter technique does not introduce significant spurious low-frequency features into the boundary layer. Downstream of the step, we observe broadband low-frequency content between  $St_\delta = 0.01 \sim 0.8$  ( $St_h = fh/u_\infty = 0.03 \sim 2.4$ ), in addition to the typical signature of boundary layer turbulence at the higher frequencies. Two significant low frequencies can be identified along the streamwise distance. The lower one is around  $St_\delta = 0.013$  (lower blue dashed line in the graph), which is most significant in a short distance behind the step ( $x/\delta_0 \leq 3.0$ ). It appears that this low frequency is not the dominant one further downstream of the separation bubble and a branch of intermediate frequencies at  $St_\delta = 0.1 \sim 0.3$  (upper region marked by green dashed lines) begins to take the lead up to  $x/\delta_0 = 20.0$ . In the traditional ramp and impinging shock cases [85, 99, 181], the medium-frequency shear-layer oscillations arise after the separation and the downstream propagation of this dynamics affects the reflected-shock dynamics at intermediate frequencies, while the interaction between separation shock and boundary layer exhibits the low-frequency behaviour. The medium frequency motions of the present BFS case are probably related to the shear-layer instability, the downstream advection of which produces a significant medium-frequency unsteadiness around the reattachment location ( $x/\delta_0 = 9.25$ ). The low-frequency contents of our BFS case are likely connected to the interactions of the reattachment shock and the separation bubble, the feedback of which leads to the low-frequency peak immediately downstream of the step ( $x/\delta_0 = 1.0$ ).

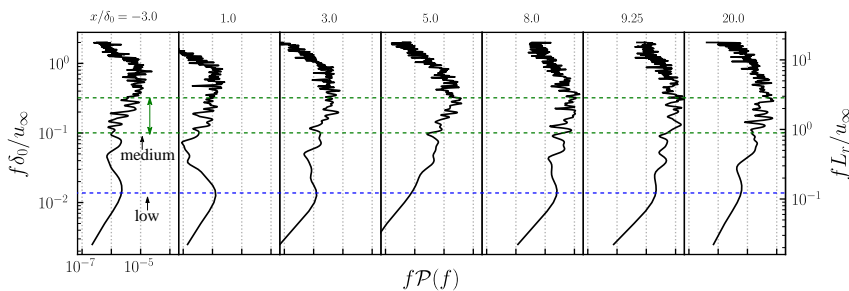


Figure 3.47: Frequency weighted power spectral density of the wall pressure with the streamwise distance for case BTB.

To further confirm this conjecture, several aerodynamic parameters are extracted from the current results. For the medium-frequency behaviour, the temporal variation

of the streamwise velocity within the separated shear layer and the spanwise-averaged reattachment position are plotted in figure 3.48. These data are extracted with the same sampling frequency as the aforementioned pressure signal. The location of the spanwise-averaged reattachment point  $x_r$  is obtained as follows: the isolines of the streamwise velocity  $u = 0$  are collected at each time step; and in each spanwise plane the most downstream position meeting this condition ( $u = 0$ ) is determined as the instantaneous value of  $x_r$ . An unsteady motion at a frequency around  $St_\delta = 0.2$  ( $St_h = 0.6$ ) appears energetically dominant for both shear layer velocity and reattachment location, which is more clear in the spectra of figure 3.48. This medium frequency is the characteristic frequency of the shedding vortices within the shear layer. These vortices are shedding downstream as the shear layer and pass through the reattachment downstream of the bubble, which explains that a similar frequency is observed in the spectrum of the reattachment location. There are also less energetic peaks at lower frequencies around  $St_\delta = 0.03$ , which will be discussed in the next paragraph. When taking a closer look on a short interval in figure 3.49, the velocity signal of the shear layer is more periodic and regular. In contrast, the curve for the reattachment point follows a more sawtooth-like trajectory, along which its value undergoes a sharp drop when the reattachment point moves upstream, while it experiences a less rapid relaxation as the reattachment location shifts downstream, for instance around  $tu_\infty/\delta_0 = 1160$ . The sawtooth-like behaviour was also reported for incident shock and ramp cases [99, 164], and is attributed to the passage of shedding vortices formed in the shear layer near the reattachment.

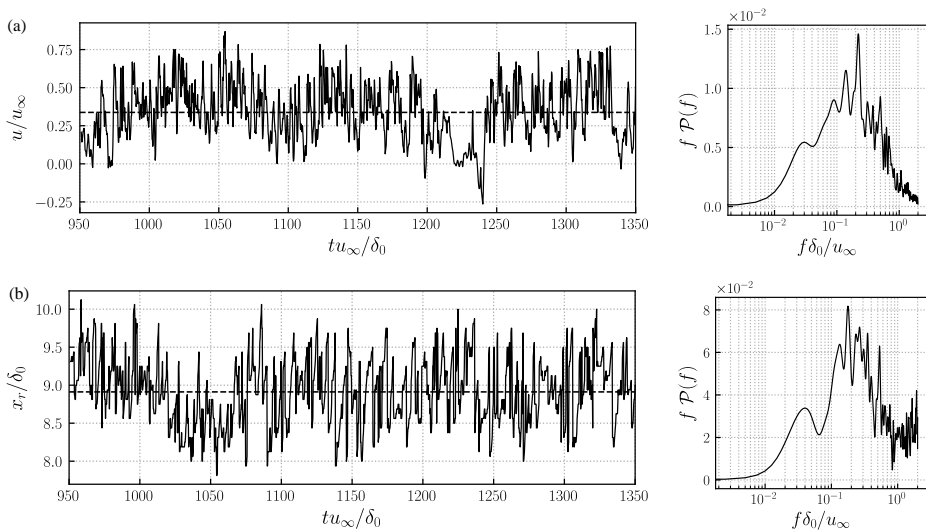


Figure 3.48: Temporal evolution and corresponding frequency weighted power spectral density of (a) streamwise velocity within the shear layer at  $x/\delta_0 = 3.0625$ ,  $y/\delta_0 = -1.0625$  and (b) the spanwise-averaged reattachment location (case BTB). The black dashed line signifies the mean value.

With regard to the global dynamics, the temporal variation of the spanwise-averaged

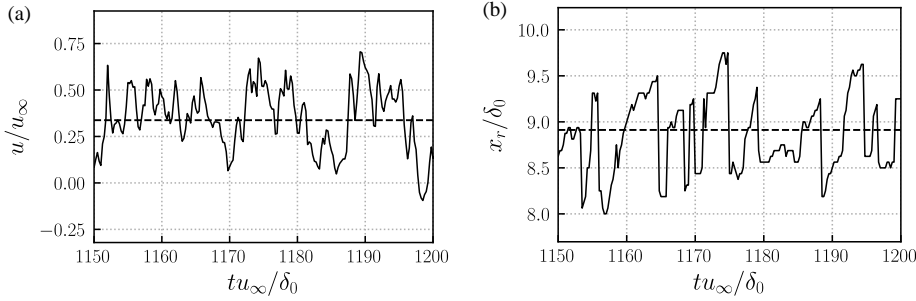


Figure 3.49: Details of figure 3.48 showing temporal evolution of (a) streamwise velocity within the shear layer at  $x/\delta_0 = 3.0625, y/\delta_0 = -1.0625$  and (b) the spanwise-averaged reattachment location in a shorter period (case BTB). The black dashed lines signify the mean values.

reattachment shock angle and volume of the separation bubble are shown in figure 3.50. The volume of bubble per unit spanwise length is defined as the area between the isoline of  $u = 0$  and the bottom wall. The shock angle is determined based on the pressure gradient outside the boundary layer by fitting the isolines of  $|\nabla p|\delta_0/p_\infty = 0.24$ . We obtain two  $x$  values by intersecting the isolines of  $|\nabla p|\delta_0/p_\infty = 0.24$  at  $y/\delta_0 = 0.5$  and then take the average of these two  $x$  values as the first streamwise coordinate of the shock position. A second point of the shock position is obtained by repeating the same operation at  $y/\delta_0 = 5.0$ . A straight line is fitted based on these two points and the angle between the fitting line and the  $x$ -direction is considered as the shock angle. Both curves of the separation bubble size and shock angle are irregular and aperiodic in time, which suggests that the unsteady motion involves a range of time scales, cf. Refs [98, 182]. For the signal of the volume of the separation bubble, shown in figure 3.50(a), there is a significant low-frequency peak at  $St_\delta = 0.023$  in the spectrum. It indicates that the bubble expands and shrinks with a frequency whose value is about two-order lower than the frequency of the typical turbulence. The spectrum of the shock angle also displays a peak at  $St_\delta = 0.023$ , see figure 3.50(b), which is much more pronounced than the peak observed for the reattachment location at the same frequency in figure 3.48(b). In addition, there is a second frequency peak around  $St_\delta = 0.13$ , which corresponds to the dominant frequency in the spectrum of reattachment location. Since the shock is formed by the compression waves originating at reattachment, spectra for the shock and reattachment locations include peaks at common frequencies.

The statistical connection between the low-frequency signals can be quantified through coherence  $C_{xy}$  and phase  $\theta_{xy}$ . The spectral coherence  $C_{xy}$  between two temporal signals  $x(t)$  and  $y(t)$  is defined as

$$C_{xy}(f) = |P_{xy}(f)|^2 / (P_{xx}(f)P_{yy}(f)), 0 \leq C_{xy} \leq 1, \quad (3.7)$$

where  $P_{xx}$  is the power spectral density of  $x(t)$  and  $P_{xy}(f)$  represents the cross-power spectral density between signals  $x(t)$  and  $y(t)$ . The phase  $\theta_{xy}$  is determined by

$$\theta_{xy}(f) = \Im(P_{xy}(f)) / \Re(P_{xy}(f)), -\pi < \theta_{xy} \leq \pi. \quad (3.8)$$

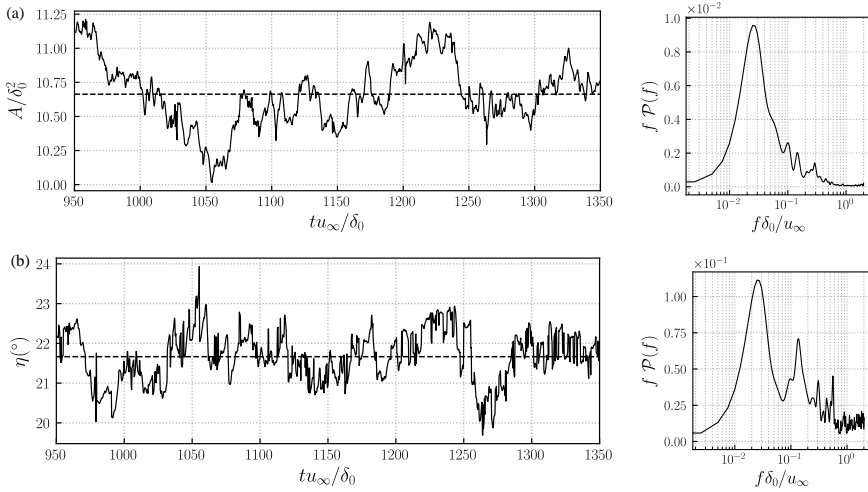


Figure 3.50: Temporal evolution and corresponding frequency weighted power spectral density of spanwise-averaged (a) bubble volume per unit spanwise length  $A$  and (b) shock angle  $\eta$  (case BTB). The black dashed line signifies the mean value.

For a specific frequency, if  $0 < C_{xy} < 1$ , it means that there is noise in the datasets or the relation between these two signals is not linear. When  $C_{xy}$  equals to 1, it indicates that the signals  $x(t)$  and  $y(t)$  are linearly related, and  $C_{xy} = 0$  signifies that they are completely unrelated.

The coherence and phase between the spanwise-averaged separation bubble size and shock location are shown in figure 3.51. A high value of coherence ( $C = 0.42$ ) is observed at the frequency  $St_\delta = 0.028$ , which manifests that the separation bubble and reattachment shock are nonlinearly related to each other around the low frequency observed in the spectrum of figure 3.50. Moreover, these two signals are approximately in phase, as can be seen from the low level of  $\theta$ . The above observations provide evidence that the unsteady low-frequency behaviour is related to the breathing of the separation bubble and the flapping motion of the shock, while the medium-frequency motions are associated with the shedding vortices of the shear layer. Thus a decoupling of the frequency scales is required to further trace the sustained source of the intrinsic unsteadiness of the interaction, which is the objective of section 3.5.4.

Similar low- and medium-frequency are also observed for the laminar cases. Figure 3.52 plots the corresponding frequency weighted power spectral density of streamwise velocity around the mean reattachment location and the spanwise-averaged separation bubble size. To compare the laminar and turbulent cases, the frequency is rescaled by the reattachment length as  $St_r = fL_r/u_\infty$ . For the signal of streamwise velocity in figure 3.52(a), the results show a broadband low-frequency spectrum for both the laminar and turbulence cases. However, a local spectrum peak is clearly observed at  $St_r = 0.15$  ( $St_\delta = 0.017$ ) in the turbulent case and at  $St_r = 0.20$  ( $St_\delta = 0.018$ ) for the laminar case. Since there are distinct shedding vortices in the shear layer for both flow

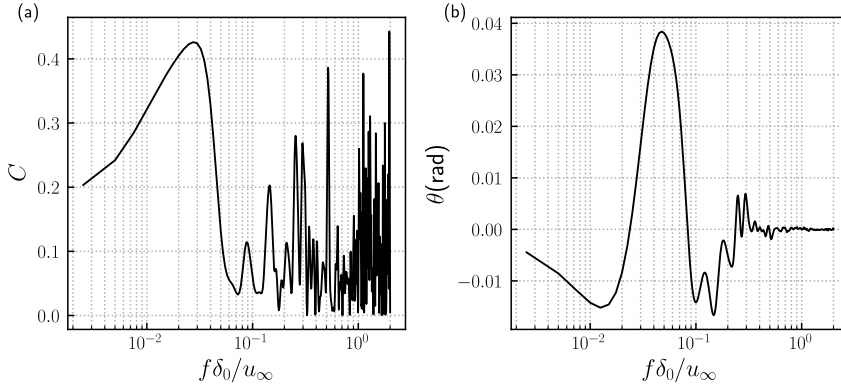


Figure 3.51: Statistical relation between the spanwise-averaged reattachment point and the area of separation bubble: (a) coherence and (b) phase (case BTB).

regimes, the relevant prevailing medium frequencies are close to each other. For the bubble size in figure 3.52(b), the dominant frequency of the separation bubble in the laminar case is  $St_r = 0.33$ , while the corresponding value is lower ( $St_r = 0.22$ ) in the turbulent case. These differences suggest that there are probably other flow dynamics involved, which leads to a lower frequency of the unsteady motions in the turbulent case. As previously discussed, Görtler-like vortices are likely to be associated with the low-frequency unsteadiness of SWBLI [98]. Therefore, we infer that the streamwise streaks in the turbulent regime may play a role in the transformation of the dominant low frequency.

### 3.5.4. DMD ANALYSIS OF THE THREE-DIMENSIONAL FLOW FIELD

To better separate the different dynamics from the coupled broadband frequency spectrum, a frequency-orthogonal modal decomposition of the three-dimensional flow field is conducted based on DMD, the details of which has been described in chapter 2. In the above analysis, we identified two types of unsteady behaviour at different frequencies. However, part of the signals was extracted from the spanwise-averaged field, like reattachment location, bubble size and shock angle; thus spanwise unsteady features may be missing from the two-dimensional flow field and a three-dimensional DMD analysis is required. Considering the large size of the data ensemble, a spatial subdomain ( $-5.0 \leq x/\delta_0 \leq 20.0$  and  $-3.0 \leq y/\delta_0 \leq 5.0$ , covering the most interesting region) is extracted with a downsampled spatial resolution in all directions. The present DMD analysis of the three-dimensional subdomain is carried out based on 1200 equal-interval snapshots with the same temporal range of the previous signals and a smaller sampling frequency  $f_s\delta_0/u_\infty = 2$  as the frequencies above the characteristic frequency of the turbulent integral scale  $u_\infty/\delta_0$  are not of our current interest. The resulting frequency resolution is  $1.67 \times 10^{-3} \leq St_\delta \leq 1$ . Figure 3.53(a) shows the calculated eigenvalue spectrum provided by the standard DMD. The obtained modes appear as complex conjugate pairs and most of them are well distributed along the unit circle  $|\mu_k| = 1$  except

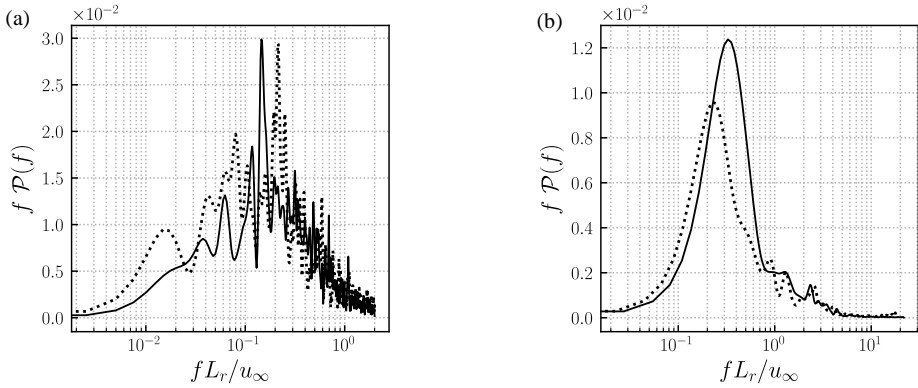


Figure 3.52: Frequency weighted power spectral density of (a) streamwise velocity around the mean reattachment location and (b) spanwise-averaged bubble volume per unit length  $A$  (case BTB). The black solid line is the laminar case BZA and dotted line represents the turbulent case BTB.

Table 3.4: Information of the selected modes

Mode	$St_\delta$	$ \psi_k $	$\beta_k$
$\phi_1$	0.02151	0.42644	-0.026404
$\phi_2$	0.07546	0.29303	-0.007900
$\phi_3$	0.59361	0.80066	-0.009204

a few decaying modes within the circle, which means the resulting modes are saturated [167]. The magnitudes of the corresponding DMD modes are shown in figure 3.53(b) for the positive frequencies and gray shaded by the growth rate  $\beta_k$ . Here, the strongly decaying modes ( $|\mu_k| \leq 0.95$ ) have been removed, as they do not contribute to the long-time flow evolution. The darker the vertical lines are, the less decayed the modes are. The convergence of the DMD results was verified by repeating the DMD using 400 snapshots less, which confirmed that the current DMD results are well-converged with respect to the number of the snapshots.

From the frequency-magnitude spectrum, we identified three interesting frequencies, a lower one (marked as A) with  $St_\delta < 0.06$ , a medium one (marked as B) with  $0.06 \leq St_\delta \leq 0.2$ , and a higher one (marked as C) with  $St_\delta > 0.2$ . Based on the growth rate and magnitudes of the modes, three modes are selected from the frequency spectrum, one representative for each of the frequency ranges, labelled as mode  $\phi_1$ ,  $\phi_2$  and  $\phi_3$ . Table 3.4 provides the frequency, magnitudes and growth rate of these modes. All these modes have comparatively large magnitudes with  $|\psi_k| > 0.1$ . At the same time, these modes are the relatively darker ones in figure 3.53(b) with decay rate  $|\beta_k| < 0.03$ , which suggests that their effects play a role during the entire process.

For the branch with lower frequencies, mode  $\phi_1$  has been selected to illustrate the flow dynamics. Figure 3.54 shows the real part of the selected mode  $\phi_1$  with the isosur-

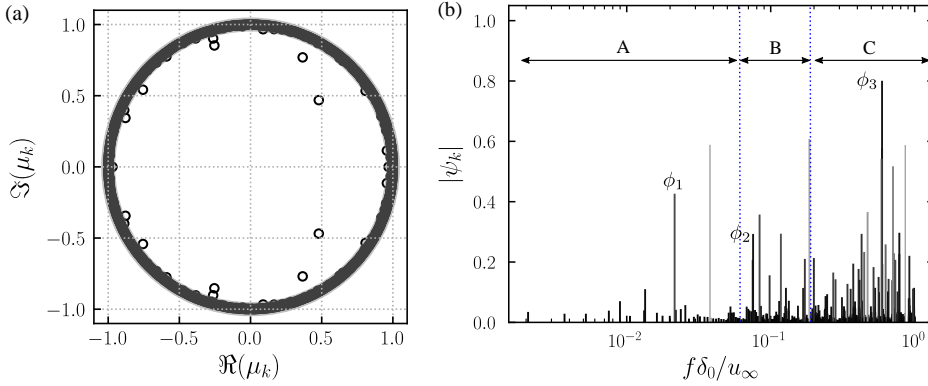


Figure 3.53: (a) Eigenvalue spectrum from the standard DMD and (b) normalized magnitudes for DMD modes with positive frequency, coloured by the growth rate  $\beta_k$  (case BTB).

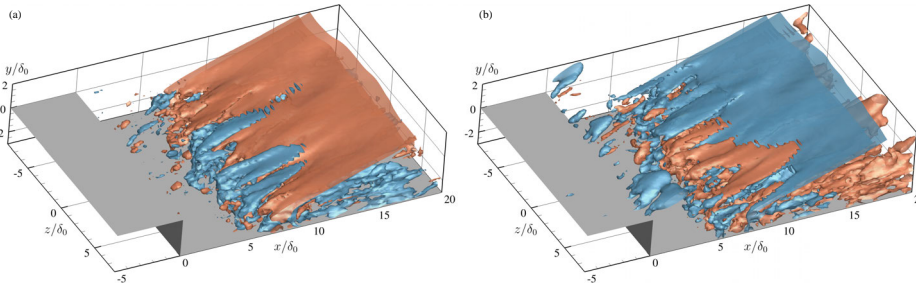
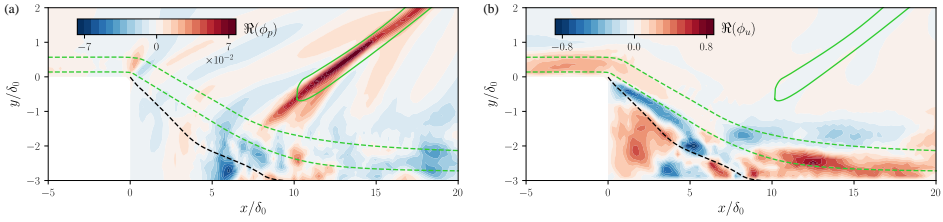


Figure 3.54: Isosurfaces of the pressure fluctuations from DMD mode  $\phi_1$  with phase angle (a)  $\theta = \pi/2$  and (b)  $\theta = 7\pi/4$  for case BTB, only including the real part (red:  $p'/p_\infty = 0.02$ , blue:  $p'/p_\infty = -0.02$ ).

faces of the pressure fluctuations at phase angle  $\theta = \pi/2$  and  $7\pi/4$ . At both instants, the key features of this mode from the pressure signals are the significant structures along the shock and compression waves caused by the reattachment. Additionally, the fluctuations around the shock and reattachment are three dimensional, and indicate a slight wrinkling of the shock. Comparing the modal fluctuations at these two phases, the sign switch between them describes the oscillation of the reattachment shock. Figure 3.55(a) provides the pressure fluctuations at the slice  $z = 0$ , in which the effect that mode  $\phi_1$  has on shock and compression waves is more clear. Note that perturbations in the upstream turbulent boundary layer are too weak to be visible at the given levels ( $|p'/p_\infty| = 0.01$ ) of isosurfaces and in the contours.

In figure 3.56, the fluctuations of the streamwise velocity component from DMD mode  $\phi_1$  (at the slice  $z = 0$ ) are given. As we can see, large fluctuations are aligned with the streamwise direction with negative and positive values alternating in the spanwise direction. These longitudinal structures appear to start within the fore part of the free shear layer and extend beyond the reattachment location. Additionally, they are mainly located in the near-wall part of the boundary layer, as shown by the streamwise velocity



3

Figure 3.55: Real part of DMD mode  $\phi_1$  indicating contours of modal (a) pressure fluctuations and (b) streamwise velocity fluctuations on the slice  $z = 0$  (case BTB). The green solid line indicates the mean reattachment shock. The dashed line signifies the dividing line. The green dashed lines represent the streamlines passing through  $x/\delta_0 = 0, y/\delta_0 = 0.125$  and  $x/\delta_0 = 0, y/\delta_0 = 0.5625$ .

fluctuations in figure 3.55(b). We also superimpose the modal fluctuations (with the optional amplification factor  $a_f = 1.0$ ) onto the mean flow and plot the contours of streamwise velocity in the  $x - z$  slice at  $y/\delta_0 = -2.875$  in figure 3.57. The high- and low-speed streaks are obvious in the contours and show very similar features as the contours of skin friction in figure 3.44. Other low-frequency modes between  $St_\delta = 0.008 \sim 0.05$  have been also examined, and they all share common structures with mode  $\phi_1$ . The pressure and velocity fluctuations of DMD mode  $\phi_1$  suggest that the low-frequency flapping motion of the shock is coupled with streamwise-elongated structures in the interaction region.

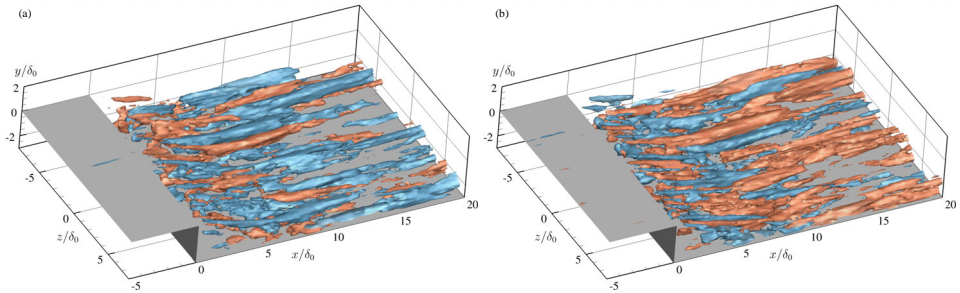


Figure 3.56: Isosurfaces of the streamwise velocity fluctuations from DMD mode  $\phi_1$  with phase angle (a)  $\theta = \pi/2$  and (b)  $\theta = 7\pi/4$  for case BTB, only including the real part (red:  $u'/u_\infty = 0.42$ , blue:  $u'/u_\infty = -0.42$ ).

These spanwise-aligned structures are the signature of counter-rotating Görtler-like vortices, as shown by the contours of modal streamwise vorticity in figure 3.58. The location and strength of these vortex pairs are changing with the phase angles. At the given instants ( $\theta = 0$  and  $\theta = 5\pi/8$ ), the spanwise wavelength of the vortex pair is ranging from  $1.9\delta_0$  to  $1.6\delta_0$ . The instantaneous snapshots of the reconstructed flow field from  $\phi_1$  shows the flapping motion of the reattachment shock, i.e., the displacement of the shock around its mean shock location. The counter-rotating Görtler vortices are also unsteady in terms of their strength. Additionally, figure 3.58 indicates that these vortices can move in both the spanwise and wall-normal directions.

For mode  $\phi_2$ , the pressure isosurfaces in figure 3.59 show high levels of fluctuations

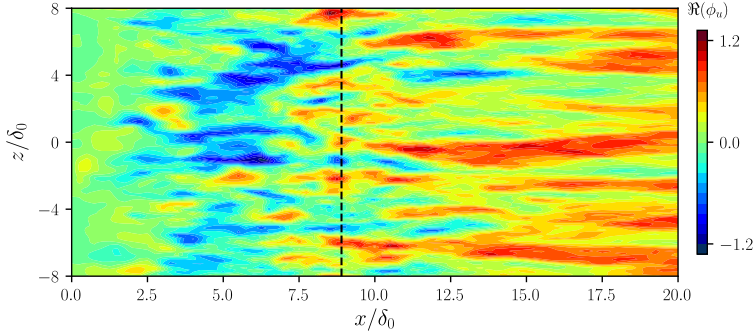


Figure 3.57: Contours of the reconstructed streamwise velocity from DMD mode  $\phi_1$  in the  $x-z$  plane at  $y/\delta_0 = -2.875$ .

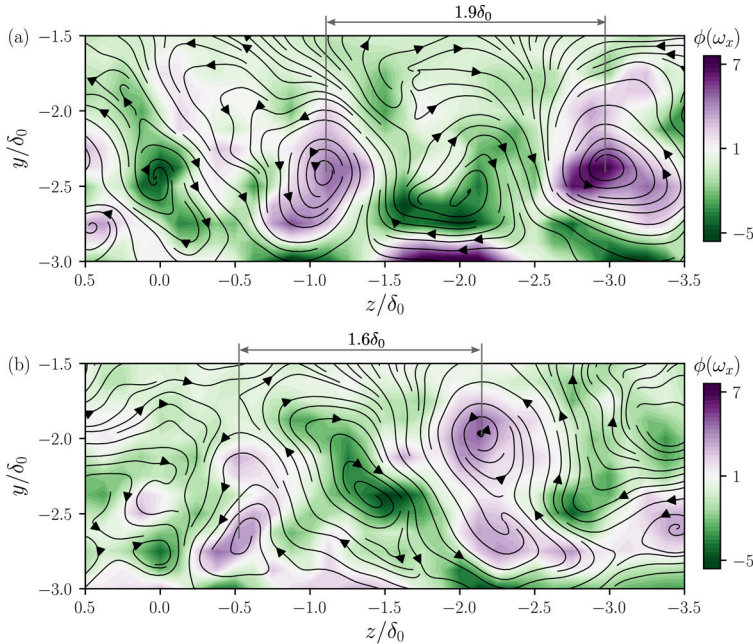


Figure 3.58: Contours of the streamwise vorticity from DMD mode  $\phi_1$  with phase angle (a)  $\theta = 0$  and (b)  $\theta = 5\pi/8$  in the  $z-y$  plane at  $x/\delta_0 = 10$ . Black arrow lines represent the streamlines on the slice.

along the reattachment shock, but the three-dimensional features are stronger compared to mode  $\phi_1$ . Positive and negative fluctuations are alternating in both spanwise and wall-normal directions, which represents a propagation of waves from the shear layer and outwards along the shock. The radiation of the Mach waves is in agreement with the results from a global linear stability analysis of an impinging shock case in laminar regime [183]. The emission of these waves induces large disturbances along the

streamwise direction in the supersonic part of the flow field. In the contours of modal spanwise-averaged pressure fluctuations in figure 3.61, the radiation of the waves along the streamwise direction and shock is easier to observe.

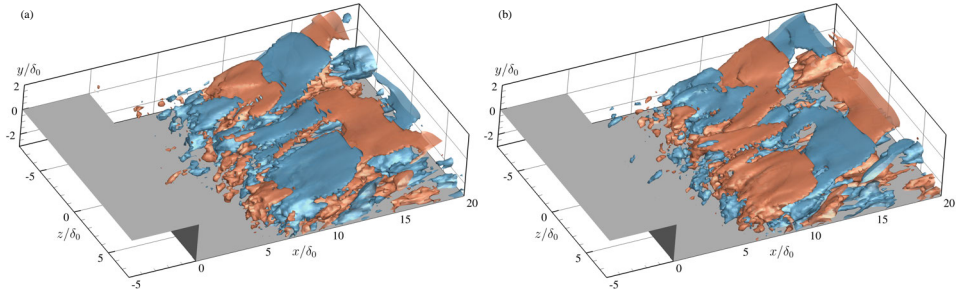


Figure 3.59: Isosurfaces of the pressure fluctuations from DMD mode  $\phi_2$  with phase angle (a)  $\theta = 0$  and (b)  $\theta = 3\pi/4$  for case BTB, only including the real part (red:  $p'/p_\infty = 0.02$ , blue:  $p'/p_\infty = -0.02$ ).

Considering the fluctuations of the streamwise velocity, shown in figure 3.60, smaller longitudinal vortical structures are observed, compared to mode  $\phi_1$ . These vortices alternate along both the spanwise and streamwise directions, and are mainly concentrated within the boundary layer. Clearly, this mode represents the convection of the shear layer vortices and the induced Mach waves in the supersonic part of the flow field, which can also be seen in the contours of modal spanwise-averaged streamwise velocity in figure 3.61 (b). Similar observations were also reported in the two-dimensional DMD analysis of an incident shock case [99].

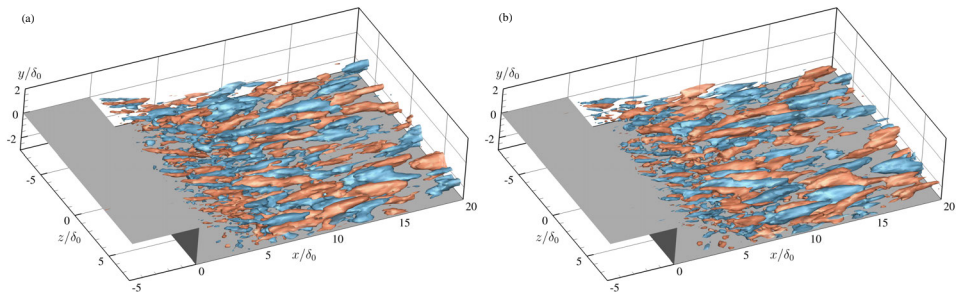


Figure 3.60: Isosurfaces of the streamwise velocity fluctuations from DMD mode  $\phi_2$  with phase angle (a)  $\theta = 0$  and (b)  $\theta = 3\pi/4$  for case BTB, only including the real part (red:  $u'/u_\infty = 0.3$ , blue:  $u'/u_\infty = -0.3$ ).

The higher frequency modes, branch C, are related to the small-scale turbulent dynamics. For example for mode  $\phi_3$ , pressure fluctuations in figure 3.62 show small highly three-dimensional arc-shaped vortices. These spanwise-aligned vortices are generated from the downstream part of the shear layer. The streamwise displacement of the fluctuations contours at different phase angles indicates the convection of the coherent vortices.

The convection behavior of this mode is also evident from isosurfaces of the streamwise velocity fluctuations, shown in figure 3.63. The velocity fluctuations originate from

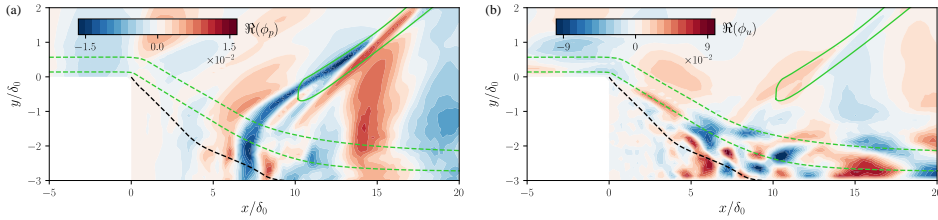


Figure 3.61: Real part of DMD mode  $\phi_2$  indicating contours of modal spanwise-averaged (a) pressure fluctuations and (b) streamwise velocity fluctuations (case BTB). The green solid line indicates the mean reattachment shock. The dashed line signifies the dividing line. The green dashed lines represent the streamlines passing through  $x/\delta_0 = 0, y/\delta_0 = 0.125$  and  $x/\delta_0 = 0, y/\delta_0 = 0.5625$ .

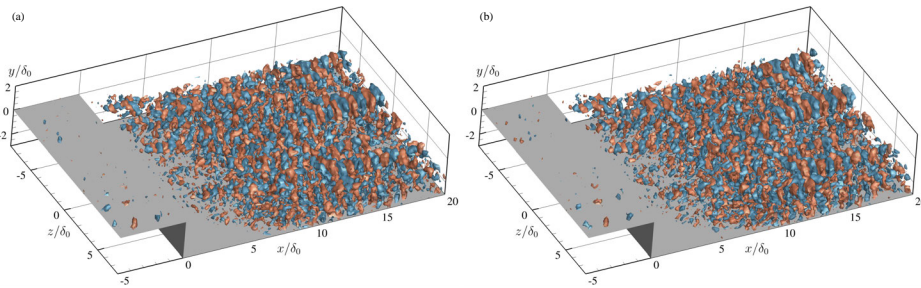


Figure 3.62: Isosurfaces of the pressure fluctuations from DMD mode  $\phi_3$  with phase angle (a)  $\theta = 0$  and (b)  $\theta = 3\pi/8$  for case BTB, only including the real part (red:  $p'/p_\infty = 0.06$ , blue:  $p'/p_\infty = -0.06$ ).

the strong shear layer behind the step. It is also noticed that these fluctuations are distributed along the free shear layer and downstream boundary layer. Additionally, this mode shows less anisotropic features, compared with the other two modes. The frequency of this mode is close to the typical frequency of the turbulence considering the thicker boundary layer downstream of the step. Thus, we consider this mode to be related to the convection of typical turbulent structures that result from an amplification of the incoming turbulence by the separation bubble, cf. the stability analysis of Guiho *et al.* [183] for an incident shock SWBLI case.

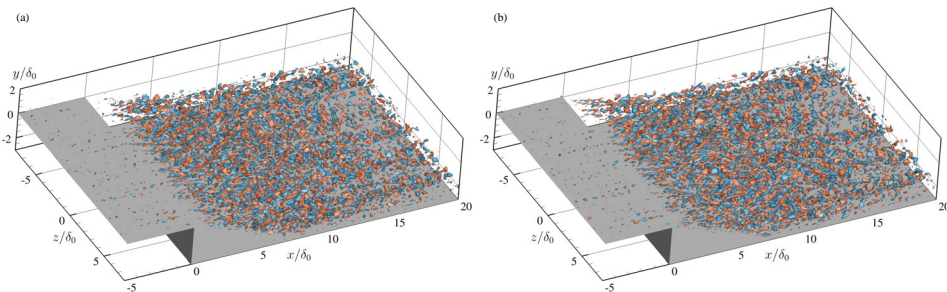


Figure 3.63: Isosurfaces of the streamwise velocity fluctuations from DMD mode  $\phi_3$  with phase angle (a)  $\theta = 0$  and (b)  $\theta = 3\pi/8$  at slice  $z = 0$  for case BTB, only including the real part (red:  $u'/u_\infty = 0.6$ , blue:  $u'/u_\infty = -0.6$ ).

Similarly, the DMD modes from the two-dimensional analysis for the laminar case are also divided into three branches [178]. The branch with higher frequencies centred at  $f\delta_0/u_\infty \approx 0.1$  is associated with the shedding of large coherent shear vortices, which is also observed in the present turbulent case. The other two branches with lower frequencies are related to the unsteady motions of the separation bubble and the shock. In contrast to the turbulent case, we found no evidence of Görtler-like vortices in the laminar case.

## 3

### 3.5.5. PHYSICAL MECHANISM OF LOW-FREQUENCY UNSTEADINESS

The current BFS case shows similar unsteady motions as those usually observed for SWBLI on flat plates and on compression ramps. Compared with these cases, however, the flow topology of the present case shows significantly different features. In canonical impinging shock and ramp cases, the separation bubble is enclosed by a separation shock and reattachment shock. In contrast, the recirculation region in a BFS case is surrounded by the step expansion fan, and reattachment shock. In terms of the mean skin friction, the recirculating flow is usually less uniform downstream of the mean separation position and recovers slower in the ramp and incident shock cases [99, 164]. The fluctuations of  $\langle C_f \rangle$  inside the separation bubble in these cases are usually related to the low-frequency unsteadiness. In the current case, however, the skin friction (figure 3.41) is relatively uniform in the fore part of the bubble, which is caused by the ‘dead-air’ region close to the stationary step wall. The wall pressure is usually increasing throughout the separation bubble in the ramp and incident shock cases [164, 176]. In the current case, the pressure drastically drops at the step and keeps a relatively steady low level in the separation bubble, which is typical for strong interactions. These differences may suggest different low-frequency features between these cases. To compare with other canonical SWBLI cases, the dimensional frequencies are rescaled based on the separation length  $L_r$  as  $St_r = fL_r/u_\infty$  in the following discussion.

The instantaneous visualizations displayed in section 3.5.2 illustrate both relatively localized and global unsteady motions in the flow field, involving high and low speed streaks, breathing bubble and oscillating reattachment shock, as well as vortex shedding in the separated shear layer. A linear stability analysis of the mean flow shows that the most unstable global mode is mainly distributed along the dividing line ( $u = 0$ ), especially around the reattachment location [183]. The RMS wall-normal velocity in figure 3.42 is consistent with this observation. The spectral analysis in section 3.5.3 reveals that there are two kinds of low-frequency unsteadiness in the interaction region and the lower frequency around  $St_r = 0.2$  ( $St_\delta = 0.023$ ) is associated with the coupling of separation bubble and reattachment shock wave. Furthermore, the three-dimensional DMD analysis separates the different dynamics contributing to low-frequency interaction. Apart from the unsteady separation bubble and reattachment shock, the low-frequency mode  $\phi_1$  also reveals the unsteady Görtler-like vortices, see figure 3.58. Although these Görtler vortices are rather weak compared to other energetic dynamics such that they are hard to identify in the vortical visualization in figure 3.9, the skin friction contours in figure 3.44 capture the footprint of the associated high- and low-speed streaks.

These observations share qualitative similarities to the low-frequency DMD modes

calculated by Priebe *et al.* [98]. In their ramp case, the fluctuations of the low-frequency mode clearly show shocks (mainly separation shock) and longitudinal Görtler vortices near the reattachment. In the impinging shock case of Pasquariello *et al.* [99], both the visualization of streamwise vorticity and the DMD analysis of the skin friction support the finding of the Görtler vortices downstream of the reattachment location. Both report that the frequency of this unsteadiness is between  $0.01 < St_r < 0.2$ , while the current results for a BFS correspond to a Strouhal number range of  $0.027 \leq St_r \leq 0.54$  ( $0.003 \leq St_\delta \leq 0.06$  in the DMD analysis), which is about three times larger than the values of other canonical cases.

We believe that the higher frequency in the current case is caused by the fixed separation location and confinement by the step wall. In the ramp and impinging shock cases, the recirculation region can move from both separation and reattachment sides. By comparison, the current case can only move in the reattachment part due to the limitation of the step, and it is reasonable to assume that this leads to a smaller oscillation amplitude and correspondingly to a higher frequency. This explanation is supported by the temporal evolution of the reattachment point. In figure 3.49(b), the calculated minimum, mean and maximum reattachment location are  $x_r/\delta_0 = 8.3, 8.9$  and  $10.2$ , which leads to an oscillation range of about  $15\%L_r$ . For ramp cases, oscillations of up to  $70\%L_r$  have been reported [164]. Moreover, the separation length is around three times the maximum separation height ( $L_r = 3h$ , the maximum separation height equals to the step height) in our BFS case, whereas the recirculating flow regions are typically much thinner in ramp and impinging shock cases. Estruch-Samper and Chandola [116] proposed an entrainment-recharge mechanism to associate the low-frequency unsteadiness with the shedding effects. In this theory, the Strouhal number of the low-frequency breathing can be related to the entrainment frequency by

$$St_r^{\text{low}} = \pi \alpha_\epsilon \xi_B \delta'^2 \frac{L_r}{h} (X_r^{\text{ent}})^2 St_r^{\text{ent}} \approx C_\epsilon \frac{L_r}{h} (X_r^{\text{ent}})^2 St_r^{\text{ent}}, \quad (3.9)$$

where  $\alpha_\epsilon$  is the length-to-thickness ratio of the shedding coherent structures;  $\xi_B$  represents the percentage of the entrainment mass and  $\delta'$  is the spreading rate of the mixing layer. Huang and Estruch-Samper [184] showed that the variations of these three parameters between different cases are small if the incoming flow conditions are close, which results in an approximate constant  $C_\epsilon \approx 0.08$ . The ratio of the bubble length to bubble height  $L_r/h$  and the dimensionless entrainment length  $X_r^{\text{ent}}$  depend on the specific geometry. In a similar entrainment and injection model by Piponniau *et al.* [94], they consider the entrainment usually only occurs in the rear half of the separation bubble, i.e., the downward part of the shear layer, which leads to a dimensionless entrainment length  $X_r^{\text{ent}} \approx 0.5$  in the impinging shock and ramp cases. The geometry dependent transformation factor is  $C^{\text{ent}} = (X_r^{\text{ent}})^2 L_r/h \approx 1.5$  for these canonical cases. In the current BFS case, the entrainment length  $X_r^{\text{ent}}$  is one, which gives the transform factor  $C^{\text{ent}} \approx 3$ . The entrainment frequencies  $St_r^{\text{ent}}$  of the shear layer shedding behaviour are similar for all these cases; thus the BFS case will yield about two times larger  $St_r^{\text{low}}$  than the impinging shock and ramp cases. However, this model only provides an estimate of the low frequency, and we do not expect to obtain an accurate value.

Several works in the literature have found evidence of Görtler-like vortices in SWBLI. Görtler vortices typically have a spanwise length-scale in the order of the incoming

boundary layer thickness [185]. The Görtler number, defined as,

$$G_t = \frac{\theta^{3/2}}{0.18\delta^*|R|^{1/2}}, \quad (3.10)$$

gives an indication on whether such vortices can form [78], where  $R$  is the radius of curvature of the streamline,  $\delta^*$  is the boundary layer displacement thickness and  $\theta$  is the boundary layer momentum thickness. Figure 3.64 shows the curvature  $\delta/R$  and Görtler number  $G_t$  along two streamlines of the mean flow inside the shear layer (shown in figure 3.55 and figure 3.61). Streamline 1 is closer to the wall and passes through the coordinate  $x/\delta_0 = 0$  and  $y/\delta_0 = 0.125$ . Significantly large streamline curvature occurs at the separation point and around the reattachment. Correspondingly, two distinct peaks are observed at these locations. The large curvature and Görtler number at the separation is mainly caused by the sudden change of the geometry at the step edge. In a laminar flow, the critical Görtler number is around  $G_t = 0.6$  (marked as gray dot-dashed line) for a wide range of  $Re$ , above which the flow exhibits significant centrifugal instability and local Görtler vortices will emerge inside the boundary layer [78]. We see that the Görtler number is larger than the critical value between  $7.7 \leq x/\delta_0 \leq 18.5$  and reaches its extremum  $G_t = 1.2$  at  $x/\delta_0 = 10.9$ , close to the reattachment. Streamline 2 is in the middle of the boundary layer and passes through the point  $x/\delta_0 = 0$  and  $y/\delta_0 = 0.5625$ . The spatial evolution of the curvature and Görtler number has a similar trend as for the streamline 1 and the Görtler number is above the critical value for  $7.0 \leq x/\delta_0 \leq 19.3$ . In figure 3.44, we show that the high and low speed streaks are observed within the region  $6.8 \leq x/\delta_0 \leq 17.8$ , which is consistent with the zones with large Görtler number. The intrinsic spanwise wavelength of these streamwise vortex pairs is reported as  $\lambda_z \approx 2\delta$  in SWBLI systems [98, 186], which is also in agreement with the current observations  $\lambda_z = 2.0\delta_0 \sim 3.1\delta_0$ . The streamwise velocity field reconstructed from DMD mode  $\phi_1$  also displays these high and low speed streaks, see figure 3.57. Although there is no general critical  $G_t$  reported in the literature for turbulent separated flow, the high levels of  $G_t$  provide an indication of sufficiently strong Görtler instability at the reattachment location, which provides an explanation for the low and high speed streaks observed in figure 3.44 and the detected streamwise-oriented structures in DMD mode  $\phi_1$ .

Görtler vortices resulting from strong curvature could be unsteady in the turbulent flow, as concluded by Floryan [24] from various experiments in low-speed turbulent flows. One of the situations proposed is that the generated streamwise-oriented vortices oscillate in the spanwise direction if they are affected by three-dimensional disturbances in the incoming flow. The unsteady streamwise vortices observed in the incident shock and ramp cases [98, 99, 187] both fall into this category. The mode structure shown in figure 3.56 oscillates in spanwise direction. It is noticed that this proposition involves incoming disturbances, which may suggest a certain dependence on upstream flow conditions. From figure 3.55(b), we can observe that weak upstream disturbances and fluctuations are part of the same DMD modes as the downstream Görtler vortices, which manifests that the observed Görtler vortices in the present study indeed have a significant correlation with upstream disturbances.

For comparison, we also show the Görtler number for our laminar case [178] in

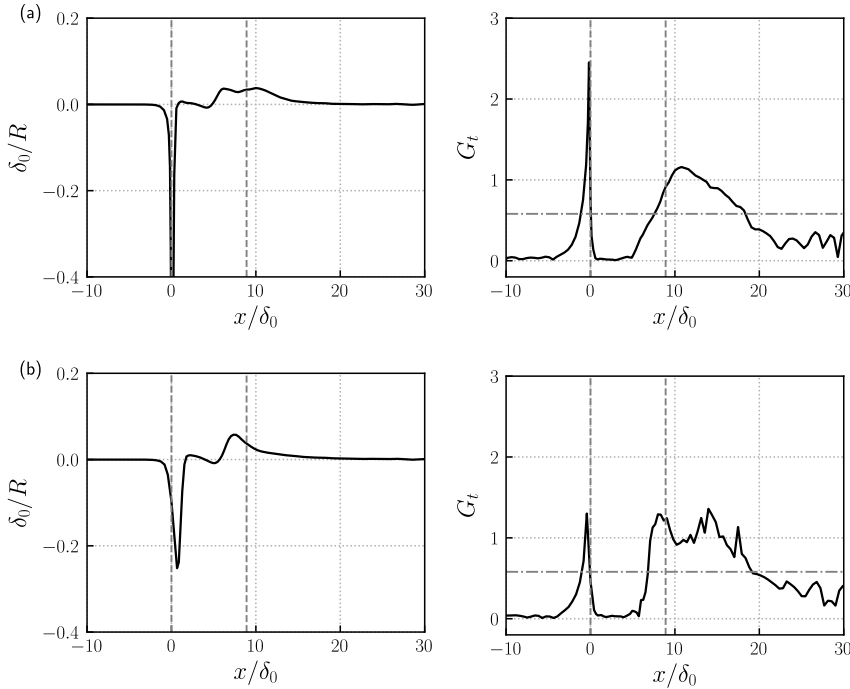


Figure 3.64: Curvature  $\delta_0/R$  and Görtler number  $G_t$  along two streamlines of the mean flow (case BTB). (a) streamline 1 through  $x/\delta_0 = 0$  and  $y/\delta_0 = 0.125$ , (b) streamline 2 through  $x/\delta_0 = 0$  and  $y/\delta_0 = 0.5625$ . Vortical dashed lines indicate the separation and reattachment point. Horizontal dot-dashed line signify the critical  $G_r$  in a laminar flow.

figure 3.65. As we can see, the curvature around the reattachment location in the laminar case is smaller than the one in the turbulent flow. As a result,  $G_t$  has a smaller value than for the turbulent case (cf. figure 3.64). Specifically,  $G_t$  is below the critical value in the whole separation bubble, which probably is the reason that there are no Görtler vortices around the reattachment point in the laminar case (cf. figure 3.46). In addition, this difference also shows how the existence of Görtler vortices is affected by upstream fluctuations: more turbulent incoming flow leads to a smaller separation length and thus stronger Görtler instability. On the other hand, the flow field around the reattachment location is more likely to reorganize and form into the spanwise-aligned vortices in the turbulent regime due to the incoming three-dimensional fluctuations.

Based on the above discussion, the following physical mechanism is proposed for the production of the low-frequency unsteadiness. The incoming turbulent flow experiences strong shear and curvature upon separation, which leads to large coherent vortical structures along the shear layer. Near the reattachment, there is significant centrifugal instability within the shear layer due to the concave streamlines. The Görtler instability, excited by incoming 3D turbulence, leads to large streamwise oriented vortices, which produce high- and low-speed streaks around the reattachment region (cf. figure 3.44

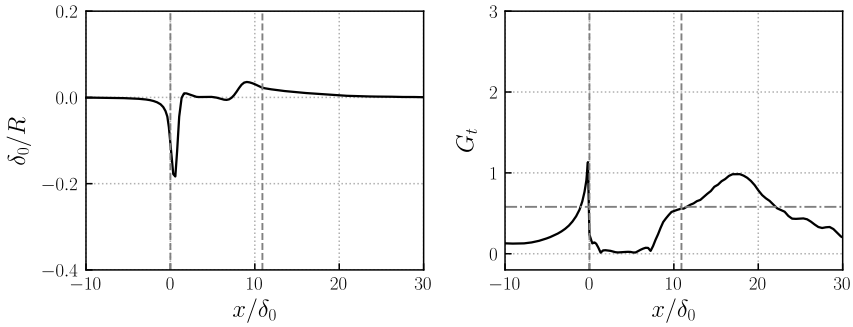


Figure 3.65: Curvature  $\delta_0/R$  and Görtler number  $G_t$  along the streamline through  $x/\delta_0 = 0$  and  $y/\delta_0 = 0.5625$  for the laminar case BZA. Vertical dashed lines indicate the separation and reattachment point. Horizontal dot-dashed line signify the critical  $G_t$  in a laminar flow.

and 3.57). These Görtler vortices are unsteady, which leads to spanwise shock wrinkling at very low frequencies, as we see from the streamwise velocity fluctuations from DMD mode  $\phi_1$ . Vortex driven mixing and mass entrainment results in the breathing of the separation bubble and the reattachment shock. Therefore, we believe that the centrifugal force and induced Görtler vortices are the main driving force of the global low-frequency unsteadiness in the turbulent case, which suggests that the low-frequency oscillation of SWBLI is inherently a three-dimensional mechanism. In the meantime, there is also notable dependence on the upstream fluctuations within the incoming turbulent boundary layer.

### 3.5.6. SUMMARY

The unsteady dynamics of SWBLI over a BFS, with particular attention to the low-frequency unsteadiness, has been investigated at  $Ma = 1.7$  using a well-resolved LES. The mean flow field illustrates the main flow topology of SWBLI in the BFS, consisting of a centred Prandtl-Meyer expansion fan originating from the fixed separation point, a separation bubble behind the step and a reattachment shock generating from the compression waves. Different from the canonical impinging shock and compression ramp cases, the separation point is stationary and only one shock occurs in the BFS case. The instantaneous flow field shows that the unsteady behavior is however similar to other SWBLI configurations, including the vortex shedding in the separated shear layer, as well as the breathing of the separation bubble and a flapping shock motion. The spectral analysis shows that there is a broad band of low-frequency oscillations, which we classify into two branches with the dominant frequencies centered near  $St_\delta = 0.02$  and 0.2 in the current case. The lower frequency dynamics is related to the unsteady separation bubble size, as well as the shock angle and position, while the second one connects to the shedding of shear layer vortices, which also affects the reattachment location.

Three-dimensional DMD analysis was used to reveal the characteristic mode structures that contribute to the observed unsteady behavior. The low-frequency mode

$\phi_1$  provides evidence for the statistical link between the shock motion (by pressure fluctuations) and the unsteady Görtler vortices (by the streamwise velocity fluctuations) around the reattachment position. The high- and low-speed streaks in the contours of  $C_f$  in figure 3.44 and the reconstructed velocity field in figure 3.57 are the signature of these spanwise-aligned vortices. The medium-frequency mode  $\phi_2$  represents shear-layer vortices and Mach waves. We thus believe that the unsteady Görtler vortices around the reattachment provide the unsteady forcing that sustains the low-frequency motions of shock and separation bubble. In particular through the comparison with a laminar inflow case [178], we show that the upstream fluctuations have a notable effect on the formation and existence of the unsteady spanwise-aligned Görtler vortices.



# 4

## FORWARD-FACING STEP

*Think twice before you leap;  
practice more once you act.*

慎而思之，勤而行之

Bai Ju-Yi  
白居易

## 4.1. FLOW CONFIGURATION AND NUMERICAL SETUP

This section presents the flow configuration and numerical setup for the FFS geometry. Four cases with different inlet conditions are considered, covering the laminar, transitional and turbulent flow regime.

### 4.1.1. FLOW CONFIGURATION

The geometry chosen is a FFS in a supersonic external flow, as shown in figure 4.1. Again, four cases are considered for this configuration with different inflow conditions, consisting of a laminar zero-pressure gradient boundary layer superimposed with zero-amplitude (case FZA, *i.e.*, clean laminar inflow), low-amplitude (case FLA) and high-amplitude oblique waves (FHA) on the inlet, as well as a turbulent inflow (case FTB), respectively. For the laminar and transitional cases, the computational domain size is  $([-120, 40] \times [0, 33] \times [-8.0, 8.0])\delta_0$  in the  $x$ ,  $y$ ,  $z$  directions, while it is  $([-70, 40] \times [0, 33] \times [-8.0, 8.0])\delta_0$  in these three directions for the turbulent case. The upstream streamwise length of the domain is relatively longer for laminar and transitional cases in order to avoid that the separation shock reaches the inflow boundary during the violent startup transient. In the turbulent case, the upstream turbulent boundary layer is able to resist this upstream propagation; thus a smaller domain size is allowed to reduce the computational cost.

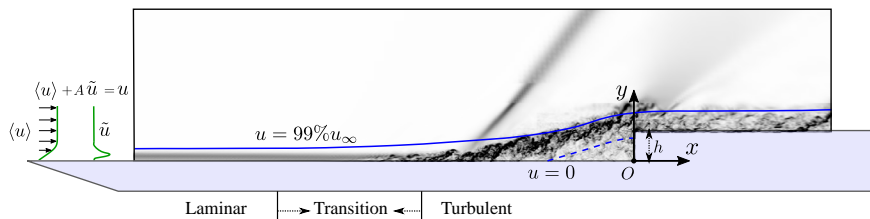


Figure 4.1: Schematic of the region of interest, which is in the center of the large computational domain. The figure represents an instantaneous numerical schlieren graph in the  $x - y$  cross section for the low-amplitude perturbed laminar flow case. Indicated are the wall-normal profiles of the mean velocity and perturbations.

To better compare with the BFS cases, the main flow parameters remain as the same with those of the BFS cases: Mach number  $Ma_\infty = 1.7$  and Reynolds number  $Re_{\delta_0} = 13718$  based on the inlet boundary layer thickness  $\delta_0$  (at  $99\%u_\infty$ ) and free stream velocity  $u_\infty$ . The main flow parameters are summarized in table 4.1. The height of the step is three times larger than the inlet boundary layer thickness.

Table 4.1: Main flow parameters of the current FFS cases

$Ma_\infty$	$U_\infty$	$\delta_0$	$\theta_0$	$Re_\infty$	$T_0$	$p_0$	$h$	$p_\infty$
1.7	469.85 m/s	1 mm	0.107 mm	$1.3718 \times 10^7 \text{ m}^{-1}$	300K	$1 \times 10^5 \text{ Pa}$	3 mm	20259 Pa

### 4.1.2. NUMERICAL SETUP

Similar as in the previous chapter, the in-house code INCA was used for the flow simulations. A Cartesian mesh based on local block refinement was generated for the flow domain, as shown in figure 4.2. The spatial resolution of the grid is  $\Delta x_{\max}^+ \times \Delta y_{\max}^+ \times \Delta z_{\max}^+ = 40 \times 1.0 \times 20$  ( $\Delta x_{\max}^+ = 1.0$  on the step wall, excluding the singular point at the step). The temporal resolution (*i.e.*, the time step) is around  $\Delta t u_{\infty} / \delta_0 = 7.6 \times 10^{-4}$ , resulting in  $\text{CFL} < 0.5$ . The four cases have the same spatial and temporal resolution.

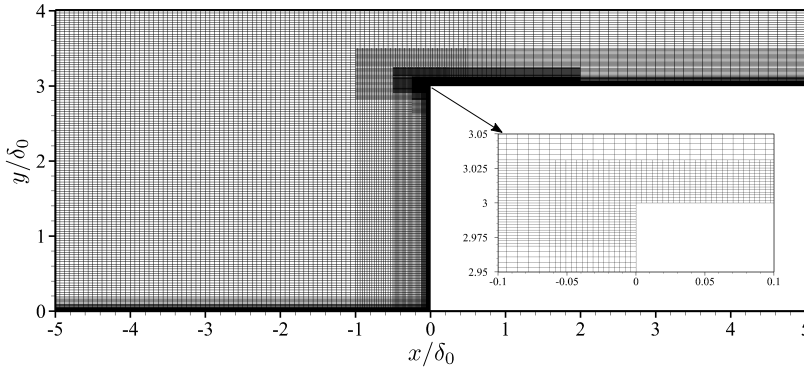


Figure 4.2: Grid distribution in the x-y plane in the computational domain near the forward-facing step.

The boundary conditions are the same as those of the BFS cases: the bottom surface and step are modeled as non-slip adiabatic walls. All the flow variables are extrapolated at the outlet of the domain. For the far field on the top, non-reflecting boundary conditions based on Riemann invariants are imposed. The spanwise borders are treated as periodic boundaries. The present four cases have different inlet boundary conditions. Case FZA is provided with a clean compressible self-similar zero-pressure-gradient laminar inflow boundary layer profile without any perturbations. The two perturbed laminar cases have the same mean flow profile as case FZA, but superimposed with a single low- and high-amplitude oblique T-S wave for the case FLA and FHA, respectively. The profiles of the T-S waves are calculated by LST and are the same as those of the BFS transitional cases given in section 3.1.3. Since a longer streamwise length of the flow domain is used upstream of the step, the averaged amplitudes of the streamwise velocity fluctuations at inlet are taken ten times smaller than those of the BFS cases, *i.e.*,  $A_{\text{in}} = 0.01\%$  for case FLA and  $A_{\text{in}} = 0.05\%$  for case FHA in the disturbed region ( $0 \leq y/\delta_0 \leq 5.0$ ). Case FTB has a turbulent inflow boundary layer produced by the digital filter technique. The inflow conditions for the present four cases are summarized in table 4.2.

### 4.1.3. GRID VALIDATION

The grid validation is provided only for case FTB because all FFS cases share the same grid topology and resolution. For the current computations, the time- and spanwise-averaged statistics were sampled at every  $t u_{\infty} / \delta_0 = 0.5$ . We simulated an initial period of  $t u_{\infty} / \delta_0 = 600$ , during which the flow reached a fully developed, statistically steady

Table 4.2: Flow information for all the investigated FFS cases

Case	FZA	FLA	FHA	FTB
flow regime	laminar	laminar	laminar	turbulent
fluctuation intensity	$I = 0$	$I = 0.08\%$	$I = 0.4\%$	$I = 6\%$

state. After this initial transient, statistics were sampled over another  $tu_\infty/\delta_0 = 400$ . The van Driest transformed mean velocity profile and Reynolds stresses in Morkovin scaling are plotted at a streamwise station  $x/\delta_0 = -50.0$  (where  $Re_\tau = 370$ ) in figure 4.3. The asymptotic solutions for the laminar sublayer and the log-law, as well as incompressible DNS data of Schlatter and Örlü [148] at  $Re_\tau = 360$  are also included for comparison. The mean velocity profile is in a good match with both the logarithmic law of the wall ( $u^+ = \frac{1}{\kappa} \log y^+ + C$  with the constants  $\kappa = 0.41$  and  $C = 5.2$ ) and DNS results. The corresponding Reynolds stresses are also in very good agreement with the reference data.

4

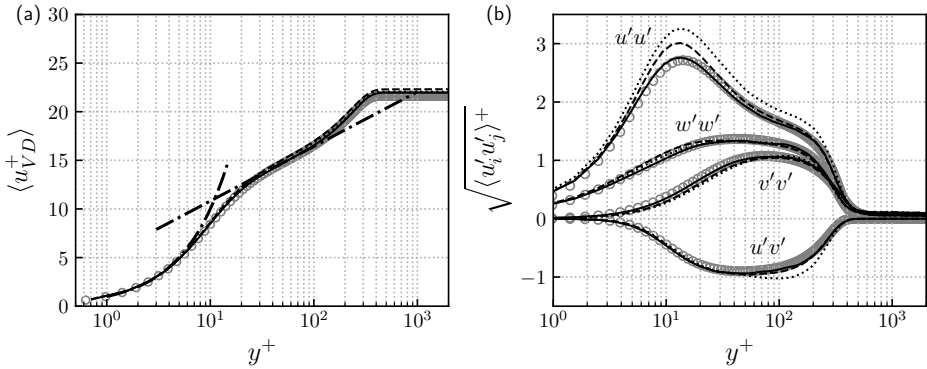


Figure 4.3: Mean profiles of the upstream turbulent boundary layer in wall units at  $x/\delta_0 = -50.0$  and  $Re_\tau = 370$ . (a) Van Driest transformed mean velocity profile and (b) Reynolds stresses normalized by  $\sqrt{\rho/\rho_w}$ . ---, law of the wall; —, present LES with the chosen fine grid; ·····, coarser grid GX; ---, coarser grid GZ;  $\circ$ , incompressible DNS data of Schlatter and Örlü [148] at  $Re_\tau = 360$  and  $Re_\theta = 1000$ .

The grid sensitivity has been checked using two coarser grids with  $\Delta x_{\max}^+ \times \Delta y_{\max}^+ \times \Delta z_{\max}^+ = 80 \times 1.0 \times 20$  and  $\Delta x_{\max}^+ \times \Delta y_{\max}^+ \times \Delta z_{\max}^+ = 40 \times 1.0 \times 40$ . As we can see from figure 4.3, these two coarser grids give very similar results as the fine grid for the mean velocity and Reynolds stress profiles, but the fine grid does produce better agreement with the reference data, especially for the streamwise Reynolds stress.

## 4.2. PRELIMINARY COMPARISONS OF DIFFERENT CASES

This section provides a general overview of the flow field for the FFS cases at different inflow conditions, i.e., among the four cases FZA, FLA, FHA, FTB. First, the evolution of the boundary layer is displayed by the streamwise variation of the time- and spanwise-averaged skin friction in figure 4.4(a). Note that the inlet position for the computations

is at  $x/\delta_0 = -120$  for the laminar cases and  $x/\delta_0 = -70$  for the turbulent case. The mean skin friction of all cases shows qualitatively the same behavior, consistent with a separation region upstream of the step. The curves for the laminar and transitional cases (case FZA, FLA, FHA) appear to almost overlap over the entire flow domain. Initially, the boundary layer remains laminar far upstream of the step, as can be inferred from the low level of  $\langle C_f \rangle$ , of the order of 0.0003. From  $x/\delta_0 = -80.0$ , the mean skin friction starts to increase gradually, which indicates the onset of transition. At  $x/\delta_0 = -29.0$ , the mean skin friction reaches a high level of  $\langle C_f \rangle \approx 0.002$ , indicating that the boundary layer is already highly perturbed and close to turbulent, at a location that is still well upstream of the separation region. Approaching the separation bubble ( $x/\delta_0 > -29.0$ ), the skin friction rapidly decreases until the boundary layer separates at  $x/\delta_0 = -15.9$ . In the fore part of the recirculation region,  $\langle C_f \rangle$  keeps a relatively low level close to zero. Then the mean skin friction drastically decreases towards a global minimum  $\langle C_f \rangle < -0.002$  near the step, followed by a sharp increase of  $\langle C_f \rangle$  across the step as reattaching on the step wall. On the upper wall, the flow reattaches again at  $x/\delta_0 \approx 0.5$ . Behind the second separation bubble, the mean skin friction reaches a local maximum  $\langle C_f \rangle \approx 0.0035$  at  $x/\delta_0 \approx 2.4$ . The mean skin friction then slightly decreases and remains at a typical turbulent level downstream. Based on the evolution of the mean skin friction, the transition probably follows a same path for case FZA, FLA and FHA. For case FTB, the initial variations of the skin friction are caused by the DF technique because the boundary layer needs to develop physical coherent structures. After this initial transient region, the mean skin friction slowly decreases in the region  $x/\delta_0 < -20$ , as the local Reynolds number increases along the streamwise distance. Then,  $\langle C_f \rangle$  drops abruptly in front of the separation point ( $x/\delta_0 = -13.0$ ) to negative values inside the separation bubble. The mean skin friction reaches its minimum very close to the step wall and then rises again across the step. Behind the step, the curves of  $\langle C_f \rangle$  follow a similar trajectory approaching a value of  $\langle C_f \rangle = 3.0 \times 10^{-3}$  for all cases, which suggests that they reach a similar turbulent state downstream. Because turbulent flow is more resistant to separation, the separation length ( $L_r/\delta_0 = 13.0$ ) is 18% shorter than for the other three cases.

The separation length  $L_r$  from the present cases is compared with existing experimental data from literature in table 4.3. Similar as for the BFS cases presented in chapter 3, the separation length  $L_r$  is normalized by the step height  $h$ . For the turbulent case FTB, the separation length  $L_r/h = 4.3$  is close to the data of most existing experiments ( $L_r/h \approx 3.9 \sim 5.1$ ). In the review of Zukoski [111], they indicated that the normalized separation length is  $L_r/h \approx 4.1$ , roughly independent of the step height and Mach number if  $h/\delta > 1.2$  and  $Ma > 2.0$  in the turbulent regime, and it increases if the Mach number decreases, which is consistent with the current results. For the laminar and transitional cases, the computed separation length is  $L_r/h = 5.3$ , larger than the value reported by Zhang *et al.* [113], which can be attributed to the lower Mach number.

The root mean square (RMS) of the wall pressure  $p_{\text{rms}} = \sqrt{\langle p'p' \rangle} / \rho_\infty u_\infty^2$  is plotted in figure 4.4(b), illustrating the level of fluctuations and reflecting the development of turbulence. Due to acoustic waves emitted by the downstream separation region, the RMS of wall pressure for the laminar and transitional cases (case FZA, FLA and FHA) rapidly grows at the inlet and reaches a similar level of  $p_{\text{rms}} = 0.003$  at  $x/\delta_0 \approx -60.0$ .

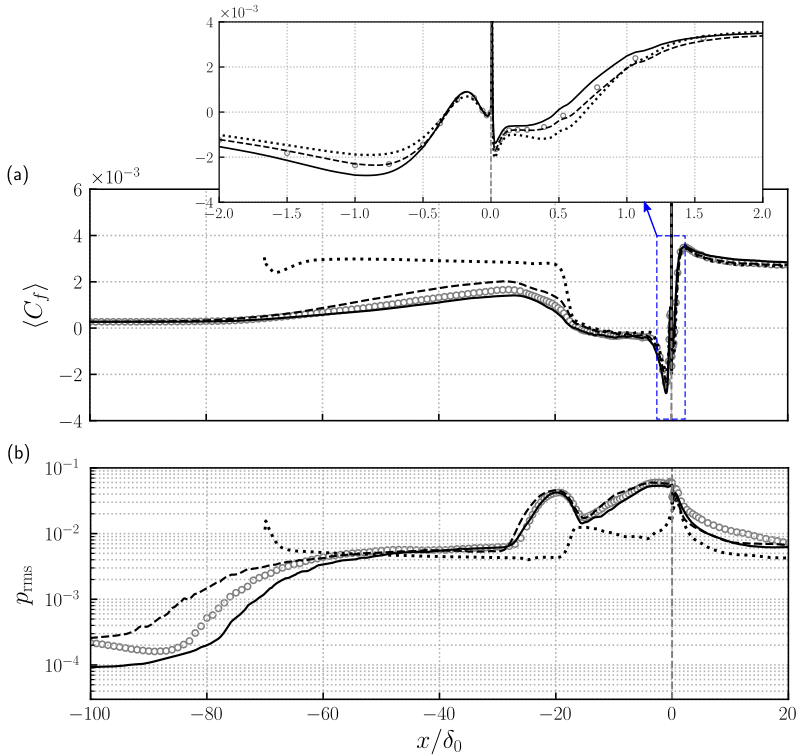


Figure 4.4: Streamwise development of time and spanwise-averaged (a) skin friction with a zoom into the region near the step and (b) root mean square of wall pressure fluctuations (normalized by  $\rho_\infty u_\infty^2$ ) for case FZA ( $\circ$ ), case FLA (—), case FHA (---), case FTB (·····).

The curves for these three cases follow a similar trend when  $x/\delta_0 > -60.0$ . The pressure fluctuations slowly increase until  $x/\delta_0 \approx -30$  and then quickly grow in front of the separation region ( $x/\delta_0 < -20.0$ ) due to the emergence of compression waves. After reaching a local maximum  $p_{rms} \approx 0.04$ , they suddenly decrease across the separation point ( $x/\delta_0 = -15.9$ ). In the separation region, the pressure fluctuations continue rising to a maximum  $p_{rms} \approx 0.055$  caused by the reattachment, followed by a quick drop after the reattachment on the step. For case FTB, the RMS of wall pressure keeps a steady level far upstream of the separation region  $x/\delta_0 > -20$ . The pressure fluctuations then grow very rapidly to a local maximum  $p_{rms} \approx 0.013$  at  $x/\delta_0 = -15.0$ , followed by a slow decrease in the fore part of the separation region. Close to the step, they increase again to a maximum  $p_{rms} \approx 0.032$  and then rapidly drop after the reattachment. All four cases display a similar variation tendency but with different rates. The fully turbulent case (FTB) has a notably lower level of wall pressure fluctuations compared to the laminar or transitional cases. The cases FLA and FHA follow nearly the same trajectory as the case FZA downstream of the step, notwithstanding they being imposed with oblique waves, which provides further support to the assumption that these three cases share

Table 4.3: Comparison of the reattachment length reported in various FFS studies, where  $I$  is the free stream or maximum inflow turbulence intensity.

Authors	$Ma$	$Re_\infty, m^{-1}$	h, mm	$\delta_0/h$	$L_r/h$	Comments
Czarnecki <i>et al.</i> [188]	1.6	$1.9 \times 10^7$	20.4	0.3	4.2	experiment, turbulent
Estruch-Samper <i>et al.</i> [116]	2.0	$6.5 \times 10^7$	22.5	0.13	3.9	experiment, turbulent
Rogers <i>et al.</i> [189]	2.2	$1.1 \times 10^4$	12.7	1.0	2.8	experiment, laminar
Murugan <i>et al.</i> [114]	2.5	$2.82 \times 10^7$	12	0.5	4.1	experiment, $I \approx 1.5\%$
Spaid [190]	2.9	$4.8 \times 10^6$	10.2	0.74	4.2	experiment, turbulent
Estruch-Samper <i>et al.</i> [116]	3.0	$6.1 \times 10^7$	22.5	0.14	4.3	experiment, turbulent
Zhang <i>et al.</i> [113]	3.0	$7.5 \times 10^6$	10	1.02	3.4	experiment, laminar
Zukoski [111]	3.0	$3.9 \times 10^8$	7.6	0.33	4.2	experiment, turbulent
Chandola <i>et al.</i> [191]	3.9	$7.01 \times 10^7$	22.5	0.17	5.1	experiment, turbulent
Zukoski [111]	3.9	$1.2 \times 10^7$	10.2	0.6	4.5	experiment, turbulent
Behrens [110]	4.0	$1.2 \times 10^7$	18.5	0.5	4.25	experiment, turbulent
Present case FZA	1.7	$1.37 \times 10^7$	3	0.33	5.3	LES, laminar
Present case FLA	1.7	$1.37 \times 10^7$	3	0.33	5.3	LES, $I \approx 0.08\%$
Present case FHA	1.7	$1.37 \times 10^7$	3	0.33	5.3	LES, $I \approx 0.4\%$
Present case FTB	1.7	$1.37 \times 10^7$	3	0.33	4.3	LES, $I \approx 6\%$

the same transition path throughout the separated shear layer region. The wall pressure fluctuations finally reach identical levels for all three cases at  $x/\delta_0 > 30$ .

The development of the oblique T-S waves is measured by the maximum root-mean-square of the streamwise velocity fluctuations. The semi-log plot in figure 4.5 shows a rapid transient growth of the incoming T-S waves far upstream of the separation region. The averaged streamwise growth rate is given by the slope of the curve  $\alpha_\delta^i \approx 0.066$ , which is much larger than the LST results  $\alpha_\delta^i \approx 0.016$  for the inlet unstable T-S waves. Approaching the separation region  $x/\delta_0 > -15.9$ , the boundary layer is almost turbulent and the level of fluctuations almost remains steady. We additionally observe small and drastic growth of the fluctuations around the separation point  $x/\delta_0 = -15.9$  and reattachment location. Correspondingly, the laminar-to-turbulent transition occurs upstream of the separation bubble, with a typical laminar shape factor  $H = 4.4$  at  $x/\delta_0 = -80.0$  to a shape factor  $H = 2.5$  (close to a typical turbulent one) at  $x/\delta_0 = -20.0$ . The computational investigation of Edelmann and Rist [69] also reported this significant amplification of the unstable waves by the FFS upstream of the step.

The instantaneous snapshots of vortical structures for cases FZA, FHA and FTB are presented by means of isosurfaces of the  $\lambda_2$  vortex criterion [155] in figure 4.6, 4.7 and 4.8, respectively. For case FZA, the transition region is divided into two sub-sections, i.e., the far upstream region ( $-80 \leq x/\delta_0 \leq -30.0$ ) and the part near the step ( $-30 \leq x/\delta_0 \leq 0$ ). Around  $x/\delta_0 = -80.0$ , negative spanwise vorticity is produced, which is caused by the growth of the oblique T-S waves. The streaks of the spanwise vorticity induce the near-wall  $\Lambda$ -shaped vortices and then develop into separate turbulent spots. The patches

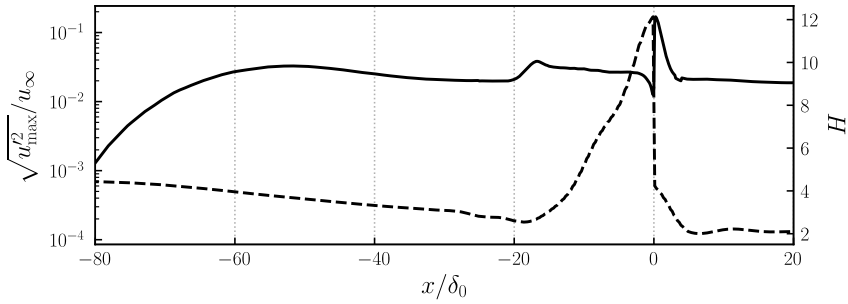


Figure 4.5: Maximum RMS of streamwise velocity fluctuations (solid line) and shape factor of the boundary layer (dashed line) along the streamwise direction for case FZA.

of the turbulent spots contain small hairpin vortices of different spatial scales. There are also small streamwise vortices located between the two legs of the hairpin vortices. Approaching the separation region, these secondary hairpin vortices are amplified and continue travelling in the shear layer of the main separation bubble. Behind the main separation, the boundary layer is highly turbulent and develops towards the canonical equilibrium state downstream of the step (see also figure 4.4). These flow structures in the present transition are typical flow phenomena for a natural modal transition induced by the T-S waves in a zero-pressure-gradient flat-plate boundary layer, as reported in the DNS of Wu and Moin [192].

Cases FLA and FHA follow the same transition path with case FZA since similar vortical structures are observed. Therefore, only the vortical visualization of case FHA is provided here. As we can see, the typical spanwise vorticity,  $\Lambda$ -shaped vortices, hairpin vortices are also identified. Therefore, we believe that the fully laminar case FZA, perturbed cases FLA and FHA belong to the same transition road, i.e, the modal transition induced by the oblique T-S waves.

For the turbulent case FTB, the near-wall region features small homogenous vortices in the incoming boundary layer in front of the step. Since the shear layer over the separation bubble is inviscidly unstable, the shear layer rolls up and vortical structures are enhanced due to the strong K-H instability, as shown in figure 4.8. However, a clear signature of K-H vortices is not observed because it is hidden by the energetic turbulent structures. In addition, the separation shock is stronger than for the laminar and transitional cases. Finally, it may be noted in summary that all the cases share similar flow features in the separation region and downstream because they all reach a turbulent state already near the separation point.

By visual comparison, we find that the flow is turbulent at or directly after the mean separation line. The fully laminar and perturbed cases share the same modal transition induced by T-S waves. Since the conventional modal transition in supersonic flows has been well studied [9, 37, 193], we focus our attention on the analysis of the unsteady behavior of the shock wave/turbulent boundary layer interaction system, especially the low-frequency unsteadiness, by analyzing case FTB in more detail.

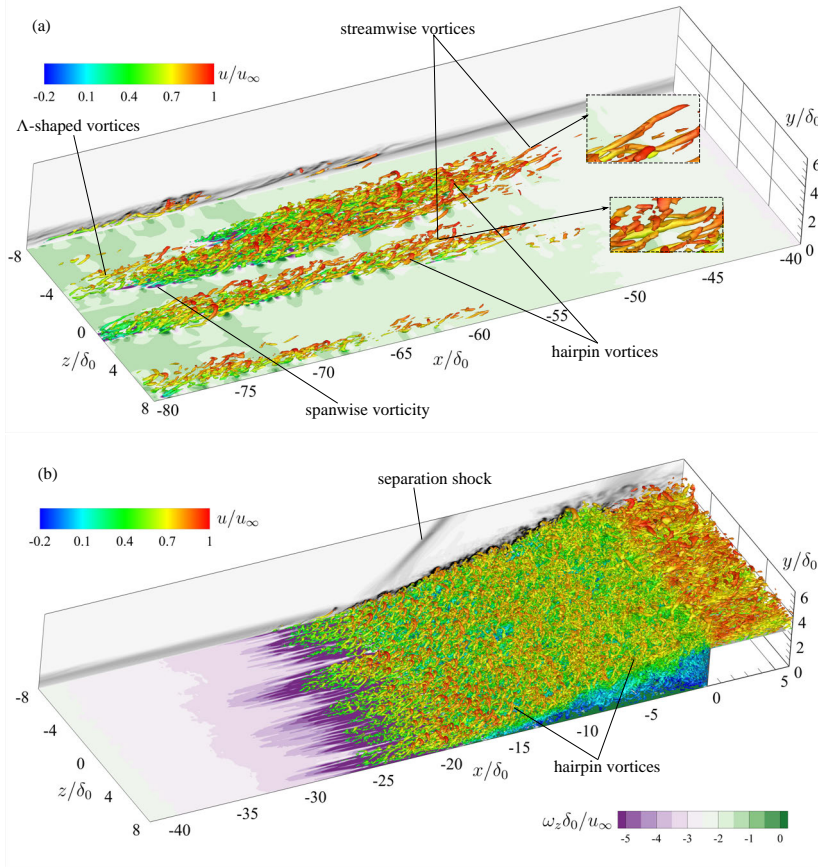


Figure 4.6: Instantaneous vortical structures of case FZA at  $tu_\infty/\delta_0 = 660$ , visualized by isosurfaces of  $\lambda_2$ . A numerical schlieren based on  $z = 0$  slice with  $|\nabla\rho|/\rho_\infty = 0 \sim 1.4$  and contours of spanwise vorticity based on  $y/\delta_0 = 0.003$  with  $\omega_z \delta_0 / u_\infty = -5.0 \sim 0$  are also included. (a) upstream of the separation bubble and (b) close to the bubble at  $\lambda_2 = -0.05$ .

### 4.3. TURBULENT REGIME

This section presents the unsteady motions of the FFS SWBLI and its frequency characteristics mainly using case FTB. The origin of the low-frequency unsteadiness is investigated.

#### 4.3.1. MEAN FLOW FEATURES

The mean flow topology of case FTB is shown in figure 4.9, visualized by means of density  $\rho$ . The incoming turbulent boundary layer is deflected by the upward step, which results in the compression of the boundary layer and produces a separation shock. The angle of the separation shock to the streamwise direction is around  $45.6^\circ$ . The shock-induced adverse pressure gradient leads to the separation of the boundary layer upstream of the step at  $x/\delta_0 = -13.0$ . As the separated flow travels over the separation region and

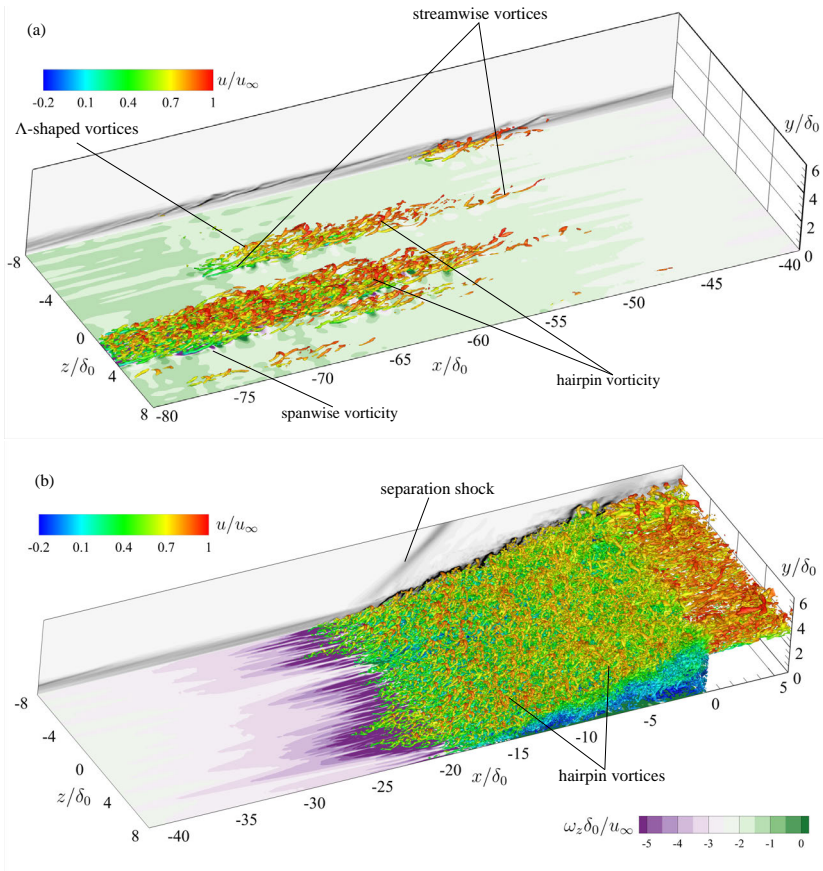


Figure 4.7: Instantaneous vortical structures of case FHA at  $t u_\infty / \delta_0 = 660$ , visualized by isosurfaces of  $\lambda_2$ . A numerical schlieren based on  $z = 0$  slice with  $|\nabla \rho| / \rho_\infty = 0 \sim 1.4$  and contours of spanwise vorticity based on  $y / \delta_0 = 0.003$  with  $\omega_z \delta_0 / u_\infty = -5.0 \sim 0$  are also included. (a) upstream of the separation bubble and (b) close to the bubble at  $\lambda_2 = -0.05$ .

reattaches on the step wall, compression waves are generated near the step corner. Behind the step, the reattached shear flow travel across the step edge and undergoes a centered Prandtl-Meyer expansion. There is a very small separation bubble and a weak reattachment shock behind it on the upper wall. Further downstream, the boundary layer starts to relax and finally returns to an equilibrium state. These mean flow features share many similarities with those of the compression ramp [98], including the relatively strong separation shock, separated shear layer, weak reattachment shock and expansion fan, as discussed in section 1.3.3. With regard to the laminar FFS case in figure 4.10, the flow structures are very similar to the turbulent ones because the oncoming boundary layer is already turbulent when it separates. However, the laminar case has a longer mean separation length ( $x/\delta_0 = -15.9$ ). The lower resistance to the adverse pressure gradient indicates that turbulence has not yet reached a fully developed state. Moreover,

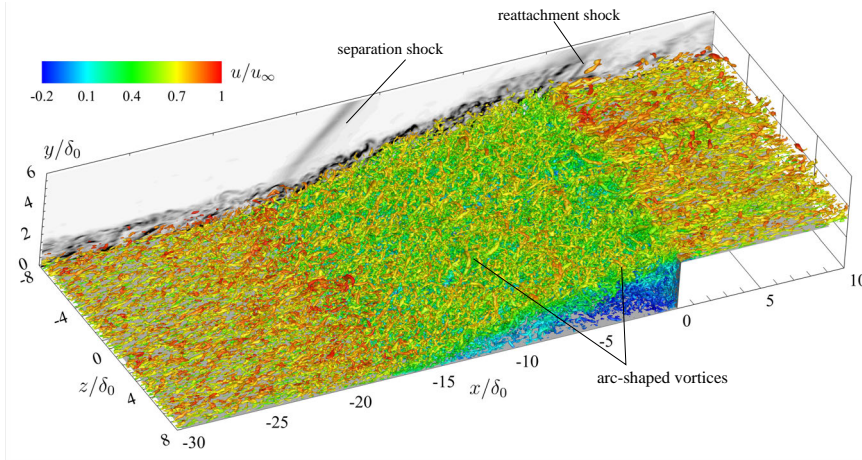


Figure 4.8: Instantaneous vortical structures at  $tu_\infty/\delta_0 = 400$  for case FTB, visualized by isosurfaces of  $\lambda_2 = -0.08$ . A numerical schlieren based on  $z = -8$  slice is also included with  $|\nabla\rho|/\rho_\infty = 0 \sim 1.4$ .

the mean separation shock is weaker with a larger shock angle ( $49.0^\circ$ ) in the laminar case, which is consistent with the longer separation length and a more gradual compression.

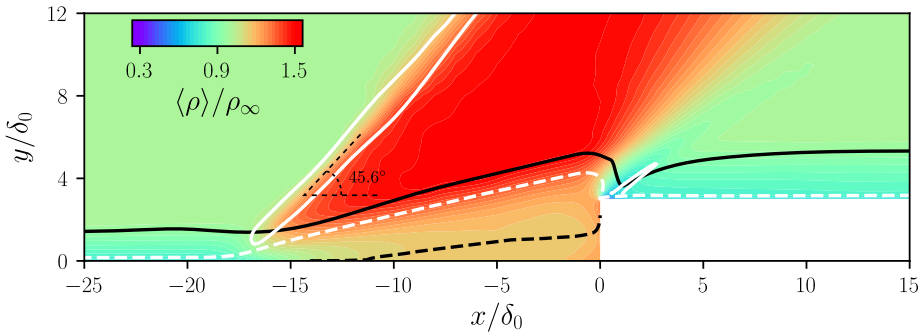
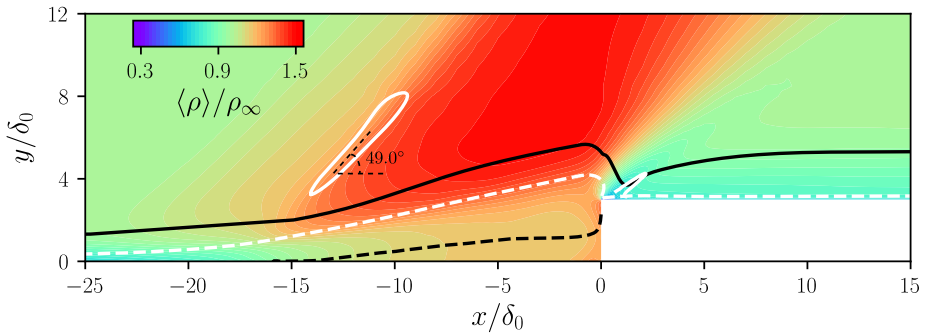


Figure 4.9: Density contours of the time- and spanwise-averaged flow field for case FTB. The white dashed and solid lines denote the isolines of  $Ma = 1.0$  and  $|\nabla p|\delta_0/\rho_\infty = 0.26$ . The black dashed and solid lines signify isolines of  $u = 0.0$  and  $u/u_e = 0.99$ .

Figure 4.11(a) provides a close comparison of the mean skin friction around the interaction region between the laminar case FZA and turbulent case FTB. As we discussed in the previous section, the mean separation (or reattachment) length (equal to  $L_r = |x_r| = 13.0\delta_0 \approx 4.3h$ ) in case FTB is shorter than that in case FZA ( $L_r = |x_r| = 15.9\delta_0 \approx 5.3h$ ). Moreover, the turbulent case has a much higher  $\langle C_f \rangle$  upstream of the separation region. Both of them reach, however, a similar level of skin friction downstream of the step, because the laminar-to-turbulent transition is accelerated within the separated shear layer.

Figure 4.11(b) compares the streamwise variation of the wall pressure. As we can



4

Figure 4.10: Density contours of the time- and spanwise-averaged flow field for case FZA. The white dashed and solid lines denote the isolines of  $Ma = 1.0$  and  $|\nabla p|\delta_0/p_\infty = 0.2$ . The black dashed and solid lines signify isolines of  $u = 0.0$  and  $u/u_e = 0.99$ .

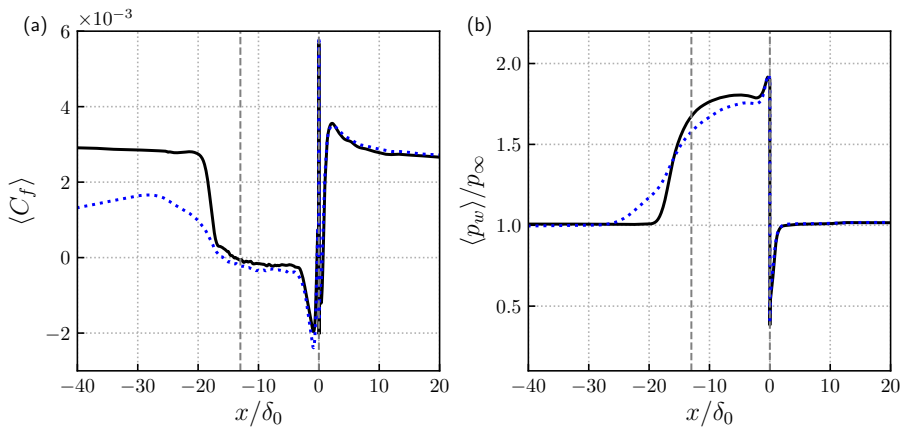


Figure 4.11: Streamwise variation of (a) skin friction and (b) wall pressure. The time- and spanwise-averaged values are indicated by the black solid lines (turbulent case FTB) and blue dotted lines (laminar case FZA). The vertical dashed line indicates the averaged separation and reattachment location for the turbulent case.

see, the wall pressure is constant upstream of the separation bubble. The wall pressure ratio starts to increase at about  $x/\delta_0 \approx -20.0$  for the turbulent case (at  $x/\delta_0 \approx -26$  for the laminar case FZA) and forms a plateau with a value of  $\langle p_w \rangle/p_\infty \approx 1.8$  inside the recirculation region. It drastically drops by about 75% of the maximum at the step corner due to the expansion and then rises again to its initial (freestream) value as the flow reattaches on the upper wall. In terms of the trend and relative variation, the current results are in a good agreement with the experimental work of Chandola *et al.* [191].

#### 4.3.2. UNSTEADY CHARACTERISTICS

The interaction system over the FFS features various unsteady motions and vortical scales, as shown in figure 4.8. The variance of the wall-normal velocity  $\langle v'v' \rangle$  presents a

general view of the distribution of the main unsteady regions. As displayed in figure 4.12, the separated shear layer (between the isoline of  $\langle u \rangle = 0$  and the boundary layer edge) and the following recompression near the step corner (i.e., around the reattachment shock) are the most energetic unsteady regions of the flow field. Moreover, there are relatively weak fluctuations along the mean separation shock. Similar observations were reported in the experimental work of Estruch-Samper and Chandola [116]. The other normal Reynolds stress components  $\langle u' u' \rangle$  and  $\langle w' w' \rangle$  allow similar observations, as has also been reported in the impinging shock and compression ramp SWBLI [96, 99].

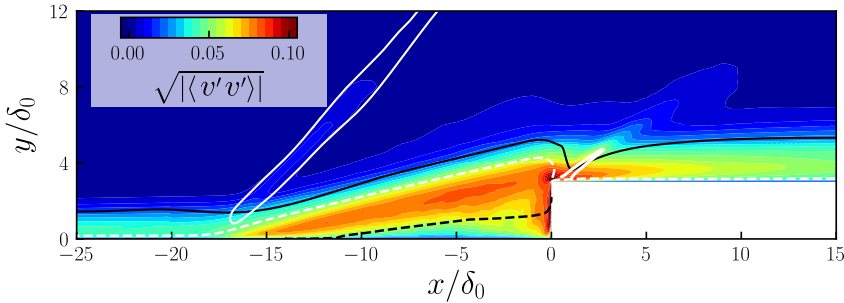


Figure 4.12: Contours of time- and spanwise-averaged variance of the wall-normal velocity for case FTB. The white dashed and solid lines denote the isolines of  $Ma = 1.0$  and  $|\nabla p| \delta_0 / p_\infty = 0.26$ . The black dashed and solid lines signify isolines of  $u = 0.0$  and  $u/u_e = 0.99$ .

We then put our focus on the regions of the separated shear layer, together with the separation and reattachment shock, to scrutinize the dynamic motions, as illustrated by snapshots of the instantaneous flow field. Figure 4.13 shows the contours of the streamwise velocity and isolines of the pressure gradient magnitude (white dashed lines) at two arbitrarily selected instants  $tu_\infty/\delta_0 = 600, 700$ . There are small turbulent vortices travelling along the separated shear layer (cf. figure 4.8). The variations of the isolines of  $u = 0$  (solid black lines) indicate the breathing of the separation bubble. Moreover, the location of the separation and reattachment shock (marked as white isolines of  $|\nabla p| \delta_0 / p_\infty = 0.4$ ) is moving with time, most notably in the shock-foot region. For the separation shock, the shock angle is  $\eta = 44.7^\circ$  at  $tu_\infty/\delta_0 = 600$ , while  $\eta = 46.2^\circ$  at  $tu_\infty/\delta_0 = 700$ . It is clear from this comparison that the recirculation area and shock location are unsteady.

To better identify the vortical topology near the wall, contours of the skin friction coefficient at the same instants are provided in figure 4.14. There are different flow features in the different regions of the flow field. Upstream of the separation region  $x/\delta_0 < -18.0$ ,  $C_f$  is uniformly distributed in the spanwise direction and show weak streamwise preferential orientation of the near-wall coherent structures. In the separation region, the skin friction remains at a low level with streamwise and spanwise streaks distributed on the wall. In the fore part of the separation bubble, the shear stress is relatively low due to the less energetic flow. There are streamwise-oriented features in the skin friction map behind the step on the upper wall. These high- and low-speed streaks are alternatingly distributed in the spanwise direction with a spanwise

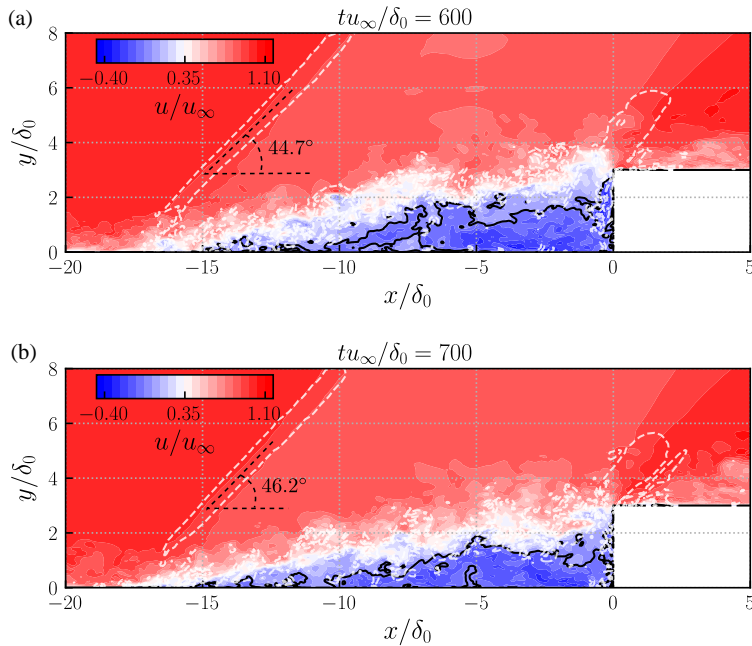


Figure 4.13: Contours of the instantaneous streamwise velocity for slice  $z = 0$  at (a)  $tu_\infty/\delta_0 = 600$  and (b)  $tu_\infty/\delta_0 = 700$  (case FTB). Black solid line denotes the isoline of  $u = 0$  and white dashed line signifies the isoline of  $|\nabla p|_{\delta_0}/p_\infty = 0.4$ .

wavelength between  $\lambda_z/\delta_0 = 2.0 \sim 4.0$ , which is consistent with previous experimental and numerical observations, reporting that the wavelength of these streaks is between two and three times the boundary layer thickness [97, 99, 104].

For the laminar case FZA (figure 4.15), we observe similar flow features, including the uniform distribution of  $C_f$  upstream of the separation region, streamwise streaks in the separation region and downstream of the step, although the instantaneous levels of  $C_f$  are different for the laminar and turbulent cases. As we indicated before, the shear layer is already turbulent in the separation region and therefore similar structures are expected for these two cases. Based on the experiments of Murugan and Govardhan [114] and our observations in the BFS cases, we believe that these alternating low and high-speed skin friction streaks are probably caused by the up-wash and down-wash effects of the Görtler-like vortices, which will be discussed in the following sections.

### 4.3.3. SPECTRAL ANALYSIS

The frequency characteristics of the flow field are quantified by the frequency weighted power spectral density. Figure 4.16 shows the variation of dominant frequency in the flow field at selected streamwise locations. All data is extracted at the local wall-normal positions where the pressure fluctuations are maximum. The sampling interval is  $tu_\infty/\delta_0 = 600 \sim 1100$  with a sample frequency  $f_s\delta_0/u_\infty = 4$ , thus excluding the

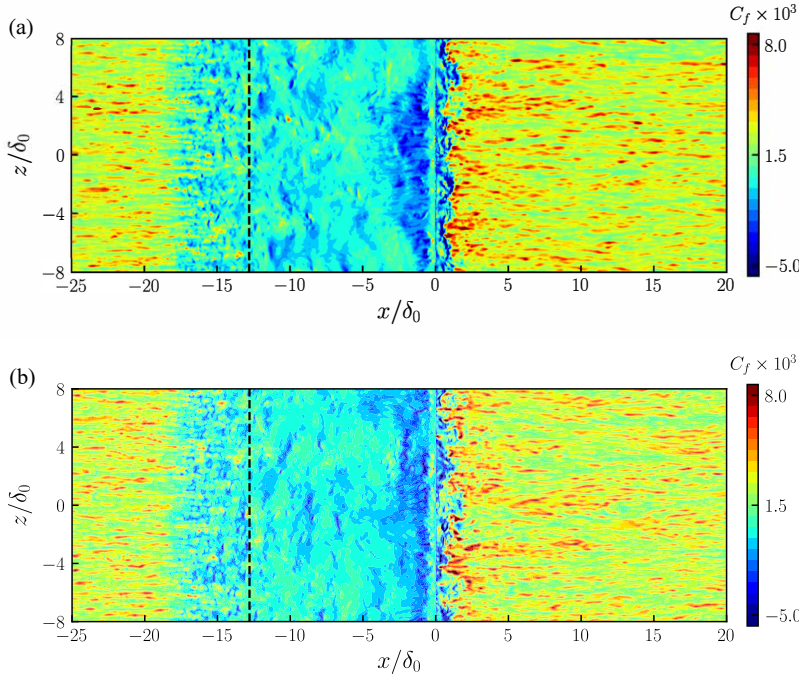


Figure 4.14: Contours of the instantaneous skin friction at (a)  $tu_\infty/\delta_0 = 600$  and (b)  $tu_\infty/\delta_0 = 700$  for the turbulent case FTB. The dashed line at  $x/\delta_0 = -13.0$  indicates the mean separation location.

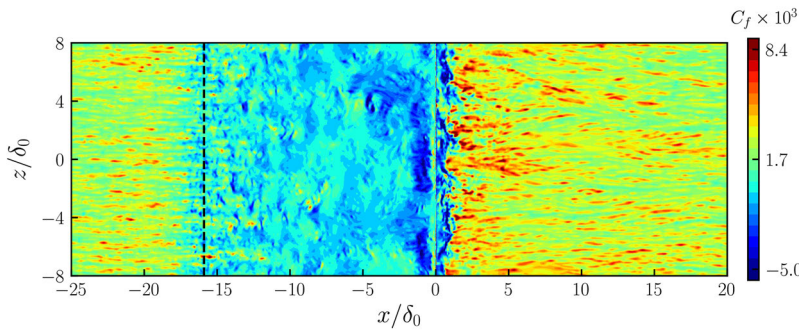


Figure 4.15: Contours of the instantaneous skin friction for the laminar case FZA. The dashed line at  $x/\delta_0 = -15.9$  indicates the mean separation location.

initial transient stage of the simulation. Upstream of the step ( $x/\delta_0 = -20.0$ ), the spectrum shows a broadband bump centered around  $St_\delta = f\delta_0/u_\infty = 0.8$ , which is close to the characteristic frequency ( $u_\infty/\delta$ ) of the upstream turbulent boundary layer [12]. The digital filter technique does not introduce spurious low-frequency features into the boundary layer, as can be concluded from the absence of any significant low-

frequency content upstream of the step. Close to the separation bubble ( $x/\delta_0 = -17.0$ ), the prevailing frequency suddenly shifts to a low frequency around  $St_\delta = 0.01$ . In the separation bubble, there is a noteworthy low-frequency bump between  $St_\delta = 0.005 \sim 0.05$  (lower blue dashed line in the graph). In addition, we can observe a medium frequency band with  $St_\delta = 0.06 \sim 0.3$  (upper region separating by green dashed lines), most clearly visible at the station in the upstream half of the separation bubble at  $x/\delta_0 = -11.0$  and at the station shortly downstream of the second separation bubble at  $x/\delta_0 = 6.0$ .

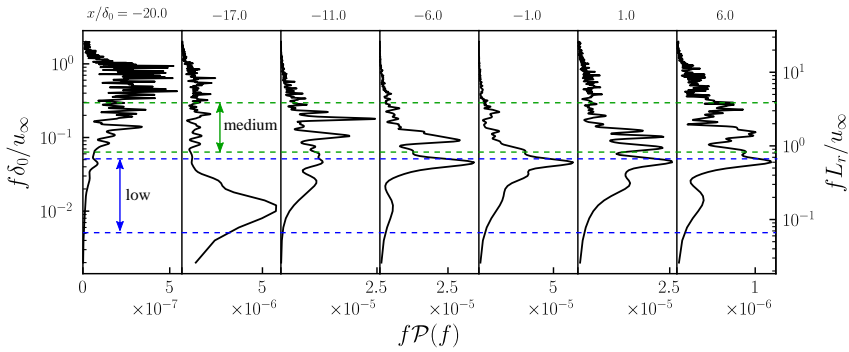


Figure 4.16: Frequency weighted power spectral density of the wall pressure with the streamwise distance (case FTB).

As we know from the previous chapter and the literature [85, 99], the low-frequency unsteadiness is usually associated with the shock wave/boundary layer interaction and the medium-frequency motions are related to the shedding of vortices. We therefore examine the frequency characteristics of several aerodynamic parameters to validate if these conclusions similarly apply to the FFS cases. The first group of the present parameters, including the spanwise-averaged streamwise velocity within the separated shear layer and the reattachment location, shows dominant medium-frequency unsteadiness. These data are extracted with the same sampling frequency as the aforementioned pressure signal. The location of the spanwise-averaged reattachment point  $y_r$  is the  $y$  coordinate of the intersection between the isolines of the streamwise velocity  $u = 0$  and the step wall. As shown in figure 4.17(a), an unsteady behavior at a frequency around  $St_\delta = 0.1$  ( $St_h = 0.3$ ) appears energetically dominant for the shear layer velocity. This medium frequency is the characteristic frequency of the shedding vortices within the shear layer. These vortices are shedding along the shear layer and travel across the step edge, which explains that a similar frequency is observed in the spectrum of the reattachment location. In addition, there are energetic disturbances with higher frequencies related to the turbulence when the flow reattaches on the wall.

The second group of parameters is mainly related to the low-frequency unsteadiness. Figure 4.18 displays the temporal evolution of the spanwise-averaged separation point, separation shock angle and separation bubble volume, as well as their frequency-weighted power spectral density. The calculation of the separation point, shock angle and bubble volume is the same with that for the BFS cases (see section 3.3.3). The

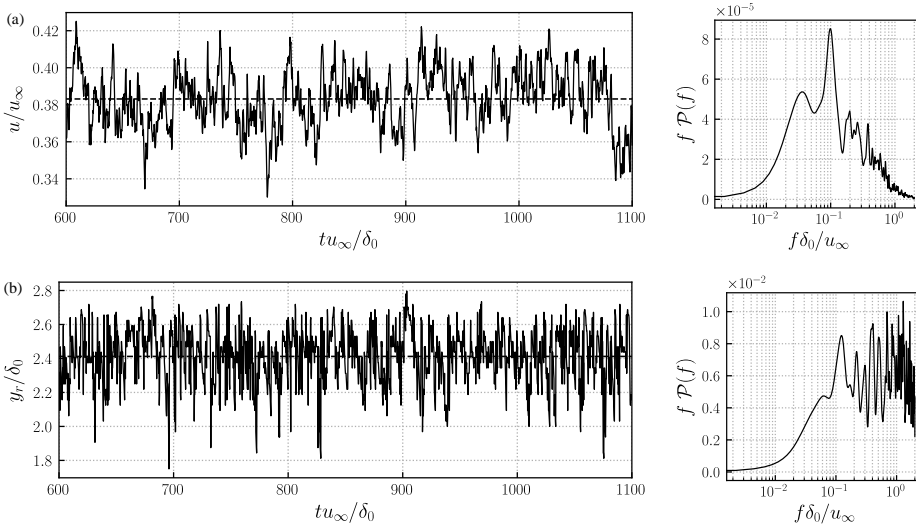


Figure 4.17: Temporal evolution and corresponding frequency weighted power spectral density of (a) streamwise velocity within the shear layer at  $x/\delta_0 = -11.0625$ ,  $y/\delta_0 = 2.5$  and (b) the spanwise-averaged reattachment location (case FTB). The black dashed line signifies the mean value.

curve of the mean separation point follows a sawtooth-like trajectory, along which its value drops drastically when the separation point moves upstream while it undergoes a less rapid relaxation when the separation position shifts downstream. The irregular and aperiodic variation of the separation shock angle suggests that the shock flapping involves a range of time scales, as reported by Dussauge *et al.* [182] and Priebe *et al.* [98], although the dominant one is the low-frequency one. For the variation of the separation bubble volume, it shows less irregular features, which indicates that the bubble expands and shrinks mainly with a leading frequency. In the PSD spectra, we observe a significant low-frequency peak between  $St_\delta = 0.02 \sim 0.05$  for these parameters. Since the separation shock is directly related to the separation of the boundary layer, it is reasonable that these signals share a peak at common frequencies. In addition, there exists a small peak at a medium frequency  $St_\delta \approx 0.1$  for the separation point. It is reasonable to assume that this parameter shares common frequencies with the shear layer velocity because the vortex shedding is usually initiated by the separation of the shear layer.

The statistical connection between the low-frequency signals can be quantified through coherence  $C_{xy}$  and phase  $\theta_{xy}$ . We first calculate the coherence and phase between the separation location and shock angle, as shown in figure 4.19. There is a significant low-frequency peak observed in the spectrum of the coherence. The high coherence of  $C = 0.32$  at  $St_\delta = 0.035$  indicates that the separation point and shock are nonlinearly related to each other at the low-frequency part. Moreover, a high value of coherence ( $C = 0.33$ ) is found at the frequency  $St_\delta = 0.15$ , which is attributed to the effects of the shedding shear layer vortices. In addition, these two signals are approximately out of phase, as can be seen from the high level of  $\theta$ . The

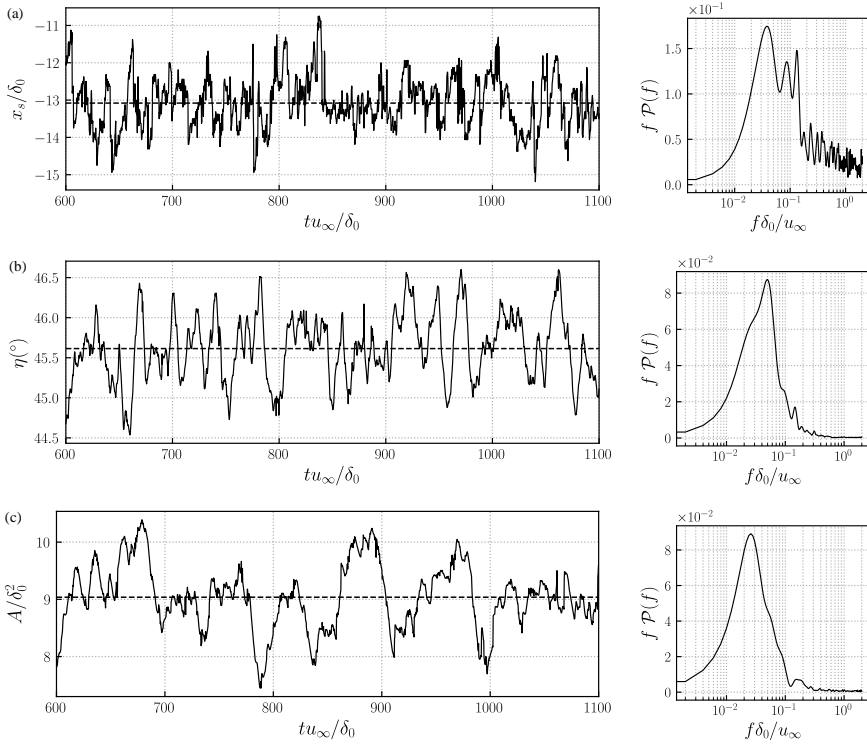


Figure 4.18: Temporal evolution and corresponding frequency weighted power spectral density of spanwise-averaged (a) separation location, (b) separation shock angle and (c) volume of the main separation bubble per unit spanwise length  $A$  (case FTB). The black dashed line signifies the mean value.

statistical connection between the separation location and the main bubble volume is also provided, displayed in figure 4.20. Similarly, a notable coherence ( $C = 0.18$ ) is observed in the low-frequency range at  $St_\delta = 0.03$  and these two signals are also out of phase. The high levels of coherence at higher frequencies ( $St_\delta > 0.2$ ) is related to the shedding vortices and turbulent structures.

The spectral and statistical analysis suggests that the low-frequency unsteady motions are related to the breathing of the main separation bubble and the flapping of the separation shock, and that these unsteady motions are coupled to each other. In addition, the shedding vortices of the shear layer are responsible for the medium-frequency unsteadiness. To decouple the various frequency scales of the interaction system and track the origin of the intrinsic unsteady behavior, a mode decomposition analysis is demanded, which is the objective of the following section.

#### 4.3.4. DMD ANALYSIS OF THE THREE-DIMENSIONAL FLOW FIELD

We use again dynamic mode decomposition to identify the different dynamics contributing to the coupled broadband frequency spectrum. In section 4.3.3, we observed

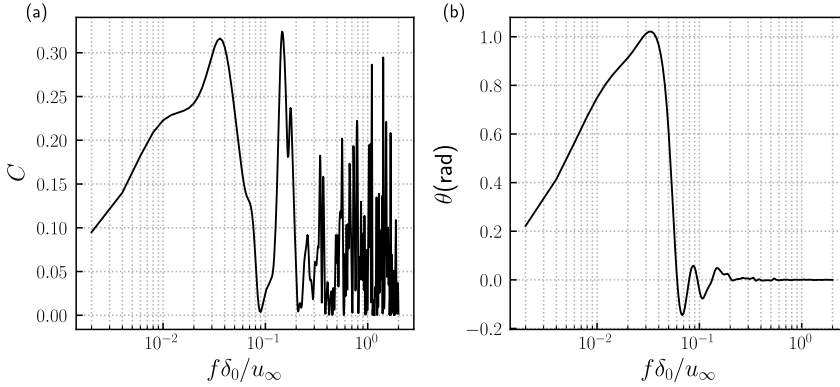


Figure 4.19: Statistical relation between the spanwise-averaged separation point and the shock angle: (a) coherence and (b) phase (case FTB).

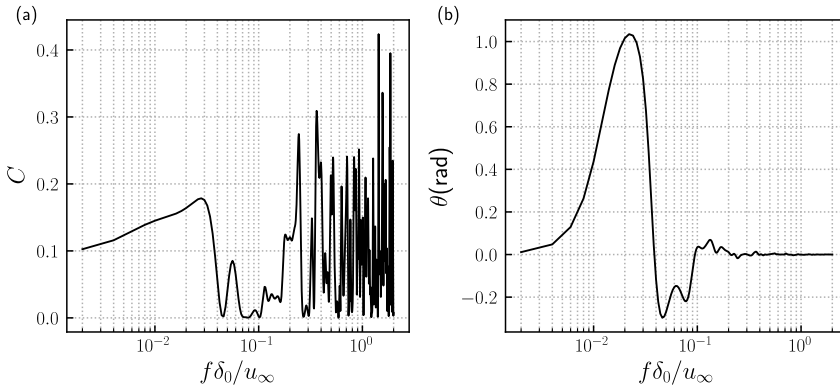


Figure 4.20: Statistical relation between the spanwise-averaged separation shock angle and the volume of separation bubble: (a) coherence and (b) phase (case FTB).

two types of frequencies for different unsteady behavior. However, part of the signals were extracted from the spanwise-averaged field, like reattachment location, bubble volume and shock angle; thus spanwise unsteady features may be missing from the two-dimensional flow field and a three-dimensional DMD analysis is required. A spatial subdomain is extracted from the simulated flow domain for the three-dimensional DMD analysis in order to reduce the computational cost. The subdomain is  $L_x \times L_y \times L_z = [-25, 15] \times [0, 8] \times [-8, 8]\delta_0$ , covering the most interesting region, with a downsampled spatial resolution in all directions. Since the frequencies above the characteristic frequency of the turbulent integral scale  $u_\infty/\delta_0$  are not of our current interest, the present DMD analysis of the three-dimensional subdomain is performed based on 1000 equal-interval snapshots with the same time range as the previous signals and a smaller sampling frequency  $f_s\delta_0/u_\infty = 2$ , which yields a frequency resolution  $1 \times 10^{-3} \leq \Delta f \leq 1$ .

The calculated eigenvalue spectrum and magnitudes of the corresponding DMD modes are displayed in figure 4.21. The resulting DMD modes come as complex conjugate pairs and most of them are well distributed along the unit circle  $|\mu_k| = 1$  except a few decaying modes within the circle, which means the resulting modes are sufficiently saturated [167]. In figure 4.21(b), the shown modes are shaded by the growth rate  $\beta_k$ . Here, the strongly decaying modes ( $|\mu_k| \leq 0.96$ ) have been removed because they do not contribute to the long-time flow development. The darker the vertical lines are, the less decaying the modes are.

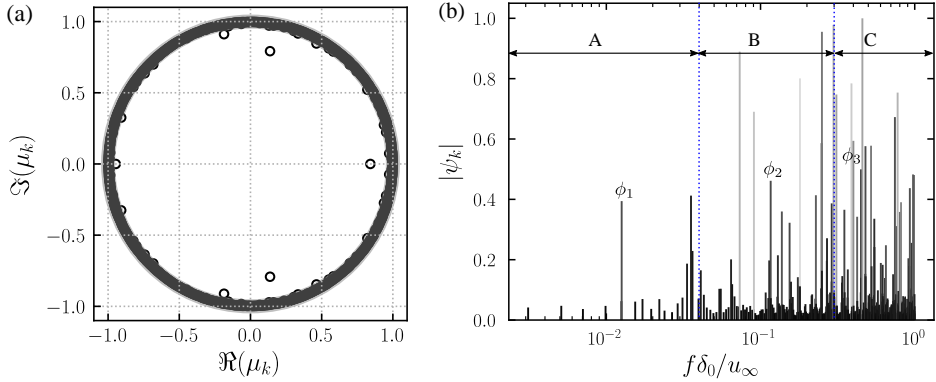


Figure 4.21: (a) Eigenvalue spectrum from the standard DMD and (b) normalized magnitudes for DMD modes with positive frequency, colored by the growth rate  $\beta_k$  (case FTB).

From the previous spectral analysis, two types of frequencies are identified. These frequencies are also significant in figure 4.21(b). Therefore, two corresponding branches of modes are extracted from the spectrum, a low-frequency branch at  $St_\delta < 0.04$  (branch A) and a medium-frequency branch at  $0.04 \leq St_\delta \leq 0.3$  (branch B), by examining the features of modal fluctuations from each mode. In addition, an extra branch of modes at  $St_\delta > 0.3$  (branch C, close to the characteristic frequency of the turbulent integral scale) is also analyzed. Based on the growth rate and magnitudes of the modes, three modes are selected from the frequency spectrum, each of which representative of a single branch, marked as mode  $\phi_1$ ,  $\phi_2$  and  $\phi_3$ , respectively. Table 4.4 gives the non-dimensional frequency, magnitude and growth rate of these selected modes. All of them have relatively large magnitude with  $|\psi_k| > 0.3$  and small growth rate with  $|\beta_k| < 0.02$  [relatively darker in figure 4.21(b)], which indicates that they have a relevant contribution to the evolution of the flow field over the full analyzed time span.

For the group of lower frequencies, mode  $\phi_1$  is the selected representative for illustrating the flow dynamics. Figure 4.22 shows the pressure fluctuations from mode  $\phi_1$  at two different phase angles. The main features of the pressure fluctuations are structures along the separation shock and the reattachment shock. The sign switch at the two phase angles indicates the oscillation of the shock. Note that the fluctuations around the separation and reattachment shock are also changing in the spanwise direction, suggesting a slight wrinkling of the shocks. Figure 4.23(a) provides the pressure

Table 4.4: Information of the selected modes

Mode	$St_\delta$	$ \psi_k $	$\beta_k$
$\phi_1$	0.01257	0.39418	-0.017209
$\phi_2$	0.11636	0.46151	-0.016515
$\phi_3$	0.44869	0.49939	-0.012177

fluctuations of  $\phi_1$  at the slice  $z = 0$ . Again, large fluctuations are observed around the separation and reattachment shock. There are also waves induced by the separation shock propagating along the streamwise direction.

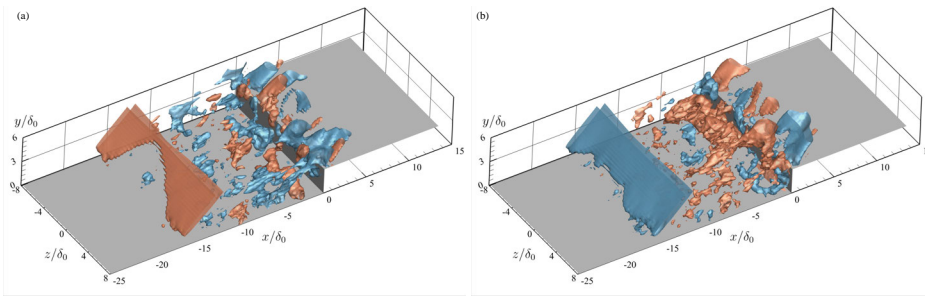


Figure 4.22: Isosurfaces of the pressure fluctuations from DMD mode  $\phi_1$  with phase angle (a)  $\theta = 0$  and (b)  $\theta = 3\pi/4$  (case FTB), only including the real part (red:  $p'/p_\infty = 0.03$ , blue:  $p'/p_\infty = -0.03$ ).

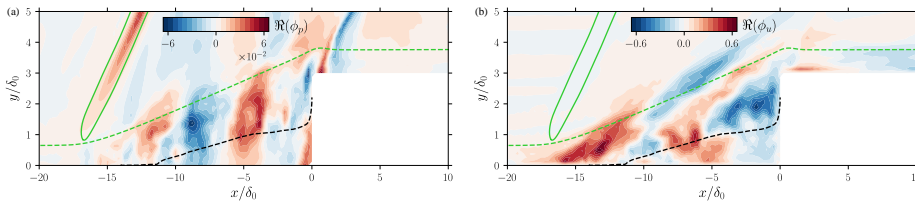


Figure 4.23: Real part of DMD mode  $\phi_1$  indicating contours of modal (a) pressure fluctuations and (b) streamwise velocity fluctuations on the slice  $Z = 0$  (case FTB). The green solid line indicates the mean separation shock. The black dashed line signifies the dividing line. The green dashed line represents the streamline passing through  $x/\delta_0 = 0$ ,  $y/\delta_0 = 3.75$ .

The fluctuations of the streamwise velocity component from DMD mode  $\phi_1$  are given in figure 4.24. We observe longitudinal streamwise structures, which emerge around the separation location and extend in the shear layer and into the downstream boundary layer. From the contours of the streamwise velocity fluctuations on the  $z = 0$  slice, figure 4.23(b), we found that these high- and low-speed structures are mainly located above the separation bubble. In addition, weak fluctuations in the upstream turbulent boundary layer are also identified.

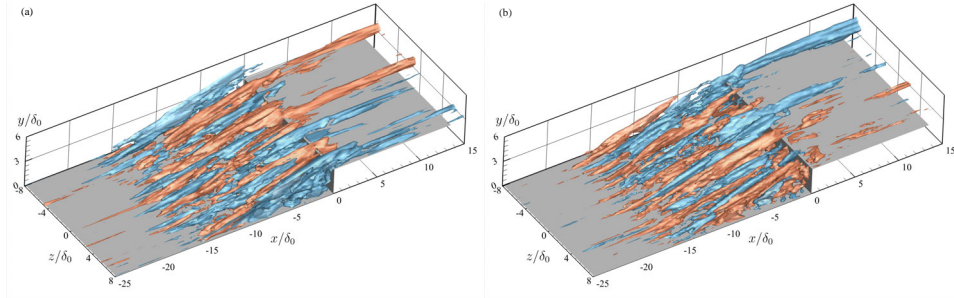


Figure 4.24: Isosurfaces of the streamwise velocity fluctuations from DMD mode  $\phi_1$  with phase angle (a)  $\theta = 0$  and (b)  $\theta = 3\pi/4$  (case FTB), only including the real part (red:  $u'/u_\infty = 0.2$ , blue:  $u'/u_\infty = -0.2$ ).

## 4

The streamwise-elongated structures could be the signature of counter-rotating Görtler-like vortices. Therefore, we plot the contours of the modal streamwise vorticity and projected streamlines at two phase angles, as shown in figure 4.25. The counter-rotating Görtler-like vortices are clearly illustrated by the arrow streamlines. Additionally, these vortices move in both the spanwise and wall-normal directions, and their strength is also changing with phase angle. At the given instants ( $\theta = 3\pi/16$  and  $\theta = 7\pi/16$ ), the spanwise wavelength of the vortex pair is ranging from  $1.5\delta_0$  to  $1.7\delta_0$ . Based on these observations, we believe that the dynamics represented by the low-frequency mode  $\phi_1$  involves the flapping motions of the separation and reattachment shock, as well as oscillating Görtler-like vortices in the shear layer. Other modes from the low-frequency branch A were found to share very similar flow features with mode  $\phi_1$ .

For the medium-frequency mode  $\phi_2$ , the pressure isosurfaces in figure 4.26 show large spanwise structures along the free shear layer. These fluctuations along the shear layer represent the travelling of the shear-layer vortices. In the contours of modal spanwise-averaged pressure fluctuations in figure 4.27, the radiation of the Mach waves along the shear layer is easier to observe. The emission of these waves induces large disturbances along the streamwise direction in the supersonic part of the flow field. The propagation of the Mach waves is in agreement with the results from a global linear stability analysis of an impinging shock case in a laminar regime [183].

Figure 4.28 shows isosurfaces of the streamwise velocity fluctuations associated with mode  $\phi_2$ . The  $\Lambda$ -shaped structures are observed in the free shear layer and alternate along both the spanwise and streamwise directions. Based on these observations, we believe this mode represents the convection of the shear layer vortices. Similar observations were also reported in the two-dimensional DMD analysis of an incident shock case [99].

Considering the high-frequency mode  $\phi_3$ , the pressure fluctuations provided in figure 4.29 show the evolution of the small-scale arc-shaped vortices. These spanwise-aligned vortices are generated from the separation region. The streamwise displacement of the fluctuations contours at different phase angles indicates the convection of the coherent vortices.

For the streamwise velocity fluctuations of mode  $\phi_3$  in figure 4.30, we can also observe the convection behavior of small arc-shaped vortices. These vortices originate

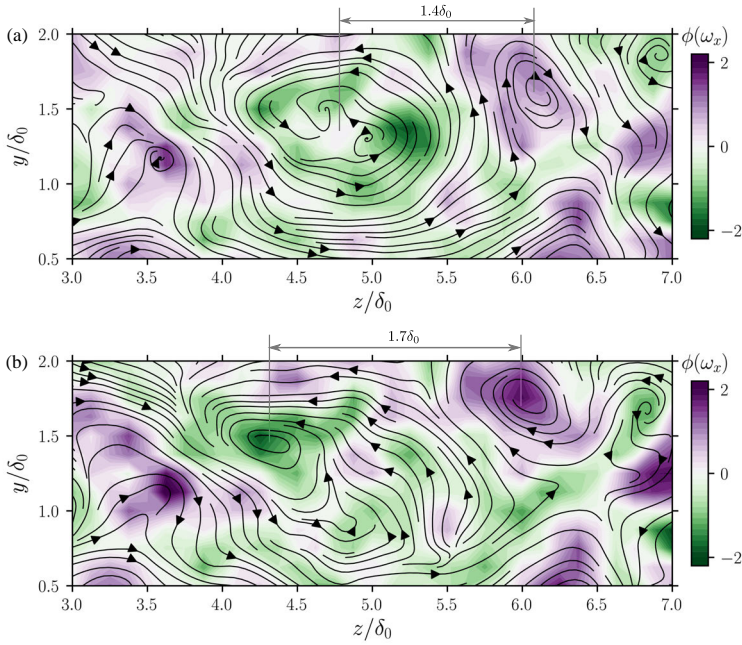


Figure 4.25: Contours of the streamwise vorticity from DMD mode  $\phi_1$  with phase angle (a)  $\theta = 3\pi/16$  and (b)  $\theta = 7\pi/16$  in the  $z - y$  plane at  $x/\delta_0 = -6.0$  (case FTB). Black arrow lines represent the streamlines on the slice.

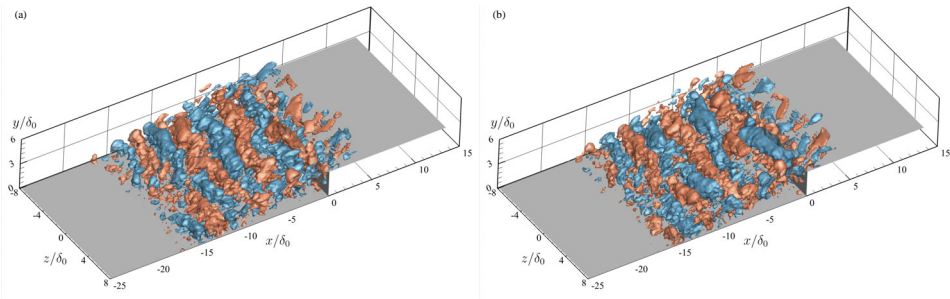


Figure 4.26: Isosurfaces of the pressure fluctuations from DMD mode  $\phi_2$  with phase angle (a)  $\theta = 0$  and (b)  $\theta = 3\pi/4$  (case FTB), only including the real part (red:  $p'/p_\infty = 0.03$ , blue:  $p'/p_\infty = -0.03$ ).

from the upstream turbulence and are considerably amplified in the separated shear layer. Additionally, this mode shows less anisotropic features, compared with the other two modes. The frequency of this mode is close to the typical frequency of the turbulence considering the thicker boundary layer downstream of the step. Thus, we consider this mode to be associated with the convection of typical turbulent structures that result from an amplification of the incoming turbulence by the separation bubble, cf. the stability analysis of Guiho *et al.* [183] for an incident shock SWBLI case.

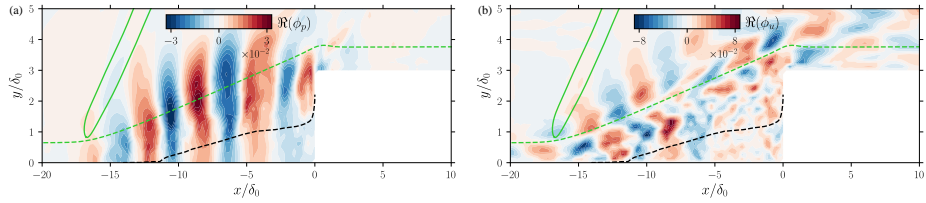


Figure 4.27: Real part of DMD mode  $\phi_2$  indicating contours of modal spanwise-averaged (a) pressure fluctuations and (b) streamwise velocity fluctuations on the slice  $Z = 0$  (case FTB). The green solid line indicates the mean separation shock. The black dashed line signifies the dividing line. The green dashed line represents the streamline passing through  $x/\delta_0 = 0, y/\delta_0 = 3.75$ .

4

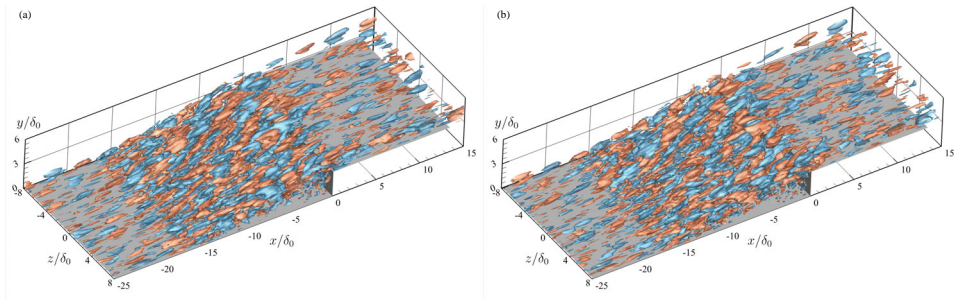


Figure 4.28: Isosurfaces of the streamwise velocity fluctuations from DMD mode  $\phi_2$  with phase angle (a)  $\theta = 0$  and (b)  $\theta = 3\pi/4$  (case FTB), only including the real part (red:  $u'/u_\infty = 0.2$ , blue:  $u'/u_\infty = -0.2$ ).

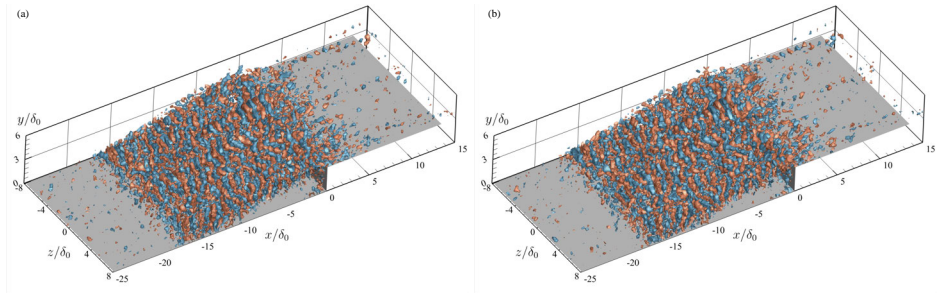


Figure 4.29: Isosurfaces of the pressure fluctuations from DMD mode  $\phi_3$  with phase angle (a)  $\theta = 0$  and (b)  $\theta = 3\pi/4$  (case FTB), only including the real part (red:  $p'/p_\infty = 0.06$ , blue:  $p'/p_\infty = -0.06$ ).

#### 4.3.5. PHYSICAL MECHANISM OF LOW-FREQUENCY UNSTEADINESS

The present FFS case shows unsteady behavior at similar low frequencies as those observed for SWBLI on flat plates, compression ramps and BFS. Similar to the compression ramp, the flow topology of the FFS case is encompassed by a separation shock, free shear layer and reattachment shock. In terms of the mean skin friction in figure 4.11, the recirculating flow is less uniform upstream of the separation region, than observed in the canonical impinging shock and ramp cases. The fluctuations of  $\langle C_f \rangle$  inside the separation bubble are usually related to the low-frequency unsteadiness [98, 99].

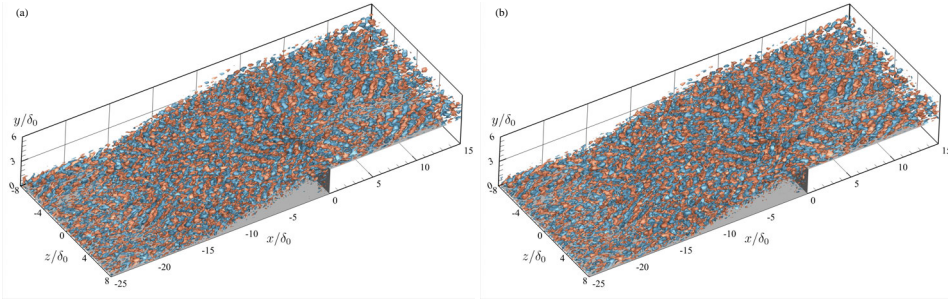


Figure 4.30: Isosurfaces of the streamwise velocity fluctuations from DMD mode  $\phi_3$  with phase angle (a)  $\theta = 0$  and (b)  $\theta = 3\pi/4$  at slice  $z = 0$  (case FTB), only including the real part (red:  $u'/u_\infty = 0.4$ , blue:  $u'/u_\infty = -0.4$ )

However, there is a drastic drop of  $\langle C_f \rangle$  downstream of the separation bubble caused by the step wall for the FFS case, which is not observed in the ramp and incident shock cases [164, 176]. The wall pressure is also increasing across the separation bubble as observed in the ramp and impinging shock cases, but has a significant drop at the step corner. The differences of the mean flow parameters probably suggest that there could be some different low-frequency features among these case.

The instantaneous flow field shown in section 4.3.2 visualize the main unsteady phenomena, including the high- and low-speed streaks, breathing bubble, and the oscillation of the separation and reattachment shock, as well as the shear layer. These unsteady flow features are also reported in the ramp and impinging shock cases. From the spectral analysis, we distinguish two kinds of low-frequency unsteadiness in the interaction region. The lower frequencies are related to the coupling of the separation bubble and shock waves. Furthermore, the DMD analysis of the three-dimensional flow field successfully decoupled the different dynamics associated with the low-frequency interaction. Moreover, the low-frequency mode  $\phi_1$  from DMD also identifies unsteady counter-rotating vortices. These Görtler-like vortices are relatively weak compared with other unsteady dynamics such that they do not show up in the vortical visualization of figure 4.8. Similar observations have been reported in the impinging shock and ramp cases, as well as in our BFS cases.

We believe that the FFS case has the same low-frequency mechanism as proposed in section 3.5.5 for the BFS case. Figure 4.31 shows the curvature  $\delta_0/R$  and Görtler number  $G_t$  along the streamline of the mean flow inside the shear layer (shown in figure 4.23). As we can see, two distinct peaks are observed in the variation of the curvature, located around the separation and reattachment points. This strong curvature induces strong Görtler instability, corresponding to the high levels of  $G_t$  around the separation and reattachment locations. At  $19 \leq x/\delta_0 \leq -10$  and  $0 \leq x/\delta_0 \leq 3$ , the Görtler number is larger than the critical value  $G_t = 0.6$ , above which local Görtler vortices will emerge for a laminar flow [78]. The streamwise velocity fluctuations (figure 4.24) and streamlines (figure 4.25) from DMD mode  $\phi_1$  visualize these Görtler-like vortices.

In terms of the magnitude of the low frequencies, the current results for a FFS yield a Strouhal number range of  $0.02 < St_r < 0.52$  (normalized by the separation length), close to the frequencies obtained in the BFS case, which is two or three times larger than the

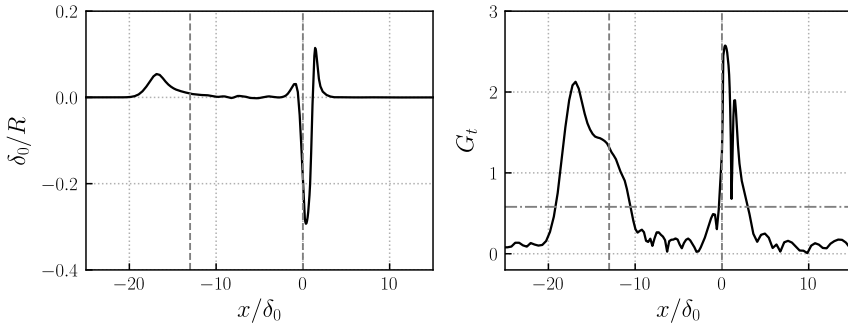


Figure 4.31: Curvature  $\delta_0/R$  and Görtler number  $G_t$  along the mean streamline passing through  $x/\delta_0 = 0$  and  $y/\delta_0 = 3.75$  (case FTB). Vortical dashed lines indicate the separation and reattachment point. The horizontal dot-dashed line denotes the critical  $G_r$  in a laminar flow.

4

values of other canonical cases. The higher frequency in the FFS case is also caused by the confinement of the step wall, which results in a fixed reattachment location, as we analyzed in section 3.5.5. Therefore, the Görtler vortices induced by the strong curvature around the separation and reattachment location are the main driver for the low-frequency unsteadiness of SWBLI in the FFS case. The weak dependence of the unsteadiness on the upstream fluctuations is also observed in the DMD analysis (figure 4.23). Moreover, both the laminar and turbulent cases that were analysed here have the same physical mechanism because the incoming boundary layer is already turbulent in the interaction region, even for the laminar inflow case.

#### 4.3.6. SUMMARY

The low-frequency unsteady dynamics of the SWBLI over a FFS is scrutinized at  $Ma = 1.7$  and  $Re_{\delta_0} = 13718$  using a well-resolved LES. The main flow topology of the SWBLI region, as shown in the mean flow field, contains a separation shock, a main separation bubble in front of the step, a centered Prandtl-Meyer expansion fan and a reattachment shock. The instantaneous vortical visualizations indicate that the unsteady behavior is similar to what we observe in the BFS case, including the vortex shedding in the separated shear layer, the breathing of the separation bubble and the flapping shock motion. From the spectral analysis, we observe that there is a broadband low-frequency motion in the interaction region, which we classify into two branches with the dominant frequencies at  $St_\delta = 0.01 \sim 0.05$  and  $St_\delta = 0.06 \sim 0.3$  in the current FFS case. The medium-frequency contents are associated with the shedding of shear layer vortices, and the lower frequency dynamics connects to the unsteady volume of the separation bubble, as well as the shock angle.

Three-dimensional DMD analysis was applied to identify the individual single-frequency mode that contributes to the observed unsteady behavior. Similar to what we observed in the BFS case, the extracted low-frequency mode  $\phi_1$  suggests that there is a statistical link between the shock motions (shown by pressure fluctuations) and the unsteady Görtler-like vortices (shown by the streamwise velocity fluctuations) along

the shear layer. These counter-rotating vortices are visualized in the contours of the modal streamwise vorticity in figure 4.25. The flow features displayed by the medium-frequency mode  $\phi_2$  represents the shedding behavior of the shear-layer vortices and the radiation of the induced Mach waves.

Based on the above observation and combined with the discussion in chapter 3, we believe that the physical mechanism of the low-frequency unsteadiness in the FFS is the same as for the BFS case, i.e, the unsteady Görtler-like vortices in the shear layer impose an unsteady forcing that sustains the low-frequency motions of shocks and separation bubble.



# 5

## CONCLUSIONS AND OUTLOOK

*One with understanding is not as good as one with interest,  
which in turn is not as good as doing something one enjoys.*

知之者不如好之者，好之者不如乐之者

Analects of Confucius  
论语

## 5.1. TRANSITION MECHANISMS

The transition mechanism behind a backward/forward-facing step in the supersonic regime at  $Ma = 1.7$  and  $Re_{\delta_0} = 13718$  was investigated using large-eddy simulation. For each geometry, different inflow conditions were considered: a fully laminar case and two perturbed cases with different levels of (unstable) oblique T-S waves. First, the transition path of the fully laminar case was scrutinized. For both BFS and FFS cases, the boundary layer transition consists of the growth of primary instabilities, the excitation of secondary modal instabilities, breakdown of various vortices and finally the turbulent state. However, there are certain differences of the transition path between these two configurations. Specifically, for the BFS case, the primary instability involved is mainly the K-H modes of the separated shear layer, while the oblique T-S waves are the primary instability for the FFS cases. The transition process behind the BFS is initiated by a K-H instability of the separated shear layer, followed by secondary modal instabilities of the K-H vortices, leading to  $\Lambda$ -shaped vortices, hair-pin vortices and finally to a fully turbulent state. The laminar-to-turbulent transition basically begins behind the step and is completed shortly downstream of the reattachment. For the FFS case, the boundary layer transition begins with the growth of the T-S waves and the relevant spanwise vorticity, followed by the development of  $\Lambda$ -shaped and hairpin vortices, the formation of the turbulent spots and finally a fully turbulent boundary layer. This transition process follows a typical natural transition path induced by the T-S waves. Due to the upstream influence of the FFS, the upstream disturbances are additionally amplified such that the boundary layer is already turbulent (though not yet in its equilibrium state) in front of the separation bubble. Then the disturbances undergo a significant amplification in the shear layer and the boundary layer becomes more energetic behind the main separation bubble (step wall). In contrast, for the BFS case, the upstream amplification effects are restricted by the step and therefore the boundary layer is still in the laminar regime before the separation.

Influence of upstream disturbances on the evolution of the boundary layer was also investigated. The imposed T-S waves have significantly different effects on the laminar-to-turbulent transition for the BFS and FFS cases. For the BFS configuration, case BLA (imposed with low-amplitude T-S waves) shares a similar transition road map with the fully laminar case BZA, with transition occurring in the separated shear flow behind the step. For the case BLA, specifically, the linear growth of the oblique T-S waves is the prevailing instability upstream of the step. Both T-S and K-H modes act as the primary mode within a short distance behind the step and undergo a quasi-linear growth with a weak coupling. Upon pairing of the large K-H vortices, subharmonic waves are produced, and secondary instabilities begin to dominate the transition. Simultaneously, the growth of T-S waves is retarded by slow resonance between subharmonic K-H and secondary instabilities. The vortex breakdown and reattachment downstream further contribute to the development of the turbulent boundary layer. In contrast, the case BHA (imposed with high-amplitude oblique T-S waves) shows a rapid modal transition due to the high initial disturbance level, such that the boundary layer transition already occurs upstream of the step in a typical natural path, before the K-H instability could get involved. For the FFS configuration, the imposed T-S waves appear not to affect the laminar-to-turbulent transition path regardless of the amplitude of the initial disturbances. In all laminar and

transitional cases of the FFS, the upstream T-S modes are significantly amplified by the feedback waves from the separation region downstream, and therefore they all follow a typical modal transition induced by the T-S waves.

## 5.2. LOW-FREQUENCY UNSTEADINESS OF SWBLI

The unsteady behavior behind a backward/forward-facing step at  $Ma = 1.7$  and  $Re_{\delta_0} = 13718$  was studied thoroughly, especially in the turbulent regime. For the BFS case, the unsteady system involves the vortex shedding in the shear layer, the flapping motions of the reattachment shock, the breathing of the separation bubble, streamwise streaks near the wall and arc-shaped vortices in the turbulent boundary layer downstream of the separation bubble. The FFS case share almost all these flow features with the BFS, but also has unique differences. For the FFS case, the streamwise streaks are located along the free shear layer and there is a separation shock in front of the separation bubble. The flow topology of the FFS configuration resembles the main flow patterns of the compression ramp cases. For both BFS and FFS cases, the interaction system features a broadband low-frequency dynamics. The spectral analysis reveals that the low-frequency behavior of both configurations is related to the interaction between shock wave and separated shear layer, while the medium-frequency motions are associated with the shedding of shear layer vortices.

The driving force of the low-frequency unsteadiness was further scrutinized using a three-dimensional dynamic mode decomposition. Based on the extracted DMD modes, we analyzed the individual contributions of each mode to the unsteadiness of SWBLI. For both configurations, the low-frequency mode provides evidence for the statistical link between the shock motions and streamwise-elongated vortices in the interaction region. Compared to SWBLI in flat plate and ramp configurations, slightly higher non-dimensional frequencies (based on the separation length) of the low-frequency modes are observed, as shown in table 5.1. Combined with the streamwise evolution of the Görtler number (larger than the critical value  $G_t = 0.6$  around the reattachment location, see table 5.1), we believe that the physical mechanism of the low-frequency unsteadiness is very similar or the same for BFS and FFS. In this theory, Görtler-like vortices, which are induced by the centrifugal forces originating from the strong curvature of the streamlines in the reattachment region (BFS case) or separation region (FFS case), are strongly correlated with the low-frequency unsteadiness of the interaction system. Our DMD analysis of the turbulent BFS flow and the comparison with an identical but laminar case provide evidence that these unsteady Görtler-like vortices are affected by upstream fluctuations in the incoming boundary layer.

## 5.3. OUTLOOK IN LAMINAR-TO-TURBULENT TRANSITION

For the current flow configuration, the laminar-to-turbulent transition behind a BFS is mainly initiated by the growth of the primary K-H instability, while the transition is induced by the amplification of the primary T-S waves in the FFS case. However, the transition path and the possibly involved instabilities vary if the flow or geometry parameters are different [46, 52]. The step height, relative to the boundary layer thickness, and free-stream Reynolds number are relatively important ones among the

Table 5.1: Aerodynamics parameters as well as Strouhal number range and maximum Görtler number  $G_t$  around the reattachment location.

References	$Ma_\infty$	$Re_\delta$	$L_r/\delta$	$St_r$	$G_t$	configuration
Pasquariello <i>et al.</i> [99]	3.0	203000	15.5	0.01 ~ 0.14	1.2	impinging shock
Priebe <i>et al.</i> [98]	2.9	43808	3.0	0.01 ~ 0.1	1.3	ramp
Present case BTB	1.7	13718	8.8	0.03 ~ 0.6	1.3	BFS
Present case FTB	1.7	13718	13.0	0.02 ~ 0.52	2.5	FFS

parameters in supersonic flows. By exploring the relationship between the transition process and flow configuration, a simple physical criterion or model could be proposed to predict the laminar-to-turbulent transition over a BFS/FFS. Therefore, the following proposals are recommended for further study.

### 5.3.1. EFFECTS OF THE STEP HEIGHT

For the BFS configuration, the dominant instability of the transitional flow may be centrifugal forces, lift-up effects or K-H instability depending on the relative step height, as reported in the literature [194, 195]. In the current BFS cases, the step height is three times larger than the inlet boundary layer thickness, which is sufficiently large to excite strong K-H vortices that form the main factor to induce the laminar-to-turbulent transition. If the step height is decreased to a value considerably smaller than the boundary layer thickness, the incoming boundary layer probably remains attached and thus K-H waves may not be initiated [70]. Under these circumstance, the transition process follows a more conventional modal transition dominated by the evolution of the T-S modes [66]. Similarly, for the FFS, the oncoming boundary layer is just disturbed by the step but no (appreciable) separation may take place when the step height is relatively small. Correspondingly, the boundary layer transition is accelerated due to the larger growth rate of T-S waves [46]. On the other hand, when the step height is strikingly increased, besides the K-H waves, strong centrifugal forces are produced by the large curvature of the streamlines. In this situation, the boundary layer transition may be dominated by the development of Görtler instability [17]. For the FFS configuration with a large step height, Görtler instability could also become one of the dominant instabilities. To determine the specific transition path and the evolution of various instabilities involved for the BFS/FFS cases with different step heights, further investigation is highly recommended.

### 5.3.2. EFFECTS OF REYNOLDS NUMBER

Free-stream Reynolds number is also one of the main parameters which have impacts on the laminar-to-turbulent transition. Existing studies reported that the mean separation length varies with the unit Reynolds number for the BFS/FFS flow [68, 154, 196]. If the separation length is too small (usually at a high Reynolds number), the large-scale K-H vortices may not be fully developed due to the short residence time of the flow in the shear layer [180]. The boundary layer transition thus may be dominated by the rapidly growth of the T-S waves. On the other hand, the T-S instability is one of the

viscous instabilities and is significantly affected by the Reynolds number [25]. When the Reynolds number is very close to the critical Reynolds number, the unstable region of the T-S waves is extremely small and the boundary layer easily becomes unstable due to large growth rate of the T-S waves. In this situation, the boundary layer transition is likely to be dominated by the rapid growth of the T-S waves in spite of the strong K-H instability induced by the step. Based on the analysis from these two aspects, the effects of Reynolds number should be considered for identifying the transition path and assessing the role of different instabilities behind the BFS/FFS.

### 5.3.3. CRITICAL STEP HEIGHT

From the investigation of the subsonic step cases by Duncan Jr [46], a critical step height, which is a function of the unit Reynolds number, is reported. When the step height exceeds the critical value, the evolution of the K-H instability is the main driver of the laminar-to-turbulent transition; otherwise, the amplification of the T-S waves dominates the transition. Similarly, we expect that there also exists a critical step height for the transition mechanism in supersonic flows. Based on a comprehensive study of the above considerations, i.e, the effects of the step height and Reynolds number on the laminar-to-turbulent transition over a BFS/FFS, a critical step height could be found. Furthermore, an approximate correlation between the step height and the unit Reynolds number would be established. This relationship could provide an instructive guideline to predict the transition mechanism or select an appropriate physical model for simulating the transition in a BFS/FFS supersonic flow. From the perspective of engineering practice, we could limit the height of the skin joints at least smaller than the critical value for the purpose of delaying the laminar-to-turbulent transition over airfoils because the initial growth rate of K-H waves is usually larger than that of T-S waves.

## 5.4. OUTLOOK IN SWBLI

In the supersonic BFS/FFS flow, there are various large-scale unsteady motions with a broadband low-frequency spectrum. This unsteadiness introduces significant fluctuations of pressure and temperature around the interaction region, which can cause intense localized mechanical and thermal loads, and even the failure of material and structural integrity [3]. To alleviate or eliminate the negative effects caused by SWBLI, a variety of flow control techniques have been developed, where one may distinguish between passive and active methods [15, 197, 198]. For the BFS/FFS configuration with a notable step height, the flow separation and the accompanying shock formation may be unavoidable, and thus the effects of controlling separation and shock are probably relatively limited. It is reasonable that we set the main objective of SWBLI control as diminishing the amplitude of the low-frequency oscillations in the BFS/FFS flow.

Based on our current investigation, we concluded that unsteady Görtler-like vortices are strongly correlated with the low-frequency unsteadiness. One of the ideas for an effective flow control method is to exchange the near-wall high and low momentum produced in the interaction region [15]. In terms of the passive control techniques, the micro vortex generator, like micro-ramps, is one of the popular options. In the PIV experiments of Blinde *et al.* [199], they reported that the micro-ramps can induce

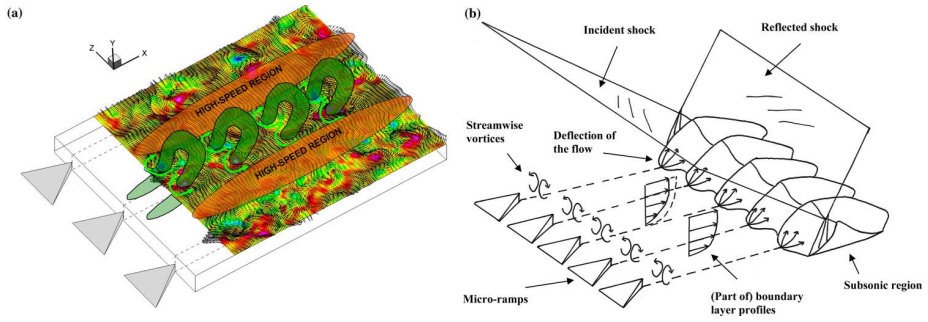


Figure 5.1: Conceptual sketch of the controlled interaction using micro-ramps: (a) presence of the vortex structures downstream of micro-ramps, and high-speed regions at intermediate locations, (b) conceptual model [199].

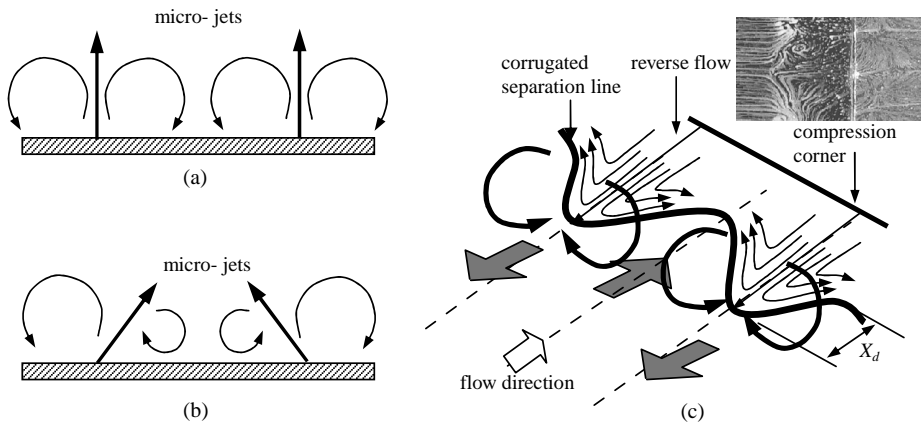


Figure 5.2: Schematic of the expected control effects generated by the microjets at a pitch angle equal to (a)  $90^\circ$  and (b)  $45^\circ$ . (c) the proposed evolution of the flow topology in the interaction region [200].

counter-rotating vortices along the wake. Based on their conceptual control model, as shown in figure 5.1, high-speed streaks occur in the space between the adjacent micro-ramps, and low-speed streaks are produced behind the ramps. The vorticity induced by the vortex generator could suppress the Görtler-like vortices generated in the separation region by entraining high momentum fluid from the main flow and increasing the boundary layer velocity near the wall [198], which weakens the low-frequency unsteadiness of SWBLI. For better control effects, the micro-ramps should be placed in front of the regions with high-speed streaks of the original flow, and the spanwise distance between two adjacent micro-ramps is approximate to the spanwise wavelength of the Görtler-like vortices. In addition, the size and deflection angle of the micro-ramps must be carefully chosen to ensure the induced vortices featuring an appropriate strength and streamwise wavelength.

Passive control methods have been popular in the past because they do not require additional energy input. However, it only works well at certain conditions. In the

recent years, active flow control techniques, like micro-jets and plasma-based actuators, have attracted considerable attention due to their flexibility. For controlling the low-frequency unsteadiness of SWBLI driven by the unsteady Görtler-like vortices, the active flow control methods are theoretically more effective for various operating conditions. Verma and Manisankar [200] experimentally studied the control effects of micro-jets. They found that this active vortex generator can induce counter-rotating vortices near the wall, where the low-speed streaks occur right behind the micro-air-jets and high-speed streaks appear between them. It is observed that these micro-jets manage to reduce the amplitude of unsteady pressure fluctuations in the interaction region by an order of magnitude. In addition, the pitching angle of the micro-jets also has impact on the control effect of SWBLI. Kinefuchi *et al.* [201] reported that plasma-based actuator could induce momentum transfer from the main flow to the boundary layer and thus suppress the low-frequency unsteadiness. Same with other control techniques, several parameters of the actuator should be carefully chosen to achieve the desired effects, including the shape of jet-hole, electrical characteristics, frequency, etc. A schematic of the flow pattern in the interaction region is shown in figure 5.2. Although several studies have demonstrated the potential effectiveness of these flow control techniques, research about the optimization of the control parameters are still needed.



## REFERENCES

- [1] R. K. Agarwal, *Sustainable (green) aviation: Challenges and opportunities*, SAE International Journal of Aerospace **2**, 1 (2010).
- [2] H. M. Blackburn, D. Barkley, and S. J. Sherwin, *Convective instability and transient growth in flow over a backward-facing step*, Journal of Fluid Mechanics **603**, 271 (2008).
- [3] J. Détery and J.-P. Dussauge, *Some physical aspects of shock wave/boundary layer interactions*, Shock Waves **19**, 453 (2009).
- [4] K. Brown, N. Molinaro, T. Meyers, A. Borgoltz, W. Devenport, J. Luedke, and D. Pesetsky, *Sensitivity of wind turbine airfoil sections to geometry variations inherent in modular blades*, Wind Engineering **42**, 529 (2018).
- [5] V. Statnikov, T. Sayadi, M. Meinke, P. Schmid, and W. Schröder, *Analysis of pressure perturbation sources on a generic space launcher after-body in supersonic flow using zonal turbulence modeling and dynamic mode decomposition*, Physics of Fluids **27**, 16103 (2015).
- [6] O. Reynolds, *An experimental investigation of the circumstances which determine whether the motion of water shall be direct or sinuous, and of the law of resistance in parallel channels*, Philosophical Transactions of the Royal Society of London , 935 (1883).
- [7] E. Reshotko, *Boundary-layer stability and transition*, Annual Review of Fluid Mechanics **8**, 311 (1976).
- [8] I. Tani, *Boundary-layer transition*, Annual Review of Fluid Mechanics **1**, 169 (1969).
- [9] A. Fedorov, *Transition and stability of high-speed boundary layers*, Annual Review of Fluid Mechanics **43**, 79 (2011).
- [10] A. Ferri, *Experimental results with airfoils tested in the high-speed tunnel at Guidonia*, Tech. Rep. (NACA-TM-946, 1940).
- [11] H. W. Liepmann, *The interaction between boundary layer and shock waves in transonic flow*, Journal of the Aeronautical Sciences **13**, 623 (1946).
- [12] D. S. Dolling, *Fifty years of shock-wave/boundary-layer interaction research: what next?* AIAA Journal **39**, 1517 (2001).
- [13] G. E. Gadd, D. W. Holder, and J. D. Regan, *An experimental investigation of the*

- interaction between shock waves and boundary layers*, Proceedings of the Royal Society of London. Series A. Mathematical and Physical Sciences **226**, 227 (1954).
- [14] J. Green, *Interactions between shock waves and turbulent boundary layers*, Progress in Aerospace Sciences **11**, 235 (1970).
- [15] D. V. Gaitonde, *Progress in shock wave/boundary layer interactions*, Progress in Aerospace Sciences **72**, 80 (2015).
- [16] D. Lanzerstorfer and H. C. Kuhlmann, *Three-dimensional instability of the flow over a forward-facing step*, Journal of Fluid Mechanics **695**, 390 (2012).
- [17] D. Lanzerstorfer and H. C. Kuhlmann, *Global stability of the two-dimensional flow over a backward-facing step*, Journal of Fluid Mechanics **693**, 1 (2012).
- [18] H. Babinsky, J. K. H. K. Harvey, G. V. Candler, J.-F. Debiève, J. M. Détery, P. Dupont, J.-P. Dussauge, M. S. Holden, G. V. Inger, D. D. Knight, and A. A. Zheltovodov, *Shock Wave-Boundary-Layer Interactions* (Cambridge University Press, Cambridge, 2011).
- [19] E. Reshotko, *Transition Issues for Atmospheric Entry*, Journal of Spacecraft and Rockets **45**, 161 (2008).
- [20] M. V. Morkovin, *Transition in open flow systems: a reassessment*, Bull APS **39**, 1 (1994).
- [21] L. M. Mack, *Linear stability theory and the problem of supersonic boundary-layer transition*, AIAA Journal **13**, 278 (1975).
- [22] M. W. Tufts, *Computational investigation of sensitivity of the crossflow instability to two-dimensional surface imperfections*, Ph.D. thesis, Texas A&M University (2015).
- [23] I. E. Abdalla and Z. Yang, *Numerical study of the instability mechanism in transitional separating-reattaching flow*, International Journal of Heat and Fluid Flow **25**, 593 (2004).
- [24] J. Floryan, *On the Görtler instability of boundary layers*, Progress in Aerospace Sciences **28**, 235 (1991).
- [25] H. L. Reed, W. S. Saric, and D. Arnal, *Linear stability theory applied to boundary layers*, Annual Review of Fluid Mechanics **28**, 389 (1996).
- [26] P. J. Schmid and D. S. Henningson, *Stability and Transition in Shear Flows*, Applied Mathematical Sciences, Vol. 142 (Springer, New York, NY, 2001).
- [27] E. Reshotko and A. Tumin, *Spatial theory of optimal disturbances in a circular pipe flow*, Physics of Fluids **13**, 991 (2001).
- [28] W. S. Saric, *Visualization of different transition mechanisms*, Physics of Fluids **29**, 2770 (1986).
- [29] P. Andersson, M. Berggren, and D. S. Henningson, *Optimal disturbances and bypass transition in boundary layers*, Physics of Fluids **11**, 134 (1999).
- [30] E. Reshotko and A. Tumin, *Role of transient growth in roughness-induced transition*, AIAA Journal **42**, 766 (2004).
- [31] P. Paredes, M. M. Choudhari, and F. Li, *Blunt-body paradox and improved application of transient-growth framework*, AIAA Journal **56**, 2604 (2018).

- [32] K. L. Suder, J. E. O'Brien, and E. Reshotko, *Experimental study of bypass transition in a boundary layer*, Tech. Rep. (NASA-TM100913, 1988).
- [33] K. H. Sohn, *Experimental study of boundary layer transition with elevated freestream turbulence on a heated flat plate*, Ph.D. thesis, Case Western Reserve University (1991).
- [34] G. Balamurugan and A. C. Mandal, *Experiments on localized secondary instability in bypass boundary layer transition*, *Journal of Fluid Mechanics* **817**, 217 (2017).
- [35] H. Schlichting and K. Gersten, *Boundary-Layer Theory*, 9th ed. (Springer, Berlin, Heidelberg, 2017).
- [36] F. M. White, *Viscous fluid flow*, 3rd ed. (McGraw-Hill, New York, 2006).
- [37] C. S. J. Mayer, D. A. Von Terzi, and H. F. Fasel, *Direct numerical simulation of complete transition to turbulence via oblique breakdown at Mach 3*, *Journal of Fluid Mechanics* **674**, 5 (2011).
- [38] C.-L. Chang and M. R. Malik, *Oblique-mode breakdown and secondary instability in supersonic boundary layers*, *Journal of Fluid Mechanics* **273**, 323 (1994).
- [39] X. Chen, J. Chen, X. Yuan, G. Tu, and Y. Zhang, *From primary instabilities to secondary instabilities in Görtler vortex flows*, *Advances in Aerodynamics* **1**, 1 (2019).
- [40] W. S. Saric, H. L. Reed, and E. B. White, *Stability and transition of three-dimensional boundary layers*, *Annual Review of Fluid Mechanics* **35**, 413 (2003).
- [41] W. S. Saric, *Görtler Vortices*, *Annual Review of Fluid Mechanics* **26**, 379 (1994).
- [42] Z. Yang and P. R. Voke, *Large-eddy simulation of boundary-layer separation and transition at a change of surface curvature*, *Journal of Fluid Mechanics* **439**, 305 (2001).
- [43] Z. Yang, *Secondary instability of separated shear layers*, *Chinese Journal of Aeronautics* **32**, 37 (2019).
- [44] A. Le Duc, J. Sesterhenn, and R. Friedrich, *Instabilities in compressible attachment-line boundary layers*, *Physics of Fluids* **18**, 044102 (2006).
- [45] C. D. Pruett, C. L. Chang, and C. L. Streett, *Simulation of crossflow instability on a supersonic highly swept wing*, *Computers and Fluids* **29**, 33 (2000).
- [46] G. T. Duncan Jr, *The effects of step excrescences on swept-wing boundary-layer transition*, Ph.D. thesis, Texas A & M University (2014).
- [47] R. K. Soni, N. Arya, and A. De, *Characterization of turbulent supersonic flow over a backward-facing step*, *AIAA Journal* **55**, 1511 (2017).
- [48] F. Schäfer, M. Breuer, and F. Durst, *The dynamics of the transitional flow over a backward-facing step*, *Journal of Fluid Mechanics* **623**, 85 (2009).
- [49] J. L. Eppink, R. W. Wlezien, R. A. King, and M. Choudhari, *Interaction of a backward-facing step and crossflow instabilities in boundary-layer transition*, *AIAA Journal* **56**, 497 (2017).
- [50] J. R. Brinkerhoff and M. I. Yaras, *Interaction of viscous and inviscid instability modes in separation-bubble transition*, *Physics of Fluids* **23**, 124102 (2011).

- [51] J. J. Ginoux, *The existence of three-dimensional perturbations in the reattachment of a two-dimensional supersonic boundary-layer after separation*, Tech. Rep. (Von Karman Institute for Fluid Dynamics, 1960).
- [52] P. Balakumar, R. A. King, and J. L. Eppink, *Effects of forward and backward facing steps on the crossflow receptivity and stability in supersonic boundary layers*, in *44th AIAA Fluid Dynamics Conference* (AIAA 2014-2639, Atlanta, Georgia, 2014).
- [53] Y. Zhu, S. Yi, D. Gang, and L. He, *Visualisation on supersonic flow over backward-facing step with or without roughness*, *Journal of Turbulence* **16**, 633 (2015).
- [54] J. Tihon, J. Legrand, and P. Legentilhomme, *Near-wall investigation of backward-facing step flows*, *Experiments in Fluids* **31**, 484 (2001).
- [55] A. T. Sriram and D. Chakraborty, *Numerical exploration of staged transverse injection into confined supersonic*, *Defence Science Journal* **61**, 3 (2011).
- [56] W. Eissler and H. Bestek, *Spatial numerical simulations of linear and weakly nonlinear wave instabilities in supersonic boundary layers*, *Theoretical and Computational Fluid Dynamics* **8**, 219 (1996).
- [57] C. S. J. Mayer, S. Wernz, and H. F. Fasel, *Numerical investigation of the nonlinear transition regime in a Mach 2 boundary layer*, *Journal of Fluid Mechanics* **668**, 113 (2011).
- [58] O. Marxen, G. Iaccarino, and E. S. G. Shaqfeh, *Nonlinear instability of a supersonic boundary layer with two-dimensional roughness*, *Journal of Fluid Mechanics* **752**, 497 (2014).
- [59] I. I. Lipatov and R. Y. Tugazakov, *Nonlinear instability in the region of laminar-turbulent transition in supersonic three-dimensional flow over a flat plate*, *Fluid Dynamics* **53**, 285 (2018).
- [60] P. Paredes, M. M. Choudhari, and F. Li, *Instability wave-streak interactions in a supersonic boundary layer*, *Journal of Fluid Mechanics* **831**, 524 (2017).
- [61] D. V. Khotyanovsky and A. N. Kudryavtsev, *Direct numerical simulation of transition to turbulence in a supersonic boundary layer*, *Journal of Applied Mechanics and Technical Physics* **58**, 826 (2017).
- [62] H. Abu-Mulaweh, *A review of research on laminar mixed convection flow over backward- and forward-facing steps*, *International Journal of Thermal Sciences* **42**, 897 (2003).
- [63] H. I. Abu-Mulaweh, B. F. Armaly, and T. S. Chen, *Measurements of laminar mixed convection flow over a horizontal forward-facing step*, *Journal of Thermophysics and Heat Transfer* **7**, 569 (1993).
- [64] W. Shao and M. Agelin-Chaab, *Turbulent flows over forward facing steps with surface roughness*, *Journal of Fluids Engineering* **138**, 21103 (2016).
- [65] A. Worner, U. Rist, and S. Wagner, *Humps/steps influence on stability characteristics of two-dimensional laminar boundary layer*, *AIAA Journal* **41**, 192 (2003).
- [66] Y. X. Wang and M. Gaster, *Effect of surface steps on boundary layer transition*, *Experiments in Fluids* **39**, 679 (2005).

- [67] D. P. Rizzetta and M. R. Visbal, *Numerical simulation of excrescence generated transition*, *AIAA Journal* **52**, 385 (2014).
- [68] M. Costantini, S. Risius, C. Klein, and W. Kühn, *Effect of forward-facing steps on boundary layer transition at a subsonic Mach number*, in *Notes on Numerical Fluid Mechanics and Multidisciplinary Design*, Vol. 132 (Springer Verlag, Switzerland, 2016) pp. 203–213.
- [69] C. A. Edelmann and U. Rist, *Impact of forward-facing steps on laminar-turbulent transition in transonic flows*, *AIAA Journal* **53**, 2504 (2015).
- [70] C. Thomas, S. M. Mughal, H. Roland, R. Ashworth, and A. Martinez-Cava, *Effect of small surface deformations on the stability of Tollmien–Schlichting disturbances*, *AIAA Journal* **56**, 2157 (2018).
- [71] M. Dong and A. Zhang, *Scattering of Tollmien-Schlichting waves as they pass over forward-/backward-facing steps*, *Applied Mathematics and Mechanics* **39**, 1411 (2018).
- [72] D. Wilhelm, C. Härtel, and L. Kleiser, *Computational analysis of the two-dimensional-three-dimensional transition in forward-facing step flow*, *Journal of Fluid Mechanics* **489**, 1 (2003).
- [73] H. Stüer, A. Gyr, and W. Kinzelbach, *Laminar separation on a forward facing step*, *European Journal of Mechanics - B/Fluids* **18**, 675 (1999).
- [74] I. E. Abdalla, Z. Yang, and M. Cook, *Computational analysis and flow structure of a transitional separated-reattached flow over a surface mounted obstacle and a forward-facing step*, *International Journal of Computational Fluid Dynamics* **23**, 25 (2009).
- [75] H. Zhu and S. Fu, *Forward-facing steps induced transition in a subsonic boundary layer*, *Science China Physics, Mechanics & Astronomy* **60**, 104712 (2017).
- [76] M. W. Tufts, H. L. Reed, B. K. Crawford, G. T. Duncan, and W. S. Saric, *Computational investigation of step excrescence sensitivity in a swept-wing boundary layer*, *Journal of Aircraft* **54**, 602 (2017).
- [77] N. T. Clemens and V. Narayanaswamy, *Low-frequency unsteadiness of shock wave/turbulent boundary layer interactions*, *Annual Review of Fluid Mechanics* **46**, 469 (2014).
- [78] A. J. Smits and J. P. Dussauge, *Turbulent shear layers in supersonic flow*, 2nd ed. (Springer Science & Business Media, 2006).
- [79] K. J. Plotkin, *Shock wave oscillation driven by turbulent boundary-layer fluctuations*, *AIAA Journal* **13**, 1036 (1975).
- [80] J. Andreopoulos and K. C. Muck, *Some new aspects of the shock-wave/boundary-layer interaction in compression-ramp flows*, *Journal of Fluid Mechanics* **180**, 405 (1987).
- [81] O. Unalms and D. Dolling, *On the possible relationship between low frequency unsteadiness of shock-induced separated flow and Goertler vortices*, in *Fluid Dynamics Conference* (AIAA 96-2002, New Orleans, Louisiana, 1996) pp. 1–18.

- [82] J. Poggie and A. J. Smits, *Shock unsteadiness in a reattaching shear layer*, Journal of Fluid Mechanics **429**, 155 (2001).
- [83] S. J. Beresh, N. T. Clemens, and D. S. Dolling, *Relationship between upstream turbulent boundary-layer velocity fluctuations and separation shock unsteadiness*, AIAA Journal **40**, 2412 (2002).
- [84] W. B. McClure, *An experimental study of the driving mechanism and control of the unsteady shock induced turbulent separation in a Mach 5 compression corner flow*, Ph.D. thesis, University of Texas at Austin, Austin (1992).
- [85] B. Ganapathisubramani, N. T. Clemens, and D. S. Dolling, *Effects of upstream boundary layer on the unsteadiness of shock-induced separation*, Journal of Fluid Mechanics **585**, 369 (2007).
- [86] R. A. Humble, G. E. Elsinga, F. Scarano, and B. W. van Oudheusden, *Three-dimensional instantaneous structure of a shock wave/turbulent boundary layer interaction*, Journal of Fluid Mechanics **622**, 33 (2009).
- [87] E. Toubert and N. D. Sandham, *Low-order stochastic modelling of low-frequency motions in reflected shock-wave/boundary-layer interactions*, Journal of Fluid Mechanics **671**, 417 (2011).
- [88] K. M. Porter and J. Poggie, *Selective upstream influence on the unsteadiness of a separated turbulent compression ramp flow*, Physics of Fluids **31** (2019), 10.1063/1.5078938.
- [89] M. E. Erengil and D. S. Dolling, *Unsteady wave structure near separation in a Mach 5 compression ramp interaction*, AIAA Journal **29**, 728 (1991).
- [90] F. O. Thomas, C. M. Putnam, and H. C. Chu, *On the mechanism of unsteady shock oscillation in shock wave/turbulent boundary layer interactions*, Experiments in Fluids **18**, 69 (1994).
- [91] P. Dupont, C. Haddad, and J. F. Debiève, *Space and time organization in a shock-induced separated boundary layer*, Journal of Fluid Mechanics **559**, 255 (2006).
- [92] S. Pirozzoli and F. Grasso, *Direct numerical simulation of impinging shock wave/turbulent boundary layer interaction at  $M=2.25$* , Physics of Fluids **18**, 065113 (2006).
- [93] E. Toubert and N. D. Sandham, *Large-eddy simulation of low-frequency unsteadiness in a turbulent shock-induced separation bubble*, Theoretical and Computational Fluid Dynamics **23**, 79 (2009).
- [94] S. Piponniau, J. P. Dussauge, J. F. Debiève, and P. Dupont, *A simple model for low-frequency unsteadiness in shock-induced separation*, Journal of Fluid Mechanics **629**, 87 (2009).
- [95] M. Wu and M. P. Martin, *Analysis of shock motion in shockwave and turbulent boundary layer interaction using direct numerical simulation data*, Journal of Fluid Mechanics **594**, 71 (2008).
- [96] M. Grilli, P. J. Schmid, S. Hickel, and N. A. Adams, *Analysis of unsteady behaviour in shockwave turbulent boundary layer interaction*, Journal of Fluid Mechanics **700**, 16 (2012).

- [97] M. Grilli, S. Hickel, and N. A. Adams, *Large-eddy simulation of a supersonic turbulent boundary layer over a compression–expansion ramp*, *International Journal of Heat and Fluid Flow* **42**, 79 (2013).
- [98] S. Priebe, J. H. Tu, C. W. Rowley, and M. P. Martín, *Low-frequency dynamics in a shock-induced separated flow*, *Journal of Fluid Mechanics* **807**, 441 (2016).
- [99] V. Pasquariello, S. Hickel, and N. A. Adams, *Unsteady effects of strong shock-wave/boundary-layer interaction at high Reynolds number*, *Journal of Fluid Mechanics* **823**, 617 (2017).
- [100] L. J. Souverein, P. Dupont, J.-F. Debiève, J.-P. Dussauge, B. W. van Oudheusden, and F. Scarano, *Effect of interaction strength on unsteadiness in shock-wave-induced separations*, *AIAA Journal* **48**, 1480 (2010).
- [101] N. Bonne, V. Brion, E. Garnier, R. Bur, P. Molton, D. Sipp, and L. Jacquin, *Analysis of the two-dimensional dynamics of a Mach 1.6 shock wave/transitional boundary layer interaction using a RANS based resolvent approach*, *Journal of Fluid Mechanics* **862**, 1166 (2019).
- [102] E. Loth, K. Kailasanath, and R. Lohner, *Supersonic flow over an axisymmetric backward-facing step*, *Journal of Spacecraft and Rockets* **29**, 352 (1992).
- [103] I. Bolgar, S. Scharnowski, and C. J. Kähler, *The effect of the Mach number on a turbulent backward-facing step flow*, *Flow Turbulence and Combustion* **101**, 653 (2018).
- [104] J. J. Ginoux, *Streamwise vortices in reattaching high-speed flows - A suggested approach*, *AIAA Journal* **9**, 759 (1971).
- [105] Z. Chen, S. Yi, L. He, L. Tian, and Y. Zhu, *An experimental study on fine structures of supersonic laminar/turbulent flow over a backward-facing step based on NPLS*, *Chinese Science Bulletin* **57**, 584 (2012).
- [106] C. Zhi, Y. Shihe, H. Lin, Z. Yangzhu, G. Yong, and W. Yu, *Spatial density fluctuation of supersonic flow over a backward-facing step measured by nano-tracer planar laser scattering*, *Journal of Visualization* **17**, 345 (2014).
- [107] A. Zheltovodov, *Shock waves/turbulent boundary-layer interactions - fundamental studies and applications*, in *Fluid Dynamics Conference (AIAA 96-1977, New Orleans, Louisiana, 1996)*.
- [108] P. E. Morgan and M. R. Visbal, *Numerical simulation exploring supersonic flow over a forward-facing cylindrical step*, in *45th AIAA Fluid Dynamics Conference (AIAA 2015-2640, Dallas, Texas, 2015)* pp. 1–21.
- [109] A. L. Kistler, *Fluctuating wall pressure under a separated supersonic flow*, *The Journal of the Acoustical Society of America* **36**, 543 (1964).
- [110] W. Behrens, *Separation of a supersonic turbulent boundary layer by a forward facing step*, in *AIAA 9th Aerospace Sciences Meeting (AIAA 71-127, New York, New York, 1971)* pp. 1–27.
- [111] E. E. Zukoski, *Turbulent boundary-layer separation in front of a forward-facing step*. *AIAA Journal* **5**, 1746 (1967).

- [112] M. D. White and M. R. Visbal, *Investigation of shock / turbulent boundary interaction unsteadiness with various obstructions*, in *46th AIAA Plasmadynamics and Lasers Conference* (AIAA 2015-3250, Dallas, Texas, 2015).
- [113] Q.-H. Zhang, T. Zhu, S. Yi, and A. Wu, *Flow control of micro-ramps on supersonic forward-facing step flow*, *Chinese Physics B* **25**, 054701 (2016).
- [114] J. N. Murugan and R. N. Govardhan, *Shock wave–boundary layer interaction in supersonic flow over a forward-facing step*, *Journal of Fluid Mechanics* **807**, 258 (2016).
- [115] M. Simonenko, A. Zubkov, and A. Kuzmin, *On the supersonic three-dimensional flow over an axisymmetric body with a forward-facing annular step*, in *AIP Conference Proceedings*, Vol. 1959 (AIP Publishing LLC, 2018) p. 050031.
- [116] D. Estruch-Samper and G. Chandola, *Separated shear layer effect on shock-wave/turbulent-boundary-layer interaction unsteadiness*, *Journal of Fluid Mechanics* **848**, 154 (2018).
- [117] D. R. Chapman, D. M. Kuehn, and H. K. Larson, *Investigation of separated flows in supersonic and subsonic streams with emphasis on the effect of transition*, Tech. Rep. (NACA technical report 1356, 1958).
- [118] S. Hickel, C. P. Egerer, and J. Larsson, *Subgrid-scale modeling for implicit large eddy simulation of compressible flows and shock-turbulence interaction*, *Physics of Fluids* **26**, 106101 (2014).
- [119] J. Smagorinsky, *General circulation experiments with the primitive equations*, *Monthly Weather Review* **91**, 99 (1963).
- [120] E. Garnier, N. Adams, and P. Sagaut, *Large Eddy Simulation for Compressible Flows* (Springer, Dordrecht, Netherlands, 2009).
- [121] S. Hickel, N. A. Adams, and J. A. Domaradzki, *An adaptive local deconvolution method for implicit LES*, *Journal of Computational Physics* **213**, 413 (2006).
- [122] S. Hickel, *Implicit turbulence modeling for large-eddy simulation*, Ph.D. thesis, Technische Universität München (2008).
- [123] S. Gottlieb and C.-W. Shu, *Total variation diminishing Runge-Kutta schemes*, *Mathematics of Computation* **67**, 73 (1998).
- [124] M. Klein, A. Sadiki, and J. Janicka, *A digital filter based generation of inflow data for spatially developing direct numerical or large eddy simulations*, *Journal of Computational Physics* **186**, 652 (2003).
- [125] Z.-T. Xie and I. P. Castro, *Efficient generation of inflow conditions for large eddy simulation of street-scale flows*, *Flow, Turbulence and Combustion* **81**, 449 (2008).
- [126] S. B. Pope, *Turbulent Flows* (Cambridge University Press, 2000).
- [127] M. Matsumoto and T. Nishimura, *Mersenne twister: a 623-dimensionally equidistributed uniform pseudo-random number generator*, *ACM Transactions on Modeling and Computer Simulation* **8**, 3 (1998).
- [128] T. S. Lund, X. Wu, and K. D. Squires, *Generation of turbulent inflow data for spatially-developing boundary layer simulations*, *Journal of Computational*

- Physics **140**, 233 (1998).
- [129] T. B. Gatski and J. P. Bonnet, *Compressibility, Turbulence and High Speed Flow*, 2nd ed. (Academic Press, 2013).
- [130] M. R. Malik, *Prediction and control of transition in supersonic and hypersonic boundary layers*, AIAA Journal **27**, 1487 (1989).
- [131] T. Herbert, *Parabolized stability equations*, Annual Review of Fluid Mechanics **29**, 245 (1997).
- [132] F. Pinna, *Numerical study of stability of flows from low to high Mach number*, Ph.D. thesis, von Karman Institute for Fluid Dynamics (2011).
- [133] K. Groot, *Derivation of and simulations with BiGlobal stability equations*, Master thesis, Delft University of Technology (2013).
- [134] J. Serpieri and M. Kotsonis, *Three-dimensional organisation of primary and secondary crossflow instability*, Journal of Fluid Mechanics **799**, 200 (2016).
- [135] S. Suryanarayanan, D. B. Goldstein, and G. L. Brown, *Roughness induced transition: A vorticity point of view*, Physics of Fluids **31**, 24101 (2019).
- [136] P. J. Schmid, *Dynamic mode decomposition of numerical and experimental data*, Journal of Fluid Mechanics **656**, 5 (2010).
- [137] T. Sayadi, P. Schmid, J. W. Nichols, and P. Moin, *Dynamic mode decomposition of controlled H-and K-type transitions*, Center for Turbulence Research Annual Research Briefs , 189 (2013).
- [138] Q. Zhang, Y. Liu, and S. Wang, *The identification of coherent structures using proper orthogonal decomposition and dynamic mode decomposition*, Journal of Fluids and Structures **49**, 53 (2014).
- [139] R. Leroux and L. Cordier, *Dynamic mode decomposition for non-uniformly sampled data*, Experiments in Fluids **57**, 94 (2016).
- [140] M. R. Jovanović, P. J. Schmid, and J. W. Nichols, *Sparsity-promoting dynamic mode decomposition*, Physics of Fluids **26**, 024103 (2014).
- [141] J. Matheis and S. Hickel, *On the transition between regular and irregular shock patterns of shock-wave/boundary-layer interactions*, Journal of Fluid Mechanics **776**, 200 (2015).
- [142] J. Casacuberta, K. J. Groot, H. J. Tol, and S. Hickel, *Effectivity and efficiency of selective frequency damping for the computation of unstable steady-state solutions*, Journal of Computational Physics **375**, 481 (2018).
- [143] L. M. Mack, *Special course on stability and transition of laminar flow*, Tech. Rep. (AGARD-R-709, 1984).
- [144] A. Tumin, *Three-dimensional spatial normal modes in compressible boundary layers*, Journal of Fluid Mechanics **586**, 295 (2007).
- [145] P. Balakumar and M. R. Malik, *Discrete modes and continuous spectra in supersonic boundary layers*, Journal of Fluid Mechanics **239**, 631 (1992).
- [146] O. Pettrache, S. Hickel, and N. A. Adams, *Large eddy simulations of turbulent enhancement due to forced shock motion in shock-boundary layer interaction*, in

- 17th AIAA International Space Planes and Hypersonic Systems and Technologies Conference* (AIAA 2011-2216, San Francisco, California, 2011).
- [147] B. Wang, N. D. Sandham, Z. Hu, and W. Liu, *Numerical study of oblique shock-wave/boundary-layer interaction considering sidewall effects*, *Journal of Fluid Mechanics* **767**, 526 (2015).
- [148] P. Schlatter and R. Örlü, *Assessment of direct numerical simulation data of turbulent boundary layers*, *Journal of Fluid Mechanics* **659**, 116 (2010).
- [149] O. Marxen and T. A. Zaki, *Turbulence in intermittent transitional boundary layers and in turbulence spots*, *Journal of Fluid Mechanics* **860**, 350 (2019).
- [150] S. Pirozzoli, F. Grasso, and T. B. Gatski, *Direct numerical simulation and analysis of a spatially evolving supersonic turbulent boundary layer at  $M = 2.25$* , *Phys. Fluids* **16**, 530 (2004).
- [151] A. Karimi, S. Wijeyakulasuriya, and M. Nalim, *Numerical study of supersonic flow over backward-facing step for scramjet application*, in *48th AIAA/ASME/SAE/ASEE Joint Propulsion Conference & Exhibit* (AIAA 2012-4001, Atlanta, Georgia, 2012).
- [152] K. Chakravarthy, K. Arora, and D. Chakraborty, *Use of digitally filtered inflow conditions for LES of flows over backward facing steps*, *European Journal of Mechanics, B/Fluids* **67**, 404 (2018).
- [153] A. Roshko and G. J. Thomke, *Observations of turbulent reattachment behind an axisymmetric downstream-facing step in supersonic flow*. *AIAA Journal* **4**, 975 (1966).
- [154] H. Liu, B. Wang, Y. Guo, H. Zhang, and W. Lin, *Effects of inflow mach number and step height on supersonic flows over a backward-facing step*, *Advances in Mechanical Engineering* **5**, 147916 (2013).
- [155] J. Jeong and F. Hussain, *On the identification of a vortex*, *Journal of Fluid Mechanics* **285**, 69 (1995).
- [156] J. H. Nie and B. F. Armaly, *Reverse flow regions in three-dimensional backward-facing step flow*, *International Journal of Heat and Mass Transfer* **47**, 4713 (2004).
- [157] P. G. Spazzini, G. Iuso, M. Onorato, N. Zurlo, and G. M. Di Cicca, *Unsteady behavior of back-facing step flow*, *Experiments in Fluids* **30**, 551 (2001).
- [158] J. Délerly, J. G. Marvin, and E. Reshotko, *Shock-wave boundary layer interactions*, Tech. Rep. (Advisory Group for Aerospace Research and Development, AGARD-AG-280, 1986).
- [159] N. D. Sandham and W. C. Reynolds, *Three-dimensional simulations of large eddies in the compressible mixing layer*, *Journal of Fluid Mechanics* **224**, 133 (1991).
- [160] T. Herbert, *Secondary instability of boundary layers*, *Annual Review of Fluid Mechanics* **20**, 487 (1988).
- [161] W. W. Willmarth and S. S. Lu, *Structure of the Reynolds stress near the wall*, *Journal of Fluid Mechanics* **55**, 65 (1972).
- [162] S. Cherubini, P. De Palma, J.-C. Robinet, and A. Bottaro, *The minimal seed of turbulent transition in the boundary layer*, *Journal of Fluid Mechanics* **689**, 221

- (2011).
- [163] T. Herbert, *Three-dimensional phenomena in the transitional flat-plate boundary layer*, in *23rd Aerospace Sciences Meeting* (AIAA 85-0489, Reston, Virginia, 1985).
- [164] S. Priebe and M. P. Martín, *Low-frequency unsteadiness in shock wave–turbulent boundary layer interaction*, *Journal of Fluid Mechanics* **699**, 1 (2012).
- [165] Y. Na and P. Moin, *Direct numerical simulation of a separated turbulent boundary layer*, *Journal of Fluid Mechanics* **374**, 379 (1998).
- [166] I. Lee and H. J. Sung, *Multiple-arrayed pressure measurement for investigation of the unsteady flow structure of a reattaching shear layer*, *Journal of Fluid Mechanics* **463**, 377 (2002).
- [167] C. W. Rowley, I. Mezić, S. Bagheri, P. Schlatter, and D. S. Henningson, *Spectral analysis of nonlinear flows*, *Journal of Fluid Mechanics* **641**, 115 (2009).
- [168] M. Chang, X. Meng, Z. Fu, and J. Bai, *Study on flow characteristics of compressible laminar flow boundary layers*, in *The Proceedings of the 2018 Asia-Pacific International Symposium on Aerospace Technology* (Springer, 2019) pp. 451–463.
- [169] Y. Ma and X. Zhong, *Receptivity of a supersonic boundary layer over a flat plate. Part 3. Effects of different types of free-stream disturbances*, *Journal of Fluid Mechanics* **532**, 63 (2005).
- [170] T. Hiejima, *Streamwise vortex breakdown in supersonic flows*, *Physics of Fluids* **29**, 054102 (2017).
- [171] T. Michelis, S. Yarusevych, and M. Kotsonis, *On the origin of spanwise vortex deformations in laminar separation bubbles*, *Journal of Fluid Mechanics* **841**, 81 (2018).
- [172] O. Marquet, D. Sipp, J.-M. Chomaz, and L. Jacquin, *Amplifier and resonator dynamics of a low-Reynolds-number recirculation bubble in a global framework*, *Journal of Fluid Mechanics* **605**, 429 (2008).
- [173] C. Cerretelli and C. H. K. Williamson, *The physical mechanism for vortex merging*, *Journal of Fluid Mechanics* **475**, 41 (2003).
- [174] T. Leweke, S. Le Dizès, and C. H. Williamson, *Dynamics and Instabilities of Vortex Pairs*, *Annual Review of Fluid Mechanics* **48**, 507 (2016).
- [175] J.-Z. Wu, H.-Y. Ma, and M.-D. Zhou, *Vorticity and Vortex Dynamics* (Springer, Berlin, Heidelberg, 2006) pp. 1–776.
- [176] A. Sansica, N. D. Sandham, and Z. Hu, *Instability and low-frequency unsteadiness in a shock-induced laminar separation bubble*, *Journal of Fluid Mechanics* **798**, 5 (2016).
- [177] C. R. Smith and S. P. Metzler, *The characteristics of low-speed streaks in the near-wall region of a turbulent boundary layer*, *Journal of Fluid Mechanics* **129**, 27 (1983).
- [178] W. Hu, S. Hickel, and B. van Oudheusden, *Dynamics of a supersonic transitional flow over a backward-facing step*, *Physical Review Fluids* **4**, 103904 (2019).
- [179] R. J. Hartfield, S. D. Hollo, and J. C. McDaniel, *Planar measurement technique for*

- compressible flows using laser-induced iodine fluorescence*, AIAA Journal **31**, 483 (1993).
- [180] C. E. Tinney and L. S. Ukeiley, *A study of a 3-D double backward-facing step*, Experiments in Fluids **47**, 427 (2009).
- [181] L. Agostini, L. Larchevêque, P. Dupont, J.-F. Debiève, and J.-P. Dussauge, *Zones of influence and shock motion in a shock/boundary-layer interaction*, AIAA Journal **50**, 1377 (2012).
- [182] J.-P. Dussauge, P. Dupont, and J.-F. Debiève, *Unsteadiness in shock wave boundary layer interactions with separation*, Aerospace Science and Technology **10**, 85 (2006).
- [183] F. Guiho, F. Alizard, and J.-C. Robinet, *Instabilities in oblique shock wave/laminar boundary-layer interactions*, Journal of Fluid Mechanics **789**, 1 (2016).
- [184] X. Huang and D. Estruch-Samper, *Low-frequency unsteadiness of swept shock-wave/turbulent-boundary-layer interaction*, Journal of Fluid Mechanics **856**, 797 (2018).
- [185] G. S. Settles, T. J. Fitzpatrick, and S. M. Bogdonoff, *Detailed study of attached and separated compression corner flowfields in high Reynolds number supersonic flow*, AIAA Journal **17**, 579 (1979).
- [186] E. Schülein and V. M. Trofimov, *Steady longitudinal vortices in supersonic turbulent separated flows*, Journal of Fluid Mechanics **672**, 451 (2011).
- [187] Z. Sun, F. E. Schrijer, F. Scarano, and B. W. van Oudheusden, *The three-dimensional flow organization past a micro-ramp in a supersonic boundary layer*, Physics of Fluids **24**, 055105 (2012).
- [188] K. Czarnecki and M. W. Jackson, *Turbulent boundary-layer separation due to a forward-facing step*, AIAA Journal **13**, 1585 (1975).
- [189] E. W. E. Rogers, C. J. Berry, and B. M. Davis, *An experimental investigation of the interaction between a forward-facing step and a laminar boundary layer in supersonic, low-density flow*, Tech. Rep. (No. 3506, London, 1965).
- [190] F. W. Spaid, *Cooled supersonic turbulent boundary layer separated by a forward facing step*, AIAA Journal **10**, 1117 (1972).
- [191] G. Chandola, X. Huang, and D. Estruch-Samper, *Highly separated axisymmetric step shock-wave/turbulent-boundary-layer interaction*, Journal of Fluid Mechanics **828**, 236 (2017).
- [192] X. Wu and P. Moin, *Direct numerical simulation of turbulence in a nominally zero-pressure-gradient flat-plate boundary layer*, Journal of Fluid Mechanics **630**, 5 (2009).
- [193] T. Sayadi, C. W. Hamman, and P. Moin, *Direct numerical simulation of complete H-type and K-type transitions with implications for the dynamics of turbulent boundary layers*, Journal of Fluid Mechanics **724**, 480 (2013).
- [194] P. T. Williams and A. J. Baker, *Numerical simulations of laminar flow over a 3D backward-facing step*, International Journal for Numerical Methods in Fluids **24**,

- 1159 (1997).
- [195] H. P. Rani, T. W. H. Sheu, and E. S. F. Tsai, *Eddy structures in a transitional backward-facing step flow*, *Journal of Fluid Mechanics* **588**, 43 (2007).
- [196] S. Risius, M. Costantini, S. Koch, S. Hein, and C. Klein, *Unit Reynolds number, Mach number and pressure gradient effects on laminar–turbulent transition in two-dimensional boundary layers*, *Experiments in Fluids* **59**, 86 (2018).
- [197] M. Gad-el Hak, *Flow control: passive, active, and reactive flow management* (Cambridge University Press, 2000).
- [198] A. G. Panaras and F. K. Lu, *Micro-vortex generators for shock wave/boundary layer interactions*, (2015).
- [199] P. L. Blinde, R. A. Humble, B. W. van Oudheusden, and F. Scarano, *Effects of micro-ramps on a shock wave/turbulent boundary layer interaction*, *Shock Waves* **19**, 507 (2009).
- [200] S. B. Verma and C. Manisankar, *Shockwave/boundary-layer interaction control on a compression ramp using steady microjets*, *AIAA Journal* **50**, 2753 (2012).
- [201] K. Kinefuchi, A. Y. Starikovskiy, and R. B. Miles, *Control of shock-wave/boundary-layer interaction using nanosecond-pulsed plasma actuators*, *Journal of Propulsion and Power* **34**, 909 (2018).



# ACKNOWLEDGEMENTS

This dissertation is based on the four-years collective research work conducted in the Aerodynamics Group, TU Delft. I am extremely grateful for the support and assistance provided by a number of wonderful persons throughout the path of my doctoral venture.

First of all, I would like to express my deepest appreciation to my brilliant supervisor and promoter, Professor Stefan Hickel. Since the beginning of my PhD, he has been patiently guiding and encouraging me to 'seek out new civilizations' in academic areas and conquer the tough challenges. Whenever I feel frustrated by the setbacks from research, he is always there to comfort me with his warm words, save me from the plight by coming up with some great solutions based on his profound knowledge and encourage me with his iconic smile. I also benefit enormously from the shining characters that he presented during my PhD, like his prudent academic attitude, spirit of diligence, enthusiasm for research. I still clearly remember that afternoon when he helped me to set up the simulation case. From four to ten o'clock, six hours without leaving his chair, he showed me the whole operation process step by step, from the installation, grid generation, parameter setting to running. His great attentiveness, dedication to the students and sharp mind really impressed me deeply. Let me devote my deep gratefulness once again to my supervisor, Stefan.

I would also like to extend my sincere gratitude to my amiable co-supervisor and promoter Bas W. van Oudheusden. During my PhD, he has been very supportive and patient. No matter when I went to his office to discuss questions, he was always willing to help me out with his rich knowledge. His meticulous academic attitude leaves a deep impression on me. When he reviewed the paper that I wrote, he looked into every detail, from physical explanation, logical structure, grammar, references even to punctuation. To be honest, the total number of comments that he made on all our papers is already over one thousand. Allow me to express my heartfelt appreciation again to my highly respected co-supervisor Bas.

I am also grateful to the staff in our group. Thanks to our beloved secretary, Colette Russo, who took care of all our administrative work professionally. Without her help, we could be disturbed from our research. I also appreciate the technical support from Nico and beneficial discussion with Marios, Fulvio, Ferry and Sander on various occasions.

I want to record my sincere thanks to all my PhD fellows: Alberto, Alessandro, Alexander, Beppe, Christoph, Constantin, Edoardo, Gabriel, Jacobo, Jordi, Koen, Kushal, Luis, Martin, Mohamad, Paul, Qingqing, Rakesh, Sagar, Shaafi, Theo, Tiago, Varun, Wouter, Zenó. Thanks for all the talk and discussion we had over all kinds of lectures,

workshops and conferences. I also quite enjoyed the time we spent together during the lunches, coffee breaks, barbecues, organized dinners and other activities.

Special thanks to my dear Chinese friends during my stay in Europe. They are Bowen, Chenteng, Haohua, Jun, Kaisheng, Ming, Wenqing, Xiaodong, Yi, Yu. The dinners and hangouts we organized brought many colors to our lives. Thanks for the wonderful trips we made together in Europe.

This work is part of the research project "Dynamics of a backward/forward-facing step in a supersonic flow" under Project No. 2019.045, which was partly financed by the Dutch Research Council (NWO). The computational parts were mostly carried out on the Dutch National e-Infrastructure with the support of SURF Cooperative.

Last but not least, I would like to express my heartfelt gratitude to my parents. Thanks for their selfless love and unconditional support throughout these years.

July 10th, 2020

## SUPPLEMENTARY INFORMATION

Most of research data and code supporting the findings described in this thesis are available in 4TU.Centre for Research Data at: <http://doi.org/10.4121/uuid:4f8c3413-9ede-4be8-bd69-4247f685f7dc>.



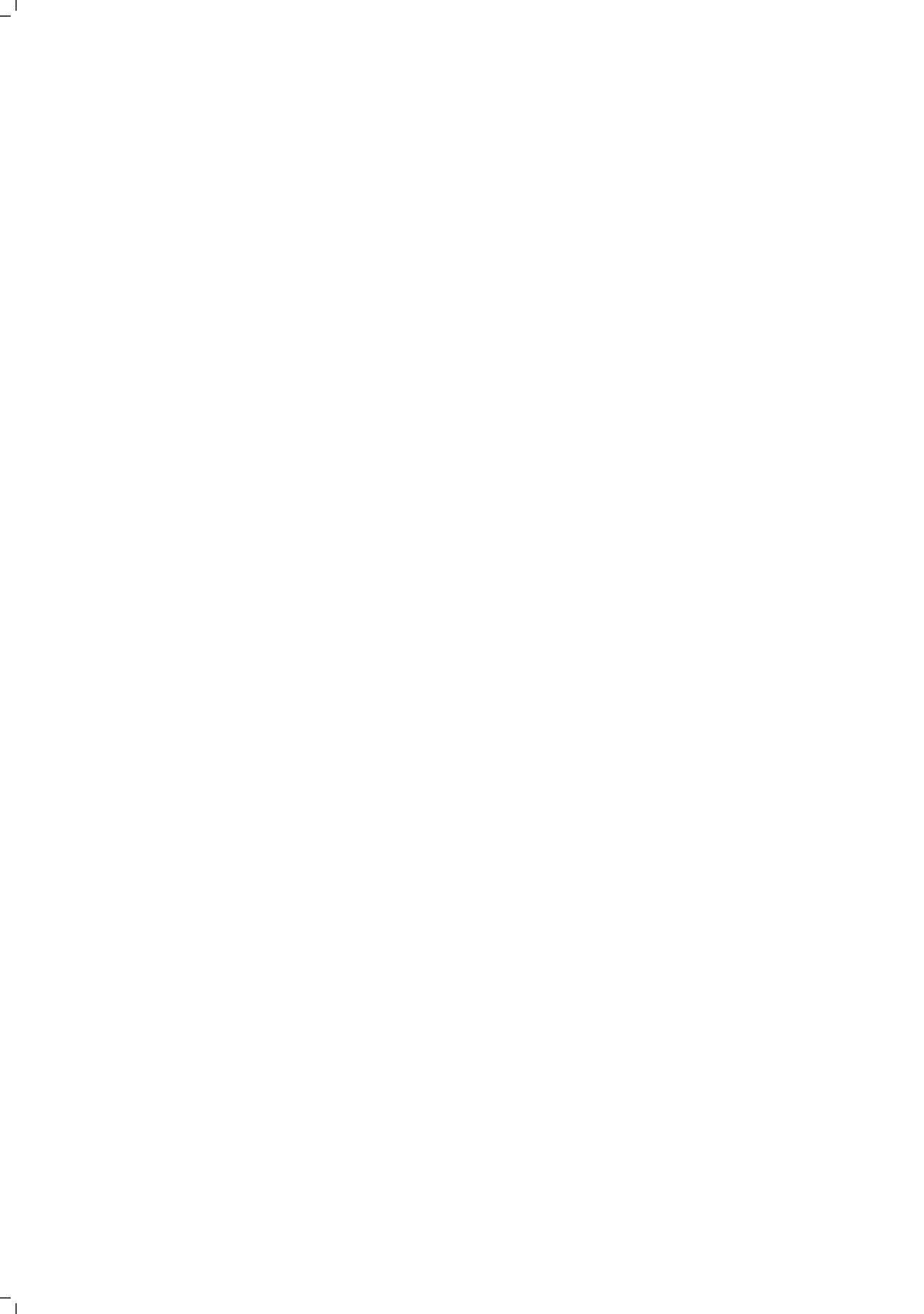
# SCIENTIFIC CONTRIBUTIONS

## JOURNAL ARTICLES

3. **W. Hu**, S. Hickel, B. van Oudheusden, *Low-frequency unsteadiness mechanisms in shock wave/turbulent boundary layer interactions over a backward-facing step*, Journal of Fluid Mechanics (under review).
2. **W. Hu**, S. Hickel, B. van Oudheusden, *Influence of upstream disturbances on the primary and secondary instabilities in a supersonic separated flow over a backward-facing step*, Physics of Fluids **32**, 56102 (2020).
1. **W. Hu**, S. Hickel, B. van Oudheusden, *Dynamics of a supersonic transitional flow over a backward-facing step*, Physical Review Fluids **4**, 103904 (2019).

## CONFERENCE PROCEEDINGS

3. **W. Hu**, S. Hickel, B. van Oudheusden, *Unsteady interaction between shock wave and separated boundary layer over a backward-facing step*, 13th International ER-COFTAC Symposium on Engineering Turbulence Modelling and Measurements, Rhodes, Greece (postponed).
2. **W. Hu**, S. Hickel, B. van Oudheusden, *Shock wave-boundary layer interaction in a transitional flow over a backward-facing step*, 54th 3AF International Conference on Applied Aerodynamics, Paris, France (2019).
1. **W. Hu**, S. Hickel, B. van Oudheusden, *Transition mechanism behind a backward-facing step in a supersonic flow*, 11th International Symposium on Turbulence and Shear Flow Phenomena, Southampton, UK (2019).



# BIOGRAPHY

Weibo Hu grew up in a small village of Gongyi, Henan Province in China. Although both of his parents were just ordinary farmers back then, they really realized the importance of good education to his personal development in the future. They put considerable efforts into his education despite the very limited resources. Perhaps the mechanical models and toys that he made in the nature class ignited his early interest in science and technology. During the primary and middle school, his curiosity and enthusiasm had led him to excel at various subjects.

Through his consistently hard work, he got accepted by a key high school in the capital city of Henan Province, with a full scholarship. With the better equipment and quality of education, he enriched his knowledge and broadened his horizon. Moreover, he met many wonderful friends and learned to be independent during his boarding life at school since then. As one of the greatest periods in his life, he really enjoyed these three years despite much pressure from the study.

At the age of eighteen, he was admitted by Air Force Engineering University in Xi'an, and majored in flight performance and propulsion engineering. Throughout his college years, he gained the basic knowledge of fluid mechanics, flight dynamics and propulsion theory, which laid the foundation for his future research work. During his master, he investigated the effects of the inflow distortion on the performance of turbo engines using numerical simulation. In addition, he also did some work about the performance calculation of various gas turbines by developing a numerical code based on C++. At late of 2015, he decided to pursue his research interest abroad and moved to Delft University of Technology in October 2016. As a PhD candidate, he worked on the fundamental aerodynamics by computational method in the Aerodynamics Group.